https://journals.vsu.ru/kcmf/about

ISSN 1606-867X
eISSN 2687-0711

Конденсированные среды и межфазные границы

РЕЦЕНЗИРУЕМЫЙ НАУЧНЫЙ ЖУРНАЛ

Condensed Matter and Interphases

PEER-REVIEWED SCIENTIFIC JOURNAL

Том / Vol. 27, № / No. 4
2025

Condensed Matter and Interphases
Kondensirovannye sredy i mezhfaznye granitsy

Peer-reviewed scientific journal
Published since January 1999
Periodicity: Quarterly
Volume 27, No. 4, 2025

Full-text version is available in the Russian language on the website: https://journals.vsu.ru/kcmf

Condensed Matter and Interphases (Kondensirovannye Sredy i Mezhfaznye Granitsy) publishes articles in Russian and English dedicated to key issues of condensed matter and physicochemical processes at interfaces and in volumes.

The mission of the journal is to provide open access to the results of original research (theoretical and experimental) at the intersection of contemporary condensed matter physics and chemistry, material science and nanoindustry, solid state chemistry, inorganic chemistry, and physical chemistry, and to share scientific data in the **following sections**: atomic, electron, and cluster structure of solids, liquids, and interphase boundaries; phase equilibria and defect formation processes; structure and physical and chemical properties of interphases; laser thermochemistry and photostimulated processes on solid surfaces; physics and chemistry of surface, thin films and heterostructures; kinetics and mechanism of formation of film structures; electrophysical processes in interphase boundaries; chemistry of surface phenomena in sorbents; devices and new research methods.

The journal accepts for publication: reviews, original articles, short communications by leading Russian scientists, foreign researchers, lecturers, postgraduate and undergraduate students.

FOUNDER AND PUBLISHER:
Voronezh State University

The journal is registered by the Russian Federal Service for Supervision of Communications, Information Technology and Mass Media, Certificate of Registration ПИ № ФС77-78771 date 20.07.2020

The journal is included in the List of peer reviewed scientific journals published by the Higher Attestation Commission in which major research results from the dissertations of Candidates of Sciences (PhD) and Doctor of Science (DSc) degrees are to be published. Scientific specialties of dissertations and their respective branches of science are as follows: 1.4.1. – Inorganic Chemistry (Chemical sciences); 1.4.4. – Physical Chemistry (Chemical sciences); 1.4.6. – Electrochemistry (Chemical sciences); 1.4.15. – Solid State Chemistry (Chemical sciences); 1.3.8. – Condensed Matter Physics (Physical sciences).

The journal is indexed and archived in: Russian Scientific Index Citations, Scopus, Chemical Abstract, EBSCO, DOAJ, CrossRef

Editorial Board and Publisher Office:
1 Universitetskaya pl., Voronezh 394018
Phone: +7 (432) 2208445
https://journals.vsu.ru/kcmf
E-mail: kcmf@main.vsu.ru

ISSN 1606-867X (Print)
ISSN 2687-0711 (Online)
Конденсированные среды и межфазные границы / Condensed Matter and Interphases. 2025, 27(4)

CONTENTS

Review

Ahmadova G. A., Rahimov R. A., Abilova A. Z., Nasibova Sh. M., Mammadova Kh. A.
The role of polymeric surfactants in enhanced oil recovery: a review 533

Shostak N. A.
Azeotropism of clathrate hydrates: a brief overview 547

Original articles

Le Ngoc Khanh Nhu, Nguyen Thi Thu Trang, Nguyen Hoang Huy, Tran Dinh Trinh, Ngoc Anh Vu Thi, Nguyen Anh Tien
Structural, optical and magnetic properties of $CoFe_{2-x}Eu_xO_4$ nanoparticles prepared by simple co-precipitation route 555

Aliev O. M., Azhdarova D. S., Agayeva R. M., Ragimova V. M.
Phase equilibria and some properties of solid solutions of $PbGa_2S_4$–$SmGa_2S_4$ and $PbGa_2Se_4$–$SmGa_2Se_4$ systems 565

Belenova A. S., Polkovnikova Yu. A., Slivkin A. I., Semenov V. N., Vasilieva S. I., Golovina A. A., Saranov I. A.
Study of the influence of the nature and concentration of the solubilizer on the process of formation of solid dispersions of chloronitrophenol 573

Vakhnin D. D., Fertikova T. E., Zheltoukhova N. A., Kravchenko T. A., Kozaderov O. A.
Redox sorption of oxygen by Pd- and Cu-containing nanocomposites in the over-limiting current mode of electrochemical polarization 581

Vdovenkov F. A., Kolosov A. N., Kuzmenko G. A., Kozaderov O. A.
Simulation of a non-stationary electrochemical process on rough electrodes under mixed kinetic-diffusion control 592

Ismayilova E. N., Mashadiyeva L. F., Bakhtiyarly I. B., Gasymov V. A., Huseynova I. F., Jafarov Y. I.
Experimental study of phase equilibria in the Cu_2SnSe_3-Cu_3SbSe_4-Se ternary system 606

Kozaderova O. A., Saranov I. A.
Hydration properties of heterogeneous ion exchange membranes after their long-term use in the electrodialysis treatment of wastewater from the production of mineral fertilizers 615

Kruzhilin A. A., Shevtsov D. S., Dmitriev I. A., Potapov M. A., Shikhaliev Kh. S.
Synthesis and anticorrosive properties of 2-alkyl-5-methyl-4,5,6,7-tetrahydro-[1,2,4] triazolo[1,5-a]pyrimidin-7-ols 630

Nabiyev E. R., Orujlu E. N., Hasanov A. A., Aghazade A. I., Aliyeva S. H., Yusibov Yu. A.
Phase equilibria in the GeTe-Sb_2Te_3-Te system 639

Nevelskaya A. K., Belenov S. V., Gavrilova A. A., Paperzh K. O., Lyanguzov N. V., Pankov I. V., Kokhanov A. A.
Study of the influence of the microstructure of Pt/C materials on the electrochemical characteristics of PtCo/C electrocatalysts based on them 651

Rakityanskaya I. L., Myasnikov D. A.
Formation of oxide films on manganese silicide-germanides of various compositions during anodic polarization in an aqueous sodium sulfate solution 661

Samoylov A. M., Dontsov A. I., Prizhimov A. S., Vakhmin S. Yu.
Phase composition and texture of palladium (II) oxide thin films on SiO_2/Si 669

Soloboeva T. P., Dabizha O. N., Batukhtin A. G.
Composition, structure, and electrophysical properties of natural zeolite clinoptilolites subjected to mechanical activation with potassium hydrosulfate 676

Shaposhnik A. V., Arefieva O. A., Zviagin A. A., Brezhnev N. Yu., Vysotskaya E. A., Vasiliev A. A., Ryabtsev S. V., Turishchev S. Yu.
Biotemplate synthesis of In_2O_3-Pd for room temperature sensor of hydrogen 689

Anniversaries

Margolin V. I.
Congratulations to Professor A. G. Syrkov 696

ISSN 1606-867X (Print)
ISSN 2687-0711 (Online)
Condensed Matter and Interphases
Kondensirovannye Sredy i Mezhfaznye Granitsy
https://journals.vsu.ru/kcmf/

Review

Review article
https://doi.org/10.17308/kcmf.2025.27/13252

The role of polymeric surfactants in enhanced oil recovery: a review

G. A. Ahmadova[1]✉, R. A. Rahimov[1,2,3], A. Z. Abilova[1], Sh. M. Nasibova[1], Kh. A. Mammadova[1]

[1]*Institute of Petrochemical Processes of the Ministry of Science and Education of Azerbaijan, 30 Hojaly ave., AZ 1025, Baku, Azerbaijan*

[2]*Department of Chemical Engineering, Baku Engineering University, 120 Hasan Aliyev st., Baku, Absheron AZ0101, Azerbaijan*

[3]*Department of Chemical Engineering, School of Engineering and Applied Science, Khazar University, 41 Mahsati st., Baku AZ 1096, Azerbaijan*

Abstract

Objective of the article: The continuously increasing demand for oil and petroleum products necessitates the further development of enhanced oil recovery (EOR) methods, including physicochemical techniques such as polymer flooding. Currently, billions of tons of oil remain dispersed and scattered within water-flooded reservoirs. This article provides a review of the literature on the synthesis and application of surfactant solutions and their mixtures with various components (polymers, salts, acids, etc.) in EOR processes.

Experimental section: The use of surfactants contributes to reducing interfacial tension and increasing wettability. Polymeric surfactants represent a promising alternative to modern systems employed in chemical EOR. They can combine the necessary rheological and interfacial properties in a single component, whereas typically, this requires mixtures of several chemical substances. Improved flooding properties using polymeric surfactants are essential for recovering residual oil. In addition to their unique characteristics, it is important to ensure synergy between the surfactant or polymer and other components that meet strict technical requirements. Furthermore, EOR based on polymeric surfactant systems is technologically compatible with conventional water flooding and does not require significant capital investment.

Conclusions: It should be noted that numerous studies have been devoted to the processes of EOR. The presented article emphasizes the efficiency and feasibility of using surfactants based on the results of tests studying the physicochem.

Keywords: Enhanced oil recovery; Polymer surfactant; Ionic liquid; Surface tension; Wettability

For citation: Ahmadova G. A., Rahimov R. A., Abilova A. Z., Nasibova Sh. M., Mammadova Kh. A. The role of polymeric surfactants in enhanced oil recovery: a review. *Condensed Matter and Interphases*. 2025;27(4): 533–546. https://doi.org/10.17308/kcmf.2025.27/13252

Для цитирования: Ахмедова Г. А., Рагимов Р. А., Абилова А. З., Насибова Ш. М., Мамедова Х. А. Роль полимерных поверхностно-активных веществ в повышении нефтеотдачи пластов. Обзор. *Конденсированные среды и межфазные границы*. 2025;27(4): 533–546. https://doi.org/10.17308/kcmf.2025.27/13252

✉ Gulnara A. Ahmadova, e-mail: ahmadovagulnara@mail.ru

The importance of oil in the global economy is well known. Its consumption by various sectors of the economy has reached colossal proportions, and further growth is expected in the near future. Currently, primary and secondary oil recovery methods account for the extraction of roughly half of the oil reserves in reservoirs [1–6]. Under unfavorable reservoir conditions (such as high heterogeneity of the formation, presence of clay impurities, high oil viscosity, low rock permeability, etc.), the oil displacement coefficient rarely exceeds 30–35 %. The depletion of total oil resources necessitates the improvement of secondary and tertiary oil recovery methods [7–9]. These methods are divided into several groups, including physicochemical ones, which encompass techniques involving surfactants, water-soluble polymers, acids, micellar solutions, as well as micellar-polymer flooding [10–13].

Physicochemical methods for increasing oil recovery are highly promising and exceptionally effective, as they can significantly raise both the oil displacement coefficient and the sweep efficiency of the reservoir by the flooding solution. It is necessary to emphasize the high efficiency of these methods in the extraction of relatively hard-to-recover heavy oils, whose share in global production continues to grow [14–16]. In addition, recent scientific and technical literature highlights studies focused on developing and applying technologies to enhance oil recovery using nanofluids and nanogels [17–21]. Researchers have found that the use of nanoparticles can alter the wettability of reservoir rocks, reduce interfacial tension, lower oil viscosity, and increase disjoining pressure.

Oil recovery from reservoirs largely depends on the properties of the interfaces between oil, water, gas, and rock. High extraction rates can be achieved by increasing the capillary number, which is defined as the ratio of viscous forces to surface tension [22–25]. To achieve a sufficiently high capillary number effective for displacing oil from the reservoir rock and pore spaces, an ultra-low interfacial tension in the range of 10^{-3} mN/m is required [26–34]. Such low interfacial tension can be achieved through the use of surfactants and/or combinations of surfactants [35–38]. The use of surfactants in tertiary oil recovery represents a promising direction that requires detailed investigation not only of the surfactants themselves but also of their mixed solutions with polymers, salts, acids, and other components capable of enhancing their performance.

The purpose of this review is to provide a concise analysis of studies on the synthesis and properties of reagents used for tertiary oil recovery.

Polymers employed to enhance oil production should dissolve well in saline water and possess the ability to reduce surface tension. For this purpose, polymers containing functional groups, surface-active polymers, surfactant–polymer complexes, surfactant–polymer mixtures, and surface-active oligomers are used [39–48].

In recent years, to avoid side effects associated with alkali–surfactant–polymer flooding (caused by the use of caustic alkalis), greater attention has been given to alkali-free surfactant–polymer flooding [49]. This approach makes surfactants more hydrophobic. Researchers have synthesized a new type of carboxybetaine surfactant – didodecyl polyoxyethylene (n) ether methylcarboxylbetaine (di$C_{12}E_nB$, n = 2, 3, 4) – in the form of homogeneous compounds, as well as dicocosyl alcohol polyoxyethylene ether methylcarboxylbetaine, and evaluated their properties as surfactants for alkali-free surfactant–polymer flooding. With an increase in the number of ethylene oxide groups, the solubility of surfactants increases, while their adsorption capacity decreases, resulting in enhanced hydrophilicity of the surfactant molecules. The use of these surfactants enables the achievement of ultra-low interfacial tension values on the order of 10^{-2} mN/m between crude oil and water.

N. V. Klyuchnikova and co-authors [50] developed a formulation for the production a polymeric surfactant based on xylene–formaldehyde resin and 4-aminoantipyrine. FTIR spectroscopic studies confirmed the proposed structure of the synthesized compound.

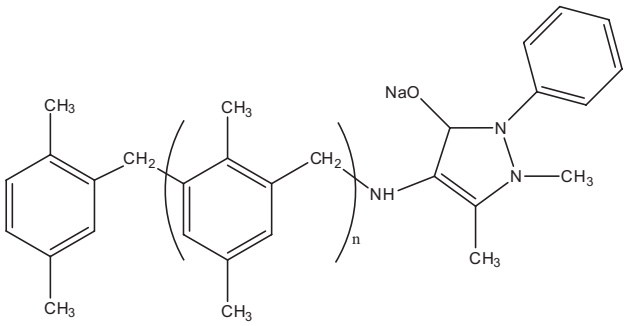

The technological characteristics of the obtained product were studied. The investigation of the wettability intensity of a solid surface by the synthesized polymeric surfactant showed that at a surfactant concentration of 0.05 %, instantaneous absorption into the surface occurs. The surface tension of the synthesized polymeric surfactant solution at the air interface was also examined. At a concentration of 1.2 %, the surface tension decreased to 38.7 mN/m. The hydrophilic–lipophilic balance was calculated using the Davies method, yielding a value of 8.33. These studies indicate the potential applicability of the synthesized polymeric surfactant as a wetting additive.

M. Madani [51] and co-authors conducted fundamental research on an environmentally friendly surfactant as a chemical agent for EOR. Surfactant injection is a key chemical EOR method that enhances oil production from underground reservoirs by reducing interfacial tension and altering wettability. However, most available or proposed synthetic surfactants have negative environmental impacts. In this study, a new synthesis procedure was described for a surfactant based on amino acids, which is non-toxic, biocompatible, and easily biodegradable. The interfacial tension (measured using the pendant drop method) at the kerosene–water interface and the wettability of the surfactant solution (measured by the contact angle method) were determined in the presence of both oil phase and characteristic rock types (carbonate and sandstone). By evaluating the critical micelle concentration (CMC), the optimal surfactant concentration was determined (under typical salinity conditions) for conducting dynamic secondary and tertiary core flooding tests. A comparison of secondary and tertiary flooding schemes using the surfactant suggests that it is potentially more effective when introduced as a secondary recovery agent.

Researchers from Bashkortostan [52] investigated the physicochemical properties of a surfactant–polymer system for EOR. As the base components, polyacrylamide

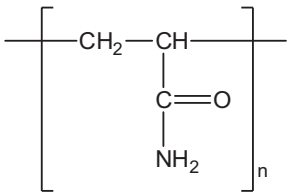

and a micelle-forming anionic surfactant (brand A) derived from plant-based raw materials were used,

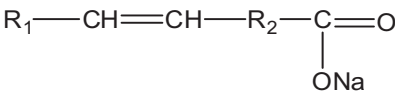

where R_1, R_2 – C_6–C_9.

Based on them, two surfactant–polymer systems were prepared. In the first case, the reagent containing a water-soluble polymer was designated as the basic formulation (grade B), while in the second case, the reagent containing both a water-soluble polymer and modifying additives was designated as the optimized formulation (also grade B). Both systems belong to the category of “green chemistry” reagents. The dependence of dynamic viscosity of the tested solutions on concentration at different temperatures was investigated. At a polyacrylamide solution concentration of 0.11 wt. %, increasing the temperature from 10 to 60 °C reduced the viscosity from 22.6 mPa·s to 7.7 mPa·s. For grade A, increasing the temperature and concentration did not cause significant changes. The grade B reagents behaved similarly to polyacrylamide solutions – that is, as temperature increased, viscosity decreased, while increasing concentration led to further rise in viscosity. The surface activity of aqueous reagent solutions at the kerosene–water interface was also examined. It was found that reagent grade A exhibited the highest surface activity: at a concentration of 0.3 %, the interfacial tension was 2.5 mN/m. Based on the experimental data, graphs were constructed showing the dependence of interfacial tension on reagent concentration at the kerosene interface (Fig. 1).

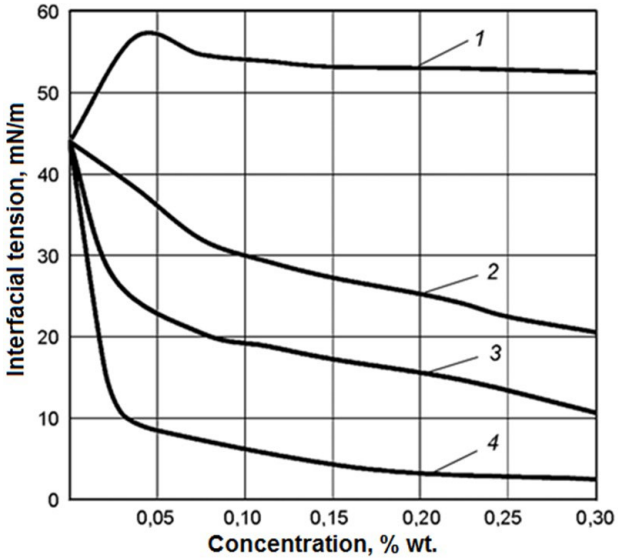

Fig. 1. Graph of the dependence of surface tension on the concentration of the reagent solution at the interface with kerosene [52]: *1* – polyacrylamide; *2* – basic (grade B); *3* – optimized (grade B); *4* – (grade A)

Analysis of these results suggests a positive influence of the developed systems on EOR processes.

Surfactants of polymeric and oligomeric nature synthesized by the authors [53–54] were tested for oil-displacing capability with the aim of using them to increase oil recovery from reservoirs [55–61]. Laboratory experiments involved propoxylated polymethacrylic acid (PPMAA) neutralized with 50 % sodium hydroxide, and propoxylated polyacrylic acid (PPAA-50). Samples of partially neutralized polyacrylic acid (using different bases) were also propoxylated, as well as propoxylated copolymers of quaternary 4-vinylpyridine salts with acrylic acid and copolymers of hydroxypropyl acrylate with acrylate salts. Bench tests demonstrated that PPMAA and PPAA-50 not only match but outperform polyacrylamide (the widely used polymer for EOR worldwide) in terms of efficiency and dosage. According to the test results, PPAA-50, in both sodium and potassium modifications, displayed the dual characteristics of a surfactant and a polymer during the oil displacement process in porous media.

Russian researchers [62] conducted laboratory tests to identify the optimal surfactant–polymer mixture composition, evaluating interfacial tension, thermal stability, phase behavior, and rheological properties. After laboratory trials, field tests were performed on two wells of the Kholmogorsk oilfield, using separating chemical tracers. Field results for the selected surfactant correlated well with laboratory findings. The tests revealed that residual oil saturation within the treated zone decreased by approximately 11 %, equivalent to about one-third of the residual oil remaining after water flooding – a strong indication of the surfactant–polymer system's effectiveness.

German scientists [63] explored a process involving grafting sulfo groups from a solvent into the polymer chain. The methyl ether sulfonate, an anionic surfactant derived from palm oil, was used as the reactive species. The optimal polymerization results were achieved at a molar ratio of methyl ether sulfonate : acrylamide = 1 : 0.3. When the polymeric surfactant was added, the interfacial tension decreased from 8.6 to 2.3 mN/m. Thermogravimetric analysis confirmed that this polymeric surfactant is thermally stable under reservoir conditions and capable of emulsifying crude oil. Adsorption studies showed that the adsorption on rock surfaces increased with surfactant concentration, and core flooding experiments demonstrated improved oil recovery across various surfactant concentrations. Despite not achieving extremely low interfacial tension, this polymeric surfactant is considered a viable alternative for EOR applications.

In [64], attention was given to the synthesis of an anionic polymeric surfactant derived from non-edible Jatropha oil for EOR applications. The surfactant was produced by reacting monomeric acrylamide with methyl ether sulfonate derived from Jatropha oil via free-radical polymerization. The synthesized surfactant was characterized using FTIR, ^{1}H NMR, FE-SEM, EDX, TGA, and DLS analyses. The polymeric surfactant exhibited properties of both surfactant and polymer components. Physicochemical testing of the aqueous solutions showed effective reduction of interfacial tension, alteration of wettability, and favorable rheological behavior. The interfacial tension between crude oil and the polymeric surfactant solution at CMC was 2.74 mN/m, which decreased to 0.37 mN/m upon addition of 2.5 wt. % NaCl. The product remained thermally

stable under reservoir conditions (80–120 °C) and enhanced oil recovery by more than 26 % after conventional water flooding, with even greater improvement at elevated temperatures.

Researchers [65] synthesized a polymeric surfactant from castor oil for chemical EOR applications. Formulations were prepared with varying mass ratios of surfactant to acrylamide, and the final products were characterized using FTIR, FE-SEM, EDX, TGA, and DLS. The performance of these polymeric surfactants was evaluated by measuring interfacial tension, rheological behavior, and contact angle with sandstone surfaces. Adding NaCl to the surfactant solution reduced the interfacial tension to an ultra-low value of $2.0 \cdot 10^{-3}$ mN/m. Core flooding experiments demonstrated additional oil recovery of 26.5, 27.8, and 29.1 % with 0.5, 0.6, and 0.7 wt.% polymeric surfactant solutions, respectively, after conventional water flooding.

Recently, ionic liquids (ILs) have been investigated as alternatives to traditional surfactants due to their tunable surface-active properties. A review by Spanish researchers [66] highlighted the advantages of ionic-liquid-based surfactants for EOR, particularly their stability under harsh conditions (high salinity and/or temperature). However, the number of core flooding experiments with ILs remains limited. After secondary flooding, oil recovery reached 32 % of the original oil in place. Most IL formulations were developed for sandstone reservoirs, with few studies involving carbonate cores. The authors proposed and analyzed 1-decyl-3-methylimidazolium triflate ([C_{10}mim][OTf]), which significantly reduced interfacial tension at the oil–water interface. The effect improved with increasing NaCl concentration and decreasing NaOH concentration. An optimized formulation containing 4000 ppm [C_{10}mim][OTf] + 1 wt. % NaOH + 2 wt. % NaCl was suggested. High adsorption in sandstone limited efficiency, but in carbonate cores, an additional 10.5 % oil recovery was achieved at room temperature. When followed by polyacrylamide polymer flooding, the process remained cost-effective. The main EOR mechanism was attributed to interfacial tension reduction, with viscosity effects playing a secondary role.

Indian scientists [67] studied the interfacial properties of imidazolium ionic liquid surfactants and their application for enhanced oil recovery. The advantage of 1-hexadecyl-3-methylimidazolium bromide (C_{16}mimBr) over the traditional cationic surfactant, cetyltrimethylammonium bromide (CTAB), was highlighted. The effectiveness of both (C_{16}mimBr and CTAB) in recovering additional oil was established by conducting laboratory core flooding experiments. The experiments showed that C_{16}mimBr more effectively reduces the interfacial tension between the water-oil system and, thus, recovers more additional oil than the traditional cationic surfactant, CTAB. The obtained results reflect the high interfacial activity, high oil solubility (due to emulsion formation), and stability of C_{16}mimBr during the EOR process under harsh reservoir conditions.

In [68], synthesized ionic liquids (C_8mimBF_4, C_{10}mimBF_4, and C_{12}mimBF_4) were analyzed for their potential application in EOR. Reactions between 1-methylimidazole and alkyl bromide (1-bromooctane for [C_8mimBF_4], 1-bromodecane for [C_{10}mimBF_4], and 1-bromododecane for [C_{12}mimBF_4]) were carried out at a 1:1 molar ratio at 70°C for 48 hours. The resulting ionic liquids were investigated in terms of surface activity, interfacial tension reduction, wettability alteration, adsorption properties, emulsification, and oil recovery. It was observed that surface activity increases with an increase in alkyl chain length. The results of studying interfacial activity as a function of the concentration of ionic liquid, salt (NaCl), and alkali (triethylamine) showed that the synthesized ionic liquids effectively reduce interfacial tension. It was found that with increasing alkyl chain length, the CMC values and interfacial tension (0.041 mN/m) decrease. The synthesized ionic liquids are capable of altering the reservoir rock wettability towards more water-wet (hydrophilic) conditions, leading to greater oil recovery efficiency. Comparative flooding tests were conducted: polymer (partially hydrolyzed polyacrylamide), ionic liquid+polymer, and ionic liquid+polymer+alkali. In terms of interfacial tension reduction, wettability alteration, and additional oil recovery (32.28%), the ionic liquid+polymer+alkali flooding stood out. The

authors concluded that ionic liquids can be considered as a new generation of surfactants in chemical EOR processes for reservoirs with harsh conditions.

Scientists from Saudi Arabia [69] conducted comparative studies to investigate the efficiency of four environmentally friendly, low-cost, and commercially available imidazolium-based ionic liquids (1-butyl-3-methylimidazolium chloride $[C_4mim]^+[Cl]^-$, 1-hexyl-3-methylimidazolium chloride $[C_6mim]^+[Cl]^-$, 1-octyl-3-methylimidazolium chloride $[C_8mim]^+[Cl]^-$, and 1-dodecyl-3-methylimidazolium chloride $[C_{12}mim]^+[Cl]^-$) with two conventionally used surfactants (CTAB and SDS) for EOR from a hydrophobic carbonate sample. The effects of various factors were studied, including ionic liquid concentration (0; 50; 100; 250; and 500 ppm), aging time (0; 2; and 8 weeks), and permeability contrast (50 and 250 mD). The experiments were conducted using Saudi Arabian crude oil at high temperature (100 °C) and high salinity (total dissolved solids (TDS) = 240,000 ppm), simulating harsh reservoir conditions. The rock samples were subjected to NMR analysis to determine the imbibition rate and evaluate the oil and water phase distribution during the process. Overall, the ionic liquids had a positive effect on EOR from the carbonate reservoir. The maximum oil recovery using the ionic liquid is 64.6%, which is almost double the performance of seawater (31.3%), while conventional surfactants SDS and CTAB only reached 40.3% and 42.8%, respectively. Furthermore, as the alkyl chain length increases, the oil recovery efficiency grows. Thus, $[C_{12}mim]^+[Cl]^-$ demonstrates the maximum efficiency. Achieving a 15–35% increase in oil production using this ionic liquid-based technology could lead to economic profit in the oil industry. Additionally, these ionic liquids demonstrate good colloidal stability under high temperature and high salinity conditions.

M. S. Benzagouta et al. [70] investigated 6 "Ammoeng" type ionic liquids as surfactants for EOR. The interfacial tension at the interface between oil and solutions of the aforementioned ionic liquids at various concentrations in a 10% wt. aqueous NaCl solution was measured as a function of temperature. The interfacial tension value increases with increasing temperature. In all cases, as the ionic liquid concentration increases, the interfacial tension value decreases. Ammoeng 102 showed the lowest surface tension value, which decreased with increasing temperature. The obtained values were compared with those of commercially available surfactants, namely Triton X-100, measured under similar conditions. The comparison showed that the surface tension values using ionic liquids are much lower. Furthermore, the interfacial tension values for all reagents used in the 10% wt. aqueous NaCl solution were lower than in deionized water under the same conditions. The possibilities of a synergistic effect when using a mixture of Ammoeng 102 and Triton X-100 were also investigated. Experiments showed that the interfacial tension value depends on the total concentration, the mass ratio of the surfactant to the ionic liquid, and the temperature. The saline solution of Ammoeng 102 showed the best results. The study of the effect of these reagents on oil recovery showed that this ability depends on the three-phase contact, namely oil, aqueous solution, and rock.

Iranian scientists [71] conducted research on well stimulation using surfactants as a practical method for EOR. Three different surfactant samples were selected: newly developed commercial (AN-120, NX-610, NX-1510, NX-2760, and TR-880), traditional (sodium dodecylbenzene sulfonate (SDBS) and SDS), and ionic liquid-based surfactants ($[C_{12}mim]^+[Cl]^-$ and $[C_{18}mim]^+[Cl]^-$). Aqueous solutions were prepared in distilled, formation, and seawater. All samples were highly compatible with distilled water. The commercial and ionic liquid-based surfactants were compatible with formation and seawater, while traditional surfactants experienced a loss of functionality as salinity increased. It was found that the commercial and ionic liquid-based surfactants tolerated harsh salinity conditions well and possessed the ability to reduce interfacial tension down to 0.07 mN/m. Contact angle measurements showed that among the investigated surfactants, $[C_{12}mim]^+[Cl]^-$, AN-120, and NX-2760 shifted the rock wettability towards more water-wet conditions, while other surfactants showed no significant effect on

altering rock wettability. To study the effect of wettability during the injection of $[C_{12}mim]^+[Cl]^-$, an imbibition process (duration 21 days) was conducted on a water-flooded core, which revealed that the tertiary oil recovery efficiency was critically increased to 12.7% of the original oil in place.

To clarify the details of the EOR process through surfactant solution flooding, the authors [72] studied the behavior of model systems consisting of a packed column of calcium carbonate (as the porous rock), n-decane (as the oil), and aqueous solutions of the anionic surfactant sodium bis(2-ethylhexyl) sulfosuccinate (AOT). Figure 2 shows a schematic of the setup for packing the powder column.

The AOT concentration was varied from zero to above the critical aggregation concentration (CAC). The salt content in the aqueous solutions was varied to obtain systems with a wide range of interfacial tension values at the oil-water interface. It was shown that the change in contact angle with the change in surfactant concentration is related to surface tension measurements and adsorption isotherms. The adsorption isotherms allow for estimating the concentration of non-adsorbed surfactant in the packed column, which, in turn, permits a detailed analysis of the change in percentage oil recovery as a function of surfactant concentration. At surfactant concentrations below the CAC, the percentage oil recovery is determined by the contact angle. In the case of concentrations above the CAC, additional oil recovery occurs due to solubilization and an emulsification mechanism.

Study [73] primarily focuses on a review of the application of the alkali-surfactant-polymer (ASP) flooding process in oil production and its limitations in onshore and offshore oil recovery. The ASP EOR technology is a versatile method of tertiary oil recovery. Alkali-surfactant-polymer flooding is a combined process in which all three components—alkali, surfactant, and polymer—are injected in a single slug. Thanks to the synergy of these three components, ASP is widely applied in both pilot and field operations with the aim of achieving optimal results at minimal cost. To take this technology to the next level, it is necessary to develop more advanced ASP systems with more cost-effective surfactants in low-alkali systems and with pH-resistant polymers. The article discusses technical solutions for some of these challenges.

The authors of [74] conducted a review of research papers on alternative alkalis, surfactants, and polymer chemical agents for EOR. Based on these works, organic alkalis have been proposed as an alternative to inorganic alkalis to address problems of incompatibility with seawater and formation brine, scaling issues, and the detrimental effect of alkali on polymer thickening. Among the organic alkalis, ethanolamine was found to be the most effective and has therefore been the most widely studied as a potential alkali for field applications. Fig. 3 provides micrographs of "oil-in-water" emulsions with different chemical solutions: surfactant, ethanolamine, and surfactant+ethanolamine.

Its performance is comparable to conventional inorganic alkalis, and in some aspects, surpasses them. Based on various studies, bio-based surfactants have been proposed as an environmentally friendly and cost-effective alternative to synthetic surfactants. Plant-oil-based surfactants have been proven to be superior to synthetic surfactants and are also

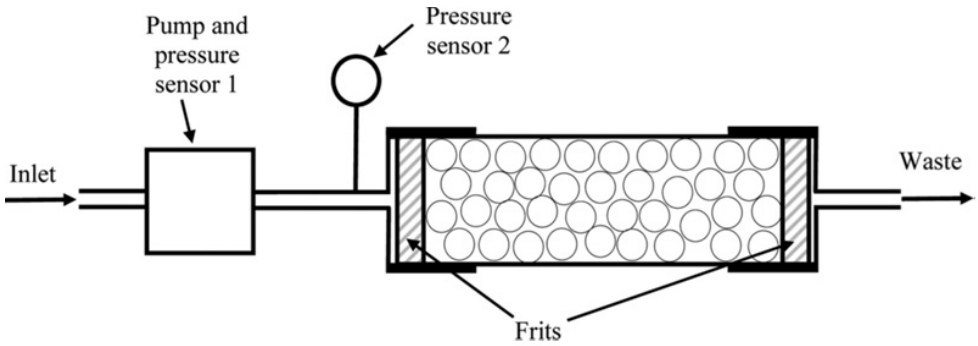

Fig. 2. Diagram of the installation for filling a column with packed powder [72]

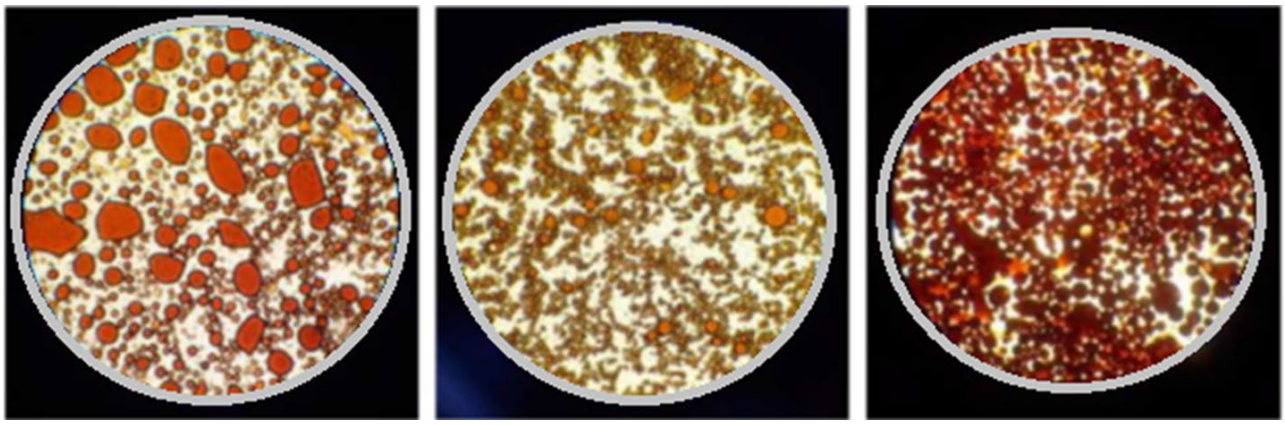

Fig. 3. Microphotographs of oil-water emulsions with various chemical solutions [74]: surfactant (left), ethanolamine (center), as well as surfactant and ethanolamine (right) [74]

environmentally safe. Ionic liquids have been proposed as alternative surfactants for harsh temperatures and high-salinity reservoirs.

However, further research is needed to improve their performance in achieving ultra-low interfacial tension. Biopolymers have been recommended as a stable alternative to synthetic polymers under harsh temperature conditions in high-salinity reservoirs.

Study [75] reported the development and testing of enzyme-based biochemical complexes in Vietnam's oil industry. Studies showed that to avoid a decrease in enzyme activity in reservoir conditions (due to high temperature and salinity), the use of a chelating agent is required to limit the influence of metal ions. To improve the properties of the enzymes, they were combined with a surfactant, for which alpha-olefin sulfonate was selected. The surface tension of the solution decreased to 2.7 mN/m. The surface tension of the initial enzyme solution increases during thermal stabilization, whereas in the enzyme-surfactant solution, the surface tension changes insignificantly. This means the added surfactant helps to increase the surface activity and thermal stability of the initial enzyme solution. Using the Modde 5.0 (Modeling and Design) program, the optimal concentration of the enzyme solution and surfactant was determined for the minimum surface tension value of the enzyme solutions. Based on the results, the following component composition was determined, %: enzyme - 50.0; surfactant - 30.0; stabilizer - 1.0; microorganism inhibitor - 0.5.

In [76], four different types of surfactants from a new class were investigated for their effectiveness in tertiary oil recovery: ditridecyl sulfosuccinate ester; coconut diethanolamide; alkyl polyglycosides (APG); and sodium salts of alkyl propoxy sulfate. The tested formulations were selected after extensive research, including measurements of interfacial tension and adsorption behaviour on kaolinite clay. The main results of this study include: ditridecyl sulfosuccinate ester showed only low (15%) tertiary oil recovery; coconut diethanolamide demonstrated high TOR (75%); APG showed good tertiary oil recovery, from 40% to 55%; sodium salts of alkyl propoxy sulfate were also effective in terms of tertiary oil recovery (recovering 35% to 50% additional oil); coconut diethanolamide and sodium salts of alkyl propoxy sulfate were effective even at high salinity (4–10 wt% NaCl). The adsorption of APG surfactants onto the solid state depended on the alkyl chain length of the APG. A longer chain length resulted in greater adsorption. All surfactant formulations were suitable in terms of EOR (after waterflooding). The observed tertiary oil recovery was in the range of 15–75% for consolidated sandstone cores. 94% recovery of the original oil in place from the reservoir was reported in the case of sandstone. The results indicate that a wide range of surfactants can meet the technical requirements for EOR agents.

Study [77] focused on gemini surfactants, examining their adsorption, rheology, wettability alteration, and interfacial properties, highlighting

their potential as next-generation reagents for EOR. The rich variety of anionic, nonionic, cationic and zwitterionic gemini surfactants makes them accessible. The structures of typical representatives of gemini surfactants are shown below.

Low CMC, excellent wetting and foam-forming properties, the ability to reduce surface tension, unique aggregation behavior, and the capacity to achieve ultra-low interfacial tension at low concentrations make gemini surfactants highly suitable for use in EOR processes. Despite the growing number of laboratory studies and promising results obtained for gemini surfactants, core flooding data remain scarce. This is likely due to the fact that gemini surfactants are still a relatively new class of surfactants; however, they are expected to replace conventional monomeric surfactants in the future.

Authors [78] presented a chronological overview of technological developments and physicochemical research related to gemini-type surfactant systems. The paper focuses primarily on cationic, anionic, nonionic, and zwitterionic gemini surfactants. Traditional EOR systems are characterized by the widespread use of monomeric surfactants, which tend to self-aggregate at high concentrations. Consequently, crude oil often remains insufficiently mobile during displacement, necessitating the use of viscous buffers to push oil toward production wells. By contrast, gemini surfactants, due to their unique dimeric molecular structure and superior properties, yield innovative and efficient results in EOR applications. Cationic gemini surfactants are the most extensively studied and have demonstrated excellent performance in thermodynamically stable solutions, microemulsions, and nanofluid-based systems, suitable for both conventional and unconventional reservoirs. Anionic surfactants, particularly sulfonates, form a diverse range of high-quality emulsifying and foaming aqueous solutions, ideal for EOR. Nonionic surfactants, when used in mixtures or formulations, exhibit salt tolerance, favorable rock adsorption, and compatibility with formation fluids. Zwitterionic surfactants, owing to their structural features, offer stability over a wide salinity range, ultra-low interfacial tension, and viscoelastic properties, combined with low binding energy, which enhance their EOR potential. Gemini surfactants are effective in small quantities, and their dimeric structures enable synergistic

The structures of typical representatives of gemini surfactants

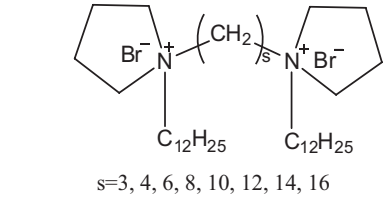

s=3, 4, 6, 8, 10, 12, 14, 16

cationic

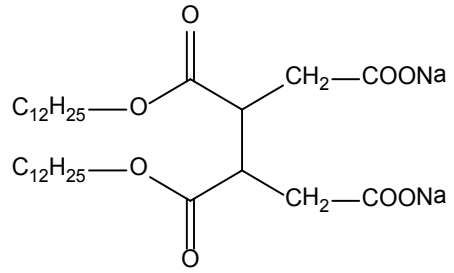

anionic

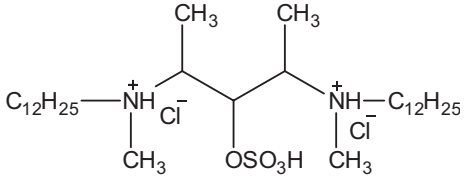

zwitterionic

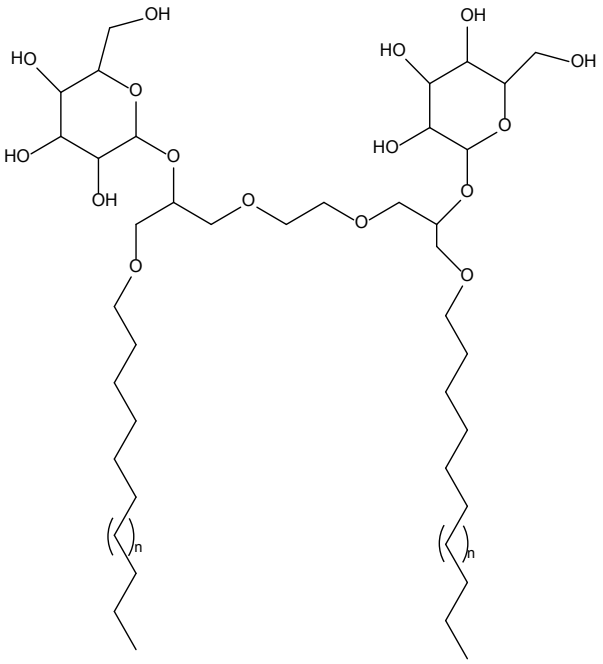

nonionic

interactions with polymers, nanoparticles, and other additives, leading to increased tertiary oil recovery. The authors concluded that it is essential to develop commercially viable strategies for applying gemini surfactants to recover additional crude oil via EOR. The use of gemini surfactants in efficient oil recovery is expected to show stable and dynamic growth in the future.

In [79], four cationic gemini surfactants with different aliphatic spacer lengths were synthesized via the reactions of 1,3-dibromopropane, 1,4-dibromobutane, 1,5-dibromopentane, and 1,6-dibromohexane with N,N-dimethyltetradecylamine. Unlike conventional surfactants, gemini surfactants exhibited very low CMC values (< 200 ppm). It was found that the CMC increases with temperature. These surfactants demonstrated excellent salt resistance and long-term thermal stability. Optimal viscosities were observed in systems where wormlike micelles formed typically in shorter-spacer systems (with longer spacers leading to spherical micelles). Dynamic surface tension measurements showed an initial decrease over time until equilibrium was reached. Ultra-low interfacial tension values, in the range of 10^{-2} mN/m, were observed in crude oil–surfactant systems, further reduced to 10^{-3}mN/m with salt addition. Both salt addition and temperature increase improved wettability. TOR in the range of 24–30% was achieved with gemini surfactants alone and 30–35% for polymer (partially hydrolyzed polyacrylamide)–gemini surfactant systems. The compound 14–6–14 exhibited the best performance for EOR applications.

Conclusions

A concise literature analysis on the study of polymeric surfactants in EOR processes leads to the conclusion that using surfactants either as independent agents or in mixtures with polymers, acids, salts, and other components enhances their properties and represents a promising direction for research and practical application. Therefore, the study of polymeric surfactants as agents for improving oil recovery remains a relevant and significant topic.

Contribution of the authors

G. A. Ahmadova – scientific supervision, research concept, writing, and final conclusions. R. A. Rahimov – scientific supervision, research concept. A. Z. Abilova – experimental research, literature selection, and text editing. Sh. M. Nasibova – formal analysis, data curation. Kh. A. Mammadova – formal analysis, data curation.

References

1. Firozjaii A. M., Saghafi H. R. Review on chemical enhanced oil recovery using polymer flooding: Fundamentals, experimental and numerical simulation. *Petroleum*. 2020;6(2): 115–122. https://doi.org/10.1016/j.petlm.2019.09.003

2. Shah D. O., Schechter R. S. *Improved oil recovery by surfactant and polymer flooding*. New York: Academic Press; 1977. 578 p. Available at: https://shop.elsevier.com/books/improved-oil-recovery-by-surfactant-and-polymer-flooding/shah/978-0-12-641750-0

3. Belhaj A. F., Elraies Kh. A., Ahmood S. M., Zulkifli N. N., Akbari S., Eldin Hussien O. S. The effect of surfactant concentration, salinity, temperature, and pH on surfactant adsorption for chemical enhanced oil recovery: a review. *Journal of Petroleum Exploration and Production Technology*. 2020;10: 125–137. https://doi.org/10.1007/s13202-019-0685-y

4. Khuzin R. R., Bakhtizin R. N., Andreev V. E., Kuleshova L. S., Mukhametshin V. V., Sultanov Sh. Kh. Oil recovery enhancement by reservoir hydraulic compression technique employment. *SOCAR Proceedings*. 2021;SI1: 98–108. https://doi.org/10.5510/ogp2021si100522

5. Tapdigov Sh. Z., Ahmad F. F., Hamidov N. N., Bayramov E. E. Increase in the efficiency of water shut-off with the application of polyethylenpolyamine added cement. *Chemical Problems*. 2022;1(20): 59–67. Available at: https://cyberleninka.ru/article/n/increase-in-the-efficiency-of-water-shut-off-with-the-application-of-polyetylenpolyamine-added-cement/viewer

6. Suleimanov B. A., Gurbanov A. Q., Tapdiqov Sh. Z. Isolation of water inflow into the well with a thermosetting gel-forming. *SOCAR Proceedings*. 2022:4: 21–26. https://doi.org/10.5510/ogp20220400779

7. Rostamzadeh A. P., Parsa S. A. M., Faramarzi M. Efficiency of ionic liquid/polymer flooding combined with smart water injection on oil recovery through secondary and tertiary patterns using Iranian carbonate rock. *Petroleum Science and Technology*. 2023;41(10): 1081–1098. https://doi.org/10.1080/10916466.2022.2092501

8. Ahmed M. E., Sultan A. S., Al-Sofi A. Optimization of surfactant-polymer flooding for enhanced oil recovery. *Journal of Petroleum Exploration and Production Technology*. 2023;13: 2109–2123. https://doi.org/10.1007/s13202-023-01651-0

9. Mammadova U. A., Fatullayeva S. S., Tapdıqov S. Z., … Rajabli A. The use of xanthan gum biopolymer for enhanced oil recovery. *Scientific Collection "Interconf"*

Proceedings of the 1st International Scientific and Practical Conference. Modern Directions and Movements in Science, Luxembourg, Luxembourg. 2022;127: 226–229. Available at: https://archive.interconf.center/index.php/conference-proceeding/article/view/1415

10. Pogaku R., Fuat N. H. M., Sakar S., Zeong Woong Cha Z. W., Musa N., Taiudin D. N., Morris L. O. Polymer flooding and its combinations with other chemical injection methods in enhanced oil recovery. *Polymer Bulletin*. 2018;75: 1753–1774. https://doi.org/10.1007/s00289-017-2106-z

11. Veliyev E. F. Application of amphiphilic block-polymer system for emulsion flooding. *SOCAR Proceedings*. 2021;3: 78–86. https://doi.org/10.5510/ogp20210300532

12. Pillai P., Mandal A. Synthesis and characterization of surface-active ionic liquids for their potential application in enhanced oil recovery. *Journal of Molecular Liquids*. 2022;345: 117900. https://doi.org/10.1016/j.molliq.2021.117900

13. Chen X., Feng Q., Liu W., Sepehrnoori K. Modeling preformed particle gel surfactant combined flooding for enhanced oil recovery after polymer flooding. *Fuel*. 2017;194: 42–49. https://doi.org/10.1016/j.fuel.2016.12.075

14. Dong X., Liu H., Chen Zh., Wu K., Lu N., Zhang Q. Enhanced oil recovery techniques for heavy oil and oilsands reservoirs after steam injection. *Applied Energy*. 2019;239: 1190–1211. https://doi.org/10.1016/j.apenergy.2019.01.244

15. Grishchenko V. A., Gareev R. R., Tsiklis I. M., Mukhametshin V. V., Yakupov R. F. Expanding the amount of preferential royalty facilities with hard-to-recover oil reserves. *SOCAR Proceedings*. 2021;2: 8–18. https://doi.org/10.5510/ogp2021si200575

16. Wang F., Xu H., Yikun L., Jiang Y., Wu Ch. Experimental study on the enhanced oil recovery mechanism of an ordinary heavy oil field by polymer flooding. *ACS*. 2023;8(15): 14089–14096. https://doi.org/10.1021/acsomega.2c08084

17. Suleimanov B. A., Abbasov H. F. Enhanced oil recovery mechanism with nanofluid injection. *SOCAR Proceedings*. 2022;3: 028-037. https://doi.org/10.5510/ogp20220300705

18. Suleimanov B. A., Ismailov F. S., Veliyev, E. F. Nanofluid for enhanced oil recovery. *Journal of Petroleum Science and Engineering*. 2011;78(2): 431–437. https://www.sciencedirect.com/science/article/pii/S0920410511001409

19. Suleimanov B. A., Veliyev E. F. Novel polymeric nanogel as diversion agent for enhanced oil recovery, *Petroleum Science and Technology*. 2017;35(4): 319–326. https://doi.org/10.1080/10916466.2016.1258417

20. Suleimanov B. A., Ismaylov F. S. Veliyev E. F. On the metal nanoparticles effect on the strength of polymer gels based on carboxymethylcellulose, applying at oil recovery. *Oil Industry*. 2014;1: 86–88. Available at: https://www.researchgate.net/publication/291309119

21. Suleimanov B. A., Ismayilov F. S., Veliyev E. F., Dyshin O. A. The influence of light metal nanoparticles on the strength of polymer gels used in oil industry. *SOCAR Proceedings*. 2013;2: 24–28. https://doi.org/10.5510/ogp20130200151

22. Veliyev E. F. Mechanisms of polymer retention in porous media. *SOCAR Proceedings*. 2020;3: 126–134. https://doi.org/10.5510/ogp20200300453

23. Zhao H., Ding X., Yu P., … Shao Q. Study on the pressure drop of crude oil-water with surfactant flow in porous media. *Journal of Dispersion Science and Technology*. 2021;44(3): 468–474. https://doi.org/10.1080/01932691.2021.1950548

24. Das A., Nguyen N., Nguyen Q. P. Low tension gas flooding for secondary oil recovery in low-permeability, high-salinity reservoirs. *Fuel*. 2020;264: 116601. https://doi.org/10.1016/j.fuel.2019.116601

25. Ahmadi M. A., Arabsahebi Y., Shadizadeh S. R., Behbahani S. S. Preliminary evaluation of mulberry leaf-derived surfactant on interfacial tension in an oil-aqueous system: EOR application. *Fuel*. 2014;117: 749–755. https://doi.org/10.1016/j.fuel.2013.08.081

26. Kang W., Liu S., Meng L. W., Cao D., Fan H. A novel ultralow interfacial tension foam flooding agent to enhance heavy oil recovery. In: *SPE Improved Oil Recovery Symposium*, *April 24–28, 2010. Tulsa, Oklahoma, USA*. Paper Number: SPE-129175-MS. https://doi.org/10.2118/129175-MS

27. Zhang G., Yu J., Du C., Lee R. Formulation of surfactants for very low/high salinity surfactant flooding without alkali. In: *SPE International Symposium on Oilfield Chemistry. April 13–15, 2015. The Woodlands, Texas, USA*. Paper Number: SPE-173738-MS. https://doi.org/10.2118/173738-MS

28. Kamal M. S., Sultan A. S., Hussein I. A. Screening of amphoteric and anionic surfactants for EOR applications using a novel approach. *Colloid Surface A*. 2014;476: 17–23. https://doi.org/10.1016/j.colsurfa.2015.03.023

29. Chen P., Mohanty K. K. Surfactant-enhanced oil recovery from fractured oil-wet carbonates: effects of low IFT and wettability alteration. In: *SPE International Symposium on Oilfield Chemistry. April 13–15, 2015. The Woodlands, Texas, USA*. Paper Number: SPE-173797-MS. https://doi.org/10.2118/173797-MS

30. Wu X., Han M., Zahrani B. H., Guo L. Effect of surfactant polymer interaction on the interfacial properties for chemical EOR. In: *SPE Middle East Oil & Gas Show and Conference, March 8–11, 2015. Manama, Bahrain*. Paper Number: SPE-172706-MS. https://doi.org/10.2118/172706-ms

31. Cao R., Yang H., Sun W., Ma Y. Z. A new laboratory study on alternate injection of high strength foam and ultra-low interfacial tension foam to enhance oil recovery. *Journal of Petroleum Science and Engineering,* 2015;125: 75–89. https://doi.org/10.1016/j.petrol.2014.11.018

32. Yuan F. Q., Cheng Y. Q., Wang H. Y., … Zhao S. Effect of organic alkali on interfacial tensions of surfactant solutions against crude oils. *Colloid Surface A*. 2015;470: 171–178. https://doi.org/10.1016/j.colsurfa.2015.01.059

33. Liyanage P. J., Lu J., Arachchilage G. W. P., Weerasooriya U.P., Pope G. A. A novel class of large-hydrophobe tristyrylphenol (TSP) alkoxy sulfate surfactants for chemical enhanced oil recovery. *Journal of Petroleum Science and Engineering*. 2015;128: 73–85. https://doi.org/10.1016/j.petrol.2015.02.023

34. Ahmadi M. A., Galedarzadeh M., Shadizadeh S. R. Wettability alteration in carbonate rocks by implementing new derived natural surfactant: enhanced oil recovery applications. *Transport Porous Media*. 2014;106(3): 645–667. https://doi.org/10.1007/s11242-014-0418-0

35. Aoudia M., Al-Maamari R. S., Nabipour M., Al-Bemani A. S., Ayatollahi S. Laboratory study of alkyl ether sulfonates for improved oil recovery in high-salinity

carbonate reservoirs: a case study. *Energy and Fuel*. 2010;24(6): 3655–3660. https://pubs.acs.org/doi/abs/10.1021/ef100266p

36. Aoudia M., Al-Shibli M. N., Al-Kasimi L. H., Al-Maamari R., Al-bemani A. Novel surfactants for ultralow interfacial tension in a wide range of surfactant concentration and temperature. *Journal of Surfactants and Detergents*. 2006;9(3): 287–293. https://doi.org/10.1007/s11743-006-5009-9

37. Kamaludin N. A., Suhaidi N. N. S., Ismail N. Green surfactants for enhanced oil recovery: a review. *Materials Today: Proceedings*. 2023. https://doi.org/10.1016/j.matpr.2023.10.100

38. Ahmadi M. A., Shadizadeh S. R. Experimental investigation of adsorption of a new nonionic surfactant on carbonate minerals. *Fuel*. 2013;104: 462–467. https://doi.org/10.1016/j.fuel.2012.07.039

39. Dong L., Li Y., Wen J., ... Liu Z. Functional characteristics and dominant enhanced oil recovery mechanism of polymeric surfactant. *Journal of Molecular Liquids*. 2022;354: 118921. https://doi.org/10.1016/j.molliq.2022.118921

40. Chen Q., Zhang S., Wang Z., Ye Z., Lai N. Synthesis and characterization of a novel active polymer for enhanced oil recovery. *Journal of Applied Polymer Science*. 2023;140(15): e53734. https://doi.org/10.1002/app.53734

41. Chen M., Deng H., Geng X., ... Jia N. Synthesis and evaluation of a low molecular weight amphiphilic polymer for enhanced oil recovery. *Journal of Surfactants and Detergents*. 2021;24: 991–1002. https://doi.org/10.1002/jsde.12531

42. Zhu Zh., Kou H., Zhang Zh., Wang Y., Wan H. Performance and mechanisms of enhanced oil recovery via amphiphilic polymer flooding in high salinity reservoir. *Petroleum Science and Technology*. 2023;41(21): 2006–2016. https://doi.org/10.1080/10916466.2022.2105358

43. Wei J., Chen Y., Zhou X., ... Zhou R. Experimental studies of surfactant-polymer flooding: an application case investigation. *International Journal of Hydrogen Energy*. 2022;47: 32876–32892. https://doi.org/10.1016/j.ijhydene.2022.07.198

44. Jouenne S. Polymer flooding in high temperature, high salinity conditions: selection of polymer type and polymer chemistry, thermal stability. *Journal of Petroleum Science and Engineering*. 2020;195: 107545. https://doi.org/10.1016/j.petrol.2020.107545

45. Sharma T., Joshi A. Jain A., Chaturvedi K. R. Enhanced oil recovery and CO_2 sequestration potential of Bi-polymer polyvinylpyrrolidone-polyvinyl alcohol. *Journal of Petroleum Science and Engineering*. 2022;211: 110167. https://doi.org/10.1016/j.petrol.2022.110167

46. Li P., Zhang F., Zhu T., Zhang C., Liu G., Li X. Synthesis and properties of the active polymer for enhanced heavy oil recovery. *Colloids and Surfaces A: Physicochemical and Engineering Aspects*. 2021;626: 127036. https://doi.org/10.1016/j.colsurfa.2021.127036

47. Mehrabianfar P., Bahraminejad H., Manshad A. K. An introductory investigation of a polymeric surfactant from a new natural source in chemical enhanced oil recovery (CEOR). *Journal of Petroleum Science and Engineering*. 2021;198: 108172. https://doi.org/10.1016/j.petrol.2020.108172

48. Wu Q., Ding L., Zhang L., ... Guérillot D. Polymer enhanced foam for improving oil recovery in oil-wet carbonate reservoirs: a proof of concept and insights into the polymer-surfactant interactions. *Energy*. 2023;264: 126256. https://doi.org/10.1016/j.energy.2022.126256

49. Song B., Hu X., Shui X., Cui Z., Wang Z. A new type of renewable surfactants for enhanced oil recovery: dialkylpolyoxyethylene ether methyl carboxyl betaines. *Colloids and Surfaces A: Physicochemical and Engineering Aspects*. 2016;489: 433–440. https://doi.org/10.1016/j.colsurfa.2015.11.018

50. Klyuchnikova N. V., Genov I., Kudina A. E. Polymer surface-active substance for oil producing industry. *Bulletin of BSTU named after V. G. Shukhov*. 2018;11: 99–104. https://doi.org/10.12737/article_5bf7e357aa4f11.67674617

51. Madani M., Zargar G., Takassi M. A., Daryasafar A., Wood D. A., Zhang Z. Fundamental investigation of an environmentally-friendly surfactant agent for chemical enhanced oil recovery. *Fuel*. 2019;238: 186–197. https://doi.org/10.1016/j.fuel.2018.10.105

52. Arslanova I. M., Prochukhan K. Yu., Prosochkina T. R., ... Arslanova D. I. The study of the physicai-chemical characteristics of a surfactant-polymer system to enhanced oil recovery. *Petroleum Engineering* 2017;11: 36–39. (In Russ., abstract in Eng.). Available at: https://www.elibrary.ru/item.asp?id=30558247

53. Ahmadova G. A., Abilova A. Z., Rahimov R. A., Asadov Z. H., Ahmadbayova S. F. Influence of head-group composition and (chloro)propoxy units disposition consequency on properties of surfactants based on lauric acid, propylene oxide, epichlorohydrin and ethanolamines. *Journal of Materials Chemistry and Physics*. 2018;205: 416–422. https://doi.org/10.1016/j.matchemphys.2017.11.035

54. Ahmadova G. A., Abilova A. Z., Rahimov R. A., Asadov Z. H., Ahmadbayova S. F., Musayeva G. M. Synthesis and Properties of surface-active cooligomers based on C_3-epoxides and lauric acid. *Processes of Petrochemistry and Oil Refining*. 2017;18(2): 150–156. Available at: https://ppor.az/jpdf/Axmedova-2(2017).PDF

55. Asadov Z. G., Aliyev V. S. Synthesis, properties and application of hydrophilic polymers and copolymers of oxyalkyl esters of (meth)acrylic acid. *Russian Chemical Reviews*. 1992;61(5): 1002–1019. Available at: https://russchemrev.org/RCR962pdf

56. Asadov Z. G., Agazade A. D., Kasimov A. A., Aliyev V. S. Regularities and mechanism of the reaction of oxypropylation of polyacrylic acid, partially neutralized with sodium hydroxide. *Polymer Science U.S.S.R.* 1990;10: 792-797.

57. Nasibova Sh. M., Rahimov R. A., Muradova S. A., Abdullayev Yu. 2-Hydroxyethyl substituted cationic surfactants with dodecyl hydrophobic chain: Properties and application. *Materials Chemistry and Physics*, 2023;296: 127268. https://doi.org/10.1016/j.matchemphys.2022.127268

58. Asadov Z. H., Ahmadova G. A., Rahimov R. A., Asadova A. Z., Nazarov I. G. Synthesis and study of nonionic surfactants based on propylene oxide and lauric acid. *Russian Journal of Applied Chemistry*. 2016;89: 559–565. https://doi.org/10.1134/S1070427216040066

59. Abilova A. Z., Ahmadova G. A., Rahimov R. A., ... Nadirova Zh. K. Synthesis and study of oligomeric surfactants based on polyethylene polyamine and propylene oxide,

enhancing the oil recovery factor. *Processes of Petrochemistry and Oil Refining*. 2025;26(4): 1288–1295. https://doi.org/10.62972/1726-4685.2025.4.1288

60. Asadov Z. H., Huseynova Kh. A., Rahimov R. A., Ahmadova G. A., Zubkov F. I. Alkyl chain and head-group effect of mono- and diisopropylolalkylamine-polymethacrylic acid complexes in aqueous solution. *Journal of Molecular Liquids*. 2017;244: 533–539. https://doi.org/10.1016/j.molliq.2017.09.042

61. Asadov Z. H., Ahmadova G. A., Rahimov R. A., Abilova A. Z., Zargarova S. H., Zubkov F. İ. Synthesis and properties of quaternary ammonium surfactants based on alkylamine, propylene oxide and 2-chloroethanol. *Journal of Surfactants and Detergents*. 2018;21: 247–254. https://doi.org/10.1002/jsde.12008

62. Bondar M. Yu., Osipov A. V., Groman A. A., Koltsov I. N., Scherbakov G. Y., Chebysheva O. V. The results of single well chemical tracer tests to assess the effectiveness of surfactant-polymer exposure at the Kholmogorskoye field. *Bulletin of the Oil and Gas Industry of Kazakhstan*. 2022;4(2): 102–112. https://doi.org/10.54859/kjogi108466

63. Wibowo A. D. K., Yoshi L. A., Handayani A. S., Joelianingsih. Synthesis of polymeric surfactant from palm oil methyl ester for enhanced oil recovery application. *Colloid and Polymer Science*. 2021;299: 81–92. https://doi.org/10.1007/s00396-020-04767-5

64. Kumar S., Saxena N., Mandal A. Synthesis and evaluation of physicochemical properties of anionic polymeric surfactant derived from Jatropha oil for application in enhanced oil recovery. *Journal of Industrial and Engineering Chemistry*. 2016;43: 106–116. https://doi.org/10.1016/j.jiec.2016.07.055

65. Babu K., Pal N., Saxena V. K., Mandal A. Synthesis and characterization of a new polymeric surfactant for chemical enhanced oil recovery. *Korean Journal of Chemical Engineering*. 2016;33: 711–719. https://doi.org/10.1007/s11814-015-0186-8

66. Somoza A., Arce A., Soto A. Oil recovery tests with ionic liquids: A review and evaluation of 1-decyl-3-methylimidazolium triflate. *Petroleum Science*. 2022;19(4): 1877–1887. https://doi.org/10.1016/j.petsci.2021.10.025

67. Nandwani K., Malek N. I., Lad N. V., Chakraborty M., Gupta S. Study on interfacial properties of Imidazolium ionic liquids as surfactant and their application in enhanced oil recovery. *Colloids and Surfaces A: Physicochemical and Engineering Aspects*. 2017;516: 383–393. https://doi.org/10.1016/j.colsurfa.2016.12.037

68. Pillai P., Kumar A., Mandal A. Mechanistic studies of enhanced oil recovery by imidazolium-based ionic liquids as novel surfactants. *Journal of Industrial and Engineering Chemistry*. 2018;63: 262–274. https://doi.org/10.1016/j.jiec.2018.02.024

69. Sakthivel S., Elsayed M. Enhanced oil recovery by spontaneous imbibition of imidazolium based ionic liquids on the carbonate reservoir. *Journal of Molecular Liquids*. 2021;340: 117301. https://doi.org/10.1016/j.molliq.2021.117301

70. Benzagouta M. S., Al Nashef I. M., Karnanda W., Al-Khidir K. Ionic liquids as novel surfactants for potential use in enhanced oil recovery. *Korean Journal of Chemical Engineering*. 2013;30(11): 2108–2117. https://doi.org/10.1007/s11814-013-0137-1

71. Nabipour M., Ayatollahi S., Keshavarz P. Application of different novel and newly designed commercial ionic liquids and surfactants for more oil recovery from an Iranian oil field. *Journal of Molecular Liquids*. 2017;230: 579–588. https://doi.org/10.1016/j.molliq.2017.01.062

72. Fletcher P. D. I., Savory L. D., Woods F., Clarke A., Howe A. M. Model study of enhanced oil recovery by flooding with aqueous surfactant solution and comparison with theory. *Langmuir*. 2015;31(10): 3076–3085. https://doi.org/10.1021/la5049612

73. Olajire A. A. Review of ASP EOR (alkaline surfactant polymer enhanced oil recovery) technology in the petroleum industry: Prospects and challenges. *Energy*. 2014;77: 963–982. https://doi.org/10.1016/j.energy.2014.09.005

74. Tackie-Otoo B. N., Mohammed M. A. A., Yekeen N., Negash B. M. Alternative chemical agents for alkalis, surfactants and polymers for enhanced oil recovery: Research trend and prospects. *Journal of Petroleum Science and Engineering*. 2020: 106828. https://doi.org/10.1016/j.petrol.2019.106828

75. Shchetnikov V. I., Mukhametshin V. V., Kuleshova L. S., Veliev E. M., Stepanova R. R., Samigullina L. Z. Surfactant enzymes combined application for oil production intensification in Vietnam. *SOCAR Proceedings*. 2022;2: 035–042. https://doi.org/10.5510/ogp20220200672

76. Iglauer S., Wu Y. Shuler P., Tang Y., Goddard III W. A. New surfactant classes for enhanced oil recovery and their tertiary oil recovery potential. *Journal of Petroleum Science and Engineering*. 2010;71: 23–29. https://doi.org/10.1016/j.petrol.2009.12.009

77. Kamal M. S. A review of gemini surfactants: potential application in enhanced oil recovery. *Journal of Surfactants and Detergents*. 2015;19(2): 223–236. https://doi.org/10.1007/s11743-015-1776-5

78. Pal N., Hoteit H., Mandal A. Structural aspects, mechanisms and emerging prospects of gemini surfactant-based alternative enhanced oil recovery technology: a review. *Journal of Molecular Liquids*. 2021;339: 116811. https://doi.org/10.1016/j.molliq.2021.116811

79. Pal N., Saxena N., Mandal A. Studies on the physicochemical properties of synthesized tailor-made gemini surfactants for application in enhanced oil recovery. *Journal of Molecular Liquids*. 2018;258: 211–224. https://doi.org/10.1016/j.molliq.2018.03.037

Information about the authors

Gulnara A. Ahmadova, Dr. Sci. (Chem.), Associate Professor, Head of the Laboratory "Surface-active reagents and preparations", Institute of Petrochemical Processes of the Ministry of Science and Education of Azerbaijan (Baku, Azerbaijan).

https://orcid.org/0009-0003-7199-6087
ahmadovagulnara@mail.ru

Ravan A. Rahimov, Dr. Sci. (Chem.), Associate Professor, Chief Researcher of the Laboratory "Surface-active reagents and preparations", Institute of Petrochemical Processes of the Ministry of Science and Education of Azerbaijan (Baku, Azerbaijan).

https://orcid.org/0000-0001-5619-4041
revan_chem@mail.ru

Aygul Z. Abilova, Cand. Sci. (Chem.), Leading Researcher of the Laboratory "Surface-active reagents and preparations", Institute of Petrochemical Processes of the Ministry of Science and Education of Azerbaijan (Baku, Azerbaijan).

https://orcid.org/ 0009-0001-3453-5770

abilova_aygul@inbox.ru

Shafiga M. Nasibova, Cand. Sci. (Chem.), Associate Professor, Leading Researcher of the laboratory "Surface-active reagents and preparations", Institute of Petrochemical Processes of the Ministry of Science and Education of Azerbaijan (Baku, Azerbaijan).

https://orcid.org/0009-0009-1446-7270

nesibova.sefiqe@mail.ru

Khuraman A. Mammadova, Cand. Sci. (Chem.), Associate Professor, Chief Researcher of the Laboratory "Surface-active reagents and preparations", Institute of Petrochemical Processes of the Ministry of Science and Education of Azerbaijan (Baku, Azerbaijan).

https://orcid.org/0009-0000-0612-5160

xuraman_akifli@hotmail.com

Received December 7, 2024; approved after reviewing January 14, 2025; accepted for publication February 14, 2025; published online December 25, 2025.

ISSN 1606-867X (Print)
ISSN 2687-0711 (Online)
Condensed Matter and Interphases
Kondensirovannye Sredy i Mezhfaznye Granitsy
https://journals.vsu.ru/kcmf/

Review

Review article
https://doi.org/10.17308/kcmf.2025.27/13253

Azeotropism of clathrate hydrates: a brief overview

N. A. Shostak✉

Kuban State Technological University,
2 Moskovskaya st., Krasnodar 350072, Russian Federation

Kuban State University,
149 Stavropolskaya st., Krasnodar 350040, Russian Federation,

Kuban State Medical University,
4 Mitrofana Sedina st., Krasnodar 350063, Russian Federation

Abstract

Objectives: The objective of this work was to provide a review of the specific features of azeotropism manifestation in hydrate-forming mixtures. The physical basis of azeotropic behavior in clathrate hydrates and its relation to molecular structures and intermolecular forces are analyzed. The influence of hydrate system stability on azeotropic properties is considered, along with the effects of individual component characteristics such as molecular size and structure on azeotropy.

Experimental: Experimental methods for identifying azeotropy in clathrate hydrates are reviewed. Computational approaches to determining the azeotropic point are analyzed, and theoretical predictions are compared with experimental data for known azeotropic hydrates. A concise overview of hydrate-forming mixtures exhibiting azeotropic behavior is also presented.

Conclusions: Possible applications of azeotropic behavior in hydrate systems are discussed, highlighting its significant potential in practical and industrial contexts.

Keywords: Azeotropism, Azeotropic behavior, Azeotropic mixture, Clathrate hydrates, Hydrate-forming

For citation: Shostak N. A. Shostak N. A. Azeotropism of clathrate hydrates: a brief overview. *Condensed Matter and Interphases*. 2025;27(4): 547–554. https://doi.org/10.17308/kcmf.2025.27/13253

Для цитирования: Шостак Н. А. Азеотропизм клатратных гидратов. Краткий обзор. *Конденсированные среды и межфазные границы*. 2025;27(4): 547–554. https://doi.org/10.17308/kcmf.2025.27/13253

✉ Nikita A. Shostak, e-mail: nikeith@mail.ru

1. Introduction

The phenomenon of azeotropism, i.e., the ability of certain multicomponent systems to form inseparable boiling mixtures under specific conditions, is typically associated with the formation of associative intermolecular bonds [1]. It is widespread: approximately half of all studied liquid–vapor systems exhibit azeotropic behavior. Although this subject has been widely investigated in the literature [1–6], azeotropism in solid clathrate hydrate solutions remains relatively unexplored.

Azeotropes arise when a mixture deviates from Raoult's and Dalton's laws, which predict the equality of phase compositions and baric conditions, respectively. Such deviations result from physical and chemical effects including dipole–dipole interactions, molecular polarization, differences in van der Waals forces, and hydrogen bonding [6]. These factors can promote molecular association, dissociation, and solvation processes.

According to Konovalov's second law, azeotropic mixtures correspond to the extremal points of isobaric boiling point or isothermal vapor pressure versus composition curves. "Positive" azeotropes are associated with endothermic formation processes, while "negative" ones are exothermic. The decomposition of azeotropes is characterized by opposite enthalpy signs and energy magnitudes an order of magnitude smaller than the heat of vaporization, differing for each specific azeotrope.

Complex azeotropes can exhibit both minimum and maximum boiling points, and so-called "saddle-type" azeotropes do not fall strictly into positive or negative categories. As the boiling point or equilibrium pressure changes, the azeotropic composition shifts accordingly. Vrevsky demonstrated that in systems with vapor-pressure extrema, the azeotrope composition varies with temperature, reflecting a shift in vapor composition at equilibrium.

This implies that, at an azeotropic extremum, increasing the temperature raises the concentration of the component with the higher enthalpy of vaporization, and vice versa. Consequently, variations in thermobaric conditions alter the component concentrations and the azeotropic point itself; in some cases, the azeotropy may even disappear entirely.

Changes in mixture composition due to additional components also influence azeotropic behavior. When a small amount of a nonvolatile component is introduced, its effect depends on its impact on the mixture's vapor pressure. Similar equality effects in equilibrium phase compositions have been observed in crystalline phase–melt [12] and solid adsorbent–solution systems [13].

Clathrate hydrates, in this context, represent an especially intriguing research subject. They are crystalline compounds that form under specific thermobaric conditions from ice-like water molecule frameworks enclosing gaseous or liquid guest molecules in a quasi-liquid state. Owing to their structural and thermodynamic characteristics, clathrate hydrates hold great potential for gas storage, energy transport, and selective separation processes. The present work examines the features and possible applications of azeotropic phenomena in hydrate systems.

2. Azeotropism in clathrate hydrates

The phenomenon of azeotropism in hydrates was first observed experimentally in [15]. That study cast doubt on earlier interpretations by [7], who had considered double hydrogen sulfide hydrates as compounds of constant composition.

When analyzing the physical nature of azeotropy in clathrate hydrates, it is important to note that, in contrast to liquid solutions, intermolecular interactions between guest molecules confined within individual hydrate cavities are limited. If only one molecule is present per cavity, direct interaction between guest molecules is impossible. Instead, guest–host interactions occur between hydrate-forming molecules and the ice-like framework of water molecules through van der Waals forces. The strength of these interactions affects the Langmuir constants of the mixture components, which can be determined either directly using intermolecular interaction potential functions or by simplified empirical methods.

As suggested in [16], a significant difference between the Langmuir constants of two components can lead to azeotropic behavior at corresponding partial pressures P_A and P_B. Qualitatively, at equilibrium the mole fraction of

component A in the vapor phase equals that of component B in the hydrate phase:

$$\frac{C_A}{C_B} > 1, \quad (1)$$

$$\frac{P_A}{P_B} < 1. \quad (2)$$

Before proceeding to discuss the specific features and conditions under which azeotropism arises, it is useful to recall that hydrate cavities (Fig. 1) typically comprise 12–20 water molecule tetrahedra with oxygen atoms at the vertices and hydrogen bonds along the edges [17]. Molecules of small characteristic diameter (up to 5.5 Å) can occupy all cavity types, whereas larger molecules (5.5–7.5 Å) are confined to the larger *T*, *T'*, *P*, and *H* cavities.

Among known hydrate structures, the cubic CS-I and CS-II types are the most common, whereas the hexagonal (structure H) occurs less frequently (Table 1). CS-I has a body-centered cubic lattice containing 46 water molecules, comprising two small and six large cavities (Fig. 2). CS-II, with a face-centered cubic lattice of 136 water molecules, contains 16 small and eight large cavities. HS-III consists of 34 water molecules forming three small, two medium, and one large cavity.

The stability of a crystalline hydrate phase depends strongly on the fraction of occupied cavities. When the number of guest molecules is insufficient for a given pressure, temperature, and composition, the hydrate becomes unstable and dissociates. Thermodynamic studies show that hydrates formed from larger guest molecules (e.g., propane) exhibit lower equilibrium dissociation pressures than those formed from smaller ones (e.g., methane). Consequently, hydrates formed from mixed gases have equilibrium pressures closer to those of the component with the lower dissociation pressure.

For instance, a mixture containing 99 mol % methane and 1 mol% propane forms hydrates with a lower dissociation pressure than either pure methane or propane. Several studies have further shown that some ternary mixtures, such as methane–propane–water, exhibit equilibrium pressures even lower than those of the corresponding binary gas–water systems. At 278 K, a 25 mol % methane–propane mixture forms hydrates with a dissociation pressure below that of either pure gas. Propane in the gas phase forms hydrates at a pressure roughly 10% lower than that required for pure propane hydrate formation. In this particular ternary system, an azeotropic composition exists at which the dissociation pressure reaches a minimum compared with both individual hydrates.

The enhanced stability of hydrates formed from certain mixtures, reflected by their reduced

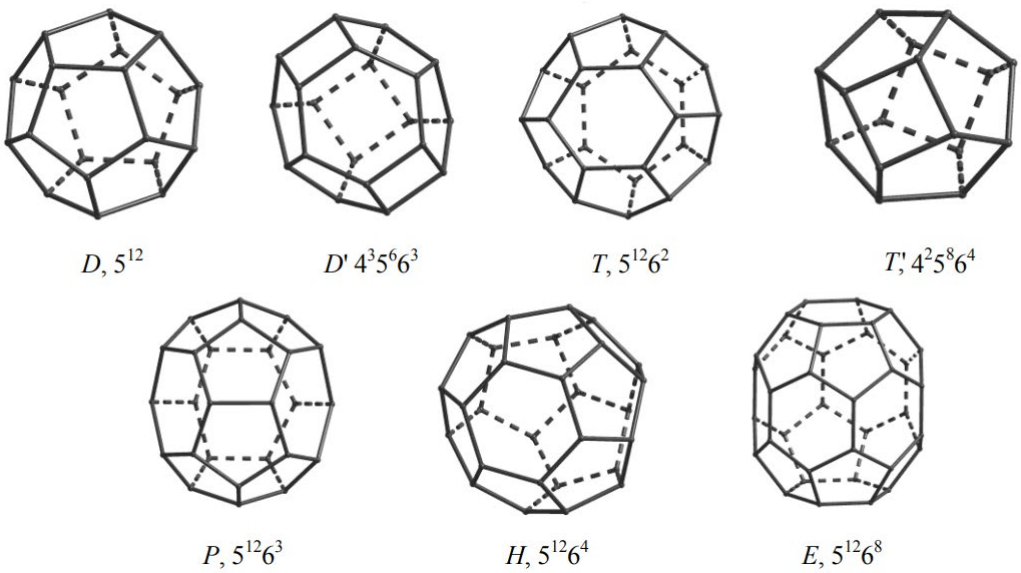

Fig. 1. Polyhedrons of hydrated frameworks – cavities (m^γ – γ faces with the number of edges m)

Table 1. Filling of small and large cavities of hydrate structures KS-I and KS-II with molecules

Molecule		Structure of CS-I		Structure of CS-II	
		Small cavities	Large cavities	Small cavities	Large cavities
Hydrate former	Diameter, Å	Ratio of molecule/cavity sizes			
He	2.28	0.447	0.389	0.454	0.342
H_2	2.72	0.533	0.464	0.542	0.408
Ne	2.97	0.582	0.507	0.592	0.446
Ar	3.80	0.756	0.649	**0.756**	**0.579**
Kr	4.00	0.795	0.683	**0.795**	**0.609**
N_2	4.10	0.815	0.700	**0.815**	**0.624**
O_2	4.20	0.835	0.717	**0.835**	**0.640**
CH_4	4.36	**0.867**	**0.744**	0.867	0.664
Xe	4.58	**0.911**	**0.782**	0.911	0.698
H_2S	4.58	**0.911**	**0.782**	0.911	0.698
CO_2	5.12	1.018	**0.874**	1.018	0.780
N_2O	5.25	1.044	**0.897**	1.044	0.800
C_2H_4	5.50	1.094	**0.939**	1.094	0.838
C_2H_6	5.50	1.094	**0.939**	1.094	0.838
C_2H_2	5.73	1.139	**0.978**	1.139	0.873
c-C_3H_6	5.80	1.153	**0.990**	1.153	**0.883**
C_3H_8	6.28	1.249	1.072	1.249	**0.957**
i-C_4H_{10}	6.50	1.292	1.110	1.292	**0.990**
n-C_4H_{10}	7.10	1.412	1.212	1.412	1.081

* Filling means the impossibility of filling the cavities, no filling and bold numbers correspond to individual, other cases – to mixed hydrates.

equilibrium pressure, results from several competing effects. In propane hydrates, propane molecules occupy only the large cavities of CS-II; the stability of this structure thus depends critically on the filling of these cavities. Methane, having a smaller molecular size, can occupy the small cavities of CS-II and thereby contribute to its stabilization. Reducing the molar fraction of propane in a methane–propane mixture increases the stability of methane hydrates and decreases that of propane hydrates. Under certain conditions, specifically at an azeotropic point, the stabilizing effect of methane exceeds the destabilizing effect of propane, producing an overall pressure reduction required for hydrate formation.

According to [16], hydrogen sulfide can occupy small cavities within the hydrate lattice in double-phase systems. In the CS-I structure, the total contribution of hydrogen sulfide to cavity filling is negligible. In contrast, in CS-II hydrates, larger guest molecules populate the large cavities while hydrogen sulfide preferentially occupies the small ones, thereby enhancing stability through selective cavity occupation.

3. Experimental methods for determining azeotropism in hydrates

The authors of [24] investigated several hydrate-forming systems: methane–propane–water at 275.15 K and 278.15 K; krypton–propane–water at 276.15 K; methane–cyclopropane–water at 277.15 K and 281.15 K; and methane–isobutane–water at 274.35 K. The temperatures were selected to prevent the appearance of a liquid hydrate-forming phase. Azeotropic compositions were identified for methane (0.19 mol%) – propane (0.81 mol%) at 275.15 K and 0.245 MPa, and for

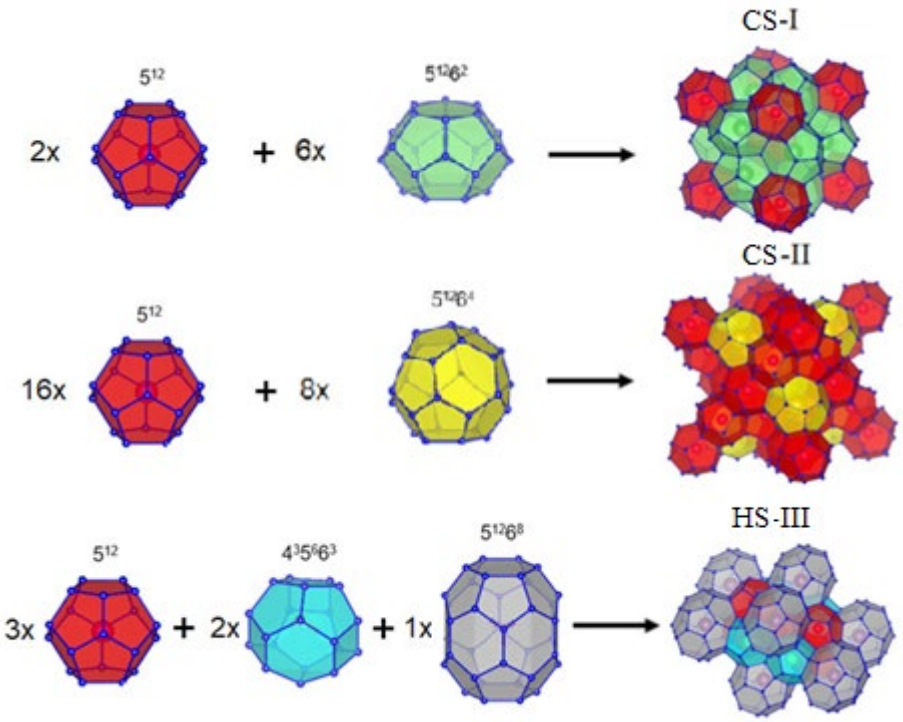

Fig. 2. Elementary cells of hydrate crystal lattices

methane (0.39 mol%) – propane (0.61 mol%) at 278.15 K and 0.458 MPa. Another azeotrope was observed for krypton (0.669 mol%) – propane (0.331 mol%) at 276.15 K and 0.231 MPa.

In [25], they presented the equilibrium conditions for hydrates of the binary mixtures Xe + C_3H_8, Kr + C3H8, and Kr + C_2H_6, for which they determined hydrate azeotrope formation temperatures of 273.5, 276.5, and 278.5 K, respectively.

A study [26] reported azeotropic mixtures of C_2F_6 and N_2 within the temperature range T > 276.5 K. X-ray powder diffraction showed that ternary systems consisting of C_2F_6, N_2, and H2O form hydrates with CS-II for all concentrations of C_2F_6 studied in this experiment. The pressure-composition diagram obtained at two different temperatures (275.15 K and 279.15 K) shows that C_2F_6 is highly enriched in the hydrate phase at 275.15 K, while at 279.15 K, the C_2F_6 + N_2 + H_2O system has an azeotrope with a hydrate composition that is the same as the vapor phase composition.

Experimental data from [24] also showed that methane–propane and propane–krypton systems form hydrate azeotropes in the temperature range 274.15–281.15 K, whereas methane–cyclopropane and methane–isobutane systems do not exhibit azeotropy under these conditions. These findings suggest that azeotropy originates from intrinsic features of hydrate crystal structures rather than from phase imperfections.

In [27], the azeotropic properties of clathrate hydrates formed by hydroquinone (HQ) with guest molecules of carbon dioxide (CO_2) and nitrous oxide (N_2O) were investigated. Structural features of β-HQ clathrates and cavity occupancy were characterized using scanning electron microscopy, X-ray diffraction, infrared and Raman spectroscopy, and solid-state nuclear magnetic resonance. Gas uptake and selectivity between CO_2 and N_2O were determined by gravimetric and concentration analyses of the clathrate phase.

4. Methods for calculating azeotropism in hydrates

The known conditions of the azeotropic state, such as temperature extrema or equality of the compositions of coexisting phases, serve as the

basis for determining the composition of an azeotrope at a given pressure.

To evaluate the hydrate composition at the azeotropic point, derivatives of the mole numbers of each component are taken with respect to pressure, while setting the derivative of the chemical potential difference to zero. This ensures the condition of extremum, since the potential difference varies monotonically with pressure at constant temperature.

Following [23], for a system composed of two gases and water, the azeotropic composition can be described by:

$$y_1 = \frac{\gamma - 1 + (\gamma \cdot C_{22} - C_{11}) \cdot P}{\left[C_{11} - C_{12}(\gamma \cdot C_{22} - C_{21})\right] \cdot P}, \quad (3)$$

$$\gamma = \frac{\nu_1}{\nu_1} \cdot \frac{C_{12} - C_{11}}{C_{21} - C_{22}}, \quad (4)$$

where ν_1 and ν_2 represent the numbers of small and large cavities per water molecule in the hydrate, C_{ji} are the Langmuir constants for the *i-th* molecule and the *j-th* cavity.

The equation shows that the hydrate composition in the azeotropic state strongly depends on the Langmuir constants, which in turn depend on the Kihara parameters of the hydrate formers and the cavity sizes.

To determine whether two hydrate formers are capable of forming an azeotrope, the ratio of their Kihara gas diameters to the cavity diameter is examined. This ratio by itself does not indicate the existence of an azeotropic state in the hydrate but only shows whether two types of gases can be geometrically combined to form an azeotropic mixture.

This ratio indicates geometric compatibility but does not necessarily guarantee azeotropy. Calculations [23] show that each cavity has an optimal ratio of Kihara diameter to cavity diameter of approximately 0.44. Based on this, the authors concluded that a ternary mixture will form azeotropic hydrates only if one of the hydrate-forming molecules has a ratio of large-to-small cavity diameters close to 0.44. Due to the presence of larger guest molecules, the cubic structure II hydrate is generally more stable than structure I; however, under certain conditions, structure I systems may also exhibit azeotropic behavior. Due to the presence of larger guest molecules, the hydrate of CS-II will generally be more stable than CS-I, however, under certain thermobaric conditions, systems with CS-I can also display azeotropic behavior.

Graphical interpolation techniques can be employed to estimate the hydrate composition at the azeotropic point for a fixed temperature. Grapho-analytical verification performed at 273.1 K confirmed azeotropy for several binary hydrate-forming mixtures: H_2S–CH_4, H_2S–C_2H_4, H_2S–C_2H_6, H_2S–CO_2, and H_2S–Br_2. Additional verification for CS-II hydrates, including H_2S–i-C_4H_{10}, H_2S–$CHCl_3$, H_2S–SF_6, C_3H_8–CH_4, C_3H_8–C_2H_6, C_3H_8–CO_2, C_3H_8–Br_2, and i-C_4H_{10}–$CHCl_3$, showed that only CS-II hydrates containing hydrogen sulfide exhibit azeotropic behavior.

A practical approach for experimentally confirming hydrate azeotropes is the chromatographic method described in [28]. It involves the gradual evaporation of liquid mixtures with helium or hydrogen in a column packed with nonporous material lacking a stationary liquid phase. The presence of azeotropy in a given concentration range can be inferred by comparing the heights of final elution peaks; variations in peak height indicate azeotropic composition.

It is noteworthy that hydrogen sulfide strongly stabilizes hydrate structures due to its positive external electron field when rotating within the cavity [29]. In contrast, carbon dioxide experiences a negative external field, reducing its stabilizing effect.

Alternatively, azeotropic behavior can be predicted using iterative methods for component distribution within the hydrate phase, as proposed in [30]. These methods utilize equilibrium constants and incorporate kinetic factors associated with phase transformation rates.

4. Conclusion

Although the azeotropic behavior of clathrate hydrates presents remarkable scientific and technological potential, the number of published studies remains limited [31–35].

Reference [27] proposed the storage of greenhouse gases in hydroquinone clathrates, which demonstrate strong molecular selectivity over a broad temperature range (up to ~353 K) and at moderate pressures (<1 MPa). For

hydroquinone clathrates with the composition 3HQβ·0.42CO_2·0.43N_2O, the total cavity occupancy was 0.82–0.84. The fraction of cavities filled with CO_2 increased linearly with its concentration in the feed mixture, while the N_2O occupancy decreased correspondingly.

From an industrial standpoint, the separation of azeotropic mixtures is one of the most challenging operations because the components undergo simultaneous vapor–liquid phase transitions. As suggested in [31], hydrate formation can be exploited as an alternative solid–liquid separation mechanism. The feasibility of such hydrate-based separation depends on the hydrate's crystal structure and bonding characteristics. For example, when separating cyclopentane and neohexane, both valuable hydrocarbon components and typical azeotrope formers, the use of hydrate formation enabled the purification of cyclopentane to 98.56 % yield, demonstrating the effectiveness of hydrate-based azeotrope separation technology.

Conflict of interests

The author declares that he has no known competing financial interests or personal relationships that could have influenced the work reported in this paper.

References

1. Khazanova N. E. *Systems with azeotropism at high pressures**. Moscow: Khimiya Publ.; 1978. 216 p. (in Russ.)

2. Horsley L. H. Table of azeotropes and nonazeotropes. *Analytical Chemistry*. 1949;21(7): 831–873. https://doi.org/10.1021/ac60031a022

3. Swietoslawski W. Azeotropy and Polyazeotropy. N.-Y.: Macmillan Company; 1963. 226 p.

4. Malesinski W. *Azeotropy and other theoretical problems of vapour-liquid equilibrium*. Warszawa: Polish Scientific Publishers; 1965. 222 p.

5. Prausnitz J. M. *Molecular thermodynamics of fluid-phase equilibria*. Canada: Prentice-Hall; 1969. 523 p.

6. *Azeotropic mixtures: Handbook** / S. K. Ogorodnikov, T. M. Lesteva, V. B. Kogan; V. B. Kogan (ed.). Leningrad: Khimiya Publ., Leningrad Department; 1971. 848 p. (in Russ.)

7. Konovalov D. P. *On the vapor elasticity of solutions**. St. Petersburg: 1909. 74 p. (in Russ.)

8. Kostyanovsky R. G. *Catenates and clathrates**. Moscow: Znanie Publ.; 1966. 32 p. (in Russ.)

9. Hilmen E.-K. *Separation of Azeotropic Mixtures: Tools for Analysis and Studies on Batch Distillation Operation*: A Thesis Submitted for the Degree of Dr. Ing. 2000. 288 p. Available at: https://skoge.folk.ntnu.no/publications/thesis/2000_hilmen/Thesis_Hilmen.pdf

10. Vrevsky M. S. *Works on the theory of solutions**. Moscow-Leningrad: 1953. 334 p. (in Russ.)

11. Kogan V. B. *Heterogeneous equilibria**. Leningrad: Khimiya Publ.; 1968. 431 p. (in Russ.)

12. Zhukhovitsky A. A., Shvartsman L. A. *Physical chemistry*. 2nd ed. Moscow: Metalurgizdat; 1968. 676 p. (in Russ.)

13. Kipling J. J. *Adsorbtion from solutions of non electrolytes*. London-New York: Acad. Press; 1965. 264 p.

14. Shostak N. A. *Modeling of formation and dissociation of hydrates during development and operation of oil and gas fields**. Cand. tech. sci. diss. Krasnodar: 2015. 118 p. (in Russ.). Available at: https://kubstu.ru/data/fdlist/FDD0427.pdf?6zm5bh

15. Platteeuw J. C., van der Waals J. H. Thermodynamic properties of gas hydrates II: Phase equilibria in the system H_2S-C_3H_8-H_2O at −3 °C. *Recueil des Travaux Chimiques des Pays-Bas*. 1959;78(2): 126–133. https://doi.org/10.1002/recl.19590780208

16. Byk S. Sh., Makogon Yu. F., Fomina V. I. *Gas hydrates**. Moscow: Nedra Publ.; 1980. 296 p. (in Russ.)

17. Dyadin Yu. A., Zhurko F. V., Bondaryuk I. V. *Clathrate hydrates at high pressures. Structure and stability**. Novosibirsk: INH Publ.; 1987. 48 p. (in Russ.)

18. Koryakina V. V., Semenov M. E., Shitz E. Yu., Portnyagin A. S. Research of structure of the synthetic hydrates of methane, ethane received in installations of the closed type. *International Research Journal*. 2016;7(49): 24–29. https://doi.org/10.18454/IRJ.2016.49.175

19. Deaton W. M., Frost E. M. *Gas hydrates and their relation to the operation of natural-gas pipe lines*. American Gas Association; 1949. 101 p.

20. Snell L. E., Otto F. D., Robinson D. B. Hydrates in systems containing methane, ethylene, propylene, and water. *AIChE Journal*. 1961;7(3): 482–485. https://doi.org/10.1002/aic.690070328

21. Verma V. K. *Gas Hydrates from Liquid Hydrocarbon–Water Systems*. Ph.D. Thesis. University of Michigan, University Microfilms; 1974. No. 75–10,324, Ann Arbor, MI. https://dx.doi.org/10.7302/10832

22. van der Waals J. H., Platteeuw J. C. Clathrate compounds. *Advances in Chemical Physics*. 1958; 1–57. https://doi.org/10.1002/9780470143483.ch1

23. Holder G. D., Grigoriou G. C. Hydrate dissociation pressures of (methane + ethane + water) existence of a locus of minimum pressures. *The Journal of Chemical Thermodynamics*. 1980: 1093–1104. https://doi.org/10.1016/0021-9614(80)90166-4

24. Thakore J. L., Holder G. D. Solid-vapor azeotropes in hydrate-forming systems. *Industrial and Engineering Chemistry Research*. 1987;26(3): 462–469. https://doi.org/10.1021/ie00063a011

25. Maekawa T. Phase equilibria for hydrate formation from binary mixtures of ethane, propane and noble gases. *Fluid Phase Equilibria*. 2006;243: 115–120. https://doi.org/10.1016/J.FLUID.2006.02.015

26. Kim E., Gyeol K., Yongwon S. Phase equilibria and azeotropic behavior of C_2F_6 + N_2 gas hydrates. *The Journal of Chemical Thermodynamics*. 2017;117: 43-47. https://doi.org/10.1016/j.jct.2017.06.016

27. Lim S. G., Jiyeong J., Jong-Won L., … Ji-Ho Y. Azeotropic clathrate: compelling similarity of CO_2 and N_2O

uptake in an organic crystalline host. *Chemical Engineering Journal*. 2021; 427: 131560. https://doi.org/10.1016/j.cej.2021.131560

28. Kiva V. N., Kozlova L. V., Krivodub V. G., Pariychuk L. V., Serafimov L. A., Sushko R. Sh. *Method for detecting azeotropy in mixtures**. USSR Patent: No. 250538. Publ. December 8, 1969. (in Russ.). Available at: https://rusneb.ru/catalog/000224_000128_0000250538_19690812_A1_SU/

29. Kvamme B., Ole K. F. Polar guest-molecules in natural gas hydrates. Effects of polarity and guest-guest-interactions on the Langmuir-constants. *Fluid Phase Equilibria*. 1993;83: 427–435. https://doi.org/10.1016/0378-3812(93)87047-5

30. Zaporozhets E. P., Shostak N. A. Calculation of the distribution of components in the formed hydrate*. *Science and Technology in the Gas Industry*. 2019; 2 (78): 21–27. (in Russ.). Available at: https://elibrary.ru/item.asp?edn=krydun

31. Landgrebe M. K. B., Nkazi D. Toward a robust, universal predictor of gas hydrate equilibria by means of a deep learning regression. *ACS Omega*. 2019;4(27): 22399–22417. https://doi.org/10.1021/acsomega.9b02961

32. Hu X., Sun L., Yuan C., … Song Y. Principle and feasibility study of proposed hydrate-based cyclopentane purification technology. *Energies*. 2023;16(12): 4681. https://doi.org/10.3390/en16124681

33. Avaji S., Javanmardi J., Mohammadi A. H., Rahmanian N., De-Gald V. The Kihara potential function parameters of methane, ethane, propane, and i-butane: the effects on clathrate hydrate structure determination. *Fluid Phase Equilibria*. 2023;567: 113716. https://doi.org/10.1016/j.fluid.2022.113716

34. Lim S. G., Jang J., Lee J.-W., … Yoon J.-H. Azeotropic clathrate: compelling similarity of CO_2 and N_2O uptake in an organic crystalline host. *Chemical Engineering Journal*. 2022;427: 131560. https://doi.org/10.1016/j.cej.2021.131560

35. Go W., Lee D., Seo Y. Synergistic inhibition effects of hydrophilic monomeric substances on CH_4 hydrate as revealed by experimental and computational approaches. *Chemical Engineering Journal*. 2021;426: 130794. https://doi.org/10.1016/j.cej.2021.130794

** Translated by author of the article*

Information about the author

Nikita A. Shostak, Cand. Sci. (Tech.), Associate Professor, Research Engineer, Kuban State University, Associate Professor of the Department of Oil and Gas Engineering named after Professor G. T. Vartumyan, Kuban State Technological University; Associate Professor of the Department of Normal Physiology, Kuban State Medical University of the Ministry of Health of the Russian Federation (Krasnodar, Russian Federation).

https://orcid.org/0000-0001-6220-9633

nikeith@mail.ru

Received January 26, 2025; approved after reviewing May 29, 2025; accepted for publication June 16, 2025; published online December 25, 2025.

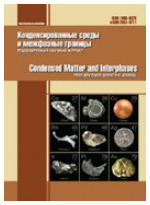

ISSN 1606-867X (Print)
ISSN 2687-0711 (Online)
Condensed Matter and Interphases
Kondensirovannye Sredy i Mezhfaznye Granitsy
https://journals.vsu.ru/kcmf/

Original articles

Research article
https://doi.org/10.17308/kcmf.2025.27/13254

Structural, optical and magnetic properties of $CoFe_{2-x}Eu_xO_4$ nanoparticles prepared by simple co-precipitation route

Le Ngoc Khanh Nhu[1], Nguyen Thi Thu Trang[1], Nguyen Hoang Huy[1], Tran Dinh Trinh[2], Ngoc Anh Vu Thi[3,4], Nguyen Anh Tien[1]✉

[1]Faculty of Chemistry, Ho Chi Minh City University of Education, No. 280 An Duong Vuong st., Ho Chi Minh City 700000, Vietnam

[2]VNU Key Laboratory of Advanced Materials for Green Growth, University of Science, Vietnam National University, No. 19 Le Thanh Tong st., Hoan Kiem, Hanoi 120000, Viet Nam

[3]Laboratory of Advanced Materials Chemistry, Institute for Advanced Study in Technology, Ton Duc Thang University, Ho Chi Minh City, Vietnam

[4]Faculty of Applied Sciences, Ton Duc Thang University, Ho Chi Minh City, Vietnam

Abstract

Objectives: Nanoparticles of $CoFe_{2-x}Eu_xO_4$ (x = 0, 0.025, 0.05, 0.075, and 0.1) were successfully synthesized by simple co-precipitation method.

Experimental: Field emission scanning electron microscopy (FE-SEM) images revealed europium-doped cobalt spinel ferrite nanoparticles formed after calcination of the precursor at 900 °C for 1 h, with sizes of approximately 20–40 nm. Energy dispersive X-ray spectra (EDXS) confirmed the presence of Co, Fe, Eu, and O elements with no evident of impurities. Results calculated from powder X-ray diffraction (PXRD) data show that the average crystallite size and lattice parameters decrease with increasing europium content.

Conclusions: The doping of Eu^{3+} ions in the cobalt ferrite structure affects the optical and magnetic properties of the substrate material. In this case, the values of band gap energy (E_g), coercivity (H_c) and remanent magnetization (M_r) increase with increasing concentration of Eu^{3+} ion, while optical absorption and saturation magnetization exhibit an opposite trend. The excellent optical and magnetic properties of un-doped and Eu-doped $CoFe_2O_4$ nanoparticles suggest great potential for applications related to optics and magnetism.

Keywords: Co-spinel, nanoparticles, Eu-doping, Co-precipitation, Optical property, Magnetic parameters

For citation: Le N. K. N., Nguyen T. T. T., Nguyen H. H., Tran D. T., Vu T. N. A., Nguyen A. T. Structural, optical and magnetic properties of $CoFe_{2-x}Eu_xO_4$ nanoparticles prepared by simple co-precipitation route. *Condensed Matter and Interphases*. 2025;27(4): 555–564. https://doi.org/10.17308/kcmf.2025.27/13254

✉ Nguyen Anh Tien, e-mail: tienna@hcmue.edu.vn

1. Introduction

Among inorganic oxides with small particle sizes, spinel ferrite-type RFe_2O_4 (where R is 3*d* transition metals such as Mn, Cr, Fe, Co, Ni, Zn) has attracted research attention due to its unique electrical, optical and magnetic properties [1–3]. The application fields of spinel ferrite RFe_2O_4 nanomaterials are also very abundant and diverse such as biochemical sensors, memory devices, computer components, high-density magnetic recording materials, transformer cores, permanent magnets, microwave absorbing materials [1–4]. In addition, spinel ferrites are also used for the removal of toxic organic substances in environmental treatment such as catalytic and photocatalytic decomposition of dyes, phenol, or nitrophenol [5], adsorption of congo red [6]. Among spinel ferrites, cobalt ferrite ($CoFe_2O_4$) is the of particular interest to many researchers due to its interesting physicochemical properties such as chemical and mechanical stability, high crystalline anisotropy ($K{\cdot}10^{-3} = 6.04$ emu·g^{-1}·Oe) [7], moderate saturation magnetization (M_s = 67.37 emu·g^{-1}) [8], high coercivity (H_c = 848.32 Oe) [9], ferromagnetism with high Curie temperature (T_c = 790 K) [10, 11].

Besides interesting magnetic properties, $CoFe_2O_4$ nanoparticles have recently been studied as catalytic materials and Fenton photocatalysts for various reactions due to their strong absorption of light in the ultraviolet and visible regions [8, 11–15]. It can be seen that, depending on the research objectives, there will be different adjustments to the optical and magnetic properties of spinel ferrite. This can be done through different synthesis conditions or doping with different metals on the spinel ferrite MFe_2O_4 substrate [10, 11, 16–20]. Among these approaches, doping with rare earth metal ions to modify the structural, optical and magnetic properties of cobalt ferrite has been explored. Indeed, studies by Alves [11] and Patankar [18] showed that increasing the Y^{3+} ion content in cobalt ferrite $CoFe_{2-x}Y_xO_4$ increases the coercivity and band gap values, but decreases the saturation magnetization and remanence. Vibrating sample magnetometry studies at room temperature showed that $CoFe_{1.8}Tb_{0.2}O_4$ and $CoFe_{1.8}Er_{0.2}O_4$ nanoparticles had saturation magnetizations of 60 and 80 emu·g^{-1} [19]. Gd^{3+} ion doping in cobalt ferrite reduced all three magnetic parameters of cobalt ferrite (M_s = 87.56–52.01 emu·g^{-1}, M_r = 21.2–3.40 emu·g^{-1}, and H_c = 575–50 Oe) reported in the study of Zhao et al. [20]. Using the citric sol-gel method [21], Boddolla and Ravinder successfully synthesized $CoFe_{1-x}Eu_xO_4$ nanoparticles (x = 0 and 0.1) after drying the precursor at 100 °C in 8 h and heating the dry gel at 500 °C in 4 h. However, the research of Boddolla and Ravinder only mentioned the structural characteristics of $CoFe_{1-x}Eu_xO_4$ nanocrystals synthesized using powder X-ray diffraction analysis (PXRD) and fourier-transform infrared spectra (FTIR) [21]. The optical and magnetic properties of $CoFe_{2-x}Eu_xO_4$ nanoparticles were not reported.

Un-doped and R-doped $CoFe_2O_4$ nanomaterials were mainly synthesized by wet chemical methods such as sol-gel using citric acid [3, 4,1 2], sol-gel with the assistance of polyethylene glycol [8], combustion synthesis using urea fuel (CON_2H_4) [11, 15, 22], combustion using glycine [14], hydrothermal [6, 20], or co-precipitation at room temperature [7, 13, 19, 23], co-precipitation using oleic acid [10]. In general, each synthesis method has its strengths and weaknesses. Therefore, the choice of experimental conditions depends on the specific objectives of the research. In our previous studies [9, 24–26], oxide nanoparticles with spinel structure MFe_2O_4 (M = Co, Ni) and perovskite $RFeO_3$ (R = Eu, Dy) have been successfully synthesized by co-precipitation method through hydrolysis of R^{3+} and Fe^{3+} ations at high temperature, then cooling to room temperature before adding a suitable precipitating agent. To the best of our knowledge, this simple co-precipitation route has not been reported in the literature for the study of europium-substituted cobalt spinel ferrite.

Therefore, the aim of this study was to synthesize $CoFe_{2-x}Eu_xO_4$ spinel nanoparticles (x = 0, 0.025, 0.05, 0.075, and 0.1) by simple co-precipitation method (without any gelling agent), followed by comprehensive analysis of their crystalline structures, chemical compositions, morphologies, particle sizes, optical and magnetic properties. In addition, the study also evaluated the effect of Eu^{3+} doping ion content on the structural, optical and magnetic parameters of the synthesized $CoFe_{2-x}Eu_xO_4$ nanoparticles. In this study, the doping ratio limit is chosen to be x = 0.1 [20, 21]. Due to the significant difference

in ionic radii between Fe^{3+} (r = 0.645 Å) and rare earth metal ions R^{3+} (r ~ 1.00 Å) [27], secondary crystal phases, such as perovskite $YFeO_3$ in $Co(Ni)Fe_{2-x}Y_xO_4$ spinel [18, 28], often appear when x > 0.1.

2. Experimental methods

$CoFe_{2-x}Eu_xO_4$ nanoparticles were synthesized by simple co-precipitation method according to the diagram shown in Fig. 1 [9, 24–26]. 50 mL of aqueous solution of $Co(NO_3)_2 \cdot 6H_2O$ (99.9 % purity, Thermo Scientific), $Fe(NO_3)_3 \cdot 9H_2O$ (99.9 % purity, Sigma-Aldrich), and $Eu(NO_3)_3 \cdot 6H_2O$ (99.9 % purity, Thermo Scientific) with the stoichiometric ratio of $Co^{2+} : Fe^{3+} : Eu^{3+} = 1 : (2- x) : x$ (x = 0, 0.025, 0.05, 0.075, and 0.1 in theory) was added dropwise into a beaker containing 450 mL of boiling water on a heated magnetic stirrer (t ~ 95 °C). The reaction system was maintained at 95 °C for about 10 minutes to completely hydrolyze the metal cations, then cooled to room temperature (~ 27 °C).

Next, 5% NaOH solution was added dropwise to the reaction mixture until pH value = 10 while continuously stirring [7, 19, 25]. NaOH solution was used instead of NH_3 because cobalt(II) hydroxide can be dissolved in excess ammonia as shown in equation (1), which leads to difficulty in controlling the composition of the precipitate after the reaction [27]:

$$[Co(OH)_2(H_2O)_4]_{(s)} + 6NH_{3(aq)} \rightarrow \rightarrow [Co(NH_3)_6]^{2+}_{(aq)} + 4H_2O_{(l)} + 2OH^-_{(aq)} \quad (1)$$

The precipitate was stirred for another 30 minutes, then filtered and washed with distilled water until neutral pH. Next, the obtained precipitate was air–dried at room temperature to constant weight (approximately 5 days), then ground into fine dark brown powder, serving as the precursor. $CoFe_{2-x}Eu_xO_4$ ($x \leqslant 0.1$) nanoparticles were obtained after calcining the precursor in the air, at 900 °C for 1 h. This temperature was selected based on previous research [8, 9, 15, 23], in which the obtained ferrite spinels are single-phase, have good crystallinity and reach nanometer size. The expected reaction to form ferrites $CoFe_{2-x}Eu_xO_4$ from the corresponding precipitate mixture can be described by the following equation (2):

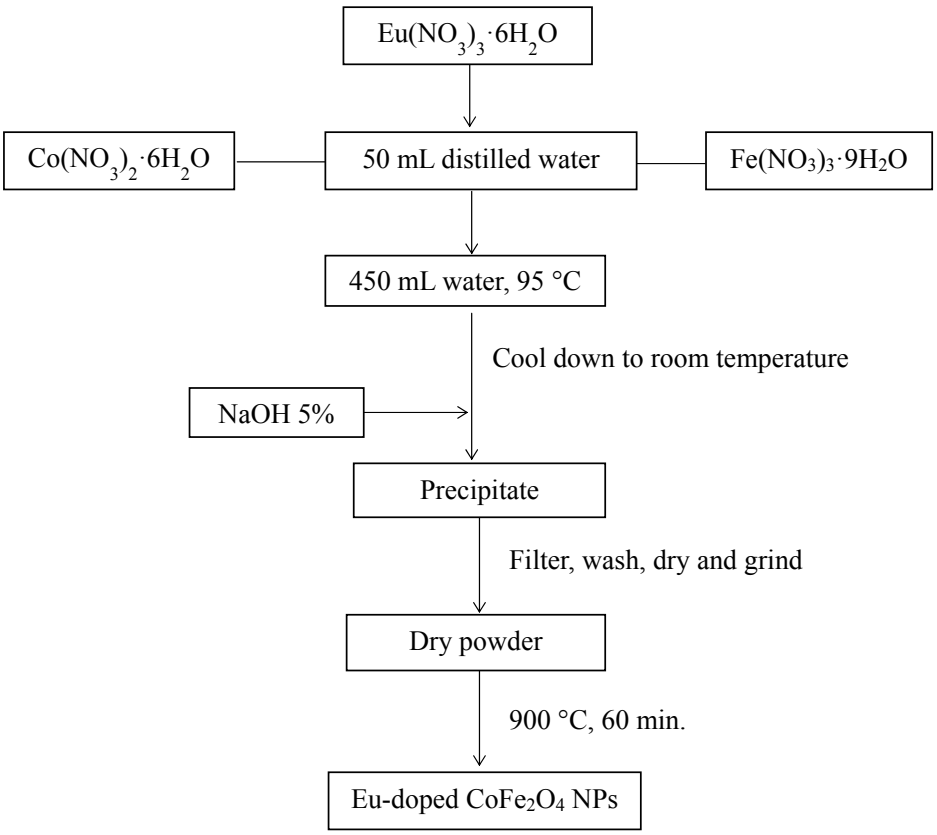

Fig. 1. Flow chart for synthesis of $CoFe_{2-x}Eu_xO_4$ nanoparticles. The synthesized samples were characterized by different methods presented in Table 1

Table 1. Analytical methods and corresponding used equipment

Analytical methods	Equipment	Experimental conditions
Powder X-ray diffraction (PXRD)	EMPYREAN X-ray diffractometer (PANanalytical, Netherlands)	– Cu*K*α radiation (λ = 1.54060 Å) – Angle range 2θ = 10–80 ° – Scanning step 0.02 °/s
Energy-dispersive X-ray spectroscopy (EDX) and EDX-mapping	FESEM S-4800 spectrometer (Hitachi, Japan)	Equipped with an EDX H-7593 (Horiba, UK)
Field emission scanning electron microscopy (FE-SEM)	FESEM S-4800 (Hitachi, Japan)	
Ultraviolet-Visible (UV-Vis) spectroscopy	Spectrophotometer UV-2600 (Shimadzu, Japan)	– Equipped with an integrating sphere (ISR-2600 Plus) – Using deuterium and halogen lamps – Using $BaSO_4$ powder as a baseline material
Vibrating-sample magnetometry (VSM)	Magnetometer MICROSENE EV11 (Japan)	– Magnetic field ranging from – 15 000 Oe to + 15 000 Oe – At room temperature

$$Co(OH)_2 + (2-x)Fe(OH)_3 + xEu(OH)_3 \rightarrow$$
$$\rightarrow CoFe_{2-x}Eu_xO_4 + 4H_2O \quad (2)$$

3. Results and discussion

Fig. 2 shows the PXRD patterns of the synthesized $CoFe_{2-x}Eu_xO_4$ nanoparticles with different doping amounts of Eu^{3+} ions. All the diffraction peaks can be indexed to the cubic spinel structure of cobalt ferrite (JCPDS > 090–3471, *Fd3m space group*) and no impurity phases are observed. The PXRD pattern exhibits 9 peaks at 2θ ~ 18.30°, 30.14°, 35.52°, 37.10°, 43.14°, 53.50°, 57.04°, 62.62°, 72.40° corresponding to the Miller indices (hkl): (111), (220), (311), (222), (400), (422), (511), (440), and (533) [23]. The PXRD patterns all have flat and smooth baselines, and the obtained peaks have high intensity, proving that the synthesized $CoFe_{2-x}Eu_xO_4$ samples have good crystallinity.

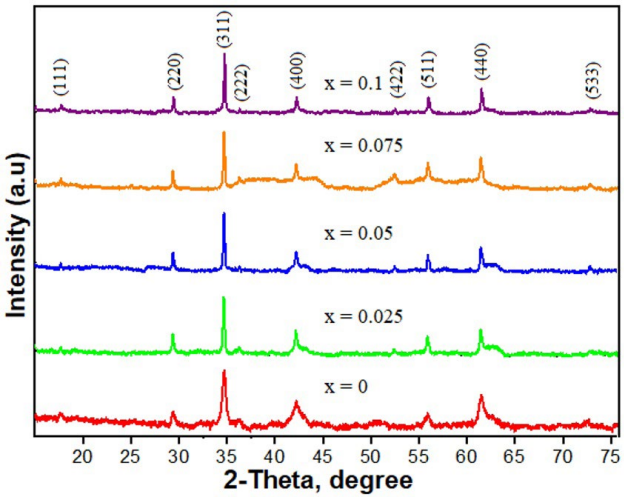

Fig. 2. PXRD patterns of Eu–doped $CoFe_2O_4$ samples annealed at 900 °C

Due to the replacement of Fe^{3+} ion by Eu^{3+} ion with larger radius ($r(Fe^{3+})$ = 0.645 Å, $r(Eu^{3+})$ = 0.950 Å), the 2θ angle is slightly shifted to the right (towards the larger angle), and a slight broadening of the peak when x increases from 0.025 to 0.1 (Fig. 3). These changes imply a decrease in the crystallite size ($D_{(hkl)}$) and the lattice parameter (a) of the $CoFe_{2-x}Eu_xO_4$ samples according to the following equations (3) and (4) [23, 28]:

$$D_{hkl} = \frac{k \cdot \lambda}{\beta_{hkl} \cdot \cos\theta}, \quad (3)$$

where β_{hkl} is the full-width at half maximum (FWHM, radian), θ is the corresponding diffraction angle of the maximum reflection (degree), and k is the shape factor (k = 0.89).

$$a = d_{hkl}\sqrt{(h^2 + k^2 + l^2)}. \quad (4)$$

Where d is the value of d-spacing of the planes and (hkl) are the corresponding Miller indices of the Planes.

The calculated values from PXRD patterns are listed in Table 2. It is obvious that the average crystallite sizes (D) and the lattice parameters (a, V) of the synthesized $CoFe_{2-x}Eu_xO_4$ samples

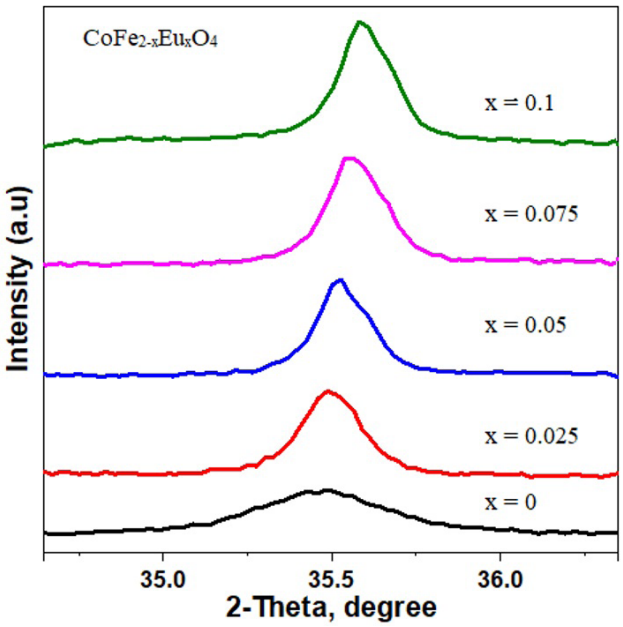

Fig. 3. PXRD patterns of peak (311) of Eu-doped $CoFe_2O_4$ samples annealed at 2θ = 34.7–36.3°

decrease with increasing the doping amount of Eu^{3+} ions. The Eu^{3+} ions, with larger radius (r = 0.950 Å), preferentially occupy octahedral positions and partially replace the Fe^{3+} ions (r = 0.645 Å). This substitution induces strains and disorders in the lattice structure. These changes limit the crystallization of material particles and hinder crystal growth. Similar results have also been reported for other spinel ferrite nanoparticles doped with various rare earth elements such as Gd-doped $CoFe_2O_4$ [20], Ce(Gd)-doped $NiFe_2O_4$ [29], and also for Eu-doped $CoFe_2O_4$ nanoparticles synthesized by hydrothermal method [30] and sonochemical technique [31].

Fig. 4 shows the EDX spectra of pure $CoFe_2O_4$ and $CoFe_{1.95}Eu_{0.05}O_4$ nanoparticles measured at room temperature. It is clear that for the x = 0 sample, only peaks of the elements Co, Fe, and O are observed. As for the Eu-doped $CoFe_2O_4$ sample (x = 0.05), in addition to the peaks of Co, Fe and O, peaks of the element Eu also appear. To accurately determine the content of elements in $CoFe_{2-x}Eu_xO_4$ samples (x = 0 and 0.05), EDXS analysis was recorded at 3 different positions in the sample. EDXS quantitative data showed that the ratios of Co/Fe/Eu/O elements for all samples were consistent with their ratios in the expected formula. This shows the high

Table 2. Refined structural parameters and crystallite size of $CoFe_{2-x}Eu_xO_4$ samples

Sample	D_{hkl}, nm	a, Å	V, Å^3
$CoFe_2O_4$	15.30	8.3554	583.31
$CoFe_{1.975}Eu_{0.025}O_4$	29.87	8.3449	581.12
$CoFe_{1.95}Eu_{0.05}O_4$	28.46	8.3405	580.20
$CoFe_{1.925}Eu_{0.075}O_4$	27.82	8.3366	579.38
$CoFe_{1.9}Eu_{0.1}O_4$	27.17	8.3215	576.24

purity of the synthesized $CoFe_{2-x}Eu_xO_4$ spinel nanoparticles.

To determine the morphology and grain size of the material synthesized, FE-SEM images of $CoFe_{2-x}Eu_xO_4$ samples (with x = 0 and 0.05) are shown in Fig. 5.

The particles have relatively uniform morphology with particle size of approximately 20–40 nm. Fig. 5 also shows that doping Eu^{3+} ion into the cobalt ferrite crystal lattice has an unclear effect on the morphology and size of the synthesized $CoFe_{2-x}Eu_xO_4$ nanoparticles. However, it is evident that both the pure doped sample have agglomeration between nanoparticles. Such agglomeration can be ascribed to the strong magnetic interactions between the particles, leading to mutual magnetization induction. Similar phenomenon was also observed in other spinel ferrites synthesized by different wet chemical methods [12, 15, 20, 28, 30, 32].

The optical properties of $CoFe_{2-x}Eu_xO_4$ nanoparticles (x = 0, 0.025, 0.05, 0.075, and 0.1) were determined through UV-Vis measurements in the wavelength range from 200 to 800 nm, corresponding to photon energy of 1.55 eV to 6.2 eV (Fig. 6). The optical band gaps (E_g, eV) of $CoFe_{2-x}Eu_xO_4$ nanoparticles were calculated using Tauc equation that correlates the absorption coefficient and E_g as below [11, 25, 28, 31]:

$$Ah\nu = \sqrt{\alpha(h\nu - E_g)}, \quad (5)$$

where A is the optical absorption coefficient, $h\nu$ is the photon energy, E_g is the direct band gap and α is a constant.

Fig. 6a shows that europium-doped cobalt ferrite nanoparticles exhibit strong optical absorption not only in the ultarviolet (λ = 200–400 nm) but also in visible light regions (λ = 400–800 nm). Particularly, the maximum absorption is observed in the wavelength range of 350–700 nm.

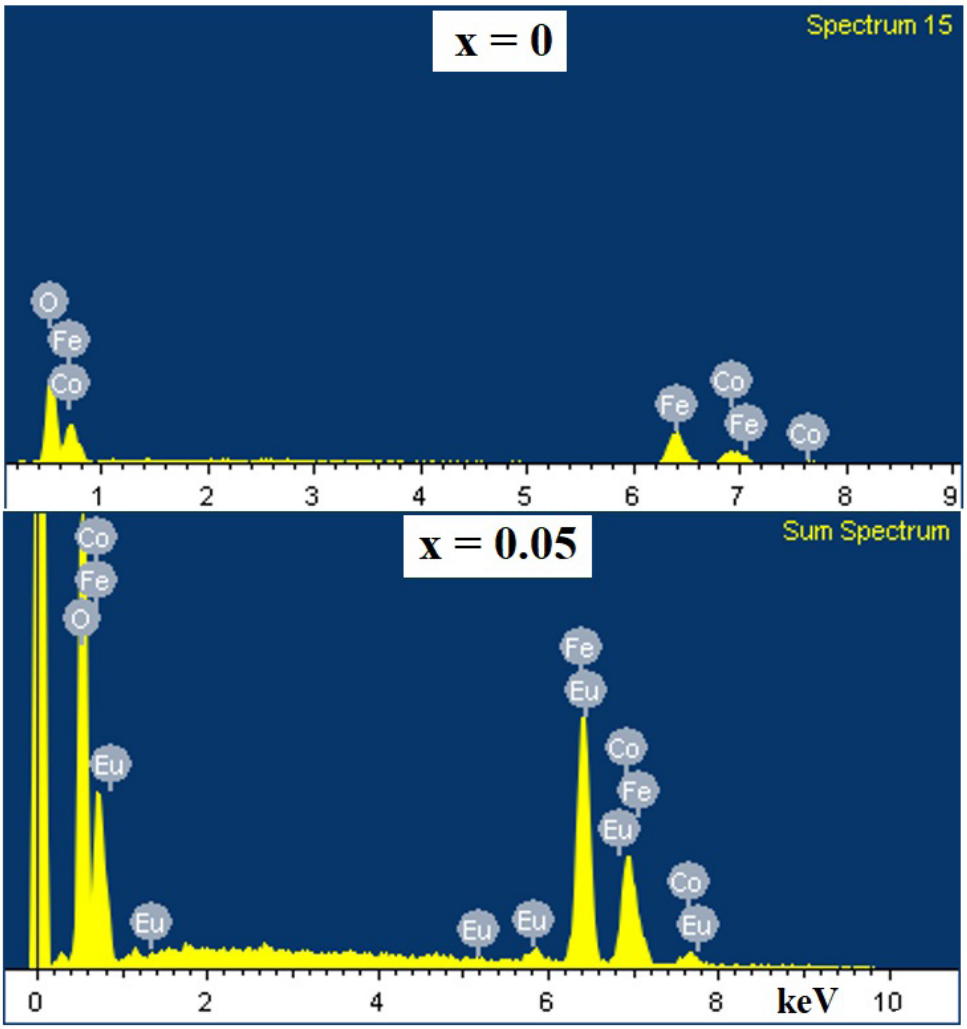

Fig. 4. Energy-dispersive X-ray spectroscopy (EDXS) spectra of pure $CoFe_2O_4$ (x = 0) and $CoFe_{1.95}Eu_{0.05}O_4$ (x = 0.05) nanoparticles

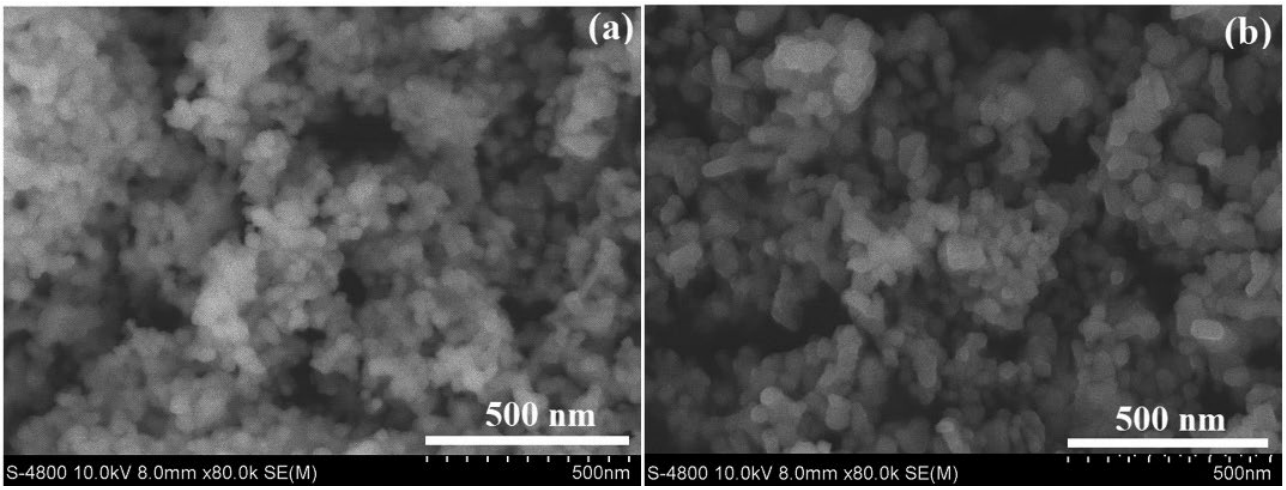

Fig. 5. Field emission scanning electron microscopy (FE-SEM) images of pure $CoFe_2O_4$ (a) and $CoFe_{1.95}Eu_{0.05}O_4$ (b) nanoparticles

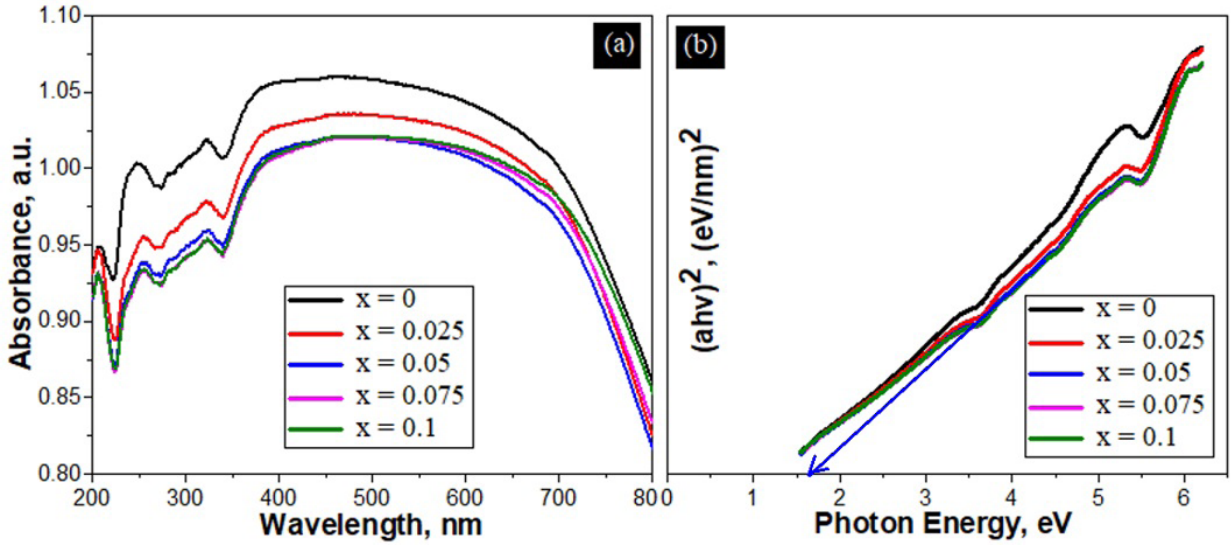

Fig. 6. (a) Room-temperature optical absorbance spectra of the $CoFe_{2-x}Eu_xO_4$ samples and (b) Plot of $(\alpha hv)^2$ as a function of photon energy for $CoFe_{2-x}Eu_xO_4$ nanoparticles

The absorption tends to decrease with increasing Eu^{3+} ion content, which also means that the band gap energy value (E_g) changes in the opposite trend (Fig. 6b and Table 3). The value of E_g increases from 1.37 eV to 1.55 eV corresponding to the value of x increasing from 0 to 0.1.

The increase of band gap energy values with increasing doping element content were also reported for other spinel cobalt ferrites systems such as $CoFe_{2-x}Y_xO_4$ ($x = 0 \rightarrow 0.04$, $E_g = 2.30 \rightarrow 2.58$ eV) synthesized by the urea-fueled combustion method [11] or $CoFe_{2-x}Eu_xO_4$ ($x = 0 \rightarrow 0.1$, $E_g = 1.34 \rightarrow 1.56$ eV) synthesized by sonochemical technique [31]. With strong optical absorption in wavelength range of 350–700 nm and semiconductor-like band gap energy values

Table 3. Optical and magnetic parameters of $CoFe_{2-x}Eu_xO_4$ nanoparticles at RT in this study and that from the published literature as a comparison

Sample	E_g, eV	H_c, Oe	M_r, emu·$^{-1}$	M_s, emu·g^{-1}	Ref.
$CoFe_2O_4$	1.37	962.96	32.97	72.08	In this work
$CoFe_{1.975}Eu_{0.025}O_4$	1.45	983.75	33.83	71.74	
$CoFe_{1.95}Eu_{0.05}O_4$	1.50	1029.67	34.20	70.05	
$CoFe_{1.925}Eu_{0.075}O_4$	1.53	1121.38	37.37	65.22	
$CoFe_{1.9}Eu_{0.1}O_4$	1.55	885.46	29.62	61.74	
$CoFe_2O_4$	–	120	9	41.2	[7]
$CoFe_2O_4$	–	495.72	23.34	67.37	[8]
$CoFe_2O_4$	–	762.04	27.83	61.80	[15]
$CoFe_2O_4$	–	575	21.2	87.56	[20]
$CoFe_2O_4$	–	880	27.7	79.5	[30]
$CoFe_2O_4$	2.30	1100	28	69	[11]
$CoFe_{1.995}Y_{0.005}O_4$	2.32	1318	27	63	
$CoFe_{1.99}Y_{0.01}O_4$	2.34	1520	26	62	
$CoFe_{1.98}Y_{0.02}O_4$	2.42	1676	20	50	
$CoFe_{1.97}Y_{0.03}O_4$	2.45	1804	19	49	
$CoFe_{1.96}Y_{0.04}O_4$	2.58	1900	12	33	

(E_g = 1.37–1.55 eV), the synthesized $CoFe_{2-x}Eu_xO_4$ nanoparticles can be applied as photocatalytic materials for the decomposition of dyes, phenol, nitrophenol, methyl orange, or methylene blue [5, 11, 13, 32].

Fig. 8a shows the *M*–*H* loops of $CoFe_{2-x}Eu_xO_4$ ferrite nanosystems with x = 0, 0.025, 0.05, 0.075, and 0.1 at room temperature (300 K) under applied magnetic field up to 15 kOe. The observed remanent magnetization (M_r) and coercivity (H_c) in all hysteresis loops indicate that all samples are hard ferrites at room temperature [34]. All three magnetic parameters (M_r, H_c, and M_s) of $CoFe_{2-x}Eu_xO_4$ nanoparticles vary with the Eu^{3+} ion content (Table 3). Specifically, H_c increases from 962.96 to 1121.38 Oe, M_r increases from 32.97 to 37.37 emu·g^{-1}, while M_s decreases from 72.08 to 61.74 emu·g^{-1}. The increase in H_c and M_r values with increasing content of doping elements (Eu^{3+} ion) is attributed to enhanced crystal anisotropy [34, 35]. Meanwhile, partial replacement of Fe^{3+} ions at octahedral sites by Eu^{3+} ions reduces the magnetization on the Fe^{3+} sites (B-sites), thereby reducing the total magnetization of the Eu-doped $CoFe_2O_4$ nanoparticles. Similar trend was also reported for the Y^{3+} doped spinel cobalt ferrites [11]. In general, all three values H_c, M_r, and M_s of $CoFe_{2-x}Eu_xO_4$ nanoparticles are larger than those reported for pure $CoFe_2O_4$ nanoparticles synthesized using different methods [7, 8, 15, 20, 30], with H_c and M_s are also larger than those of Y-doped $CoFe_2O_4$ nanoparticles [11] (Table 3).

Another noteworthy observation is that the synthesized $CoFe_{2-x}Eu_xO_4$ nanoparticles are strongly attracted by rare earth magnets. This, combined this with the semiconductor bandgap energy value, suggests that the synthesized Eu-doped $CoFe_2O_4$ nanoparticles can be used as photocatalytic materials under the influence of sunlight with easy recovery and reuse by rare earth magnets.

4. Conclusions

Undoped and Eu-doped $CoFe_2O_4$ nanoparticles were successfully prepared by the simple co-precipitation method with 5% NaOH as a precipitant. Eu^{3+} ion doping at the Fe^{3+} site in spinel cobalt affects not only the structural parameters (D_{hkl} and a) but also their magneto-optical properties. The FE-SEM images confirms the nanostructure character of the $CoFe_{2-x}Eu_xO_4$ samples with particle sizes ranging from 20 to 40 nm. When the Eu^{3+} ion doping content increased, the E_g (1.37–1.55 eV), M_r (32.97–37.37), and H_c (962.96–1121.38 Oe) increased, while the M_s (72.08–61.74 emu·g^{-1}) decreases. Synthesized $CoFe_{2-x}Eu_xO_4$ nanoparticles exhibit the behavior of a hard ferromagnetic material with a small band gap energy, making them suitable not only for photocatalytic applications but also for the production of permanent magnets, magnetic tapes, and magnetic recording materials in hard drives.

Contribution of the authors

Le N. K. N: Investigation, methodology & Software. Nguyen T. T. T.: Methodology, writing–

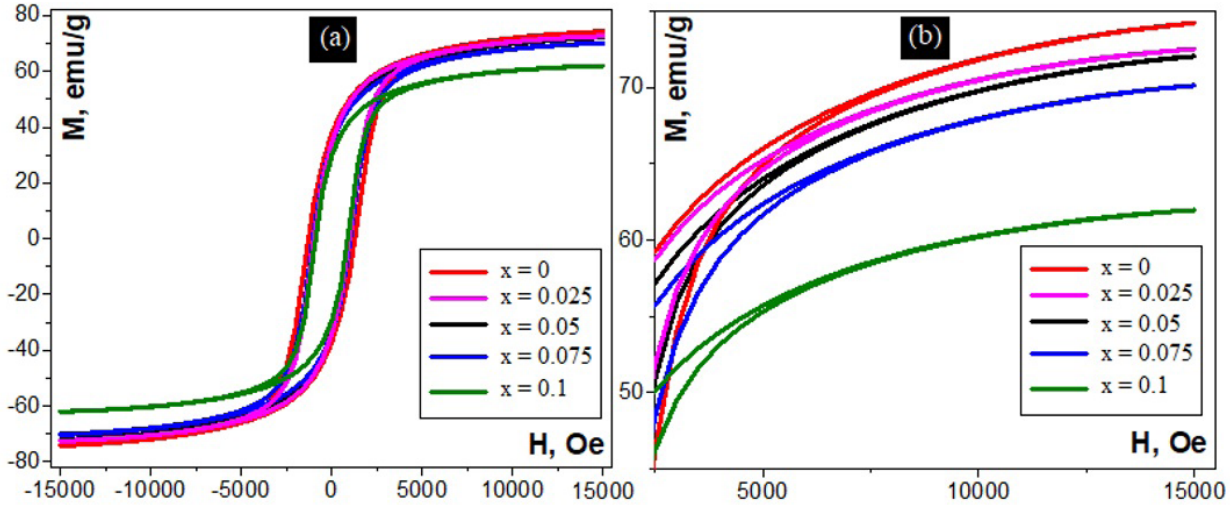

Fig. 7. *M*–*H* loops of $CoFe_{2-x}Eu_xO_4$ nanoparticles measured at room temperature

original draft. Nguyen H. H.: Methodology & Software. Tran D. T.: Validation, Supervision & writing-original draft. Vu T. N. A.: Investigation, methodology & Formal analysis. Nguyen A. T.: Investigation, Data curation, Writing–review and editing. All authors have read and agreed to the published version of the manuscript.

Data availability statement

The data that support the findings of this study are available from the corresponding author upon reasonable request.

Conflict of interest

The authors maintain that they have no conflict of interest to be described in this communication.

References

1. Kebede K. K., Msagati T. A. M., Mamba B. B. Ferrite nanoparticles: synthesis, characterization and applications in electronic device. *Materials Science and Engineering: B*. 2017;215: 37–55. https://doi.org/10.1016/j.mseb.2016.11.002

2. Tomina E. V., Sladkopevtsev B. V., Nguyen A. T., Vo Q. M. Nanocrystalline ferrites with spinel structure for various functional applications. *Inorganic Materials*. 2023;59: 1363–1385. https://doi.org/10.1134/S0020168523130010

3. Zhang F., Wei C., Wu K., Zhou H., Hu Y., Preis S. Mechanistic evaluation of ferrite AFe_2O_4 (A = Co, Ni, Cu, and Zn) catalytic performance in oxalic acid ozonation. *Applied Catalysis A: Genenal*. 2017;547: 60–68. https://doi.org/10.1016/j.apcata.2017.08.025

4. Ivashenko D. V., Urbanovich D. A., Palyn I. Y., Bushinsky M. V., Trukhanov A. V., Pankov V. V. Synthesis dispersed powders of CoZn ferrites for microwave absorption. *Condensed Matter and Interphases*. 2023;25: 37–46. https://doi.org/10.17308/kcmf.2023.25/10646

5. Kefeni K. K., Mamba B. B. Photocatalytic application of spinel ferrite nanoparticles and nanocomposites in wastewater treatment: review. *Sustainable Materials and Technology*. 2020;23: e00140. https://doi.org/10.1016/j.susmat.2019.e00140

6. Wang L., Li J., Wang Y., Zhao L., Jiang Q. Adsorption capability for congo red on nanocrystalline MFe_2O_4 (M = Mn, Fe, Co, Ni) spinel ferrites. *Chemical Engineering Journal*. 2012;181: 72–79. https://doi.org/10.1016/j.cej.2011.10.088

7. Jain R., Kumar S., Meena S. K. Precipitating agent (NaOH and NH_4OH) dependent magnetic properties of cobalt ferrite nanoparticles. *AIP Advances*. 2022;12: 095109. https://doi.org/10.1063/5.0098157

8. Ngo T. P. H., Le T. K. Polyethylene glycol-assisted sol-gel synthesis of magnetic $CoFe_2O_4$ powders as photo-Fenton catalysts in the presence of oxalic acid. *Journal of Sol-Gel Science and Technology*. 2018;88: 211–219. https://doi.org/10.1007/s10971-018-4783-y

9. Nguyen A. T., Nguyen T. D., Mittova V. O., Berezhnaya M. V., Mittova I. Ya. Phase composition and magnetic properties of $Ni_{1-x}Co_xFe_2O_4$ nanocrystals with spinel structure synthesized by co-precipitation method. *Nanosystems: Physics, Chemistry, Mathematics*. 2017;8: 371–377. https://doi.org/10.17586/2220-8054-2017-8-3-371-377

10. Maaz K., Khalid W., Mumtaz A., Hasanain S. K., Liu J., Duan J. L. Magnetic characterization of $Co_{1-x}Ni_xFe_2O_4$ nanoparticles prepared by co-precipitation route. *Physical E: Low-dimensional Systems and Nanostructures*. 2009;41: 593–599. https://doi.org/10.1016/j.physe.2008.10.009

11. Alves T. E. P., Pessoni H. V. S., Franco Jr. A. The effect of Y^{3+} substitution on the structural, optical band-gap, and magnetic properties of cobalt ferrite nanoparticles. *Physical Chemistry Chemical Physics*. 2017;25: 16395–16405. https://doi.org/10.1039/C7CP02167D

12. Tomina E. V., Kurkin N. A., Doroshenko A. V. Synthesis of nanoparticulate cobalt ferrite and its catalytic properties for Fenton-like processes. *Inorganic Materials*. 2022;58: 727–732. https://doi.org/10.31857/S0002337X22070132

13. Thomas J., Thomas N., Girgsdies F., M. Beherns, ... Sebastiane V. Synthesis of cobalt ferrite nanoparticles by constant pH co-precipitation and their high catalytic activity in CO oxidation. *New Journal of Chemistry*. 2017;41: 7356–7363. https://doi.org/10.1039/c7nj00558j

14. Sumathi S., Lakshmipriya V. Structural, magnetic, electrical and catalytic activity of copper and bismuth co-substituted cobalt ferrite nanoparticles. *Journal of Materials Science: Materials in Electronics*. 2017;28: 2795–2802. https://doi.org/10.1007/s10854-016-5860-z

15. Nguyen T. T. L., Nguyen T. H. L., Nguyen T. T. H., ... Tran T. V. $CoFe_2O_4$ nanomaterials: effect of annealing temperature on characterization, magnetic, photocatalytic, and photo-Fenton properties. *Processes*. 2019;7: 885. https://doi.org/10.3390/pr7120885

16. Petrova E., Kotsikau D., Pankov V., Fahmi A. Influence of synthesis methods on structural and magnetic characteristics of Mg–Zn-ferrite nanopowders. *Journal of Magnetism and Magnetic Materials*. 2019;473: 85–91. https://doi.org/10.1016/j.jmmm.2018.09.128

17. Hoang B. K., Mittova V. O., Nguyen A. T., Pham T. H. D. Structural and magnetic properties of Ho-doped $CuFe_2O_4$ nanoparticles prepared by a simple co-precipitation method. *Condensed Matter and Interphases*. 2022;24: 109–115. https://doi.org/10.17308/kcmf.2022.24/9061

18. Patankar K. K., Jadhav P. S., Devkar J., Ghone D. M., Kaushik S. D. Synthesis and characterization of $CoFe_{2-x}Y_xO_4$ (x = 0.05 – 0.2) by auto combustion method. *AIP Conference Proceedings*. 2017;1832: 050172. https://doi.org/10.1063/1.4980405

19. Gingasu D., Mindru I., Ianculescu A.-C., ... Chifiriuc M. C. Chifiriuc, soft chemistry synthesis and characterization of $CoFe_{1.8}Re_{0.2}O_4$ (R = Tb, Er) ferrite. *Magnetochemistry*. 2022;8: 1–15. https://doi.org/10.3390/magnetochemistry8020012

20. Zhao X., Wang W., Zhang Y., Wu S., Li F., Liu P. Synthesis and characterization of gadolinium doped cobalt ferrite nanoparticles with enhanced adsorption capability for Congo Red. *Chemical Engineering Journal*. 2014;250: 164–174. https://doi.org/10.1016/j.cej.2014.03.113

21. Boddolla S., Ravinder D. Eu^{3+} doped $CoFe_2O_4$ nanoparticles with XRD and FTIR analysis. *Journal for*

Research in Applied Sciences and Biotechnology. 2024;3: 135–138. https://doi.org/10.55544/jrasb.3.2.23

22. Franco A. Jr., Pessoni H. V. S., Alves T. E. P. Enhanced dielectric permittivity on yttrium doped cobalt ferrite nanoparticles. *Materials Letters*. 2017;208: 115–117. https://doi.org/10.1016/j.matlet.2017.04.101

23. Basak M., Rahman M. L., Ahmed M. F., Biswas B., Sharmin N. Calcination effect on structural, morphology and magnetic properties of nano-sized $CoFe_2O_4$ developed by a simple co-precipitation technique. *Materials Chemistry and Physics*. 2021;264: 124442. https://doi.org/10.1016/j.matchemphys.2021.124442

24. Nguyen A. T., Nguyen T. T., Mittova V. O., ... Bui X. V. Structural, thermal, and magnetic properties of orthoferrite $EuFeO_3$ nanoparticles prepared by a simple co-precipitation method. *Journal of Materials Science: Materials in Electronic*. 2023;34: 1370. https://doi.org/10.1007/s10854-023-10779-y

25. Nguyen A. T., Cam T. S., Mittova V. O., ... Bui X. V. Influence of synthesis conditions on the crystal structure, optical and magnetic properties of *o*-$EuFeO_3$ nanoparticles. *Coatings*. 2023;13: 1082. https://doi.org/10.3390/coatings13061082

26. Tran D. T., Nguyen H. C. H., Le T. T. T., Nguyen A. T. Effect of annealing temperature and precipitation agent on the structure, optical and magnetic characteristics of dysprosium orthoferrite nanoparticles. *Materials Today Commnunications*. 2024;40: 109733. https://doi.org/10.1016/j.mtcomm.2024.109733

27. Housecroft C. E.; Sharpe A. G. *Inorganic Chemistry*, 2nd ed. NJ, USA: Pearson, Prentice Hall, Upper Saddle River; 2005. 950 p.

28. Tien N. A., Mittova V. O., Sladkopevtsev B. V., ... Vuong B. X. Structural, optical and magnetic properties of Y-doped $NiFe_2O_4$ nanoparticles prepared by simple co-precipitation method. *Solid State Sciences*. 2023;138: 107149. https://doi.org/10.1016/j.solidstatesciences.2023.107149

29. Dixit G., Singh J. P., Srivastava R. C., Agrawal H. M. Magnetic resonance study of Ce and Gd doped $NiFe_2O_4$ nanoparticles. *Journal of Magnetism and Magnetic Materials*. 2012;324: 479–483. https://doi.org/10.1016/j.jmmm.2011.08.027

30. Mohamed W. S., Abu-Dief A. M. Impact of rare earth europium (Re-Eu^{3+}) ions substitution on microstructural, optical and magnetic properties of $CoFe_{2-x}Eu_xO_4$ nanosystems. *Ceramics International*. 2020;46: 16196–16209. https://doi.org/10.1016/j.ceramint.2020.03.175

31. Almessiere M. A., Slimani Y., Korkmaz A. D., ... Ozcelik B. Sonochemical synthesis of Eu^{3+} substituted $CoFe_2O_4$ nanoparticles and their structural, optical and magnetic properties. *Ultarsonics Sonochemistry*. 2019;58: 104621. https://doi.org/10.1016/j.ultsonch.2019.104621

32. Chung N. T. K., Tien N. A. Structural, optical and magnetic properties of Y-doped $CoFe_2O_4$ nanoparticles prepared by a simple co-precipitation method. *Journal of Materials Science: Materials in Electronic*. 2023;34: 448. https://doi.org/10.1007/s10854-023-09914-6

33. Ahmadi H., Shokrollah N., Aghaei S., ... Tightiz N. Nanocrystalline $CuFe_{2-x}Sm_xO_4$: synthesis, characterization and its photocatalytic degradation of methyl orange. *Journal of Materials Science: Materials in Electronic*. 2016;27: 4689–4693. https://doi.org/10.1007/s10854-016-4347-2

34. Cullity B. D., Graham C. D. *Introduction to Magnetic* Materials, 2nd ed. Canada: John Wiley & Sons, Inc., Publication; 2009. http://doi.org/10.1002/9780470386323

35. Moriya Y. New mechanism of anisotropic superexchange interaction. *Physical Review Letters*. 1960;4: 228–230. https://doi. org/10.1103/PhysRevLett.4.228

Information about the authors

Khanh Nhu Le Ngoc, 3nd year student, Faculty of Chemistry, Ho Chi Minh City University of Education (Ho Chi Minh City, Vietnam).
nhukhanhngoc1010@gmail.com

Thu Trang Nguyen Thi, PhD in Chemistry, Faculty of Chemistry, Ho Chi Minh City University of Education (Ho Chi Minh City, Vietnam).
https://orcid.org/0009-0009-6825-4625
thutrang@hcmue.edu.vn

Hoang Huy Nguyen, 1st postgraduate student, Inorganic Chemistry Department, Faculty of Chemistry, Ho Chi Minh City University of Education (Ho Chi Minh City, Vietnam).
https://orcid.org/0009-0001-7209-2114
huynh@phd.hcmue.edu.vn

Dinh Trinh Tran, PhD in Chemistry, Associate Professor, VNU Key Laboratory of Advanced Materials for Green Growth, University of Science, Vietnam National University (Hanoi, Vietnam).
https://orcid.org/0000-0001-9936-1823
trinhtd@vnu.edu.vn

Ngoc Anh Vu Thi, PhD in Chemistry, Ton Duc Thang University (Ho Chi Minh City, Vietnam).
https://orcid.org/0000-0002-0510-1762
vuthingocanh@tdtu.edu.vn

Anh Tien Nguyen, PhD in Chemistry, Associate Professor, Head of the Inorganic Chemistry Department, Ho Chi Minh City University of Education (Ho Chi Minh City, Vietnam).
https://orcid.org/0000-0003-3919-8571
tienna@hcmue.edu.vn

Received February 27, 2025; approved after reviewing March 19, 2025; accepted for publication March 25, 2025; published online December 25, 2025.

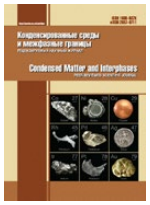

ISSN 1606-867X (Print)
ISSN 2687-0711 (Online)
Condensed Matter and Interphases
Kondensirovannye Sredy i Mezhfaznye Granitsy
https://journals.vsu.ru/kcmf/

Original articles

Research article
https://doi.org/10.17308/kcmf.2025.27/13293

Phase equilibria and some properties of solid solutions of $PbGa_2S_4$–$SmGa_2S_4$ and $PbGa_2Se_4$–$SmGa_2Se_4$ systems

O. M. Aliev[1]✉, D. S. Azhdarova[1], R. M. Agayeva[2], V. M. Ragimova[1]

[1]Institute of Catalysis and Inorganic Chemistry,
113 H. Javid ave., Baku AZ-1143, Azerbaijan,

[2]Azerbaijan State Pedagogical University,
68 U. Hajibeyli st., Baku AZ-1000, Azerbaijan

Abstract

Objectives: In connection with the transition to green energy, the search for, synthesis of, and investigation into alternative energy sources and the materials required for them are of great importance. One of the methods for obtaining such promising materials is the study of phase diagrams between isostructural compounds. In this regard, phase equilibria in the $PbGa_2S_4$–$SmGa_2S_4$ and $PbGa_2Se_4$–$SmGa_2Se_4$ systems were investigated using physicochemical analysis methods (DTA, XRD, measurements of microhardness and density), and their phase diagrams were constructed.

Conclusions: It has been established that the specified systems are quasi-binary and are characterized by the formation of continuous substitution-type solid-solution areas. The solid solutions $Pb_{1-x}Sm_xGa_2S_4$ and $Pb_{1-x}Sm_xGa_2Se_4$ crystallize in the orthorhombic crystal system and belong to the $EuGa_2S_4$ structural type. Their unit-cell parameters vary within the following ranges: $Pb_{1-x}Sm_xGa_2S_4$ a = 20.745–20.706 Å; b = 20.464–20.380 Å; c = 12.236–12.156 Å; $Pb_{1-x}Sm_xGa_2Se_4$ a = 21.722–21.782 Å; b = 21.202–21.350 Å; c = 12.3047–12.390 Å; Space group: *Fddd*, Z = 32. Several physicochemical properties of the $Pb_{1-x}Sm_xGa_2S_4$ and $Pb_{1-x}Sm_xGa_2Se_4$ solid solutions have been investigated.

Keywords: System, Solid solution, Unit cell, Lattice parameter, Phase diagram

For citation: Aliev O. M., Azhdarova D. S., Agayeva R. M., Ragimova V. M. Phase equilibria and some properties of solid solutions of $PbGa_2S_4$–$SmGa_2S_4$ and $PbGa_2Se_4$–$SmGa_2Se_4$ systems. *Condensed Matter and Interphases*. 2025;27(4): 565–572. https://doi.org/10.17308/kcmf.2025.27/13293

Для цитирования: Алиев О. М., Аждарова Д. С., Агаева Р. М., Рагимова В. М. Фазовые равновесия и некоторые свойства твердых растворов систем $PbGa_2S_4$–$SmGa_2S_4$ и $PbGa_2Se_4$–$SmGa_2Se_4$. *Конденсированные среды и межфазные границы*. 2025;27(4): 565–572. https://doi.org/10.17308/kcmf.2025.27/13293

✉ Ozbek M. Aliev, e-mail: ozbek.aliyev41@gmail.com

1. Introduction

Modern scientific and technological progress is largely driven by the use of functional materials possessing unique properties. This necessitates systematic research, synthesis, design, and comprehensive investigation of their fundamental characteristics. In this context, the study of phase diagrams between isostructural compounds forming continuous series of solid solutions provides an opportunity to control the functional properties of the resulting materials [1–7].

At present, the study of alternative energy sources is one of the highest-priority areas of scientific research worldwide. Solving this problem is closely associated with the development of new efficient energy converters, particularly thermoelectric and photovoltaic materials [8–15].

The primary compounds ($PbGa_2S_4$, $SmGa_2S_4$; $PbGa_2Se_4$, $SmGa_2Se_4$) have been studied in sufficient detail [16–25]. According to [17], the compound $PbGa_2S_4$ is formed by the peritectic reaction $L+PbS \leftrightarrow PbGa_2S_4$ and melts incongruently at 1203 K, it crystallizes in the orthorhombic system with the following unit-cell parameters: a = 20.44 Å; b = 20.64 Å; c = 12.09 Å, space group Fddd, Z = 32, d = 4.94 g/cm³, and belongs to the $EuGa_2S_4$ structural type. According to [13], $PbGa_2S_4$ melts congruently at 1163 K and has lattice parameters: a = 20.706 Å; b = 20.380 Å; c = 12.156 Å. An analysis of the literature data [13, 16–18] shows that, with the exception of one study [18], all other authors assert that $PbGa_2S_4$ melts congruently. Therefore, in the present study we relied on the results of the most recent works [13]. Our synthesized and investigated $PbGa_2S_4$ sample confirmed the congruent nature of its melting, which is consistent with [16, 17]. $PbGa_2S_4$ is a wide-bandgap semiconductor and exhibits multifunctional properties: laser [13], paramagnetic [26], and optically active characteristics [27–29]. $PbGa_2Se_4$ also melts congruently at 1050 K [19–21] and has a structural type of $EuGa_2S_4$ (a = 21.72 Å; b = 21.20 Å; c = 12.30 Å).

$SmGa_2S_4$ melts congruently at 1750 K [23–25] and crystallizes in the orthorhombic system with lattice parameters: a = 20.745 Å; b = 20.464 Å; c = 12.236 Å, space group Fddd, Z = 32, microhardness Hμ = 2800, density d = 4.28 g/cm³. $SmGa_2S_4$ is a semiconductor with a bandgap ΔE = 2.20 eV [23, 24]. Unlike $SmGa_2S_4$, the compound $SmGa_2Se_4$ melts incongruently at 1200 K and has a structural type of $EuGa_2S_4$ (a = 21.700 Å; b = 21.23 Å; c = 12.39 Å), with Hμ = 2700, d = 6.02 g/cm³, and ΔE = 1.40 eV [1, 25].

Since the thio- and selenogallates of lead and samarium exhibit laser, optical, and luminescent properties, the study of their chemical interactions holds promise for obtaining materials with multifunctional characteristics.

The aim of the present work is to investigate the phase equilibria in the $PbGa_2S_4$-$SmGa_2S_4$ and $PbGa_2Se_4$–$SmGa_2Se_4$ systems and to study the physicochemical properties of the $Pb_{1-x}Sm_xS_4$ (Se_4) solid solutions.

2. Experimental

The alloys were obtained by melting ternary sulfides or selenides of lead and samarium ($PbGa_2S_4$, $PbGa_2Se_4$, $SmGa_2S_4$, $SmGa_2Se_4$) in evacuated quartz ampoules at temperatures of 1300–1400 K. The initial ternary sulfides and selenides of lead and samarium were synthesized by melting high-purity elemental components. The molten alloys were held at the maximum temperature (1300–1400 K) for 30–40 minutes, then cooled to 1000 K and kept at this temperature for 1200 hours for homogenization. As a result, yellow-colored alloys suitable for physicochemical analysis were obtained.

The alloys (samples weighing 0.1–0.3 g) were examined using differential thermal analysis (DTA) on a Netzsch STA 449 F3 instrument (platinum–platinum/rhodium thermocouples, in the temperature range from room temperature to ~1450 K, heating rate 10 K·min^{-1}), X-ray phase analysis (XRD, Bruker D2 PHASER, CuKα radiation), microhardness measurements (on an PMT-3 microhardness tester), and density determination (using the pycnometric method with toluene as the filling medium). The measurement errors for DTA, XRD, microhardness, and density were ±3 K, ±0.001 Å, ±3 MPa, and ±0.3 g/cm³, respectively.

3. Results and discussion

The phase diagram of the $PbGa_2S_4$–$SmGa_2S_4$ system, constructed on the basis of physicochemical analysis, is shown in Fig. 1a.

As seen from Fig. 1a, the $PbGa_2S_4$–$SmGa_2S_4$ system is characterized by the complete mutual

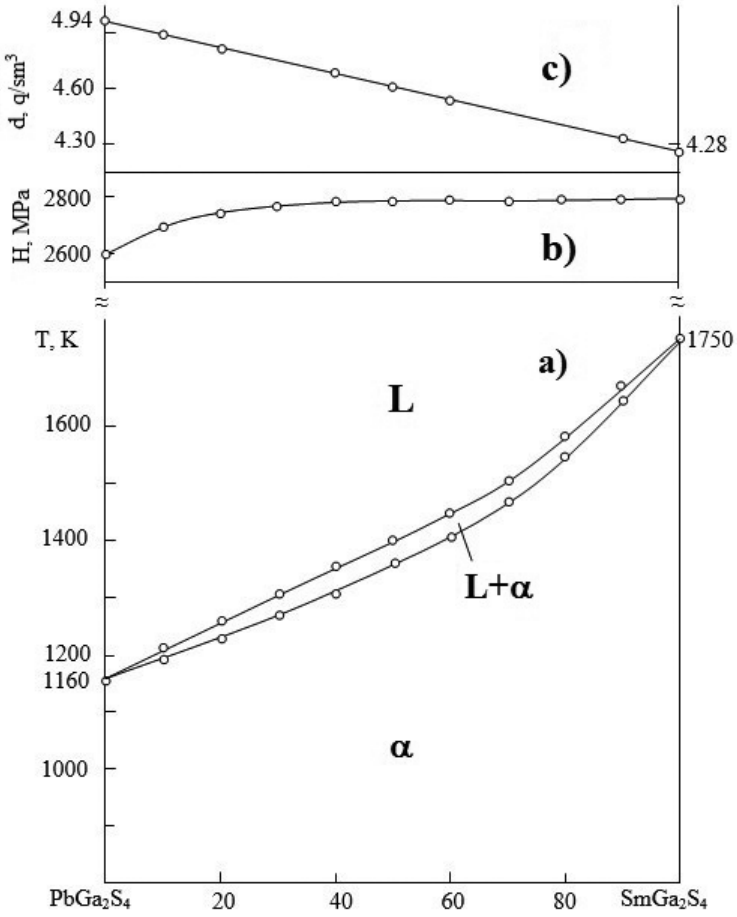

Fig. 1. *T-x* phase diagram of the $PbGa_2S_4$–$SmGa_2S_4$ system (a), dependence of microhardness (b) and density (c) on the composition

solubility of the components in both the liquid and solid states and corresponds to a first-type phase diagram according to Rosenbaum [30]. No extremum point is observed on the liquidus and solidus curves; their temperatures vary monotonically between the melting points of the initial ternary sulfides ($PbGa_2S_4$ and $SmGa_2S_4$).

The maximum temperature difference between corresponding points on the liquidus and solidus lines is 25 K (see Fig. 1a). Therefore, one could expect a common extremum point (minimum or maximum) on these curves. On the other hand, it should be noted that Rosenbaum first-type phase diagrams usually occur in systems where the thermodynamic functions of mixing in both the liquid and solid states are very low or very similar. The composition dependences of microhardness and density for the $PbGa_2S_4$–$SmGa_2S_4$ system are presented in Figs. 1b and 1c.

X-ray phase analysis of the samples annealed at 1000 K after thermal treatment shows that all samples of the $PbGa_2S_4$ - $SmGa_2S_4$ system, including the starting sulfides, exhibit diffraction patterns characteristic of the orthorhombic crystal system (Fig. 2). This indicates that at 1000 K continuous series of solid solutions with orthorhombic structure are formed between the initial compounds. The compositional dependence of lattice parameters, shown in Fig. 3, has a linear character, which indeed confirms the formation of a continuous solid-solution series. Using the TOPAS-3 software, the structural type and the unit-cell parameters of the $Pb_{1-x}Sm_xGa_2S_4$ solid solutions were determined; the results are presented in Table 1.

Table 1 also contains the DTA results obtained after thermal treatment at 1000 K. Based on these data, along with the XRD results, the *T*–*x* phase diagram of the $PbGa_2S_4$–$SmGa_2S_4$ system was constructed (Fig. 1a).

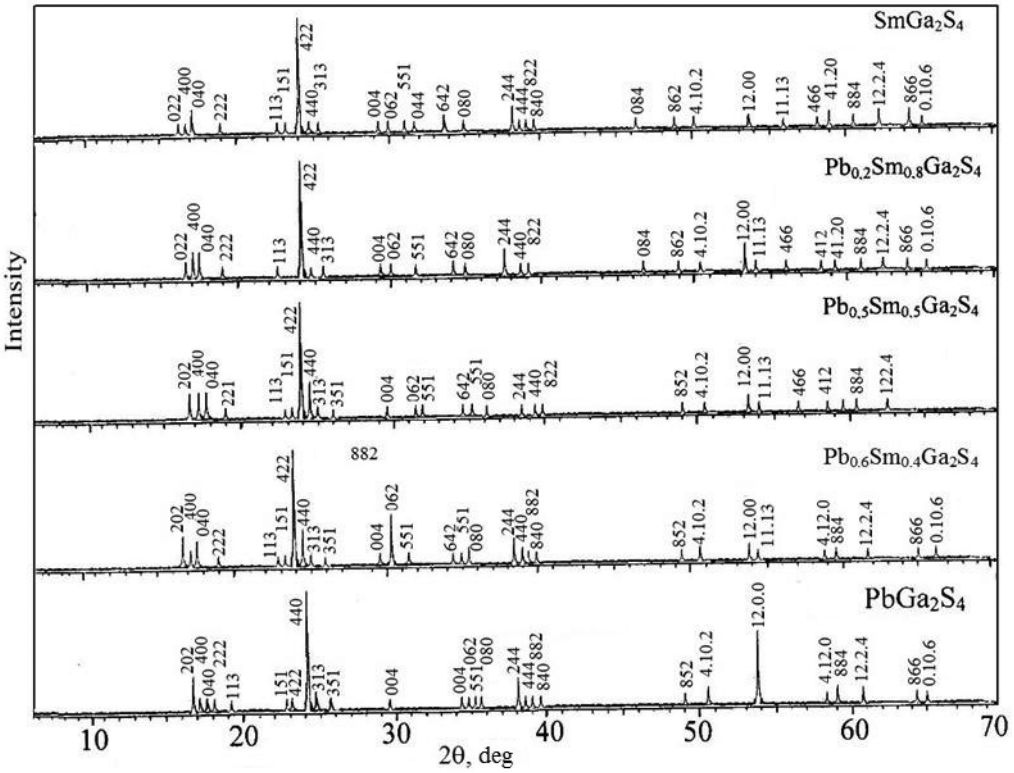

Fig. 2. The XRD patterns of the $PbGa_2S_4$–$SmGa_2S_4$ system

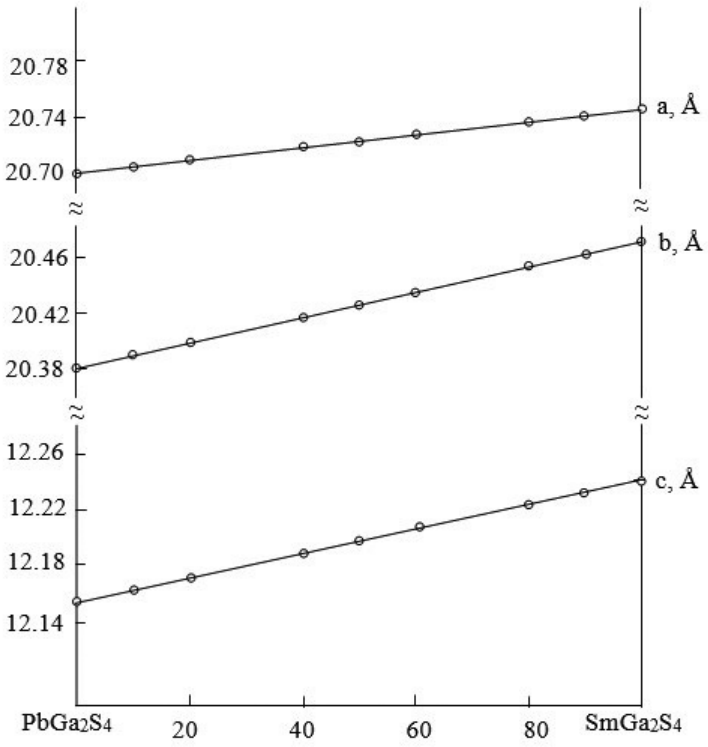

Fig. 3. Dependence of lattice parameters on the composition of solid solutions of the $PbGa_2S_4$–$SmGa_2S_4$ system

Table. 1. Results of DTA, XRD, microhardness, and density of alloys of the $PbGa_2S_4$–$SmGa_2S_4$ system

Composition, mol % $SmGa_2S_4$	Thermal effects, K	Lattice parameters, Å			Space group	*Z*	$H_μ$, MPa	d_{pik}, g/sm^3
		a	*b*	*c*				
$PbGa_2S_4$	1163	20.706	20.380	12.156	*Fddd*	32	2650	4.94
10	1205, 1225	20.708	20.378	12.164	*Fddd*	32	2700	4.85
20	1230, 1260	20.712	20.384	12.180	*Fddd*	32	2750	4.70
40	1320, 1350	20.716	20.420	12.198	*Fddd*	32	2760	4.56
50	1390, 1410	20.728	20.425	12.218	*Fddd*	32	2780	4.48
60	1455, 1480	20.732	20.440	12.220	*Fddd*	32	2790	4.36
80	1575, 1610	20.736	20.460	12.226	*Fddd*	32	2800	–
90	1666, 1680	20.740	20.462	12.234	*Fddd*	32	2800	4.30
$SmGa_2S_4$	1750	20.745	20.464	12.236	*Fddd*	32	2800	4.28

Thus, in both the liquid and solid solutions, the deviation from ideality in the substitution of lead by samarium is very small.

As shown in Fig. 4a, the $PbGa_2Se_4$–$SmGa_2Se_4$ system is partially quasi-binary. Due to the incongruent melting of $SmGa_2Se_4$, the quasi-binary nature of the system is disrupted in alloys near this compound. Therefore, in the concentration range of 60–100 mol % $SmGa_2Se_4$, a three-phase area appears at high temperatures; however, at low temperatures, continuous solid solutions of the $EuGa_2S_4$ type are formed. In the composition interval 0–40 mol % $PbGa_2Se_4$, α-solid-solution crystals precipitate primarily from the melt. In compositions richer in $SmGa_2Se_4$, the SmSe compound crystallizes. As

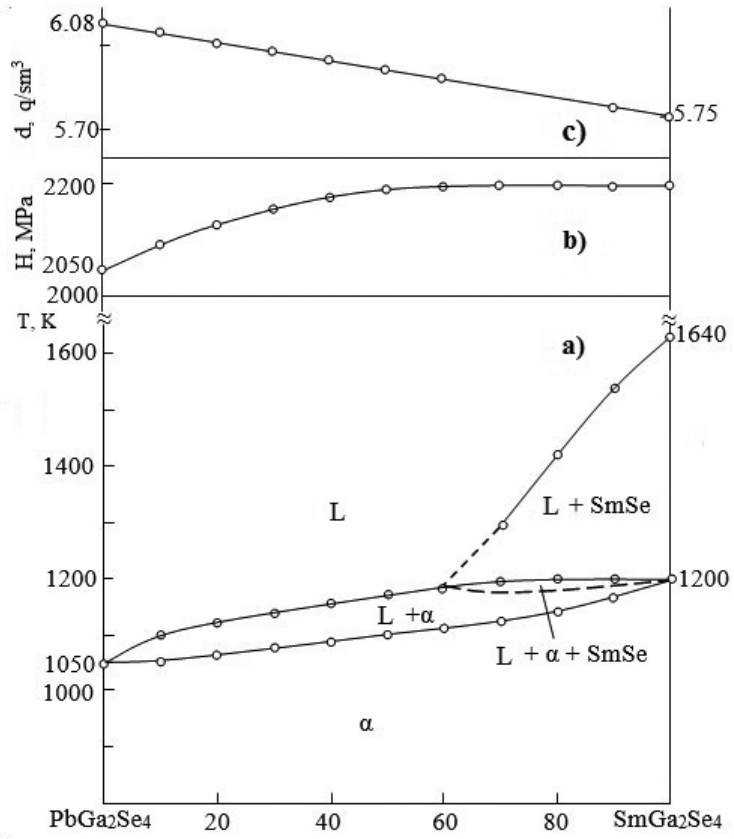

Fig. 4. *T-x* phase diagram of the $PbGa_2Se_4$–$SmGa_2Se_4$ system (a) and the dependence of microhardness (b) and density (c) on the composition

a result of the univariant peritectic reaction L + SmSe ↔ α, a three-phase area L + SmSe + α should form below 1200 K. However, this field was not experimentally detected due to its narrow temperature interval and is shown schematically by a dashed line.

The liquidus of the $PbGa_2Se_4$ – $SmGa_2Se_4$ system contains two areas corresponding to the primary crystallization of SmSe and of the α-phase.

The XRD results, the composition dependences of lattice parameters (Fig. 5), as well as the microhardness and density measurements (Figs. 4b, 4c) are consistent with the phase diagram of the $PbGa_2Se_4$ – $SmGa_2Se_4$ system.

In the $PbGa_2Se_4$ – $SmGa_2Se_4$ system, the initial compounds and all alloys exhibit similar diffraction patterns, with slight shifts of the reflections. The variation in orthorhombic lattice parameters of the $Pb_{1-x}Sm_xGa_2Se_4$ solid solutions as a function of composition, along with the DTA results, are given in Table 2.

4. Conclusion

Phase equilibria in the $PbGa_2S_4$-$SmGa_2S_4$ and $PbGa_2Se_4$–$SmGa_2Se_4$ systems were investigated for the first time using physicochemical analysis methods, and their phase diagrams were constructed. It has been established that the $PbGa_2S_4$-$SmGa_2S_4$ system is quasi-binary and is characterized by the formation of a continuous series of solid solutions. The $PbGa_2Se_4$–$SmGa_2Se_4$ system is partially quasi-binary; at low temperatures (in the subsolidus area), the initial components dissolve completely in one another. It was determined that the solid solutions crystallize in the orthorhombic system and have a structural type of $EuGa_2S_4$.

Contribution of the authors

O. M. Aliyev – scientific supervision, text editing. D. S. Ajdarova – research concept, discussion of results, participation in data processing, manuscript preparation. R. M. Agaeva – data processing and participation in manuscript preparation. V. M. Rahimova – literature search and participation in experimental work.

Conflict of interests

The authors declare that they have no known competing financial interests or personal

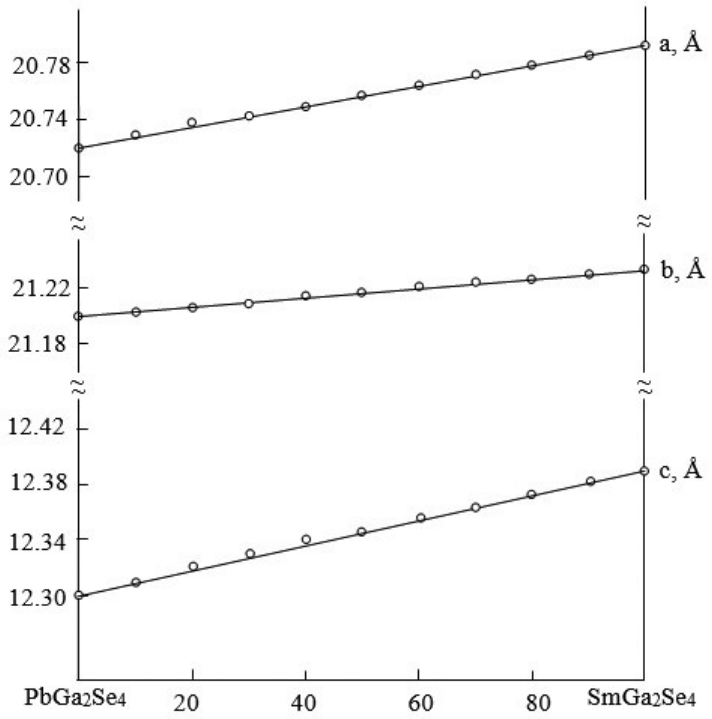

Fig. 5. Dependence of lattice parameters on the composition of solid solutions of the $PbGa_2Se_4$ – $SmGa_2Se_4$ system

Table. 2. Results of DTA, XRD, microhardness, and density of alloys of the $PbGa_2Se_4$ – $SmGa_2Se_4$ system

Composition, mol % $SmGa_2Se_4$	Thermal effects, K	Lattice parameters, Å			$H_μ$, MPa	d_{pik}, g/sm³
		a	*b*	*c*		
$PbGa_2Se_4$	1150	21.722	21.202	12.304	2050	6.08
10	1060, 1090	21.724	21.204	12.310	2100	5.90
20	1065, 1120	21.735	21.205	12.320	2140	5.85
30	1070, 1140	21.740	21.207	12.330	2180	5.84
40	1080, 1160	21.748	21.208	12.338	2180	5.82
50	1100, 1180	21.752	21.210	12.344	2190	5.80
60	1110, 1190	21.758	21.218	12.358	–	5.78
70	1120, 1200, 1390	21.760	21.220	12.364	–	–
80	1140, 1210, 1470	21.775	21.224	12.378	2200	–
90	1170, 1210, 1570	21.780	21.225	12.384	2200	5.77
$SmGa_2Se_4$	1200, 1640	21.782	21.235	12.390	2220	5.75

relationships that could have influenced the work reported in this paper.

Referenses

1. Rustamov P. G., Aliev O. M., Eynullaev A. V., Aliev I. P. *Chalcolantanates of rare elements**. Moscow: Nauka Publ., 1989, 284 p. (in Russ.)

2. Mammadov F. M., Babanly D. M., Amiraslanov I. R., Tagiev D. B., Babanly M. B. System FeS– Ga_2S_3–In_2S_3. *Russian Journal of Inorganic Chemistry*. 2021;66(10): 1533. https://doi.org/10.1134/S0036023621100090

3. Amiraslanova A. J., Babanly K. N., Imamaliyeva S. Z, Yusibov Y. A., Babanly M. B. Phase equilibria in the Ag_8SiSe_6-Ag_8SiTe_6 system and characterization of solid solutions $Ag_8SiSe_{1-x}Te_x$. *Applied Chemical Engineering*. 2023;6(2): 1. https://doi.org/10.24294/ace.v6i2.2162

4. Mammadov F. M., Imamaliyeva S. Z., Jafarov Ya. I., Bakhtiyarly I. B., Babanly M. B. Phase equilibria in the MnTe–$MnGa_2Te_4$–$MnIn_2Te_4$ system. *Condensed Matter and Interphases*. 2022;24(3): 335. https://doi.org/10.17308/kcmf.2022.24/9856

5. Kondrotas R., Colina M., Guc M., ... Saucedo E. Towards In-reduced photovoltaic absorbers: evaluation of zinc-blende $CuInSe_2$–ZnSe solid solution. *Solar Energy Materials and Solar Cells*. 2017;160: 26. https://doi.org/10.1016/j.solmat.2016.10.023

6. Skoug E. J., Cain J. D., Morelli D. T. High thermoelectric figure of merit the Cu_3SbS_4–Cu_3SbSe_4 solid solution. *Appled Physics Letters*. 2011;98(26): 261911. https://doi.org/10.1063/1.3605246

7. Singh U. P., Patra S. P. Progress in polycrystalline thin-film Cu(In,Ga)Se_2 Solar Cells. *Internationals Journal of Photoenergy*. 2010; 201(1): 1. https://doi.org/10.1155/2010/468147

8. Navratil J., Kucek V., Plechacek T. Thermoelectric properties of $Cu_2HgSnSe_4$–$Cu_2HgSnTe_4$ solid solution. *Journals Electronic Materials*. 2014;43(10): 3719. https://doi.org/10.1007/s11664-014-3075-8

9. Chand S., Sharma P. Synthesis and characterization of Ag-chalcogenide nano particles for possible applications in photovoltaics. *Materials Science-Poland*. 2018;36(3): 375. https://doi.org/10.2478/msp-2018-0064

10. Orokov M. M., Klimovskikh I. I., Bentmann H., ... Chulkov E. V. Prediction and observation of an antiferromagnetic topological insulator. *Nature*. 2019;576: 416. https://doi.org/10.1038/s41586-019-1840-9

11. Shevelkov A. V. Chemical aspects of the thermoelectric materials engineering. *Russian Chemical Review*. 2008;77(1): 19. https://doi.org/10.1070/RC2008v077n01ABEH003746

12. Wang Y., Zhao Y., Ding X., Qiao L. Recent advances in the electrochemistry of layered post transition metal chalcogenids nanomaterials for hydrogen evulation reaction. *Journal of Energy Chemistry*. 2021;60(1): 451. https://doi.org/10.1016/j.jechem.2021.01.021

13. Badikov D., Badikov V., Doroshenko M., Fintisova A., Shevyrdyaeva G. Low-phonon lead thiogallate crystal as a matrix for mid-IR lasers. *Photonics*. 2008;4: 24. Available at: https://www.photonics.su/files/article_pdf/2/article_2631_62.pdf

14. Marshall J. M., Dimova-Malinovska D. (Eds.). *Photovoltaic and photoactive materials, propertics, technology and applications*. NATO Science Series II: Mathematics, Physics and Chemistry (NAII, volume 80). 2002. https://doi.org/10.1007/978-94-010-0632-3

15. *Chalcogenides advances in research and applications* / P. Woodrow (Ed.). Nova Science Publ.; 2018, 111 p.

16. Golovey V. M., Obolonchik V. A., Golovey M. I. The Ga_2S_3–PbS system. *Russian Journal of Inorganic Chemistry*. 1981:26(7): 1970–1978.

17. Chilout A., Mazurier A., Guittaed M. Systeme Ga_2S_3-PbS. Diagramma de phase, etude cristallographique. Materials Researsh Bulletin. 1979;14(9): 1119. https://doi.org/10.1016/0025-5408(79)90205-8

18. Eholie R., Kom I. K., Flahaut J. Diagram de phase PbS–Ga_2S_3 system. *Acad. Sci. Paris, ser. C*. 1969;268: 700-702.

19. Klee N., Schofer H. Zur kennznis von $PbAl_2Se_4$ and $PbGa_2Se_4$. *Materials Researsh Bulletin*. 1980;15(7): 1033. https://doi.org/10.1016/0025-5408(80)90230-5

20. Sosovska S. M., Olekseyuk I. D., Parasyuk O. V. The CdSe–Ga_2Se_3–PbSe system. *Journal of Alloys and Compounds*. 2008;453: 115. https://doi.org/10.1016/j.jallcom.2006.11.051

21. Bellagra H. K., Kogut T. M., Piskach V. V. Component interaction in the quasi-ternary system PbSe-Ga_2Se_3-$GeSe_2$. *Journal of Phase Equilibria and Diffusion*. 2022;44(1): 3. https://doi.org/10.1007/s11669-022-01017-9

22. Chen W.-F., Liu B.-W., Jiang X.-M., Guo G.-C. Infrared nonlinear optical performances of a new sulfide β-$PbGa_2S_4$. *Journal of Alloys and Compounds*. 2022;905: 164090. https://doi.org/10.1016/j.jallcom.2022.164090

23. Aliyev O. M., Akhmedova N. R. Physicochemical and photoelectric properties of crystals of samarium tetrathioindates and tetrathiogallates and solid solutions based on them. *Azerbaijan Chemical Journal*. 2010;3: 67.

24. Aliev O. M., Alieva O. A., Eynullaev A. V. Triple system Sm–Ga–S. *Journal of Inorganic Chemistry.* 1993;38(8): 1418.

25. Aliev O. M., Alieva O. A., Aliev I. P. Synthesis and physico-chemical properties of samarium chalcogallates and chalcoindates. *ChemInform*. 1993;24(48): https://doi.org/10.1002/chin.199348031

26. Asatryan G. R., Badikov V. V., Kramushchenko D. D., Khramtsov V. A. Electron paramagnetic of Dy^{3+} ions in lead thiogallate single crystals. *Physics Solid State*. 2012;54(6): 1245. https://doi.org/10.1134/S1063783412060042

27. Kamenshchikov V. N., Suslikov L. M. Calculotion of the optical properties of $PbGa_2S_4$ crystal. *Optics and Spectroscopy*. 2014;116(4): 564. https://doi.org/10.1134/S0030400X14040134

28. Badikov V., Badikov D., Doroshenko M., Panyutin V., Chizhikov V. I., Shevyrdyaeva G. Optical properties of lead thiogallate. *Optical Materials*. 2008;31(2): 184. https://doi.org/10.1016/j.optmat.2008.03.001

29. Basiev T. T., Doroshenko M. E., Osiko V. V., Shevyrdyaeva G. S. Qualitative improvement in the lasing performance of $PbGa_2S_4$: Dy^{3+} crystals through Na^+ doping. *Quantum Electronics*. 2010;40(7): 596–598. https://doi.org/10.1070/QE2010v040n07ABEH014351

30. Anosov V. Ya., Ozerova M. I., Fialkov Yu. Ya. *Fundamentals of physical and chemical analysis*. Moscow: Nauka Publishing House; 1976. p. 114–116. (in Russ.) Available at: https://www.geokniga.org/bookfiles/geokniga-osnovyfiziko-himicheskogoanaliza.pdf

* *Translated by author of the article*

Information about the authors

Ozbek M. Aliev, Dr. Sci. (Chem.), Professor, Institute of Catalysis and Inorganic Chemistry (Baku, Azerbaijan).
https://orcid.org/0000-0002-6411-108X
ozbek.aliyev41@gmail.com

Dilbar S. Azhdarova , Dr. Sci. (Chem.), Associate Professor, Institute of Catalysis and Inorganic Chemistry (Baku, Azerbaijan).
https://orcid.org/0000-0002-8119-733X
zangi1941@mail.ru

Reyhan M. Agayeva, PhD (in Chem.), Associate Professor, Azerbaijan State Pedagogical University (Baku, Azerbaijan).
https://orcid.org/0000-0002-2924-3204
agayeva.reyhan@mail.ru

Valida M. Raqimova, PhD (in Chem.), Associate Professor, Leading Researcher, Institute of Catalysis and Inorganic Chemistry (Baku, Azerbaijan).
https://orcid.org/0009-0008-9157-1592
Valide.rehimova1945@gmail.com

Received January 7, 2025; approved after reviewing March 4, 2025; accepted for publication April 15, 2025; published online December 25, 2025.

ISSN 1606-867X (Print)
ISSN 2687-0711 (Online)
Condensed Matter and Interphases
Kondensirovannye Sredy i Mezhfaznye Granitsy
https://journals.vsu.ru/kcmf/

Original articles

Research article
https://doi.org/10.17308/kcmf.2025.27/13294

Study of the influence of the nature and concentration of the solubilizer on the process of formation of solid dispersions of chloronitrophenol

A. S. Belenova[1]✉, Yu. A. Polkovnikova[1], A. I. Slivkin[1], V. N. Semenov[1], S. I. Vasilieva[1], A. A. Golovina[1], I. A. Saranov[2]

[1]Voronezh State University,
1 Universitetskaya pl., Voronezh 394018, Russian Federation

[2]Voronezh State University of Engineering Technologies,
19 Revolution Avenue, Voronezh 394036, Russian Federation

Abstract

Objectives: The aim of the work was to study the influence of surfactants on the release and solubility of chloronitrophenol (CNP) from solid dispersions in water. The object of study was a solid dispersion of chloronitrophenol with PEG 1500.

Experimental: The concentration of the pharmaceutical substance in solutions was determined spectrophotometrically at a wavelength of 410 nm. The study of the solubility and dissolution rate of pharmaceutical substances (PS) in the form of powder and in the composition of solid dispersed systems (SDS) was carried out according to the method proposed by I. I. Krasnyuk. The study of the optical properties of solutions of the initial compounds and solid dispersions was carried out using the method described in the study of V. V. Grikh. IR spectroscopy, differential scanning calorimetry, and electron microscopy were used for investigation of SDS.

Conclusions: The influence of solubilizers on the process of formation of solid dispersions of chloronitrophenol was studied. It has been shown that the presence of solubilizers allows the use of lower concentrations for the carrier when obtaining solid dispersed systems of chloronitrophenol. The conducted complex of physicochemical methods of analysis allows us to more accurately explain the phenomenon of increasing the solubility and dissolution rate of PS from solid dispersions in the presence of a solubilizer. Based on the conducted studies, it can be concluded that the production of solid dispersions based on a carrier polymer in the presence of a solubilizer allows to reduce or completely eliminate the crystallinity of the pharmaceutical substance, converting it into an amorphous state. The presence of the phenomenon of light scattering and the opalescent Faraday-Tyndall cone in solutions containing solid dispersions of CNP confirmed the assumption about a colloidal-dispersed state of the pharmaceutical substance in water when dissolving CNP from solid dispersions.

Keywords: Chloronitrophenol, Solid dispersions, Solubility, Crystallinity

Funding: The study was supported by the Russian Science Foundation grant No. 24-25-20015, https://rscf.ru/project/24-25-20015/

Acknowledgements: IR spectroscopy studies were conducted at the Voronezh State University Center for Collective Use of Scientific Equipment of Voronezh State University. Differential scanning calorimetry were obtained using the equipment of the Centre for Collective Use "Experiential Center" of Voronezh State University of Engineering Technologies.

For citation: Belenova A. S., Polkovnikova Yu. A., Slivkin A. I., Semenov V. N., Vasilieva S. I., Golovina A. A., Saranov I. A. Study of the influence of the nature and concentration of the solubilizer on the process of formation of solid dispersions of chloronitrophenol. *Condensed Matter and Interphases*. 2025;27(4): 573–580. https://doi.org/10.17308/kcmf.2025.27/13294

Для цитирования: Беленова А. С., Полковникова Ю. А. Сливкин А. И, Семенов В. Н. Васильева С. И., Головина А. А. Саранов И. А. Изучение влияния природы и концентрации солюбилизатора на процесс образование твердых дисперсий хлорнитрофенола. *Конденсированные среды и межфазные границы*. 2025;27(4): 573–580. https://doi.org/10.17308/kcmf.2025.27/13294

✉ Belenova Alena Sergeevna, e-mail: alenca198322@mail.ru

1. Introduction

Chloronitrophenol (CNP) is a medicinal substance used to treat fungal skin diseases, as well as mycosis of the external auditory canal. In high concentrations, CNP exhibits activity against gram-positive and gram-negative bacteria of the genera Proteus and Pseudomonas [1].

Due to its poor solubility in water, CNP exists on the pharmaceutical market as only one dosage form: an alcohol solution for external use. However, this dosage form has significant disadvantages.

To solve the problem of solubility of substances such as chloronitrophenol, a method for obtaining solid dispersions can be used. The method is easy to implement, economical, and versatile. It is used in the production of dosage forms for both internal and external use [2-13].

Another way to increase solubility is solubilization, a process of spontaneous transition of compounds that are insoluble or difficult to dissolve in a given solvent into a stable solution using surfactants. Sodium lauryl sulfate, alginates, proteins, lecithins, esters formed by fatty acids, and various glycols are effective surfactants [14].

Therefore, the purpose of our study was to study the influence of surfactants on the release and solubility of chloronitrophenol from solid dispersions (SD) in water.

2. Experimental

The object of study was a solid dispersion of chloronitrophenol with PEG 1500. Chloronitrophenol and PEG from Sigma, as well as sodium lauryl sulfate as a solubilizer, were used in the experiment. To prepare solid dispersions of chloronitrophenol with polymers, the solvent removal method was used [15].

The concentration of PS in solutions was determined spectrophotometrically at a wavelength of 410 nm [16].

The study of the solubility and dissolution rate of pharmaceutical substances in powder form and as part of solid dispersed systems was carried out according to the method proposed by I. I. Krasnyuk Jr. [17].

The study of the optical properties of solutions of the initial compounds and solid dispersions was carried out using the method described in the study of V. V. Grikh [18].

IR spectroscopy was performed in the Centre for Collective Use of Scientific Equipment of Voronezh State University using a VERTEX 70 IR Fourier spectrometer with the unit for measuring the absorption/transmission of thin-film samples (BRUKER).

Differential scanning calorimetry was carried out using an STA 449 F3 synchronous thermal analysis device (NETZSCH, Germany) in the Centre for Collective Use "Experiential Center" of Voronezh State University of Engineering Technologies. The studies were conducted under the following conditions: atmospheric pressure, maximum temperature of 473 K, temperature change rate of 5 K/min.

Analysis of the morphology and size of the obtained samples of solid dispersed systems (SDS) was performed using a JEOL JSM-6380LV scanning electron microscope (JEOL Ltd., Japan) in the Centre for Collective Use of Scientific Equipment of Voronezh State University.

3. Results and discussion

During the first stage of the study, the solubility of solid dispersions of chloronitrophenol with PEG 1500 was studied. The results are presented in Fig. 1.

Obtaining SD in the ratio of 1:1, 1:2, and 1:5 did not lead to an increase in the solubility of chloronitrophenol. Experimental data demonstrated that in the presence of PEG-1500 in a ratio of 1:15 and 1:20, the concentration of released chloronitrophenol was maximal. SDS with a ratio of 1:10 also showed good results in solubility.

In SD prepared using sodium lauryl sulfate, the solubility of chloronitrophenol was higher. As can be seen (Fig. 2), the use of a solubilizer allowed to increase the solubility of the CNP SD.

Studies have shown that solutions of solid dispersions with this polymer exhibit opalescence and demonstrate the Tyndall-Faraday effect. Unlike solutions containing only the chloronitrophenol or polymer substance, or their physical mixture, when a thin beam of light passes through a solution of a solid dispersion, the light flux is scattered.

The effect of the opalescent Tyndall-Faraday cone in solutions of solid dispersions is associated with their colloidal-dispersed state.

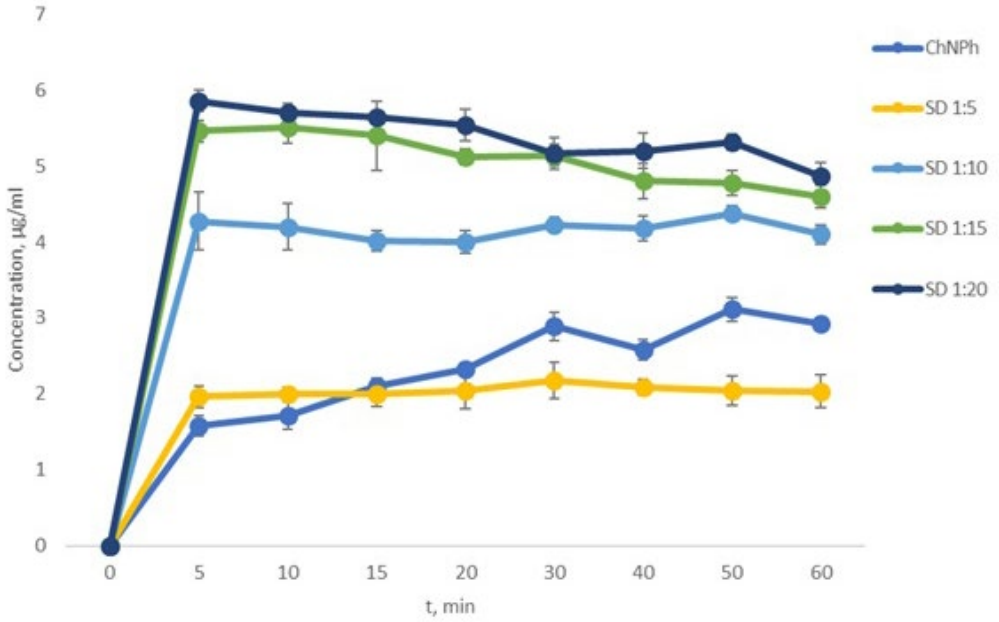

Fig. 1. Dissolution kinetics of chloronitrophenol solid dispersions with PEG 1500

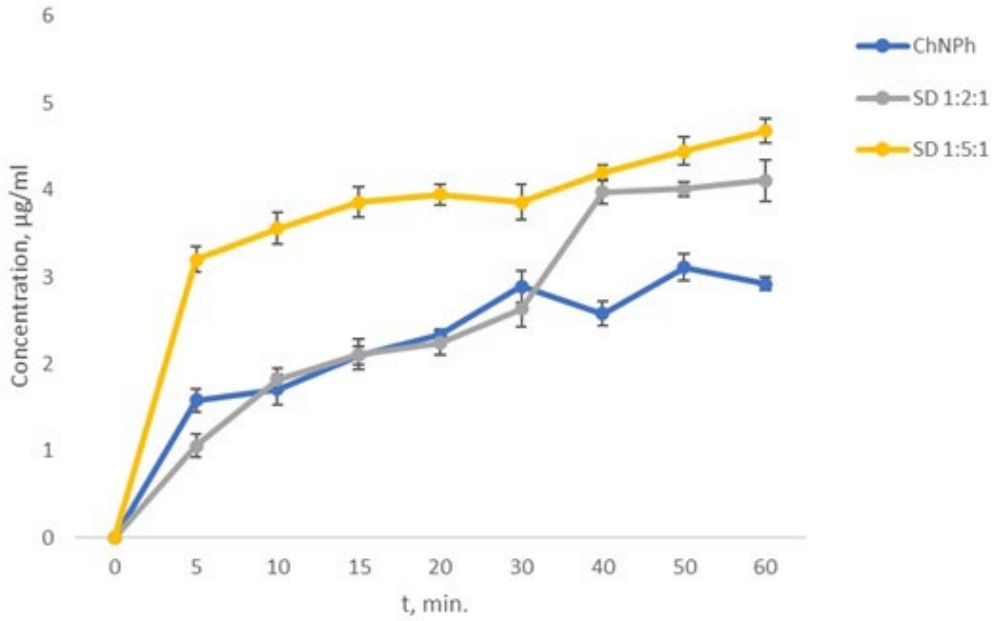

Fig. 2. Dissolution kinetics of chlornitrophenol solid dispersions with PEG 1500 in the presence of a solubilizer

To identify the reasons for the increased solubility of chloronitrophenol in a SDS composition, physicochemical methods were used.

According to scanning electron microscopy data (Fig. 3), the chloronitrophenol substance consists of square and rectangular crystals of approximately the same size. PEG 1500 is a homogeneous, transparent mass without a pronounced internal structure (Fig. 4).

The SD with PEG (Fig. 5) had a non-crystalline structure. Typical crystals of CNP were not observed.

Solid dispersions of CNP with PEG 1500 in the presence of a solubilizer (1:5:1) also represent an amorphous structure in the absence of crystalline structures (Fig. 6).

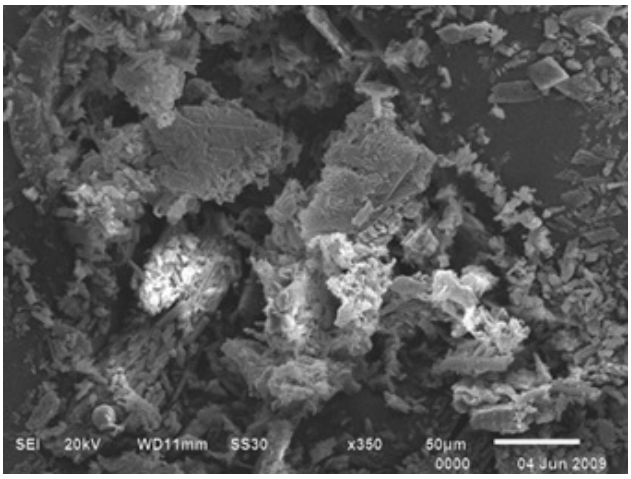

Fig. 3. Scanning electron microscopy of chloronitrophenol substance

Several studies indicate the possibility of using thermal methods, including differential scanning calorimetry for the analysis of solid dispersions [19, 20]. When conducting differential scanning calorimetry of chloronitrophenol, a peak at 112 °C was observed, for PEG 1500 it was 51 °C (Fig. 7, 8), which corresponds to the literature data. For the CNP SD with PEG-1500, a shift of the melting peak to the left at 41 °C was observed (Fig. 9). For SD in the presence of a solubilizer, even greater mixing and broadening of the peak (up to 38 °C) was observed (Fig. 10).

IR spectra of the chloronitrophenol substance, polymer, and solid dispersions with PEG 1500 showed that no new absorption bands were observed for the SD compared to the PS, which may indicate the absence of covalent bonds between the PS and the polymer in the SD (Fig. 11).

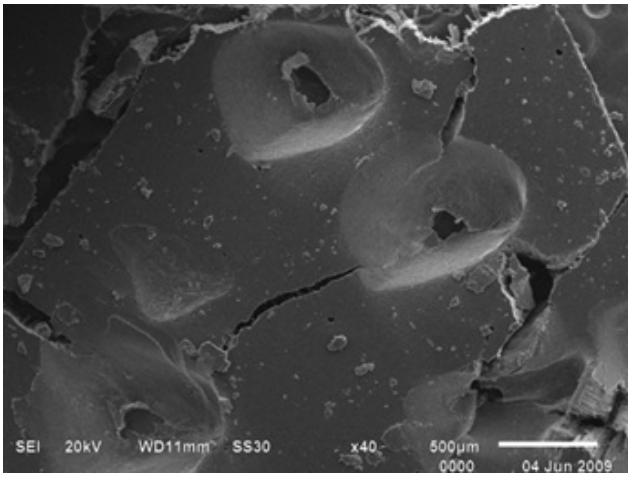

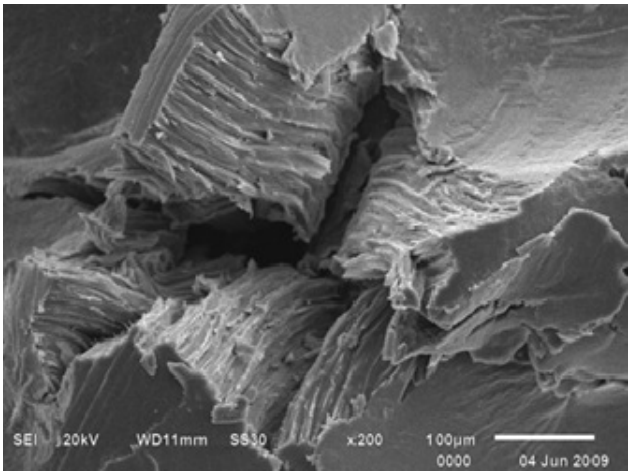

Fig. 4. Scanning electron microscopy of PEG 1500

4. Conclusions

Thus, the influence of solubilizers on the process of dissolution of chloronitrophenol from SD was studied. It has been shown that the

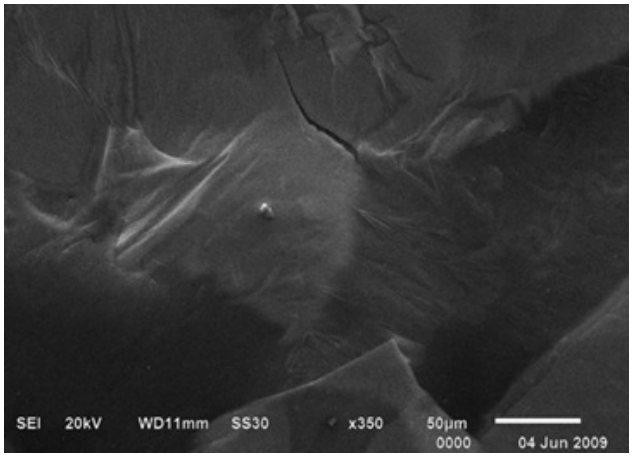

Fig. 5. Scanning electron microscopy of CNP solid dispersions with PEG 1500 (1:10)

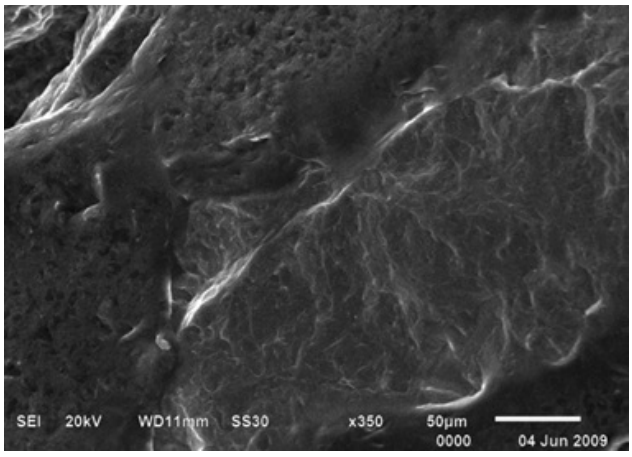

Fig. 6. Scanning electron microscopy of CNP solid dispersions with PEG 1500 in the presence of a solubilizer (1:5:1)

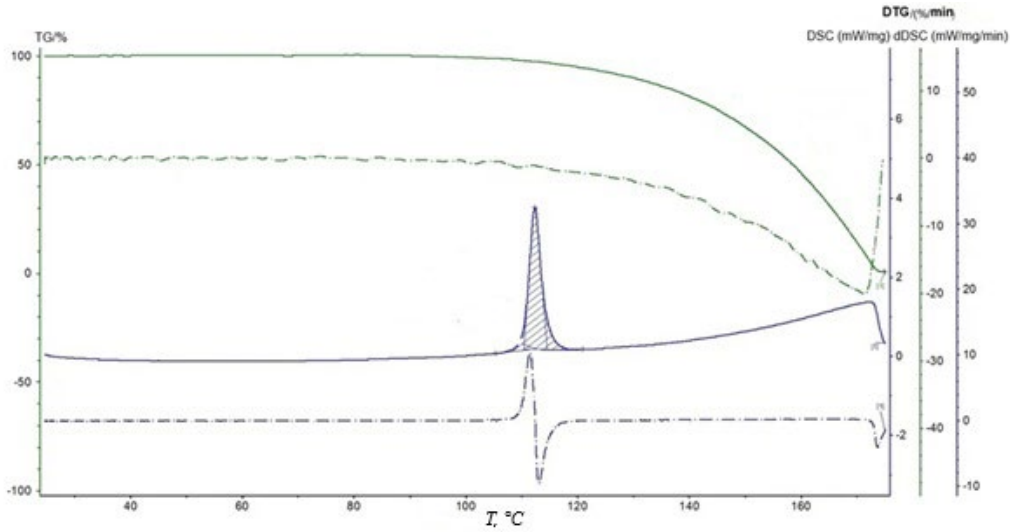

Fig. 7. DSC curve of chloronitrophenol

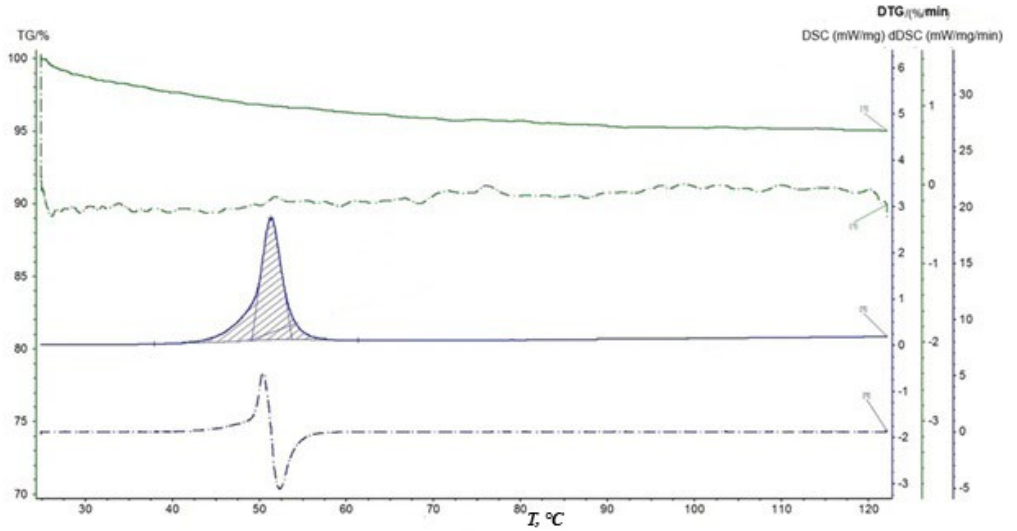

Fig. 8. DSC curve of PEG 1500

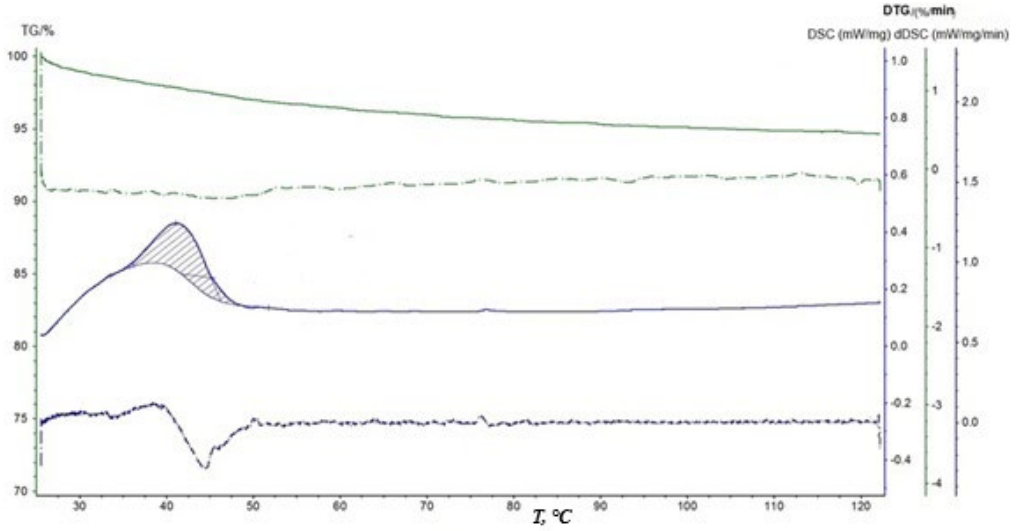

Fig. 9. DSC curve of chloronitrophenol solid dispersions with PEG 1500 (1:10)

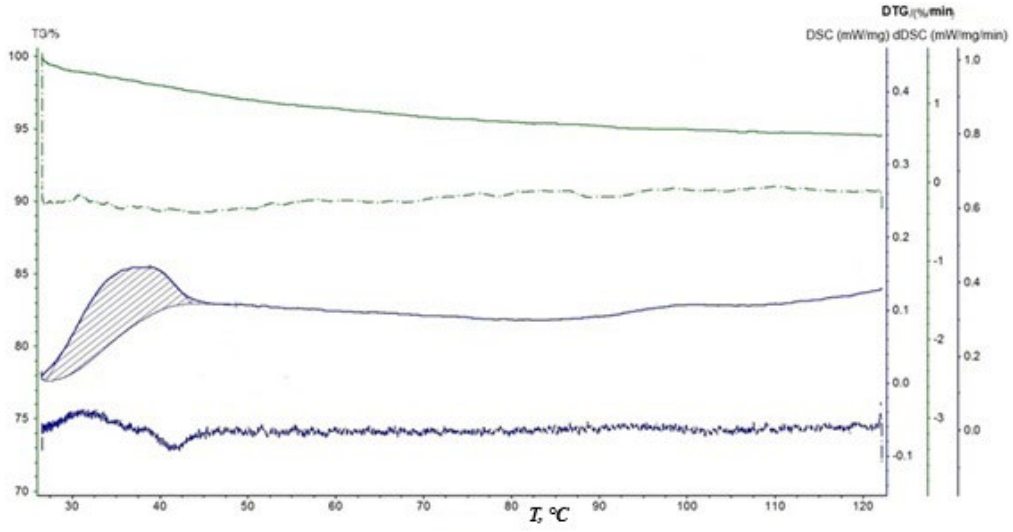

Fig. 10. DSC curve of chloronitrophenol solid dispersions with PEG 1500 in the presence of a solubilizer (1:5:1)

presence of solubilizers allows the use of lower concentrations of the carrier when obtaining SDS.

Based on the conducted research, it can be concluded ibn the production of solid dispersions of chloronitrophenol with a solubilizer, the crystallinity of the PS decreases, increasing the solubility. The properties of chloronitrophenol in the presence of a solubilizer do not change, but its solubility and dissolution rate are modified.

Contribution of the authors

The authors contributed equally to this article.

Conflict of interests

The author declares that they have no known competing financial interests or personal relationships that could have appeared to influence the work reported in this paper.

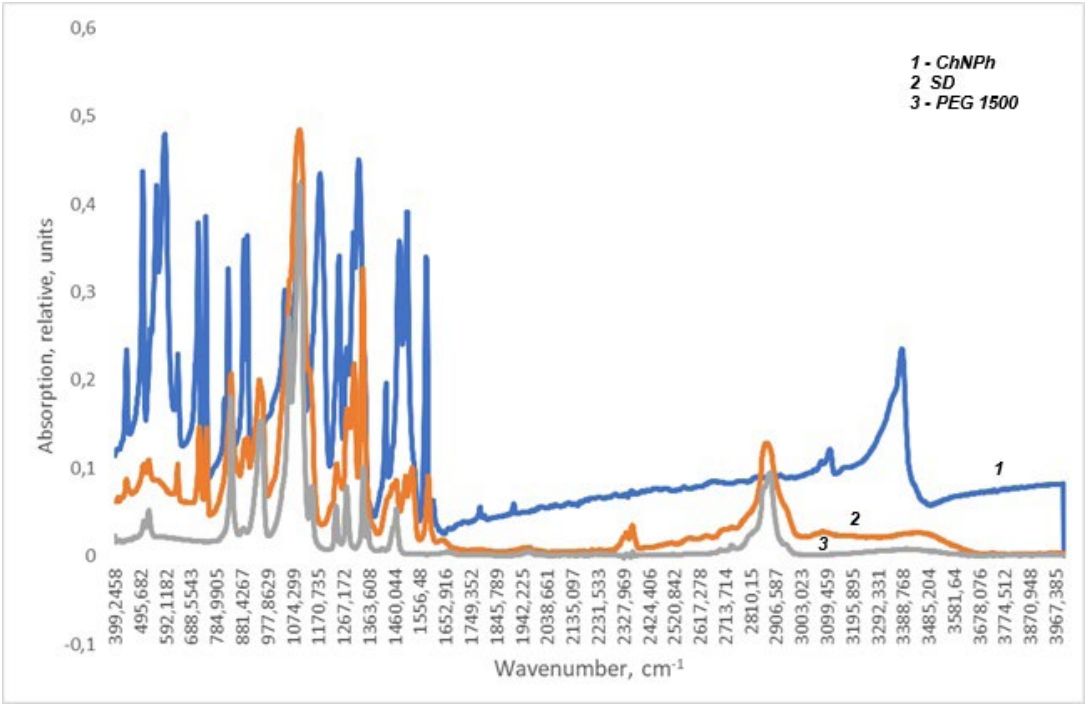

Fig. 11. IR spectrophotometry of chlornitrophenol substance, PEG 1500, solid dispersions of chlornitrophenol with PEG 1500 in the presence of a solubilizer (1:5:1)

References

1. *Register of medicinal products*. (in Russ.). Available at: https://www.rlsnet.ru/active-substance/xlornitrofenol-819

2. Censi R., Gigliobianco M. R., Dubbini A., Malaj L., Di Martino P. New nanometric solid dispersions of glibenclamide in neusilin® UFL2. *AAPS PharmSciTech*. 2016;17(5): 1204–1212. https://doi.org/10.1208/s12249-015-0457-z

3. Khabriev R. U., Popkov V. A., Reshetnyak V. Yu., Krasnyuk I. I. (ml.), Manakhova O. V. Increasing the solubility of an angioprotector by the method of solid dispersions. *Pharmaceutical Chemistry Journal*. 2009;43: 472–476. https://doi.org/10.1007/s11094-009-0326-8

4. Krasnyuk I. I. (ml.), Manakhova O. V., Khabriev R. U., Popkov V. A., Reshetnyak V. Yu., Krasnyuk O. I. Increasing the solubility of phenazepam by obtaining its solid dispersions. *Pharmaceutical Chemistry Journal*. 2010;44(5): 274–277. https://doi.org/10.1007/s11094-010-0448-z

5. Terentyeva O. A, Teslev A. A., Loginov K. Yu. Modern approaches to enhancing the bioavailability of poorly water-soluble drugs. *Sciences of Europe*. 2016;7(7): 27–31. (in Russ.). Available at: https://www.europe-science.com/wp-content/uploads/2020/10/VOL-2-No-7-7-2016.pdf

6. Kolpaksidi A. P., Dmitrieva M. V., Orlova O. L., Ektova L. V., Krasniuk I. I. Application of solid dispersion technology to obtain a model of injectable dosage form of indolocarbazole derivative. *Drug Development & Registration*. 2022;11(4): 73–78. (in Russ.). https://doi.org/10.33380/2305-2066-2022-11-4-73-78

7. Krasnyuk (Jr.) I. I., Naryshkin S. R., Krasnyuk I. I., … Vorobiev A. N. Effect of solid dispersions on the solubility of metronidazole. *Pharmacy & Pharmacology*. 2021;9(3): 195–204. https://doi.org/10.19163/2307-9266-2021-9-3-195-204

8. Gulyakin I. D., Nikolaeva L. L., Obolova N. A., … Bunyatyan N. D. Common methods increasing the solubility of poorly soluble hydrophobic substances. *Drug Development & Registration*. 2016;(2): 52–59. (in Russ.). Available at: https://www.pharmjournal.ru/jour/article/view/83

9. Silaeva S. Yu., Belenova A. S., Slivkin A. I., Chupandina E. E., Naryshkin S. R., Krasnyuk I. I. Use of solid dispersion systems in pharmacy. *Condensed Matter and Interphases*. 2020;22(2): 173–181. https://doi.org/10.17308/kcmf.2020.22/2820

10. Dmitrieva M. V., Kolpaksidi A. P., Orlova O. L., … Krasnyuk I. I. Development of a technology for producing a stable injectable dosage form of a hydrophobic indolocarbazole derivative. *International Journal of Applied Pharmaceutics*. 2021;13(6): 232–235. https://doi.org/10.22159/ijap.2021v13i6.42685

11. Nair A. R., Lakshman Y. D., Anand V. S. K., Sree K. S. N., Bhat K., Dengale S. J. Overview of extensively employed polymeric carriers in solid dispersion technology. *AAPS PharmSciTech*. 2020;21(8): 309. https://doi.org/10.1208/s12249-020-01849-z

12. Dahiya S. Studies on formulation development of a poorly water-soluble drug through solid dispersion technique. *The Thai Journal of Pharmaceutical Sciences*. 2010;34: 77–87. https://doi.org/10.56808/3027-7922.2171

13. Akiladevi D., Shanmugapandian P., Jebasingh D., Sachinandan B. Preparation and evaluation of paracetamol by solid dispersion technique. *International Journal of Pharmacy and Pharmaceutical Sciences*. 2011;3(1): 188–191.

14. Gladyshev V. V., Davtyan L. L., Drozdov A. L., Biryuk I. A., Kechin I. L. *Biopharmacy**. Dnipro: ChMP "Economy Publ.; 2018. 250 p. (in Russ.)

15. *Measurement of concentrations of harmful substances in the air**. Collection of methodological guidelines MUK 4.1.1706-03 "Spectrophotometric measurement of mass concentrations of 4-nitro-2-chlorophenol (nichlorfen, nitrofungin, chloronitrophenol) in the air of the working area." Moscow: Federal Center for Hygiene and Epidemiology of Rospotrebnadzor; 2007. 287 p. (in Russ.). Available at: http://libnorm.ru/Files2/1/4293755/4293755416.pdf

16. Silaeva S. Yu., Belenova A. S., Zvyagintseva T. K., Tsivilka M. V. Selection of carriers for obtaining solid dispersions of chloronitrophenol*. In: *Ways and forms of improving pharmaceutical education. Topical issues of development and research of new drugs. Collection of works of the 8th International Scientific and Methodological Conference, March 31 – April 02, 2022. Voronezh*. VSU Publishing House; 2022. p. 476–479. (in Russ.)

17. Krasnyuk I. I. *Increasing the bioavailability of dosage forms using solid dispersions**. Dr. pharm. sci. diss. Moscow: 2010. 298 p. (in Russ.). Available at: https://www.dissercat.com/content/povyshenie-biodostupnosti-lekarstvennykh-form-s-primeneniem-tverdykh-dispersii

18. Grikh V. V. *Development of dosage forms of nifedipine using solid dispersions**. Cand. pharm. sci. diss. Moscow: 2018. 151 p. (in Russ.). Available at: https://www.dissercat.com/content/razrabotka-lekarstvennykh-form-nifedipina-s-primeneniem-tverdykh-dispersii

19. Karolewicz B., Gajda M., Pluta J., Gorniak A. Dissolution study and thermal analysis of fenofibrate–Pluronic F127 solid dispersions. *Journal of Thermal Analysis and Calorimetry*. 2016;125(2): 751–757. https://doi.org/10.1007/s10973-015-5013-2

20. Gorniak A., Gajda M., Pluta J., Czapor-Irzabek, H., Karolewicz B. Thermal, spectroscopic and dissolution studies of lovastatin solid dispersions with acetylsalicylic acid. *Journal of Thermal Analysis and Calorimetry*. 2016;125(2): 777–784. https://doi.org/10.1007/s10973-016-5279-z

**Translated by author of the article*

Information about the authors

Alena S. Belenova, Cand. Sci. (Biol.), Associate Professor, Department of Pharmaceutical Technology, Voronezh State University (Voronezh, Russian Federation).

https://orcid.org/0000-0002-9036-7302

alenca198322@mail.ru

Yulia A. Polkovnikova, Dr. Sci. (Pharmacy), Associate Professor, Associate Professor of the Department of Pharmaceutical Technology and Pharmaceutical Chemistry, Faculty of Pharmacy, Voronezh State University (Voronezh, Russian Federation).

https://orcid.org/0000-0003-0123-9526

juli-polk@mail.ru

Alexey I. Slivkin, Dr. Sci. (Pharmacy), Professor, Head of the Department of PharmaceuticalChemistry andPharmaceutical Te-chnology, Faculty of Pharmacy, Voronezh State University (Voronezh, Russian Federation).

https://orcid.org/0000-0001-6934-0837

slivkin@pharm.vsu.ru

Svetlana I. Vasilyeva, Cand. Sci. (Pharmacy), Associate Professor, Department of Pharmaceutical Technology, Voronezh State University (Voronezh, Russian Federation).
https://orcid.org/0000-0002-7592-5097
provotorova-svetlana@mail.ru

Victor N. Semenov, Dr. Sci. (Chem.), Professor, Chair of Department of General and Inorganic Chemistry, Voronezh State University (Voronezh, Russian Federation).
https://orcid.org/0000-0002-4247-5667
office@chem.vsu.ru

Anastasia A. Golovina, 5th year student of the Faculty of Pharmacy, Voronezh State University (Voronezh, Russian Federation).
https://orcid.org/0009-0005-4763-7038
golovina.anas2013@gmail.com

Igor A. Saranov, Cand. Sci. (Tech.), Associate Professor, Department of Information Security, Voronezh State University of Engineering Technologies (Voronezh, Russian Federation).
https://orcid.org/0000-0002-9510-5168
mr.saranov@mail.ru

Received February 11, 2025; approved after reviewing March 10, 2025; accepted for publication April 15, 2025; published online December 25, 2025.

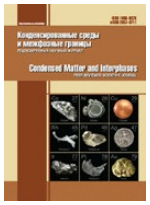

ISSN 1606-867X (Print)
ISSN 2687-0711 (Online)
Condensed Matter and Interphases
Kondensirovannye Sredy i Mezhfaznye Granitsy
https://journals.vsu.ru/kcmf/

Original articles

Research article
https://doi.org/10.17308/kcmf.2025.27/13296

Redox sorption of oxygen by Pd- and Cu-containing nanocomposites in the over-limiting current mode of electrochemical polarization

D. D. Vakhnin[1], T. E. Fertikova[2], N. A. Zheltoukhova[1], T. A. Kravchenko[1]✉, O. A. Kozaderov[1]

[1]*Voronezh State University,*
1 Universitetskaya pl., Voronezh 394018, Russian Federation

[2]*Voronezh State Medical University named after N. N. Burdenko,*
12 Studencheskaya st., Voronezh 394036, Russian Federation

Abstract

Objectives: Palladium- and copper-containing nanocomposites have been synthesized with different capacities for a metal component chemically deposited in a macroporous sulfocation exchange matrix.

Experimental: It has been revealed that in the over-limiting mode of electrochemical polarization, the reduction of oxygen dissolved in water on a palladium-containing nanocomposite proceeds by a catalytic mechanism. In addition to the targeted O_2 cathodic reduction process, adsorbed hydrogen is formed, which reacts catalytically with oxygen, which contributes to an additional decrease in O_2 concentration. It was found that in the over-limiting polarization mode of the Pd-containing nanocomposite, the oxygen concentration decreases significantly compared to the limiting mode.

Conclusions: The specific amount of absorbed oxygen increases with a decrease in the content of the deposited metal, which is associated with the high adsorption capacity of atomic hydrogen by weakly associated palladium nanoparticles. When using copper instead of palladium, the effectiveness of water deoxygenation decreases.

Keywords: Nanocomposite metal-ion exchange materials, Redox sorption, Deoxygenation of water

Funding: The study received financial support from the Ministry of Science and Higher Education of the Russian Federation within the framework of State Contract with universities regarding scientific research in 2025–2027, project No. FZGU-2025-0001.

For citation: Vakhnin D. D., Fertikova T. E., Zheltouhova N. A., Kravchenko T. A., Kozaderov O. A. Redox sorption of oxygen by Pd- and Cu-containing nanocomposites in the over-limiting current mode of electrochemical polarization. *Condensed Matter and Interphases*. 2025;27(4): 581–591. https://doi.org/10.17308/kcmf.2025.27/13296

Для цитирования: Вахнин Д. Д., Фертикова Т. Е., Желтоухова Н. А., Кравченко Т. А., Козадеров О. А. Редокс-сорбция кислорода Pd- и Cu-содержащими нанокомпозитами в сверхпредельном токовом режиме электрохимической поляризации. *Конденсированные среды и межфазные границы*. 2025;27(4): 581–591. https://doi.org/10.17308/kcmf.2025.27/13296

✉ Tamara A. Kravchenko, e-mail: krav280937@yandex.ru

1. Introduction

Modern physical chemistry pays special attention to systems containing nanometer-sized particles, since such systems have a huge specific surface area and, as a result, high excess energy, contributing to the intensification of industrially significant chemical or electrochemical processes. However, an unambiguous relationship between the reaction rate, size, and nature of the particles has not yet been established due to the simultaneous manifestation of a number of specific adsorption, structural, and percolation effects.

Special attention is paid to metal-ion exchanger nanocomposite materials, primarily because of their higher stability compared to single nanoparticles [1-5], as well as unique physical, chemical, and biological properties that arise due to the presence of particles smaller than one hundred nanometers in the composite material. The introduction of metal into the pores and on the surface of the ion exchanger matrix, which is a product of polymerization or polycondensation of unsaturated organic compounds, is ensured by the presence of acidic (-SO_3H, -COOH, -OH, -PO_3H_2, etc.) or basic (-$N(CH_3)_3$, -NH_3, =NH_2, etc.) functional groups in its structure. The metal can be embedded in an ion exchanger in the form of metal particles (usually nanometer-sized) or enter its matrix as oxides and poorly soluble hydroxides. The resulting hybrid nanostructures include reaction spaces and particles of composite components of the order of nanometers in size. By varying the polymer matrix material and the synthesis method, it is possible to obtain a nanocomposite with the necessary controlled structural properties. The pore volume of the matrix sets limits on the size of nanoparticle agglomerates, while the porous space depends on the degree of polymer crosslinking. In principle, there can be several nanoparticles in each individual pore. The minimum critical size of the nucleus depends on the initial concentration of atoms in the pore and the potential energy barrier of nucleation reduced due to the effect of the pore walls [6].

The particle size has a significant effect on the physicochemical characteristics of nanocomposites. An increase in the dispersion of the particles contained in them not only leads to a significant increase in the specific surface area, but also provides a dimensional effect of the first kind, which consists in the dependence of chemical and catalytic activity on the size of the cluster of nanoparticles. In addition, an energy dependence on the size of nanoparticles often occurs, and structural changes on the surface of nanoclusters additionally occur (changes in curvature, the appearance of crystallographic defects on the surface) [7-10]. The ambiguity of the role of the dimensional effect in the kinetics of electrochemical processes was revealed, for example, in [11] when studying the reaction of oxygen electroconduction on electrodes with platinum deposited on carbon. It turned out that in the methanol-containing electrolyte, the mass activity of the catalyst continuously increased with a decrease in the size of platinum nanoparticles from 4.6 to 2.3 nm. However, in an electrolyte without methanol, the activity of the same catalysts did not depend on the size of metal nanoparticles with a diameter of less than 3.5 nm.

The particle size is a thermodynamic variable that characterizes its state along with other system parameters [12]. The nanostructures have a higher surface energy by orders of magnitude than that of the medium and low-dispersed phases. As the particle size decreases, the ratio of the fractions of the surface and intraphase regions increases. If, for infinitely long phases, the internal energy, entropy, or volume at constant pressure and temperature depend linearly on the mass and amount of matter, then for the surface area of dispersed particles *S,* this dependence will be a power law:

$$S \approx n^{2/3}, \quad (1)$$

where n is the number of moles of the substance. As a result, none of the thermodynamic functions is linearly dependent on the mass. At the same time, the chemical parameters of particles of various sizes differ significantly from the specific values. If a crystal has a volume V and a surface S constructed of various faces with areas S_i and edges of length l_k, then the Gibbs energy is:

$$G = g^V V + \sum \sigma_i S_i + \sum \tau_k l_k, \quad (2)$$

where g^V is the specific G value per unit volume, σ_i is the specific G value per 1 cm^2 for i-faces, τ_k is the same value per unit length of k-edges.

In the special case of a spherical nanoparticle with radius r, the excess chemical potential

relative to the continuum potential is determined by the Gibbs-Thomson (Kelvin) equation:

$$\Delta\mu_r = \mu_r - \mu_\infty = \frac{\sigma V_m g}{r}, \quad (3)$$

where σ is the reversible work of a surface unit (for a liquid, this is surface tension); V_m is the molar volume of a substance, g is the geometric factor (g = 2 for spherical particles).

A secondary dimensional effect occurs at a certain size of nanoparticles, when there is a fluctuating redistribution of charges between particle ensembles, which can lead to an increase in the catalytic activity of the material [13]. However, a decrease in particle size does not entail such an increase under all conditions. In [14], the extreme dependence of the catalytic activity of platinum on a carbon substrate on the size of nanoparticles in the oxygen reduction reaction was shown. To explain this phenomenon, the concept of surface effects was formulated, which assumes that as the particle size decreases, the surface energy increases and changes occur in the electronic structure of the surface. This can lead to a change in the activity of the catalytic surface, for example, to a change in the donor-acceptor properties of the surface and the electronic structure of the metal on the surface. However, the dimensional effects can be compensated by other factors, such as changes in the shape and structure of the particles, the composition of the starting materials, the degree of particle dispersion on the substrate, and others. In addition, the catalytic activity may change as the reaction conditions change. Obviously, studying the size effects and other factors affecting the catalytic activity of nanoparticles is important for developing effective catalysts for various reactions.

Nanocomposites are characterized by the manifestation of percolation effects, that is, an abrupt change in the physico-chemical characteristics with a linear change in the amount of one of the constituent components. Thus, in [15], an increase in the mass transfer rate on a complex metal polymer doped with gold was revealed at the threshold of electron conduction percolation due to a decrease in the interparticle distance. After 5 cycles of chemical deposition of silver nanoparticles onto the MF-4SK membrane, the ohmic resistance of the modified membrane dropped sharply [16]. In the case of the CU-23 sulfocation exchanger, the oxygen reduction rate increased sharply with a copper content of ~5 meq/cm^3 [17]. The authors explain the drop by the transition from single nanoparticles to their unified system with generalized electrons. Ionic conductivity is similarly susceptible to percolation effects [18], which is expressed in an increase in sorption of mobile ions due to a large surface defect.

The most common and significant factor in the applied aspect reaction is oxygen electroreduction, and therefore it is being actively investigated. Oxygen reduction is widely used in fuel cells [19] and electrocatalysis [20]. Oxygen acts as a depolarizer in metal corrosion [21]. Deep deoxygenation of water is also required for the needs of microelectronics, where ultrapure water is used at the stage of flushing silicon wafers in the manufacture of integrated circuits. To prevent the formation of an oxide layer on the plate surface, the O_2 content level should not exceed 1 μg/l [22]. Thus, the oxygen reduction reaction undoubtedly plays a huge role in many industrially significant processes. The problem of organizing a potable water supply for the populations of large cities is caused, among other things, by the presence of dissolved oxygen in the water. Being a strong corrosive agent and interacting with pipeline materials, O_2 causes a change in their composition and structure, which leads to a deterioration in the quality of potable water supplied to the population and a violation of hygienic standards [23, 24]. It should be noted that at present, official data from the Federal Service for Surveillance on Consumer Rights Protection and Human Wellbeing indicate an improvement in the quality of drinking water in water pipes [25, 26]. Within the territory of the Russian Federation, there has been a decrease in the proportion of water samples that do not meet hygienic standards for sanitary and chemical indicators from 17.2 to 15.5%, and for microbiological ones from 3.6 to 1.9% in 2022 compared with 2013. According to microbiological indicators, the proportion of samples that did not meet the requirements was at the level of 2021 and amounted to 0.9%. However, this information is based on the results of a study of water before entering the distribution network,

which does not preclude a decrease in its quality as a result of passing through pipelines.

Hybrid catalytic nanocomposite systems in which oxygen reduction is organized by both the chemical interaction of dissolved O_2 with gaseous hydrogen [3, 27, 28] and its electrochemical reduction, when both processes occur on metal nanoparticles stabilized in an ion exchange matrix [29-31], seem to be the most promising for deep deoxygenation of water. Obviously, depending on the nature of the metallic and ion-exchange components of the nanocomposite, as well as on the conditions of electrochemical polarization, the contributions to the overall process of each of the partial reactions will be different. For comparison with a copper-containing nanocomposite, a palladium-containing nanocomposite was studied, on which, as is known, the catalytic reaction between adsorbed hydrogen and oxygen proceeds best. At the same time, the issues of both the mechanism of redox sorption of molecular oxygen from water in over-limiting polarization regimes and the contributions of partial stages of the process remain insufficiently resolved.

The purpose of the work was to study the process of redox oxygen sorption on palladium- and more affordable copper-containing ion-exchange nanocomposites in the mode of over-limiting polarization.

2. Experimental

A macroporous strongly acidic ion exchange matrix CU-23 15/100 was used for the synthesis of nanocomposites (NC) (Table 1). It is characterized by the presence of sulfogroups on the surface and in the volume of the polymer and the predominance of macropores with a fairly wide size distribution.

The polymer chain of the ion exchange matrix has the following form:

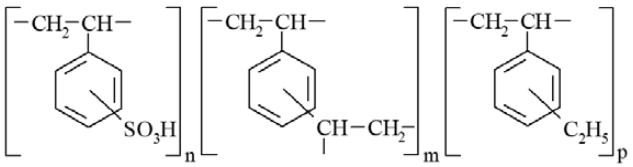

where n, m, p are the number of components in the polymer. The selected ion-exchange porous matrix has sufficient mechanical strength, is resistant to acid-base influences, and does not undergo thermal decomposition over a sufficiently wide temperature range.

The chemical deposition of metal into the ion exchange matrix was preceded by its preliminary preparation [33]. The ion exchanger was placed in 2 M NaCl for a day, then its acid-base conditioning was carried out, consisting in sequential dynamic passage through a column for the synthesis of HCl and NaOH solutions with a solution:ion exchanger volume ratio of 3:1 with decreasing concentration (1.0 M; 0.5 M; 0.25 M). After each acid/alkali pass, the ion exchanger was washed with a large amount of distilled water. The ANION-4100 ionomer (Infraspak-Analyte, Russia) recorded the alignment of pH of the solution at the outlet of the column and pH of distilled water.

The synthesis of the nanocomposite consisted of two stages: saturation of the matrix with metal ions and their subsequent chemical reduction. To saturate the cation exchanger with copper (II) ions, a 6% solution of copper (II) sulfate in water was passed through the bulk layer of the ion exchanger at the rate of 10 volumes of solution per 1 volume of resin at a volumetric rate of $5 \cdot 10^{-4}$ m^3/h. During this stage, the ion exchange of metal cations and hydrogen of the ionogenic centers of the sulfogroups of the ion exchanger took place. Then, the non-exchangeably sorbed electrolyte was washed out of the cation exchanger with distilled water deoxygenated with argon. Chemical reduction of the metal was carried out with 0.35 M sodium dithionite $Na_2S_2O_4$ solution in 0.63 M NaOH in a volume ratio of reducing agent solution/ion exchanger equal to 10:1. Then the copper-containing nanocomposite was washed from the reducing agent, neutralizing the alkali with an hydrochloric acid solution

Table 1. Basic physico-chemical characteristics of an ion exchanger [32]

The cation exchanger	CU-23 15/100
Polymer base	Stitched polystyrene
Ion exchange (redox) capacity of granular volume, meq/cm^3	1.25
Characteristic pore diameter, nm	10–100
Specific pore volume, cm^3/g	0.40–0.60
Diameter of granules, mm	0.40–1.25

followed by passing deoxygenated distilled water. If necessary, to convert the nanocomposite to the Na^+ form, a solution of sodium sulfate was passed through the synthesis column and washed with distilled water, deoxygenated by hour-long argon bubbling. The cycles of ion exchange saturation and reduction of the metal deposited in the ion exchange matrix were repeated several times until a nanocomposite with the required metal capacity was obtained.

In the case of palladium-containing nanocomposites, the saturation solution was a 6% palladium (II) chloride solution, which was passed from bottom to top in even cycles of palladium deposition and from top to bottom in odd cycles at a speed of 5 m/h. The amount of solution consumed was in a ratio of 5:1 to the volume of resin; the transmission time was 30–40 minutes. After washing with deoxygenated water, a solution of the reducing agent, sodium borohydride, was passed through in an alkaline medium at a rate of 5 m/h for an hour. Washing with distilled water was carried out from the top down at a rate of 10 m/h. The water volume to resin volume was 10:1, with a flow time of 1 hour. The synthesis of the palladium-containing composite was accompanied by a rapid release of gas.

To determine the redox capacity of NC for copper, a titrimetric method was used, for which 1 cm^3 of the test sample was placed in a heat-resistant glass in a water bath, and 10% nitric acid was sequentially added to it in 10 ml portions. The copper cations formed during dissolution passed into a solution, which was then transferred to a measuring flask until the entire metal of the composite dissolved, which was visually detected by the absence of a change in the color of the nitric acid solution. The resulting solution containing copper ions was brought to the mark in a measuring flask and the redox capacity was determined. The metal capacity was determined by transferring the entire metal sample into a 100 cm^3 solution using nitric acid. Then, an aliquot of 10 cm^3 was taken from the resulting solution, which was additionally diluted with 20 cm^3 of distilled water and treated with an ammonia buffer solution (20 g/l NH_4Cl + 100 cm^3 NH_3) until an alkaline medium was obtained and the solution acquired a blue color. The concentration of copper ions was determined by complexometric titration using 0.1 mol-eq/cm^3 of trilon B and murexide as an indicator before the color of the solution changed to purple.

Titrimetric determination of palladium in solution began with the preparation of an analyte – standard solutions of palladium and EDTA, a titrant – a standard solution of zinc, an indicator solution of "eriochrome black T". Preparation of a standard palladium solution: 1.5 g of pure palladium was dissolved in several milliliters of aqua regia. Nitrogen oxides were removed by evaporation with hydrochloric acid. The dry residue was dissolved in 0.2 M hydrochloric acid and adjusted with the same solution to a volume of 500 ml. Preparation of a standard zinc solution: 1.8 g of zinc oxide was dried at 100 °C for 2 hours, dissolved in a minimum volume of nitric acid (1:1) and brought to a volume of 1 liter. Preparation of a standard EDTA solution: 5.5 g of sodium salt of EDTA was dissolved in a liter of distilled water. The titer of the solution was determined by complexometric titration with a standard zinc solution and "eriochrome black T" as an indicator. Preparation of the indicator solution: 0.1 g of "eriochrome black T" was dissolved in 50 ml of distilled water, to which several drops of 1 M solution of caustic potassium were added. The course of the analysis: a small excess of the standard EDTA solution was added to the standard palladium (II) chloride solution. By adding 0.1 M solution of caustic potassium, the pH was set to 10±1. 5 drops of "eriochrome black T" solution were added and titrated with a standard zinc solution until the equivalence point, which was determined by the color change from blue or green to bright pink.

The redox capacity of the deposited metal ε_{Me^0}, mol-eq/cm^3 in the sample was calculated by the formula:

$$\varepsilon_{Me^0} = \frac{C_T V_T V}{V_{NC} V_{Al}}, \quad (4)$$

where C_T is the titrant concentration, mol-eq/cm^3; V_T, V, V_{NC}, V_{Al} are the volumes of the titrant, the total solution, the sample of NC granules taken for analysis, and the aliquot taken for titration, respectively. All volumes are taken in the same units, for example, cm^3.

The approach described in [29] was used to select the value of the polarizing current. It

is based on the concepts of external diffusion oxygen transport and the density of the limiting oxygen diffusion current. The maximum allowable current for the entire granular layer, i.e. the limiting current of I_{lim}, is equal to

$$\frac{I_{lim}}{I_{com}} = \frac{Al}{1+Al}, \quad (5)$$

where I_{com} is the current required to reduce all oxygen entering the column:

$$I_{com} = nFSuc_0, \quad (6)$$

S is the cross-sectional area of the granular layer (1.2 cm); u is the flow rate (0.23 cm/s); l is the height of the granular layer (1 cm), and c_0 is the oxygen concentration in the water at the entrance to the granular layer (7.7 mg/l).

The value of the constant A is found by the formula:

$$A = \frac{3\chi i_{lim}(0)}{nFuR_0c_0}, \quad (7)$$

where χ is the coefficient of column filling with sorbent, $i_{lim}(0)$ is the density of the limiting diffusion current on the surface of the NC granule, R_0 is the radius of the NC granule. The calculated parameters are shown in Table 2.

Table 2. Calculated parameters of the experiment

$i_{lim}(0)$, A/m^2 [29]	A, cm^{-1}	I_{com}, mA	I_{lim}, mA
1.03	0.24	25.6	5.0

Granular nanocomposite materials were loaded into the cathode compartment of a sorption-membrane electrochemical cell, the scheme of which is shown in Fig. 1. The three-chamber electrolyzer contains a cathode compartment separated from the two anode membranes by MC-40. The bulk cathode was a thin copper wire surrounded by a layer of NC. The anodes were made of platinum wire twisted into a spiral. An appropriate ion exchanger was loaded into the anode chambers, which did not contain any deposited metal particles inside.

A MC-40 cation exchange membrane was used to ensure proton transfer from the anode to the cathode. The height of the thin granular nanocomposite layer was l = 1 cm, and the cross-sectional area of the nanocomposite layer was S = 1.2 cm^2. Water flowed through the electrolyzer at a rate of u = 0.23 cm/s. An AKIP-1111 (Russia) was used as an external current source. To measure the concentration of the oxidizer, an AKPM-01 oxygen meter (Alfa-Bassens LLC, Russia) was used, protected from external electromagnetic radiation by a metal mesh screen. The oxygen input concentration was kept constant by continuously supplying atmospheric air to a container with distilled water before entering the reactor. After the thin granular layer of the nanocomposite, a filter was installed that performed the functions of sorption and membrane filtration. The value of water pH at the outlet of the electrolyzer was measured using an ionomer ANION-4100 manufactured by "Infraspak-Analyt", Russia.

3. Results and discussion

As a result of the procedures of saturation of the ion exchanger with counterions of the deposited metal, their subsequent reduction with an alkaline solution of a reducing agent and conversion to the initial ionic form, metal-ion exchange nanocomposites with different capacities for the metal component were obtained. Chemical precipitation of copper into a macroporous sulfocation exchanger with sodium dithionite in an alkaline medium occurred according to the scheme:

$$2\text{R-SO}_3^-\text{H}^+ + \text{Cu}^{2+} \rightleftarrows (\text{R-SO}_3^-)_2\text{Cu}^{2+} + 2\text{H}^+ \quad (8)$$

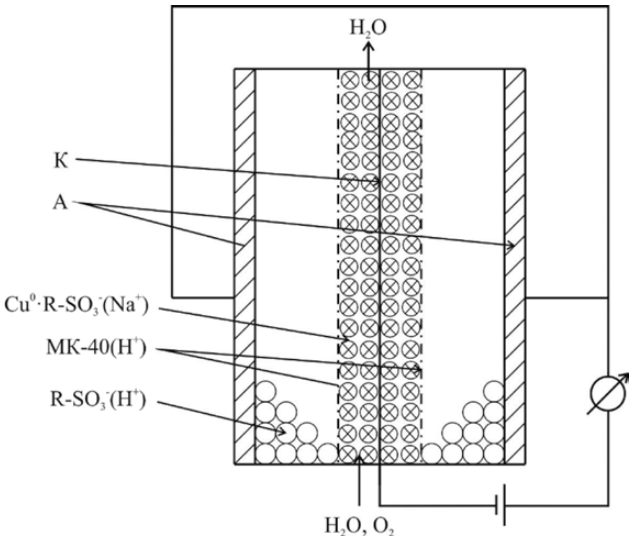

Fig. 1. Scheme of a three-chamber sorption-membrane electrolyzer for deoxygenation of flowing water. C is a copper wire current supply, $\text{Cu}^0 \cdot \text{R-SO}_3^-$ is a bulk layer of nanocomposite; A is platinum wire anodes, R-SO_3^- are bulk layers of a sulfocation exchanger; MC-40 (H^+) is a cation exchange membrane

$$(R\text{-}SO_3^-)_2Cu^{2+} + Na_2S_2O_4 + 4NaOH \rightarrow \rightarrow \left[R - SO_3^-Na^+\right]_2 \cdot Cu^0 + 2Na_2SO_3 + 2H_2O \quad (9)$$

$$\left[R - SO_3^-Na^+\right]_2 \cdot Cu^0 + 2H^+ \rightarrow \rightarrow \left[R - SO_3^-H^+\right]_2 \cdot Cu^0 + 2Na^+ \quad (10)$$

The chemical precipitation of palladium in a sulfocation exchanger with sodium borohydride in an alkaline medium occurred according to the scheme:

$$2R\text{-}SO_3^-H^+ + PdCl_2 \rightarrow \left(R\text{-}SO_3^-\right)_2 Pd^{2+} + 2HCl \quad (11)$$

$$(R - SO_3^-)_2Pd^{2+} + 2NaBH_4 + 6H_2O \rightarrow \rightarrow \left[R - SO_3^-Na^+\right]_2 \cdot Pd^0 + 2B(OH)_3 + 7H_2 \quad (12)$$

The values of the metal capacity of the obtained nanocomposites are given in Table 3.

The current I = 50 mA was selected for polarization in the over-limiting mode, i.e. the excess of the maximum current was I/I_{lim} was 10. The current was turned on for 4 hours after the oxygen concentration was established for an hour, and after 5 hours of the experiment, the current was turned off. Oxygen concentration measurements were continued for another 5 hours. During this time, the oxygen concentration in the water at the outlet of the granular layer of NC reached the initial value at the inlet.

The amount of dissolved oxygen removed from the water (moles) was calculated based on the difference in the amount of oxygen dissolved in the water at the entrance to the granular layer of the nanocomposite and at the exit:

$$Q(O_2) = (c_0 - \bar{c})\frac{u \cdot t}{M_r(O_2)}, \quad (13)$$

where c_0 is the concentration of oxygen dissolved in water at the inlet (mg/l), $\bar{c}$ is the average value of the residual (output) concentration in three duplicate experiments, t is the experiment time, u is the volume flux of water (0.8 l/h), M_r (O_2) is the molar mass of oxygen.

The calculation results are presented in Table 3. It can be seen that during the deoxygenation of water in the selected over-limiting mode of electrochemical polarization, a significant amount of gas was released. Oxygen dissolved in water is removed in various ways: 1) by direct electroreduction, 2) by catalytic interaction with electrochemically obtained adsorbed atomic hydrogen or chemical oxidation of electrochemically reduced active metal nanoparticles from oxides, and 3) by physical removal with released hydrogen. At the same time, all these stages took place under the influence of cathodic polarization. After the current was turned off, the oxygen concentration gradually equalized to the initial level due to the finite mixing time of the running water in the measuring vessel.

Oxygen can electrochemically interact with hydrogen ions, which leads to the basic reaction with the formation of water. At pH < 7, which is true for the hydrogen ionic form of the

Table 3. Metal capacity, volume of released gas, and amount of oxygen removed from water for Pd^0·CU-23 (H^+) and Cu^0·CU-23 (H^+) nanocomposites. Experimental conditions: granular layer height l = 1 cm, water flow rate u = 0.23 cm/s, I = 50 mA, I/I_{lim} = 10

Nanocomposites, number of metal deposition cycles	ε_{Mr^0}, mmole-eq/cm^3 (mmol/cm^3)	V(H_2,O_2), cm^3	Q (H_2,O_2) n the gas mixture, mmol	$\sum Q(O_2)$, removed from water, mmol	$Q(O_2)$, emoved under current (stage 2), mmol	$Q(O_2)$, removed without current (stage 3), mmol
Pd^0·CU-23 (H^+), 1	0.76±0.23 (0.38±0.12)	22.3±1.0	0.91	0.72	0.49	0.23
Pd^0·CU-23 (H^+), 3	3.22±0.23 (1.61±0.12)	27.7±2.0	1.13	0.78	0.50	0.28
Pd^0·CU-23 (H+), 5	5.02±0.14 (2.51±0.07)	30.0±2.0	1.23	0.74	0.44	0.30
Cu^0·CU-23 (H^+), 10	9.68±0.07 (4.84±0.04)	58.3±3.0	2.39	0.79	0.44	0.35
CU-23 (H^+), 0	0	45.0±1.2	1.84	0.44	0.41	0.03

nanocomposite, the oxygen reduction reaction can be represented as [34]:

$$O_2 + 4H^+ + 4e^- \rightarrow 2H_2O \ (E^0 = 1.23 \text{ V}), \quad (14)$$

and in a neutral and alkaline environment according to the equation:

$$O_2 + 2H_2O + 4e^- \rightarrow 4OH^- \ (E^0 = 0.40 \text{ V}). \quad (15)$$

During the over-limiting polarization on the palladium surface, the formation of adsorbed hydrogen became possible, due to the catalytic activity of which the oxygen reduction reaction with the formation of water was carried out [27]:

$$2H^+ + 2e^- \xrightarrow{I} 2H_{ads} \quad (16)$$

$$O_2 + 4H_{ads} \xrightarrow{Pd} 2H_2O \quad (17)$$

On copper-containing nanocomposites, due to interaction with oxygen, the formation of copper oxides is possible: Cu_2O and CuO. The chemical activity of the nanocomposite is kept due to the electroreduction of copper from oxides [29]:

$$O_2^{\text{dif.ext}} \rightarrow O_2^{\text{dif.int}} \rightarrow O_2^{\text{ads}} + Cu^0 \rightarrow$$

$$\xrightarrow{+4e^-} H_2O$$

$$\rightarrow \left[Cu\left(Cu^*\right)...O_2\right] \xrightarrow[+e^-]{+\overline{H}^+} \overline{Cu}^+ \xrightarrow[+e^-]{+\overline{H}^+} \overline{Cu}^{2+}$$

$$+2e^-$$

Here $\overline{H}^+$, $\overline{Cu}^+$, $\overline{Cu}^{2+}$ are the counterions.

It is possible to physically displace oxygen dissolved in water with an inert gas, which can be released by molecular hydrogen.

The experiment can be divided into 3 stages. The first lasting 1 hour is the establishment of stationarity, the second (2-5 hours) is the time of electrochemical reactions, and the third (5-10 hours) is catalytic for palladium-containing NC, or chemical for copper–containing NC oxygen reduction. Fig. 2 shows a decrease in the relative oxygen concentration to ~0.3 at Pd^0·CU-23 (H^+), which is associated with the high ability of palladium to hydrogenate and an active catalytic reaction between oxygen and molecular hydrogen on the Pd surface. During the polarization of the Pd^0·CU-23 (H^+) nanocomposite, the pH value of water was in the range of 6.4–7.0. Compared with palladium nanocomposites for Cu^0·CU-23 (H^+), the concentration of C/C_0 oxygen dissolved in water decreased to ~0.4 (Fig. 3). During the experiment, the pH value increased from 6.5 to 6.7.

The current efficiency for molecular hydrogen evolution and the efficiency of oxygen removal are shown in Table 4. They show the ratio of the contributions of electrochemical processes. A dimensionless efficiency coefficient of nanocomposites for water deoxygenation has been introduced:

$$f_{\text{deox}} = \frac{\sum Q(O_2)}{\nu \varepsilon_{Me^0} V_{NC}}, \quad (19)$$

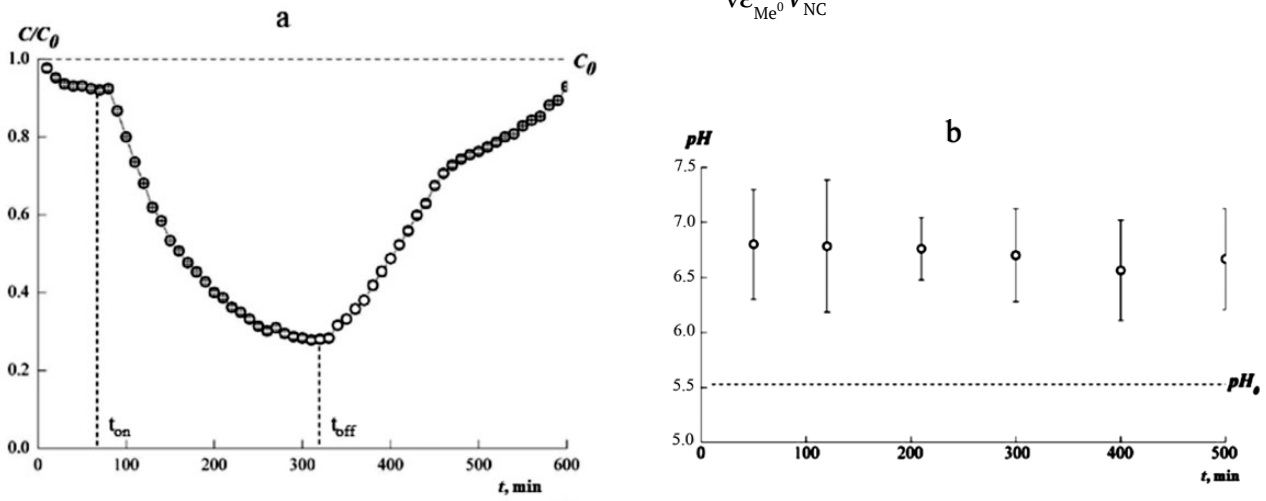

Fig. 2. Relative concentration C/C_0 of dissolved oxygen (a), and pH of water (b) at the outlet of a thin granular layer of the Pd^0·CU-23(H^+) nanocomposite in the over-limiting polarization mode. Experimental conditions: the height of the granular layer is l = 1 cm, 1 cycle of metal deposition. C_0 is the initial oxygen concentration (7.9 mg/l), pH_0 is the hydrogen index of the source water. Ionic forms in the cathode and anode chambers of CU-23(H^+), I = 50 mA, I/I_{lim} = 10, limiting current I_{lim} =5.0 mA, t_{on}, t_{off} are the times of switching on and off the current, respectively

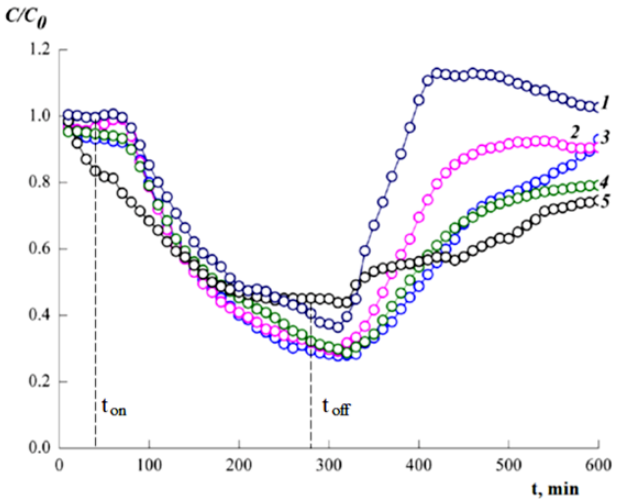

Fig. 3. Relative concentration C/C_0 of dissolved oxygen in water at the outlet of a thin granular layer of nanocomposites. Experimental conditions: granular layer height l = 1 cm, water flow velocity u = 0.23 cm/s, I = 50 mA, I/I_{lim} = 10, I_{lim} =5.0 mA. C_0 is the initial oxygen concentration (7.4-8.0 mg/l), t_{on}, t_{off} are the times of switching on and off the current, respectively. Curves: 1 – CU-23 (H^+); 2 – Pd^0·CU-23 (H^+), one deposition cycle; 3 – Pd^0·CU-23 (H^+), three deposition cycles; 4 – Pd^0·CU-23 (H^+), five deposition cycles; 5 – Cu^0·CU-23 (H^+), ten deposition cycles

in which the amount of oxygen removed (mmole) is normalized to the stoichiometric coefficient of the metal (Pd, Cu) in reaction with oxygen (2), the metal capacity (mmol/cm^3) and the volume of the granular layer of the V_{NC} nanocomposite. The efficiency coefficient of water deoxygenation

Table 4. Oxygen and hydrogen current efficiency, and nanocomposites efficiency coefficient for water deoxygenation. The polarizing current I = 50 mA, I/I_{lim} = 10

Nanocomposites, number of metal deposition cycles	$\eta_T(H_2)$, %	$\eta_T(O_2)$, %	f_{deox}, %
Pd^0·CU-23 (H+), 1	58.0	42.0	78.9
Pd^0·CU-23 (H+), 3	63.0	37.0	20.2
Pd^0·CU-23 (H+), 5	67.7	32.3	12.3
Cu^0·CU-23 (H+), 10	73.0	27.0	6.8
CU-23 (H+), 0	70.0	30.5	–

decreased significantly with an increase in the number of plantings of deposited palladium (Table 4).

Thus, an increase in the amount of palladium embedded in NC does not increase the efficiency of the redox sorption process. Only the amount of released hydrogen gas increases. The specific amount of reduced oxygen decreases steadily with increasing palladium capacity. Based on the corresponding dependencies in Fig. 4, it can be concluded that in order to intensify the process of water deoxygenation, it is not necessary to increase the amount of metal in the nanocomposite. On the contrary, an increase in the specific content of reduced oxygen will occur with a small number of metal nanoparticles that are not combined into aggregates, and therefore their surfaces are characterized by the greatest access for adsorption.

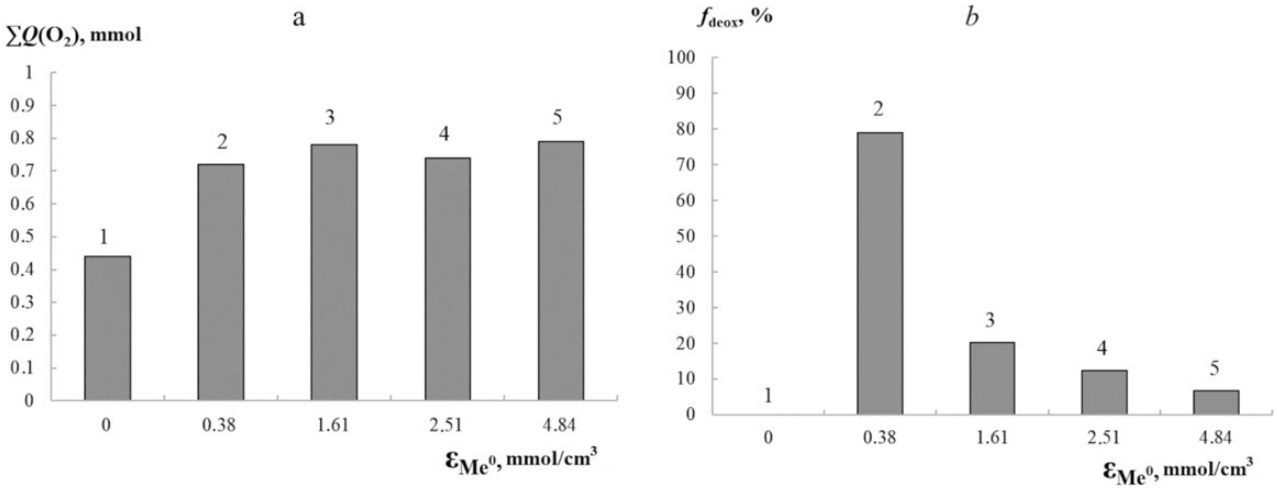

Fig. 4. Histograms of the distribution of the amount of oxygen removed $\sum Q(O_2)$ (a) and the efficiency coefficient of nanocomposites for water deoxygenation f_{deox} on the metal capacity (b): 1 – CU-23(H^+), 2-4 – Pd^0·CU-23 (H^+); 5 – Cu^0·CU-23 (H^+). Experimental conditions: granular layer height l = 1 cm, 1, 3, 5, and 10 cycles of metal deposition, water flow rate u = 0.23 cm/s, polarizing current I = 50 mA, I/I_{lim} = 10, I_{lim} = 5 mA

4. Conclusions

Palladium- and copper-containing nanocomposites with different capacities for the metal component deposited in a macroporous sulfocation exchange matrix have been synthesized.

In the over-limiting polarization mode on paladium-containing nanocomposites, the concentration of oxygen dissolved in water passing through the granular layer decreases significantly compared to the limiting mode. In addition to the electroreduction of oxygen, adsorbed hydrogen is formed, which enters into a catalytic reaction with dissolved oxygen, as well as the physical displacement of oxygen by gaseous hydrogen, which leads to an additional decrease in oxygen concentration.

The specific amount of absorbed oxygen increases with a decrease in the content of deposited metal, which is associated with a decrease in the size of nanoparticle aggregates. With some reduction in efficiency, it is possible to use copper instead of palladium.

Contribution of the authors

The authors contributed equally to this article.

Conflict of interests

The author declares that they have no known competing financial interests or personal relationships that could have appeared to influence the work reported in this paper.

References

1. *Nanoparticle Technology Handbook. Masuo Hosokawa, Kiyoshi Nogi, … Toyokazu Yokoyama* (eds.). Elsevier Science; 2008. https://doi.org/10.1016/B978-0-444-53122-3.X5001-6

2. *Nanocomposites: Synthesis, Characterization and Applications* X. Wang (ed.). New York: Nova Sc. Publ.; 2013. 422 p.

3. Volkov V. V., Kravchenko T. A., Roldughin V. I. Metal nanoparticles in catalytic polymer membranes and ion-exchange systems for advanced purification of water from molecular oxygen. *Russian Chemical Reviews*. 2013;82(5): 465–482. https://doi.org/10.1070/rc2013v082n05abeh004325

4. Povolotskaya A. V., Povolotskiy A. V., Manshina A. A. Hybrid nanostructures: synthesis, morphology and functional properties. *Russian Chemical Reviews*. 2015;84(6): 579–600. https://doi.org/10.1070/RCR4487

5. Lateef A., Nazzir R. Metal Nanocomposites: Synthesis, Characterization and their Applications. In book: *Science and applications of Tailored Nanostructures*. *Ch. 12*. Paolo Di Sia (ed.). Publisher: One central press; 2017. p. 239–256. Available at: https://www.researchgate.net/publication/313634485

6. Capek I. *Nanocomposite structures and dispersions*. Amsterdam: Elsevier; 2006. 301 p.

7. Proch S., Wirth M., White H. S., Anderson S. L. Strong effects of cluster size and air exposure on oxygen reduction and carbon oxidation electrocatalysis by size-selected Ptn ($n \leqslant 11$) on glassy carbon electrodes. *Journal of the American Chemical Society*. 2013;135: 3073–3086. https://doi.org/10.1021/ja309868z

8. Nesselberger M., Roefzaad M., Hamou R F., … Arenz M. The effect of particle proximity on the oxygen reduction rate of size-selected platinum clusters. Nature Materials. 2013;12: 919–924. https://doi.org/10.1038/nmat3712

9. *Nanoparticles and catalysis*. Astruc D. (ed.). Weinheim: Wiley-VCH Verlag GmbH & Co; 2008. 663 p.

10. Reske R., Mistry H., Behafarid F., Roldan Cuenya B., Strasser P. Particle size effects in the catalytic electroreduction of CO_2 on Cu nanoparticles. *Journal of the American Chemical Society*. 2014;136(19): 6978–6986. https://doi.org/10.1021/ja500328k

11. Maillard F., Martin M., Gloaguen F., Lйger J.-M. Oxygen electroreduction on carbon-supported platinum catalysts. Particle-size effect on the tolerance to methanol competition. *Electrochimica Acta*. 2002;47(21): 3431–3440. https://doi.org/10.1016/s0013-4686(02)00279-7

12. Poltorak O. M. *Lectures on chemical thermodynamics**. Moscow: Vysshaya shkola Publ.; 1971. 256 p. (in Russ.)

13. Rostovshchikova T. N., Smirnov V. V., Kozhevin V. M., Yavsin D. A., Gurevich S. A. Intercluster interactions in catalysis by nanosized particles*. *Nanotechnologies in Russia*. 2007;2(1-2): 47–60. (in Russ.). Available at: https://elibrary.ru/item.asp?id=9321693

14. Leontyev I. N., Belenov S. V., Guterman V. E., Haghi-Ashtiani P., Shaganov A. P., Dkhil B. Catalytic activity of carbon-supported Pt nanoelectrocatalysts. Why reducing the size of Pt nanoparticles is not always beneficial. The Journal of Physical Chemistry C. 2011;115(13): 5429–5434. https://doi.org/10.1021/jp1109477

15. Forster R. J., Keane L. Nanoparticle–metallopolymer assemblies: charge percolation and redox properties. *Journal of Electroanalytical Chemistry*. 2003;554-555: 345–354. https://doi.org/10.1016/S0022-0728(03)00258-4

16. Shel'deshov N. V., Mel'nikov S. S., Solov'eva T. T., … Zabolotskii V. I. The effect of silver ions and nanoparticles on the properties of ion-exchange materials. *Russian Journal of Electrochemistry*. 2011;47(2): 200–208. https://doi.org/10.1134/s1023193511020157

17. Chaika M. Yu., Kravchenko T. A., Polyanskii L. N., Krysanov V. A. Electroreduction of molecular oxygen on dispersed copper in an ion-exchange matrix. *Russian Journal of Electrochemistry*. 2008;44(11): 1244–1250. https://doi.org/10.1134/s1023193508110086

18. Yaroslavtsev A. B. Correlation between the properties of hybrid ion-exchange membranes and the nature and dimensions of dopant particles. *Nanotechnologies in Russia*. 2012;7(9–10): 437–451. https://doi.org/10.1134/s1995078012050175

19. Gattrell M., MacDougall B. Reaction mechanisms of the O_2 reduction/evolution reaction. In book: Handbook of Fuel Cells – Fundamentals, Technology and Applications.

Vol. 2. Part 5. Electrocatalysis. John Wiley & Sons; 2003. p. 443-464. https://doi.org/10.1002/9780470974001.f205034

20. *PEM Fuel Cell Electrocatalysts and Catalyst Layers. Fundamentals and Applications*. J. Zhang (ed.). Springer; 2008. 1137 p.

21. Semenova I. V., Florianovich G. M., Khoroshilov A. V. *Corrosion and corrosion protection*. I. V. Semenova (ed.). Moscow: Fizmatlit Publ.; 2002. 336 p. (in Russ.)

22. Volkov V. V., Petrova I. V., Yaroslavtsev A. B., Tereshchenko G. F. Deep purification of water from dissolved oxygen for microelectronics, power plants and the food industry*. *Russian Membrane Society website*. (in Russ.). Available at: http://memtech.ru/index.php/ru/glavnaya/publications/200-udalenie-kisloroda-iz-vody

23. SanPiN 2.1.3684-21 *"Sanitary and epidemiological requirements for the maintenance of the territories of urban and rural settlements, water bodies, drinking water and drinking water supply, atmospheric air, soils, residential premises, operation of industrial and public premises, organization and implementation of sanitary and anti-epidemic (preventive) measures*."* 66 p. (in Russ.)

24. SanPiN 1.2.3685-21 "*Hygienic standards and requirements for ensuring the safety and (or) harmlessness of environmental factors for humans*."* 1143 p. (in Russ.)

25. On the state of sanitary and epidemiological well-being of the population in the Russian Federation in 2022. *State report*. Moscow: Federal Service for Surveillance on Consumer Rights Protection and Human Welfare, 2023. 368 p. (in Russ.)

26. Report *"On the state of sanitary and epidemiological well-being of the population in the Voronezh region in 2023*"*. Voronezh: Office of the Federal Service for Surveillance on Consumer Rights Protection and Human Wellbeing in the Voronezh Region, 2024. 199 p. (in Russ.)

27. Gurskii V. S., Kirpikov D. A., Kharitonova E. Yu., Tsapko Yu. V., Yasnev I. M. Catalytic deoxygenation of high-purity water using membrane electrode units. *Russian Journal of Applied Chemistry*. 2015;88(10): 1656–1660. https://doi.org/10.1134/s107042721510016x

28. Kirpikov D. A., Pykhteev O. Ju., Kharitonova E. Ju., Tsapko Ju. V., Chistjakov I. V., Gurskij V. S. *Device for electrochemical deoxygenationof highly pure water*. Patent RF, no. 2494974, 2012. Publ. 10.10.2013, bull. no. 28. 9 p. (in Russ.)

29. Kravchenko T. A., Zolotukhina E. V., Chaika M. Yu., Yaroslavtsev A. B. *Electrochemistry of metal-ion exchanger nanocomposites*. Moscow: Nauka Publ.; 2013. 363 p. (in Russ.)

30. Fertikova T. E., Fertikov S. V., Isaeva E. M., Krysanov V. A., Kravchenko, T. A. New nanocomposites for deep water deoxygenation. *Condensed Matter and Interphases*. 2021;23(43): 614–625. https://doi.org/10.17308/kcmf.2021.23/3682

31. Vakhnin D. D., Fertikova T. E., PolyanskiL. N., Kozaderov O. A., Kravchenko T. A. On the electrochemical deoxygenation of water with a nanocomposite containing copper metal nanoparticles and an ion-exchange polymer matrix. *Nanobiotechnology Reports*. 2022;17(6): 766–773. https://doi.org/10.1134/s2635167622060143

32. *Ion exchange resins. Cationites*. Specifications: GOST 0298-2022. Moscow: FGBU «RST»; 2022. 16 p. (in Russ.)

33. Kravchenko T. A., Kalinichev A. I., Polyansky L. N., Konev D. V. *Metal-ion exchanger nanocomposites*. Moscow: Nauka Publ.; 2009. 392 p. (in Russ.)

34. Damaskin B. B., Petriy O. A., Tsirlina G. A. *Electrochemistry: A Textbook*. 3rd ed., corrected. St. Petersburg: Lan' Publ.; 2021. 672 p. (in Russ.)

** Translated by author of the article*

Information about the authors

Dmitry D. Vakhnin, postgraduate student, Department of Physical Chemistry, Voronezh State University (Voronezh, Russian Federation).

vakhnin.dima@rambler.ru

Tatyana E. Fertikova, Cand. Sci. (Med.), Associate Professor, Department of General Hygiene, Voronezh State Medical University (Voronezh, Russian Federation).

https://orcid.org/0000-0002-4370-9197

tefertikova@vrngmu.ru

Natalya A. Zheltoukhova, master's Student, Department of Physical Chemistry, Voronezh State University (Voronezh, Russian Federation).

zheltoukhova.natali@yandex.ru

Tamara Aleksandrovna Kravchenko, Dr. Sci. (Chem.), Full Professor, Department of Physical Chemistry, Voronezh State University (Voronezh, Russian Federation).

https://orcid.org/0000-0001-9214-7357

krav2809837@yandex.ru

Oleg Aleksandrovich Kozaderov, Dr. Sci. (Chem.), Associate Professor, Leading Researcher, Laboratory of organic additives for the processes of chemical and electrochemical deposition of metals and alloys used in the electronics industry, Voronezh State University (Voronezh, Russian Federation).

https://orcid.org/0000-0002-0249-9517

ok@chem.vsu.ru

Received January 28, 2025; approved after reviewing February 14, 2025; accepted for publication March 17, 2025; published online December 25, 2025.

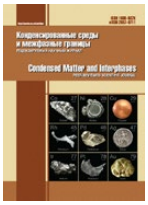

ISSN 1606-867X (Print)
ISSN 2687-0711 (Online)
Condensed Matter and Interphases
Kondensirovannye Sredy i Mezhfaznye Granitsy
https://journals.vsu.ru/kcmf/

Original articles

Research article
https://doi.org/10.17308/kcmf.2025.27/13297

Simulation of a non-stationary electrochemical process on rough electrodes under mixed kinetic-diffusion control

F. A. Vdovenkov, A. N. Kolosov, G. A. Kuzmenko, O. A. Kozaderov✉

Voronezh State University,
1 Universitetskaya pl., Voronezh 394018, Russian Federation

Abstract

Objectives: In this work, the effect of electrode surface roughness on the rate of a transient electrochemical process under mixed transport-kinetic control is established. A mathematical model of the electrochemical process occurring on an electrode with a rough surface and characterized by a different ratio of the rate constant of the charge transfer stage and the coefficient of non-stationary bulk diffusion is constructed.

Experimental: Using the numerical method of finite element modeling, chronoamperograms of a transient electrochemical process were obtained under conditions of mixed transport and kinetic control on electrodes with different surface profiles defined by harmonic and fractal functions. The transient "roughness function - time" curves are calculated and the boundaries of the transition region are determined, within which it varies from the roughness factor to unity. It is found that the shape of the chronoamperogram depends in a complex way both on the geometric characteristics of the rough surface and on the ratio of the diffusion-kinetic parameters of the process. With relatively short durations, the gross process rate is equal to the charge transfer rate at a given potential and is proportional to the roughness factor. With relatively long durations, the chronoamperogram transforms into a current decay curve of the diffusion-controlled process, while the effect of roughness is nonlinear in this case and manifests itself only with relatively short process durations. Under these conditions, the thickness of the diffusion layer is much smaller than the size of the irregularities, and the rate of the process on the rough electrode is proportional to the true surface area and roughness factor.

Conclusions: The position of the transition region depends on the value of the rate constant of the charge transfer: in the case of a slow kinetic stage, the transition manifests itself over increasingly long periods and gradually widens, while depending on the geometric shape of the irregularity.

Keywords: Electrode process, Mixed kinetics, Roughness factor, Chronoamperogram, Finite element method, Roughness function, Harmonic profile, Fractal function

Funding: The study received financial support from the Ministry of Science and Higher Education of the Russian Federation within the framework of State Contract with universities regarding scientific research in 2025–2027, project No. FZGU-2025-0001.

For citation: Vdovenkov F. A., Kolosov A. N., Kuzmenko G. A., Kozaderov O. A. Simulation of a non-stationary electrochemical process on rough electrodes under mixed kinetic-diffusion control *Condensed Matter and Interphases*. 2025;27(4): 592–605. https://doi.org/10.17308/kcmf.2025.27/13297

Для цитирования: Вдовенков Ф. А., Колосов А. Н., Кузьменко Г. А., Козадеров О. А. Моделирование нестационарного электрохимического процесса на шероховатых электродах в условиях смешанного транспортно-кинетического контроля. *Конденсированные среды и межфазные границы*. 2025;27(4): 592–605. https://doi.org/10.17308/kcmf.2025.27/13297

✉ Oleg A. Kozaderov, e-mail: ok@chem.vsu.ru

1. Introduction

Morphological irregularity, or geometric heterogeneity of the electrode surface, is one of the most important factors affecting the kinetics of electrochemical processes. The shape, size, and distribution of irregularities along the electrode/solution interface are of both practical and fundamental importance. For example, in microelectronics, they strongly influence the efficiency and modes of implementation of TSV (through silicon vias) technology, when uniform electrodeposition of copper onto an electrode of complex macrogeometric configuration is required [1, 2]. In both theoretical and applied electrochemistry, the microgeometry of the surface, or the roughness of the electrode, plays an important role [3]. The roughness effect is most complexly manifested in the case of a tertiary current distribution, when concentration gradients form in an electrochemical system, and the mass transfer stage makes a significant contribution to the rate of a multi-stage heterogeneous electrode process. When studying the kinetics of such processes on solid electrodes, it is necessary to take into account that their roughness factor always differs from unity, since their surface is rough regardless of pretreatment. The roughness factor f_r is the ratio of the true area S, which is equal to the sum of the areas of all irregularities, to the geometric (visible) area S_g corresponding to the projection of the electrode boundary [4]:

$$f_r = S/S_g. \quad (1)$$

As a result, the extensive parameters of electrode reactions, corrosion processes, double electric layer, and adsorption are proportional to the area of the electrode/solution interface. At the same time, the influence of roughness on such parameters is often very significant. Thus, in double-layer phenomena, the roughness of the electrode leads to a large increase in the accumulated charge [5] and significantly reduces the interfacial resistance [6], which indicates that strongly roughened electrodes are promising for use in supercapacitor technology [7], where an increase in energy density is crucial. To reduce the effectiveness of the corrosion process, on the contrary, it is important to reduce the surface roughness of the electrode [8–11].

In order to correctly compare the extensive electrochemical parameters of various systems and processes with each other, they should generally be normalized to the area of the electrode/solution interface. However, the procedure for such normalization is not trivial, especially in the case of non-stationary electrochemical measurements, and it is far from always reduced to a simple division based on the area of the true surface of the electrode $S > S_g$, and normalization based on the area of the visible surface is generally applicable only in the case of liquid electrodes, since only they are perfectly smooth, so for them $S = S_g$. In [12–14], we theoretically substantiated and developed an algorithm for accounting for the effect of non-fractal, fractal, and statistically irregular roughness in the kinetics of diffusion-controlled processes. Within the framework of a number of theoretical models describing the electrode process, when the diffusion mass transfer stage is slow, and the charge transfer stage is very fast, it has been shown that the ratio of the thickness of the diffusion layer and the average size of the rough surface irregularities play a decisive role. It should be noted that most of the theoretical models available in the literature in non-stationary systems with rough electrodes have been developed specifically for reversible electrode processes, the limiting stage of which is diffusion mass transfer [15–17].

However, the kinetics of electrode processes are often not purely diffusive and/or the roughness effect is not limited to a geometric increase in the area of the electrochemically active surface. For example, the use of rough sensor electrodes allows for a higher sensitivity of electrochemical sensors not only due to an increase in area [18, 19], but also surface activity, which in the case of a rough surface is usually higher due to an increase in the number of active sites [20] or certain functional groups [21]. Such a dual effect of roughness plays a special role in the kinetics of electrocatalytic processes, since a correct estimation of the properties of an electrocatalyst requires a separation of the two effects: 1) an increase of its activity in a particular electrode reaction, and 2) an extensive rise in current due to an increase in the true surface area of the electrode. Otherwise, the estimation of electrocatalytic activity may

lead to incorrect results, since the current density after normalization to the true surface area may be unchanged compared to a smooth electrode [22]. Therefore, it is urgent to identify a purely geometric roughness effect in the study of electrochemical processes occurring in the mixed transport-kinetic control, when the rates of the kinetic and diffusion stages are comparable.

The range of practically significant electrochemical processes occurring under mixed transport-kinetic control is quite wide, and for many of them a noticeable effect of roughness on the kinetics of the process has been revealed. For instance, a complex multi-stage process of cathodic reduction of CO_2 is morphologically sensitive, for which an enhancement in the efficiency of the electrochemical conversion of carbon dioxide into formic acid with an increase in the roughness of the electrode was found in [23, 24]. However, a procedure for the correct accounting of geometric roughness for such processes using non-stationary electrochemical methods (chronoampero-, chronopotentio-, and chronovoltamperometry) has not been developed. This is because the corresponding diffusion-kinetic problems have not been solved with different ratios of the charge transfer rate constant and the diffusion coefficient, which determine the contributions of kinetic and diffusion stages to the overall rate of the electrochemical process occurring on the surface of a rough electrode.

The purpose of the work is to establish the effect of electrode surface roughness on the rate of a non-stationary electrochemical process under mixed transport-kinetic control and potentiostatic polarization.

The objectives are as follows:

1. To obtain the theoretical chronoamperograms of an electrochemical process taking place in the mixed kinetics mode on a perfectly smooth flat surface of an electrode, as well as on surfaces with harmonic and fractal profiles with a given roughness factor and with a different ratio of the diffusion coefficient and the kinetic stage rate constant.

2. To calculate the roughness functions for the studied electrode surface profiles and various ratios of the diffusion coefficient and the rate constant of the kinetic stage.

3. By comparing the roughness functions obtained for different surface profiles, to identify the role of the shape of surface irregularities of a harmonic or fractal type, the surface roughness factor, as well as the ratio of contributions from the diffusion and charge transfer stages, in the potentiostatic current transient of the electrochemical process occurring under a mixed transport-kinetic control.

2. Formulation of the diffusion-kinetic problem and the method of computational experiment

The main task of the simulation was to find the spatiotemporal concentration profile of the electrochemically active diffusant *Ox*, a participant in the two-stage electrode process:

$$Ox^{v} \xrightarrow[D]{\text{diffusion}} Ox^{s} + ne^{-} \xrightarrow[k]{\text{charge transfer}} Red^{s}, \quad (2)$$

proceeding under a mixed transport-kinetic control on a rough (f_r = const) electrode/solution interface. The stages of non-stationary diffusion mass transfer and charge transfer are quantitatively characterized by certain values of the diffusion coefficient D (cm^2/s) and the charge transfer rate constant k (cm/s), respectively. Based on the ratio of these parameters, more precisely, based on the value of a dimensionless complex parameter k^2t/D in the case of a perfectly smooth flat electrode, one can judge the contribution of a particular stage to the kinetics of the process. The corresponding dependence of the process (2) rate on time, expressed in current units (chronoamperogram), for the potentiostatic conditions of electrode polarization, i.e. at constant overvoltage, η = const, is described by the following expression [25]:

$$i(t)_{\text{flat}} = nFkc^{v} \cdot \exp\left(k^2t/D\right) \cdot \operatorname{erfc}\left(kt^{1/2}/D^{1/2}\right). \quad (3)$$

Here F is the Faraday number (96485 C/mol), c^v is the bulk (initial) concentration of *Ox* in the electrolyte solution. In the limiting case, when the rate constant of the charge transfer stage (and the exchange current proportional to it) is very high, i.e. the parameter $k^2t/D \gg 1$, equilibrium is quickly established during the second stage of the electrode process (2), therefore, the rate is limited by diffusion mass transfer, and the chronoamperogram is described by the Cottrell equation [25]:

$$i(t)_{\text{Cottrell}} = \frac{nFD^{1/2}c^{\text{v}}}{(\pi t)^{1/2}}. \quad (3a)$$

On the contrary, if the kinetic stage is slowed down, which is performed using very small parameters $k^2t/D \ll 1$, then the rate of the electrode process does not change over time, but is determined by the overvoltage:

$$i(\eta) = nFk(\eta)c^{\text{v}}. \quad (3b)$$

In this work, the chronoamperograms of the process (2) were calculated in a wide range of k^2t/D values for electrodes with a rough surface. The rough interphase boundary was represented as a two-dimensional surface corrugation of three different types: non-fractal, fractal, and statistically irregular. Non-fractal surface profiles (sinusoidal, sawtooth, trapezoidal, and a system of single projections) were modeled using various harmonic functions with a characteristic wavelength λ equal to the distance between adjacent irregularities [13]. Fractal surface profiles were modeled using a range-limited continuous modified one-dimensional Weierstrass function [3, 14, 26, 27]. A statistically irregular surface profile modeled using the Weierstrass–Mandelbrot random fractal function [14, 28, 29] most accurately reflected the real surface of a solid electrode. A feature of both fractal and statistically irregular surfaces is the dispersion of the characteristic wavelengths of irregularities in the range from minimum λ_{min} to maximum λ_{max}, inherent in the vast majority of solid surfaces. The method of mathematical modeling of the studied surface profiles is described in detail in [13, 14].

An electrolyte solution with a bulk concentration of diffusant c^{v} undergoing electrochemical transformation according to scheme (2) under potentiostatic cathodic polarization is considered as a model electrochemical system. The concentration of the diffusant in this case obeys the differential equation of Fick's second law:

$$\frac{\partial c}{\partial t} = D\nabla^2 c \quad (4)$$

with the initial condition

$$c\big|_{t=0} = c^{\text{v}} \quad (5)$$

and the first boundary condition

$$c\big|_{z\to\infty} = c^{\text{v}}. \quad (6)$$

It was assumed that the charge transfer stage is irreversible ($\vec{k} \gg \overleftarrow{k}$), i.e. *Red* oxidation has no effect on the overall rate of the process. In this case, the second boundary condition is valid, written in the following form:

$$D\frac{\partial c}{\partial \vec{n}}\bigg|_S = kc_S,$$

which is a condition for continuity of flux at the interface (*S*) and implies equality of the rate of charge transfer $\upsilon = kc_S$ and the density of the diffusion flux $j(t)\big|_S = D\frac{\partial c}{\partial \vec{n}}\Big|_S$ along the normal to the surface ($\vec{n}$). The diffusion flux density $j(t)\big|_S$ per unit geometric surface area of the electrode was calculated using the numerical finite element method [30] using the COMSOL Multiphysics software platform [31–34] for the following process parameters: bulk concentration of diffusant c^{v} = 1 mol/m^3; number of electrons n = 1; temperature 298 K; diffusion coefficient: 10^{-6} cm^2/s; overvoltage: –0.1 V; the distance between adjacent irregularities (characteristic wavelength of the profile) of the rough electrode is λ = 10^{-3} m. The value of the charge transfer rate constant varied in a wide range from 10^{-8} to 1 cm/s. The current density was calculated using the formula:

$$i(t)_{\text{rough}} = nF\, j(t)\big|_S. \quad (8)$$

The effect of morphological heterogeneity of the electrode surface on the mixed kinetics of the electrochemical process (2) was analyzed using the roughness function:

$$\varphi = \frac{i(t)_{\text{rough}}}{i(t)_{\text{flat}}}. \quad (9)$$

Here $i(t)_{\text{flat}}$ is the current density calculated by the formula (3), $i(t)_{\text{rough}}$ – current density found in COMSOL Multiphysics by numerical simulation. Obviously, if $i(t)_{\text{rough}} = i(t)_{\text{flat}}$, then the roughness function is equal to the roughness factor f_{r}, which is determined by formula (1). The transient current density $i(t)_{\text{rough}}$ was numerically calculated for different values of the dimensional-kinetic complex:

$$k_D = \frac{k}{D}\lambda, \quad (10)$$

the value of which can be used to judge the ratio of the contributions of the diffusion and kinetic stages to the rate of the overall process in the case of rough electrodes. The transient of the roughness function is represented in dimensionless coordinates $\varphi - Dt/\lambda^2$, which makes it possible to determine how many times at a given time the rate of the process (2) on a morphologically inhomogeneous electrode is higher due to the presence of irregularities on it compared to a perfectly smooth flat electrode. The use of the roughness function and the dimensionless parameters of the system (k_D, Dt/λ^2, k^2t/D) makes it possible to evaluate the role of roughness in the kinetics of electrochemical processes occurring under mixed transport-kinetic control, with a different ratio of the contributions of the stages of diffusion mass transfer and charge transfer to the overall rate of the process. The relative contribution of a particular stage is determined by the value of the dimensional-kinetic complex k_D, at the limiting values of which diffusion ($k_D \gg 1$) or kinetic ($k_D \ll 1$) control is realized. In this work, the simulation was carried out in a wide range of k_D values from 10^{-3} to 10^5.

During the preliminary stage of simulation, using the example of a perfectly smooth flat electrode, the adequacy of the numerical simulation results was verified by comparing it with the known exact solution described by the mathematical function (3) obtained in [25] by the analytical method of Laplace transformation. Fig. 1 presents logarithmic dimensionless Y,τ-chronoamperograms ($Y = \frac{i}{nFkc^v}$, $\tau = Dt/\lambda^2$) for an electrochemical process proceeding under mixed transport-kinetic control on a perfectly smooth flat electrode, obtained by equation (3) (solid lines), as well as calculated by the finite element method in the COMSOL Multiphysics program (markers). As expected, the calculated chronoamperograms have two linear sections in bilogarithmic coordinates. The first (horizontal) section corresponds to the slowed down stage of charge transfer, and formula (3b). The second section has a slope of $d\lg Y/d\lg\tau = -1/2$, which corresponds to the slowed down diffusion stage and the Cottrell equation (3a). The calculation showed that the results obtained by two methods, analytically and numerically, completely coincide, which makes it possible to use this approach for more complex systems with a rough electrode/solution interface.

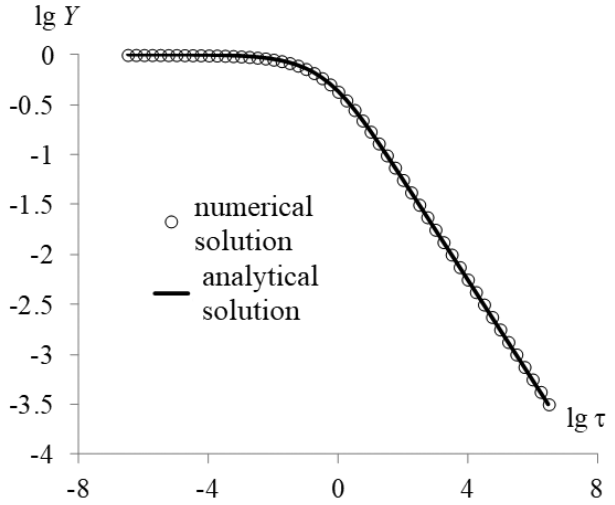

Fig. 1. Chronoamperograms of a non-stationary electrochemical process (1) on a flat electrode obtained by numerical and analytical methods for the mixed transport-kinetic control mode

3. Results and discussion

Harmonic roughness. Typical chronograms of the roughness function for electrodes, the surface of which is modeled by harmonic functions, are shown in Fig. 2. It turned out that for relatively large values of the dimensional-kinetic complex $k_D \geqslant 1$, the curve coincides with a similar dependence obtained earlier for processes controlled by the stage of non-stationary diffusion mass transfer [13]. This situation occurs with high values of the rate constant of the charge transfer stage and/or low values of the diffusion coefficient. The shape of the chronogram is quite indicative: for dimensionless time values $Dt/\lambda^2 < 10^{-3}$, the roughness function φ is equal to the roughness factor f_r (formula (1)). This means that the current density on a rough electrode is f_r times higher than on a flat electrode, i.e. $i(t)_{\text{rough}} = i(t)_{\text{flat}} \cdot f_r$, therefore, in this case, additional normalization of the experimental current density value by the roughness factor is necessary to correctly estimate the process speed. If $Dt/\lambda^2 > 1$, then the roughness function is equal to one, therefore

$i(t)_{\text{rough}} = i(t)_{\text{flat}}$, and roughness accounting is not required.

In another limiting case, when the value of the dimensional-kinetic complex k_D is very small (curve *1* in Fig. 2), during the entire period of transient measurements, the roughness function is equal to the roughness factor. As expected, if the kinetics of the process is purely electrochemical (k_D << 1), the current density should always be normalized by the roughness factor.

The position and shape of the chronograms of the roughness function with intermediate values of the dimensional-kinetic complex k_D, i.e. for the mixed-kinetic control, depends on the ratio of the charge transfer rate constant and the diffusion coefficient, therefore, on the contribution of one stage or another to the rate of the electrochemical process. As the rate constant k increases, i.e. as the kinetic stage accelerates, a transition region appears on the chronogram of the roughness function, the position and duration of which depends on the dimensional-kinetic complex k_D: as it decreases, the transition region appears, firstly, with increasing durations, and secondly, it gradually widens. This effect is also confirmed by analyzing similar dependences of the roughness function on time found for different harmonic roughness factors (Fig. 3). It can be seen that the higher the f_r, the greater the value of the roughness function with short durations. In turn, with a decrease in k_D, the area of constancy of the roughness function is noticeably widened.

Since the roughness function is the ratio of currents on a rough and flat electrode, the

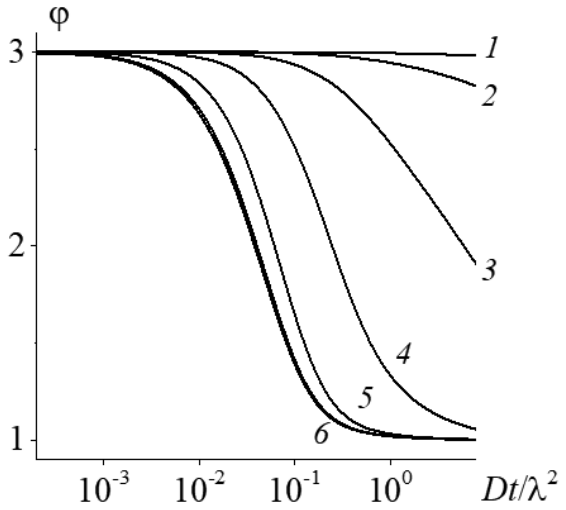

Fig. 2. Chronograms of the roughness function for an unsteady electrochemical process operating in mixed transport-kinetic control mode on an electrode with a sinusoidal surface (f_r = 3) for different values of the dimensional-kinetic complex $k_D = 10^{-5}$ (*1*), 10^{-4} (*2*), 10^{-3} (*3*), 10^{-2} (4), 10^{-1} (*5*), ⩾1 (*6*)

described effects are reflected in the form of chronoamperograms, which are shown in Fig. 4 for different values of the dimensional-kinetic complex k_D in comparison with similar curves for a perfectly smooth flat electrode.

It can be seen that if $k_D \gg 1$ (diffusion kinetics, Fig. 4a), then the chronoamperogram over the entire time range is a current decay curve, partially (with short and long durations) straightening in double logarithmic coordinates with a slope $d\lg i/d\lg t = -1/2$, which corresponds to the Cottrell equation (3a). At the same time, in the region with short durations, the currents on

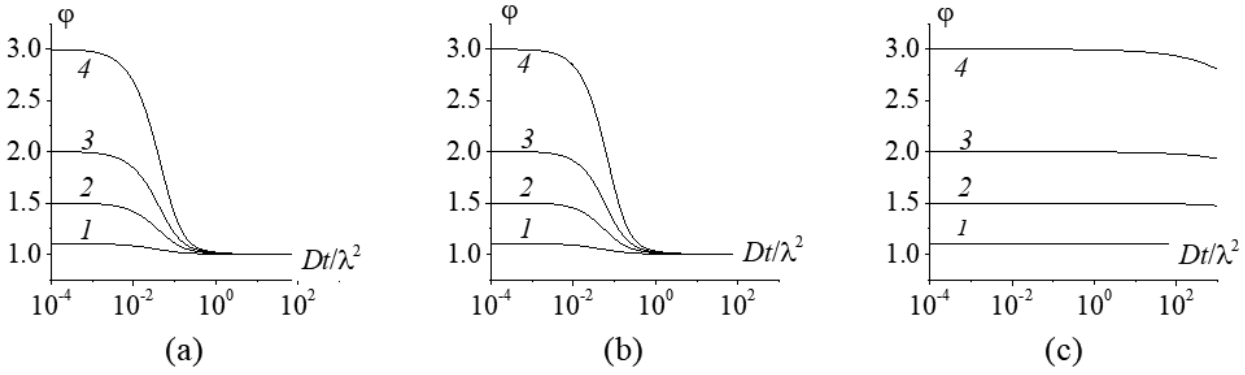

Fig. 3. Transients of the roughness function calculated for a sinusoidal surface profile for different values of the roughness factor f_r = 1.1 (*1*), 1.5 (*2*), 2.0 (*3*), 3.0. (*4*) and the dimensional kinetic complex $k_D = 10^5$ (a), 10 (b), 10^{-3} (c)

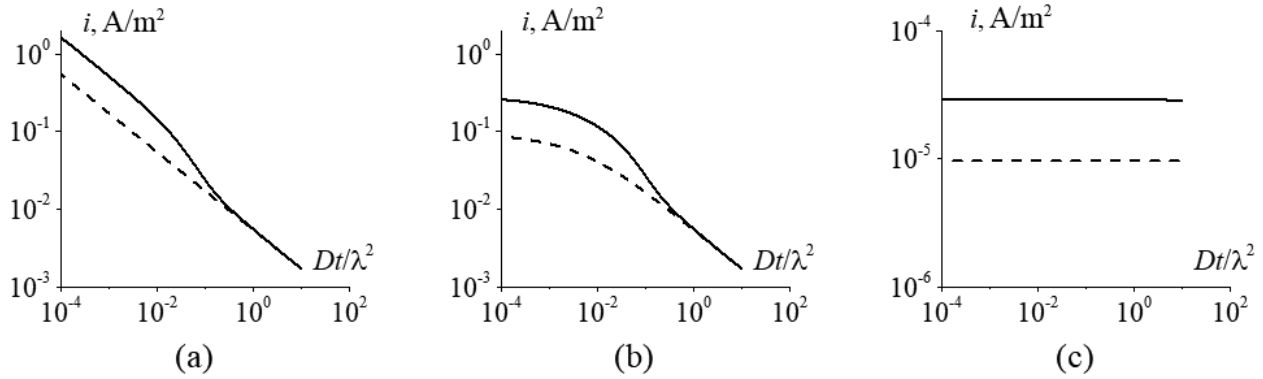

Fig. 4. Chronoamperograms of a non-stationary electrochemical process occurring in mixed transport-kinetic control mode on an electrode with a sinusoidal surface (f_r = 3) for different values of the dimensional-kinetic complex $k_D = 10^5$ (a), 10 (b), 10^{-3} (c). Dotted lines are chronoamperograms for an ideal smooth flat electrode

the rough electrode are f_r times higher than on the flat one, and with long durations, the curves for both electrodes, on the contrary, coincide.

If $k_D \ll 1$ (electrochemical kinetics, Fig. 4b), then in almost the entire time interval the process proceeds under kinetic control, so the current density takes a constant value corresponding to a given overvoltage. In this case, the ratio of currents on the rough and flat electrodes is equal to the roughness factor during the entire period of transient measurements.

In the intermediate range of values of the dimensional-kinetic complex k_D, the chronoamperogram takes on the most complex and non-trivial form. With short durations, chronoamperograms on both rough and flat electrodes are nonlinear in double logarithmic coordinates, since the mixed transport-kinetic control is implemented. The region of *i* relative constancy, when the contribution of the charge transfer stage to the kinetics is large enough, is replaced by a decrease in current caused by an increase in concentration polarization. The ratio of currents on rough and flat electrodes in a given time interval is equal to the roughness factor. Over time, the bilogarithmic curves of the rough and flat electrodes gradually converge, as the contribution of the kinetic stage decreases. With long durations, both chronoamperograms coincide and are linearized in accordance with the Cottrell equation (3a): the control completely passes to the stage of diffusive mass transfer.

Thus, when studying the kinetics of processes characterized by comparable rates of diffusion and kinetic stages on solid rough electrodes, it is necessary to take into account the complex, non-linear and non-stationary effect of electrode roughness on the current density recorded during the experiment. As a result, the normalization procedure for the roughness factor is not always reduced to a simple division by the roughness factor, and under certain conditions is not necessary at all. Correct consideration of the roughness effect in such cases requires a preliminary estimation of the k_D value, which means necessity of the exchange current, diffusion coefficient, and estimated average size of the irregularities.

The potentiostatic response of the rough electrode on the surface of which the process (2) is taking place can be interpreted using data on the concentration distribution near the rough electrode/solution interface. Figures 5 and 6 show the concentration profiles of the electroactive diffusant *Ox*, calculated for the value of the dimensional-kinetic complex k_D = 10 in the time range from 30 to 10^4 s, i.e. over a wide range of values of the complex diffusion-kinetic parameter k^2t/D from 0.3 to 10^2. It can be seen that only with short durations the diffusion front completely repeats the surface profile, and over time, the sensitivity to irregularities is leveled, and the diffusion front is smoothed out. As a result, only when $k^2t/D < 1$, the density of the diffusion flux, and hence the current density, should be normalized to the roughness factor. Obviously, such a situation can occur over a fairly wide time range, but only if the charge transfer rate constant is so small that the electrode process (2) is almost completely controlled by the electrochemical stage, as is observed in Fig. 4c.

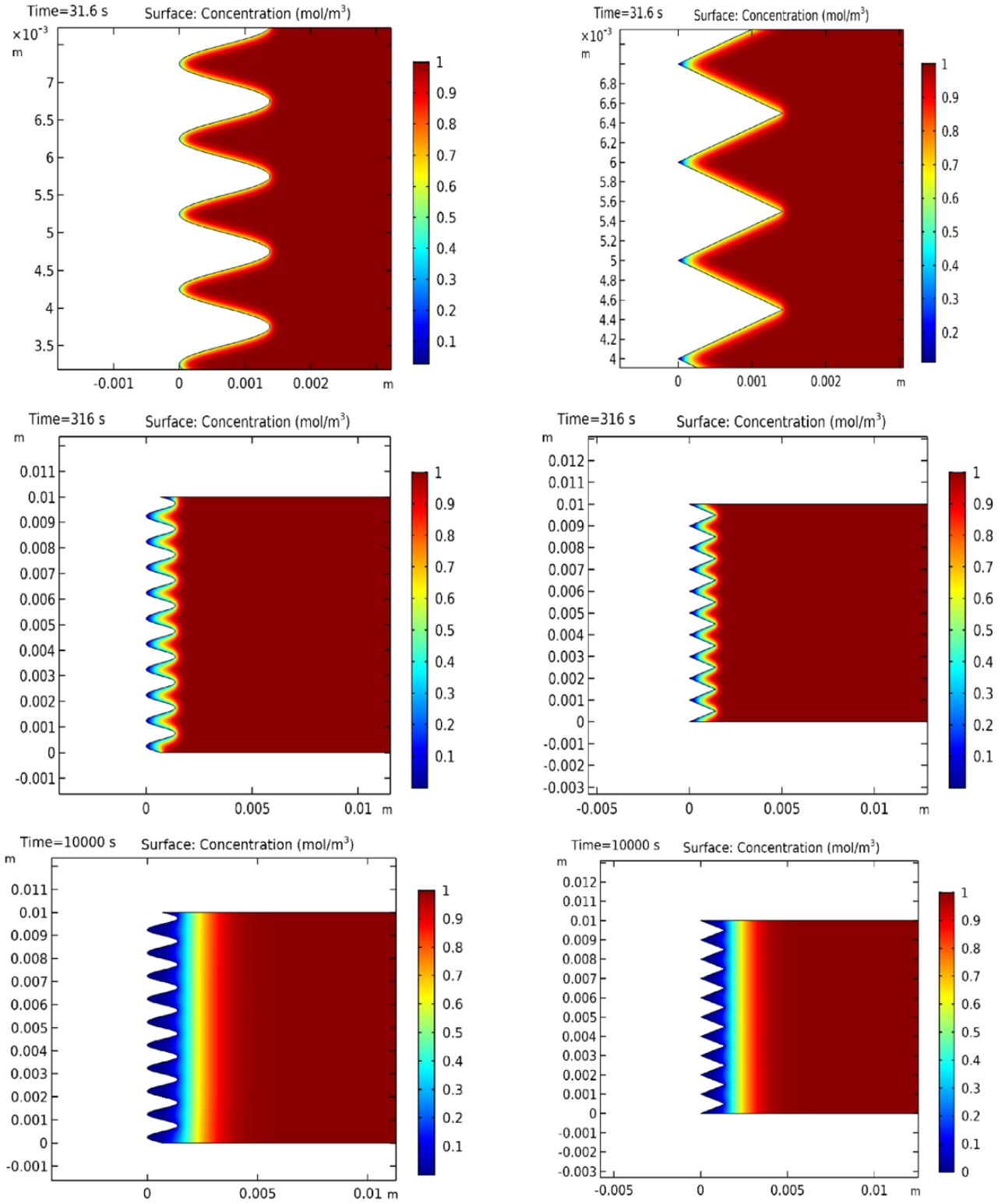

Fig. 5. The concentration field of a diffusant near a sinusoidal and sawtooth surface (f_r = 3) during a non-stationary potentiostatic process in mixed transport-kinetic control mode with different durations. The dimensional-kinetic complex k_D = 10

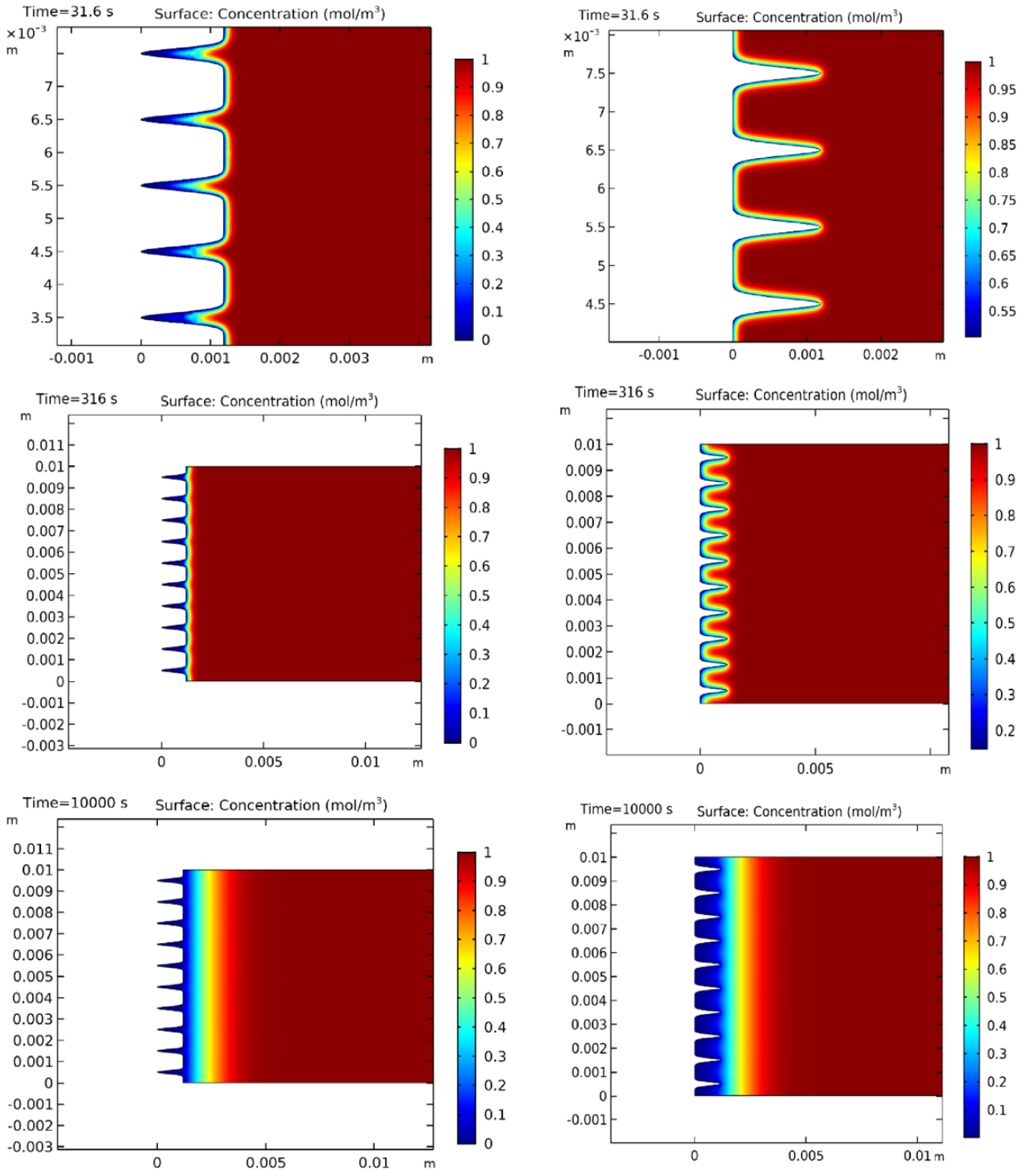

Fig. 6. The concentration field of a diffusant near single protrusions and a trapezoidal surface (f_r = 3) during a non-stationary potentiostatic process in mixed transport-kinetic control mode with different durations. The dimensional-kinetic complex k_D = 10

Comparative analysis has shown that the difference in transients of roughness functions of different harmonic types is quite noticeable (Fig. 7), although it decreases with decreasing size-kinetic complex k_D. At $k_D \ll 1$, the chronograms coincide, which indicates that under conditions of purely electrochemical control, the determining role is played not by the shape of the micro irregularities, but by the macrogeometric parameter, i.e. by the roughness factor. Considering that the real surface profile of a solid electrode usually consists of a set of harmonics of various sizes and shapes, the roughness effect was modeled using fractal and statistically irregular functions. The fact is that their use makes it possible to describe the morphology of the electrode/solution interface as realistically as possible [14], since the profiles constructed according to these mathematical functions are a combination of various irregularities, the average lateral size of which lies in a given range from λ_{min} to λ_{max}.

Fractal and statistically irregular roughness. Figure 8 shows the chronograms of the roughness function for a non-stationary electrochemical process proceeding under mixed transport and kinetic control on model surfaces defined by the fractal Weierstrass function and the statistically rough Weierstrass-Maldenbrot function. As in the case of the process on harmonic-type surfaces, for relatively small values of k_D, a horizontal section is formed on the current decay curves, within which the function $\varphi = f_r$. The duration of this section increases with a decrease in k_D, i.e. with a decrease in the rate constant of the charge transfer stage and/or an increase in the diffusion coefficient.

A distinctive feature of the chronograms of roughness functions for fractal and statistically irregular surfaces is a significant broadening of the transition region compared to roughened electrodes with a harmonic-type surface. This effect is probably due to the presence of irregularities of various sizes on the surface. Indeed, the average distance between adjacent irregularities in the case of both fractal and statistically irregular surfaces lies in the range $\lambda_{min} < \lambda < \lambda_{max}$ [14], while harmonic profiles are characterized by the absence of a distribution of irregularities in their size (λ = const).

This effect can be explained by analyzing the concentration profiles of an electrochemically active diffusant near the fractal and statistically irregular electrode surface, calculated for k_D = 10 in the time range t from 0.5 to $5 \cdot 10^4$ s, i.e. over a wide range of values of the diffusion-kinetic parameter k^2t/D (Fig. 9). It can be seen that with short durations, the diffusion front completely repeats the profile of the surface with a minimum wavelength (λ_{min}). However, over time, the sensitivity to such irregularities decreases, and therefore the diffusion front gradually smooths out, taking the form of a longer-wavelength harmonic, until at some point it coincides in shape with the profile with the maximum wavelength (λ_{max}), after which it quickly becomes flat.

The described changes in the shape of the diffusion front lead to a gradual decrease in its area, and consequently, the flow and the roughness function over time. In contrast to the φ obtained for surfaces defined by harmonic

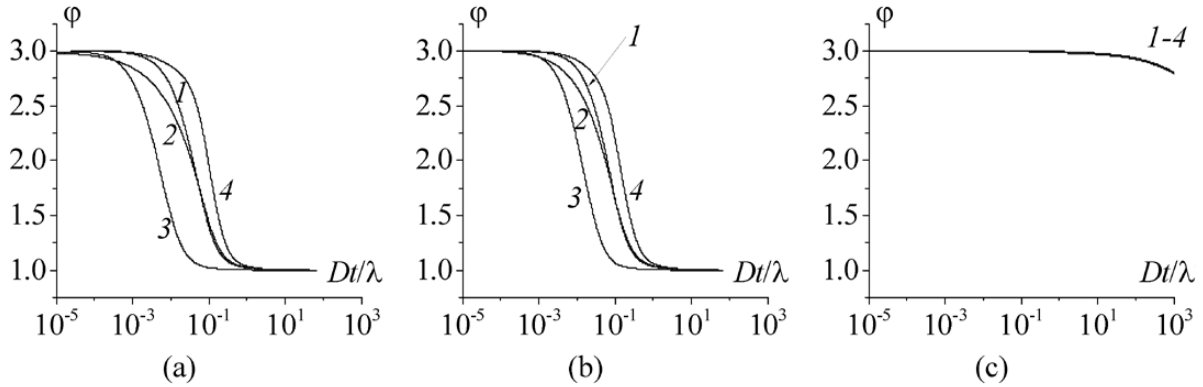

Fig. 7. Transients of the roughness function calculated for different harmonic surface profiles: sinusoidal (*1*), sawtooth (*2*), trapezoidal (*3*), a system of single protrusions (*4*) with a roughness factor f_r = 3 for the values of the dimensional kinetic complex $k_D = 10^5$ (a), 10 (b), 10^{-3} (c)

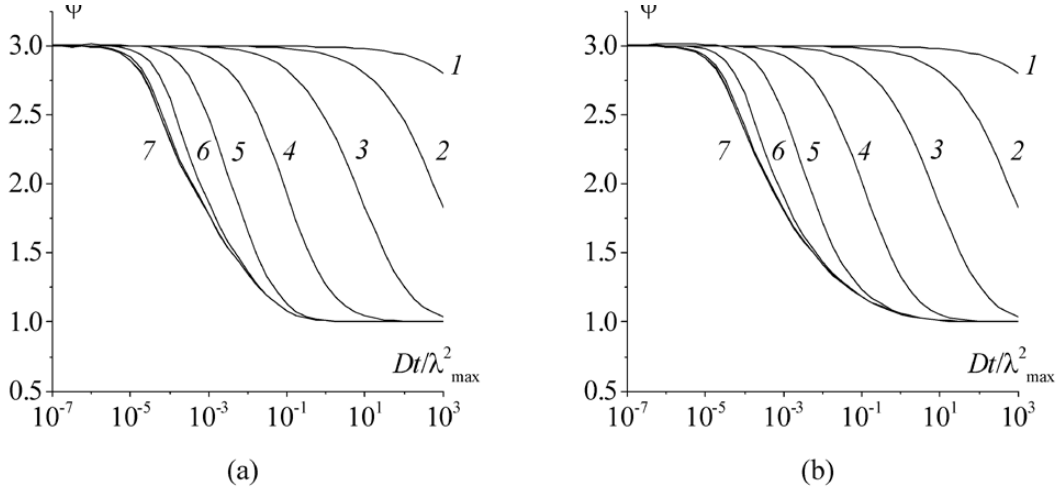

Fig. 8. Transients of the roughness function (f_r = 3.0) calculated for fractal (a) and statistically irregular (b) surfaces for different values of the dimensional-kinetic complex $k_D = 10^{-3}$ (*1*), 10^{-2} (*2*), 10^{-1} (*3*), 1 (*4*), 10^{1} (*5*), 10^{2} (*6*), $\geq 10^{3}$ (*7*)

functions, the transition region in the case of Weierstrass and Weierstrass-Mandelbrot profiles is characterized by significant broadening not only at low k_D corresponding to the purely electrochemical kinetics of the process (2), but also at values of the dimensional kinetic complex valid for diffusion control. In addition, a decrease in the rate constant of the charge transfer stage leads to a significant shift of the transition region to the region of a larger *t*.

Thus, the roughness effect in the kinetics of electrochemical processes, which are characterized by mixed transport-kinetic control, turns out to be much more complex than in cases of purely diffusion or electrochemical kinetics. The characteristic criterion for the correct estimation of the roughness effect on the kinetics of such processes is, first of all, the dimensional-kinetic complex $k_D = \frac{k}{D}\lambda$. The simplest way is to take into account the roughness effect when $k_D \ll 1$, i.e. the charge transfer stage is limiting. In this case, the current density must necessarily be normalized to the roughness factor of the electrode surface. In the case where the electrochemical stage and the diffusion mass transfer stage proceed at comparable rates $(k_D \geq 1)$, or diffusion is slowed down compared to charge transfer, roughness accounting is reduced to dividing the current density by the roughness factor only for very short durations, otherwise an estimation of the roughness function at a given time is required.

4. Conclusions

1. The concentration profiles of an electroactive diffusant have been calculated by numerical finite element modeling. The chronoamperograms of an electrochemical process occurring under mixed transport and kinetic control on rough surfaces described by various harmonic and fractal functions with a given roughness factor with different ratios of the rate constant of the kinetic stage of the electrochemical process have been obtained.

2. The shape of the chronoamperogram of an electrochemical process in a mixed diffusion-kinetic regime depends both on the characteristics of the rough surface (roughness factor, average size of irregularities) and on the ratio of the rate constant of the charge transfer stage and the diffusion coefficient. With short durations, the overall process rate is equal to the charge transfer rate at a given potential. With long durations, the chronoamperogram coincides with the curve of the diffusion-controlled process, which is explained by the transition from the kinetic to the diffusion mode of the electrochemical process.

3. The effect of roughness is manifested only at relatively short process durations, and if the thickness of the diffusion layer is much smaller than the size of the irregularities, then the ratio

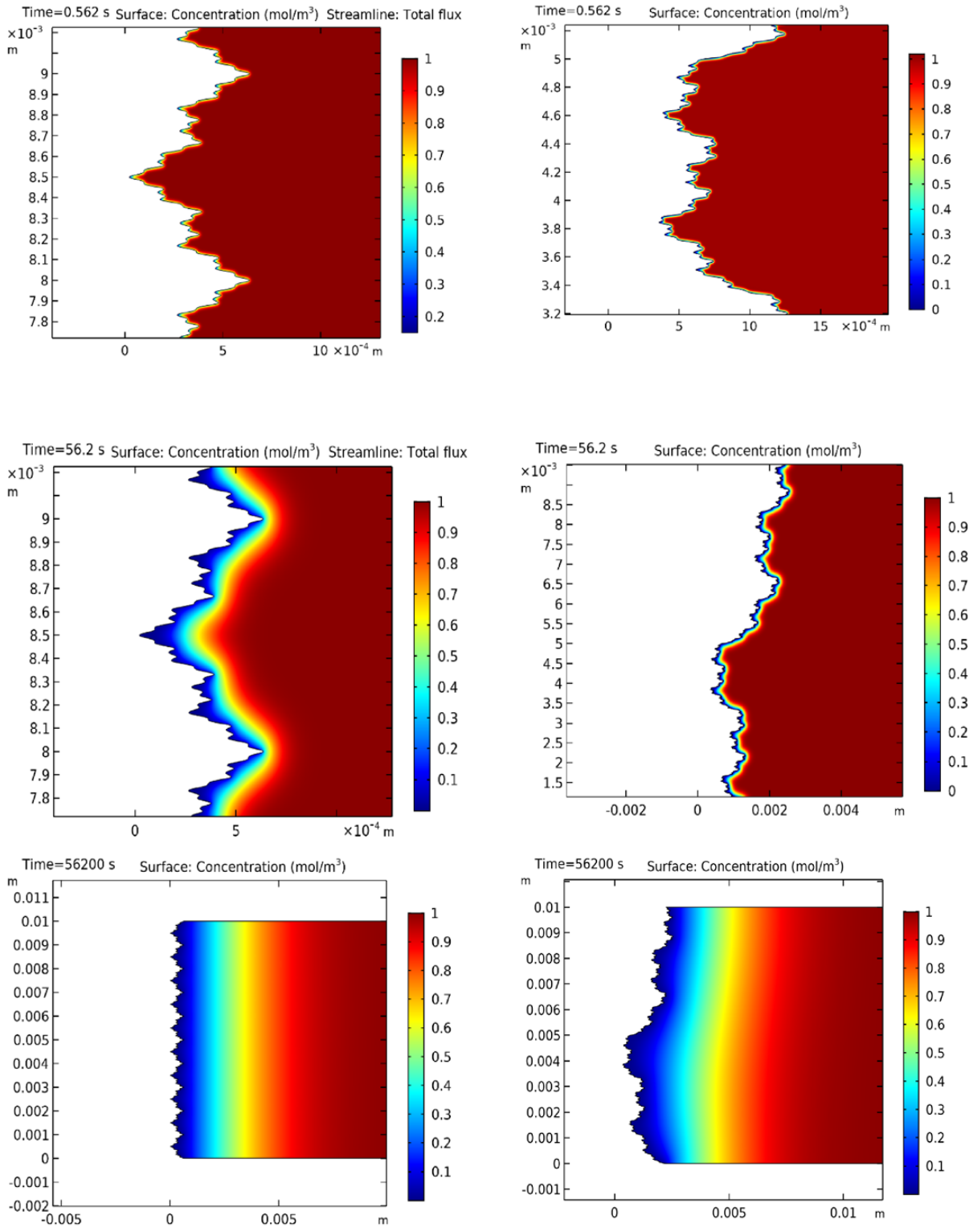

Fig. 9. The concentration field of a diffusant near a fractal and statistically rough surface (f_r = 3) during a non-stationary potentiostatic process in the mixed transport-kinetic control mode for different durations. The dimensional-kinetic complex k_D = 10

of process rates on rough and perfectly smooth electrodes is equal to the roughness factor. With long durations, the diffusion front is smoothed out so that there is no need to take roughness into account when calculating the process rate. In the intermediate time interval, the effect of roughness on the process rate is nonlinear. When the rate constant decreases, i.e. as the kinetic stage decelerates, the transition region manifests itself over increasingly long periods of time and gradually widens, while it is almost independent of the shape of the irregularity. As a result, under these conditions, taking into account the roughness effect is mandatory and amounts to normalizing the current density by the roughness factor.

Contribution of the authors

Vdovenkov F. A. – conducting a computational experiment. Kolosov A. N. – conducting a computational experiment, writing a text. Kuzmenko G. A. – conducting a computational experiment. Kozaderov O. A. – scientific guidance, research concept, methodology development, text editing, final conclusions.

Conflict of interests

The authors declare that they have no known competing financial interests or personal relationships that could have influenced the work reported in this paper.

References

1. Wang F., Zeng P., Wang Y., Ren X., Xiao H., Zhu W. High-speed and high-quality TSV filling with the direct ultrasonic agitation for copper electrodeposition. *Microelectronic Engineering*. 2017;180: 30–34. https://doi.org/10.1016/j.mee.2017.05.052

2. Beica R., Siblerud P., Erickson D. Advanced TSV copper electrodeposition for 3D interconnect applications. *IMAPSource Proceedings* 2010(DPC): 774–802. https://doi.org/10.4071/2010DPC-tp13

3. Kozaderov O.A. Surface roughness effect in the kinetics of heterogeneous processes. Review. *Condensed Matter and Interphases*. 2017;19(1): 6–21. https://doi.org/10.17308/kcmf.2017.19/171

4. McNaught A. D., Wilkinson A. *Compendium of chemical terminology*. The Gold Book, Second Edition. New York: Blackwell Science; 1997. 464 p.

5. Aslyamov T. Properties of electrolyte near rough electrodes: Capacity and impedance. *Current Opinion in Electrochemistry*. 2022;35: 101104. https://doi.org/10.1016/j.coelec.2022.101104

6. Koklu A., Sabuncu A., Beskok A. Rough gold electrodes for decreasing impedance at the electrolyte/electrode interface. *Electrochimica Acta*. 2016;205(2): 215–225. https://doi.org/10.1016/j.electacta.2016.04.048

7. Song F., Ma J., Wang G., Zhang R., Li J., Fan J. Novel rough nanorods NiO-(NiFeCo)O as positive electrode of high-performance asymmetric supercapacitors assembled with SiO_2/rGO negative electrode. *Energy*. 2025;326: 136360. https://doi.org/10.1016/j.energy.2025.136360

8. Sovík J., Knap V., Obertova V., Pastorek F., Florková Z., Hadzima B. Assessment of the effect of surface roughness on electrochemical characteristics of AZ80 magnesium alloy treated by PEO. *Transportation Research Procedia*. 2023;74(6): 465–471. https://doi.org/10.1016/j.trpro.2023.11.169

9. Chi G., Yi D., Liu H. Effect of roughness on electrochemical and pitting corrosion of Ti-6Al-4V alloy in 12 wt.% HCl solution at 35 °C. *Journal of Materials Research and Technology*. 2020;9(2): 1162–1174. https://doi.org/10.1016/j.jmrt.2019.11.044

10. Wang M. Influence of surface roughness on the anticorrosion performance of plasma sprayed amorphous coating and its electrochemical evaluation. *International Journal of Electrochemical Science*. 2023;18(11): 100326. https://doi.org/10.1016/j.ijoes.2023.100326

11. Tang Y. Investigation of influence of surface roughness on pitting corrosion of duplex stainless steel 2205 using various electrochemical techniques. *International Journal of Electrochemical Science*. 2019;14(7): 6790–6813. https://doi.org/10.20964/2019.07.51

12. Kozaderov O.A., Vvedenskii A.V. Diffusion-controlled potentiostatic process of selective dissolution of an alloy with a rough surface: finite element simulation. *Condensed Matter and Interphases.* 2014;16(1): 32–41. (in Russ., abstract in Eng.). Available at: https://www.elibrary.ru/item.asp?id=21490888

13. Kozaderov O. A. Chronoammetry and chronopotentiometry on electrodes with a microrough surface: Theoretical consideration. *Protection of Metals*. 2005;41(3): 211–220. https://doi.org/10.1007/s11124-005-0032-1

14. Kozaderov O. A., Kuzmenko G. A., Vdovenkov F. A. Theoretical model of voltammetry of selective dissolution of an alloy with accounting the effects of equilibrium solid-phase adsorption and surface roughness. *Sorbtsionnye I Khromatograficheskie Protsessy.* 2024;24(5): 753–764. https://doi.org/10.17308/sorpchrom.2024.24/12514

15. Menshykau D., Streeter I., Compton R. Influence of electrode roughness on cyclic voltammetry. *Journal of Physical Chemistry C*. 2008;112(37): 14428-14438. https://doi.org/10.1021/jp8047423

16. Parveen, Kant R. General theory for pulse voltammetric techniques at rough electrodes: multistep reversible charge transfer mechanism. *Electrochimica Acta*. 2016;220: 475–485. https://doi.org/10.1016/j.electacta.2016.10.061

17. Parveen, Kant R. General theory for pulse voltammetric techniques on rough and finite fractal electrodes for reversible redox system with unequal diffusivities. *Electrochimica Acta*. 2016;194: 283-291. https://doi.org/10.1016/j.electacta.2016.02.039

18. Gamero M., Pariente F., Lorenzo E., Alonso C. Nanostructured rough gold electrodes for the development of lactate oxidase-based biosensors. *Biosensors &*

Bioelectronics. 2010;25: 2038–2044. https://doi.org/10.1016/j.bios.2010.01.032

19. García Mendiola T., Gamero M., Campuzano S., ... Lorenzo E. Nanostructured rough gold electrodes as platforms to enhance the sensitivity of electrochemical genosensors. *Analytica chimica Acta*. 2013;788C: 141–147. https://doi.org/10.1016/j.aca.2013.06.009

20. Pei Y., Hu M., Xia Y., Huang W., Li Z., Chen S. Electrochemical preparation of Pt nanoparticles modified nanoporous gold electrode with highly rough surface for efficient determination of hydrazine. *Sensors and Actuators B: Chemical*. 2019;304: 127416. https://doi.org/10.1016/j.snb.2019.127416

21. Leuaa P., Priyadarshani D., Tripathi A. K., Neergat M. What decides the kinetics of V^{2+}/V^{3+} and VO^{2+}/VO_2^+ redox reactions – Surface functional groups or roughness? *Journal of Electroanalytical Chemistry*. 2020;878: 114590. https://doi.org/10.1016/j.jelechem.2020.114590

22. Herraiz-Cardona I., Ortega E., Antón J., Pérez-Herranz V. Assessment of the roughness factor effect and the intrinsic catalytic activity for hydrogen evolution reaction on Ni-based electrodeposits. *Fuel and Energy Abstracts*. 2011;36(16): 9428–9438. https://doi.org/10.1016/j.ijhydene.2011.05.047

23. Qin B., Wang H., Peng F., Yu H., Cao Y. Effect of the surface roughness of copper substrate on three-dimensional tin electrode for electrochemical reduction of CO_2 into HCOOH. *Journal of CO_2 Utilization*. 2017;21: 219–223. https://doi.org/10.1016/j.jcou.2017.07.012

24. Wang Y., Zhou J., Lv W., Fang H., Wang W. Electrochemical reduction of CO_2 to formate catalyzed by electroplated tin coating on copper foam. *Applied Surface Science*. 2015;362: 394–398. https://doi.org/10.1016/j.apsusc.2015.11.255

25. Galus Z. *Fundamentals of electrochemical analysis*. Chichester: Ellis Horwood; New York: Halsted Press, a division of Wiley; 1974. 520 p.

26. Kutateladze S. S. *Fundamentals of functional analysis*. Novosibirsk: Publishing House of the Institute of Mathematics; 2000. 336 p. (in Russ.)

27. Potapov A. A. *Fractals in radiophysics and radar: sampling topology*. Moscow: Universitetskaya kniga Publ.; 2005. 848 p. (in Russ.)

28. Berry M.V., Lewis Z.V. On the Weierstrass-Mandelbrot fractal function. *Proceedings of the Royal Society of London. A. Mathematical and Physical Sciences*. 1980;370(1743): 459-484. https://doi.org/10.1098/rspa.1980.0044

29. Lin N., Lee H. P., Lim S. P., Lee K. S. Wave scattering from fractal surfaces. *Journal of Modern Optics*. 1995;42(1): 225–241. https://doi.org/10.1080/09500349514550181

30. Gallagher R. *The finite element method: fundamentals**. Moscow: Mir Publ.; 1984. 428 p. (in Russ.)

31. Trukhan S. N., Derevshchikov V. S. C*omputer modeling of processes and phenomena of physical chemistry**. Novosibirsk: NNRSU Publ.; 2012. 75 p. (in Russ.)

32. Egorov V. I. *The use of computers for solving problems**. St. Petersburg: St. Petersburg State University of ITMO Publ.; 2006. 77 p. (in Russ.)

33. Voznesensky A. S. *Computer methods in scientific research**. Moscow: MGSU Publ.; 2010. [Part 2]. 107 p. (in Russ.)

34. Krasnikov G. E., Nagornov O. V., Starostin N. V. *Modeling of physical processes using the Comsol Multiphysics package**. Moscow: NRU MEPhI Publ.; 2012. 184 p. (in Russ.)

* *Translated by author of the article*

Information about the authors

Frol A. Vdovenkov, postgraduate student, Department of Physical Chemistry, Faculty of Chemistry, Voronezh State University (Voronezh, Russian Federation).

https://orcid.org/0009-0009-4737-9218

f.vdovenkov@gmail.com

Alexey N. Kolosov, student, Department of Physical Chemistry, Faculty of Chemistry, Voronezh State University (Voronezh, Russian Federation).

https://orcid.org/0009-0005-7622-4830

kolosov54aleksei@gmail.com

Grigory A. Kuzmenko, student, Department of Physical Chemistry, Faculty of Chemistry, Voronezh State University (Voronezh, Russian Federation).

https://orcid.org/0009-0004-7854-0960

kuzmyenko.chemistry.physics@mail.ru

Oleg A. Kozaderov, Dr. Sci. (Chem.), Associate Professor, Leading Researcher at the Laboratory of organic additives for the processes of chemical and electrochemical deposition of metals and alloys used in the electronics industry, Voronezh State University (Voronezh, Russian Federation).

https://orcid.org/0000-0002-0249-9517

ok@chem.vsu.ru

Received July 2, 2025; approved after reviewing September 22, 2025; accepted for publication October 15, 2025; published online December 25, 2025.

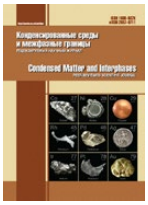

ISSN 1606-867X (Print)
ISSN 2687-0711 (Online)
Condensed Matter and Interphases
Kondensirovannye Sredy i Mezhfaznye Granitsy
https://journals.vsu.ru/kcmf/

Original articles

Research article
https://doi.org/10.17308/kcmf.2025.27/13298

Experimental study of phase equilibria in the Cu_2SnSe_3-Cu_3SbSe_4-Se ternary system

E. N. Ismayilova[1]✉, L. F. Mashadiyeva[1], I. B. Bakhtiyarly[1], V. A. Gasymov[1], I. F. Huseynova[1], Y. I. Jafarov[2]

[1]Institute of Catalysis and Inorganic Chemistry n.a. M. Nagiyev, 113 H. Javid av., Baku Az1143, Azerbaijan

[2]Baku State University, 33 Zahida Khalilova av., Baku Az1148, Azerbaijan

Abstract

Objectives: Copper-tin and copper-antimony chalcogenides are highly desirable for the creation of novel, affordable, and ecologically friendly thermoelectric materials. Due to the potential for improving their thermoelectric performance through different cationic and anionic substitutions, these compounds have recently attracted increased attention. The aim of the work was to establish the nature of the physicochemical interaction in the Cu_2SnSe_3-Cu_3SbSe_4-Se compositions region of the Cu-Sn-Sb-Se quaternary system by experimentally studying phase equilibria.

Experimental: Elemental components of high purity (⩾ 99.999 %) from EVOCHEM Advanced Materials GmbH (Germany) were used for the synthesis of the ternary compounds. The synthesis was carried out in evacuated (~10^{-2} Pa) quartz ampoules at temperatures 50 °C above the melting points of the ternary compounds. Phase equilibria in the Cu_2SnSe_3*Cu_3SbSe_4-Se system were experimentally studied using differential thermal analysis (NETZSCH 404 F1 Pegasus system) and X-ray diffraction (diffractometer Bruker D2 PHASER). This paper presents the *T-x* diagram of the Cu_2SnSe_3-Cu_3SbSe_4 boundary system, the isothermal section at 300 K, the liquidus surface projection, as well as three polythermal sections of the phase diagram. The primary crystallization fields of the phases and the types and coordinates of non- and monovariant equilibria are also determined.

Conclusions: The Cu_2SnSe_3-Cu_3SbSe_4 system has been established to be a quasi-binary eutectic system. Eutectic equilibrium is established at 68 mol % Cu_3SbSe_4 and 727 K. The liquidus surface of the studied system consists of two wide regions of primary crystallization of the Cu_2SnSe_3 and Cu_3SbSe_4 phases and one degenerate region near the selenium corner of the concentration triangle. A wide immiscibility area of two liquid phases is observed in the system, which has the form of a continuous solid solutions between the corresponding regions of the Cu_2SnSe_3-Se and Cu_3SbSe_4-Se boundary systems.

Keywords: Copper-antimony-tin selenides, Phase diagram, Immiscibility region, Solid solutions

For citation: Ismayilova E. N., Mashadiyeva L. F., Bakhtiyarly I. B., Gasymov V. A., Huseynova I. F., Jafarov Y. I. Experimental study of phase equilibria in the Cu_2SnSe_3-Cu_3SbSe_4-Se ternary system. *Condensed Matter and Interphases*. 2025;25(4): 606–614. https://doi.org/10.17308/kcmf.2025.27/13298

Для цитирования: Исмаилова Э. Н., Машадиева Л. Ф., Бахтиярлы И. Б., Гасымов В. А. Гусеинова И. Ф., Джафаров И. Я. Экспериментальное исследование фазовых равновесий в тройной системе Cu_2SnSe_3-Cu_3SbSe_4-Se. *Конденсированные среды и межфазные границы*. 2025;25(4): 606–614. https://doi.org/10.17308/kcmf.2025.27/13298

✉ Elnara N. Ismayilova, e-mail: eismayilova672@gmail.com

Introduction

During the global energy and climate crisis, the widespread use of thermoelectric (TE) materials in low-emission energy conversion technologies is a key priority in the scientific community [1–5]. Among these materials, multicomponent chalcogenides, especially those based on Cu, have attracted considerable attention as environmentally friendly materials [6–13]. Many of these compounds, due to their optical and electronic properties, can be used in various types of electrical devices such as electrochemical sensors, solid-state electrolytes, ion-selective electrodes, displays, etc. In particular, phases of variable composition formed in Cu-Sn-Sb-X systems and being synthetic analogs of the tetrahedrite mineral $Cu_{12}Sb_4S_{13}$ exhibit high ZT values and can be considered good candidates as thermoelectric materials [14–20]. It is well known that changing the composition and structure of materials is one of the effective methods for optimizing their functional properties. On the other hand, the availability of reliable data on phase equilibria and thermodynamic properties of the corresponding multicomponent systems is particularly important for the search and development of new materials and a better understanding of the relationship between composition, structure, and properties [21–30]. For this reason, it is advisable to conduct studies of the physicochemical interactions in the Cu–Sn–Sb–Se system, identify the phases of variable composition formed in it, and establish a general picture of phase equilibria.

In our earlier reports, phase equilibria in the Cu-Sn-Sb-Se system were studied in the composition ranges of Cu_2Se-Cu_2SnSe_3-Cu_3SbSe_4, Cu_2Se-SnSe-Sb_2Se_3, and Cu_2SnSe_3-Sb_2Se_3-Se using differential thermal analysis (DTA) and X-ray diffraction (XRD) [31-34]. The fields of primary crystallization of phases and the boundaries of homogeneity regions were determined, and the characters and types of non- and monovariant equilibria of these systems were established. It was found that the quaternary compound $CuSnSbSe_3$ is formed by a peritectic reaction in the Cu_2Se-SnSe-Sb_2Se_3 system and exists in a very narrow temperature range (~ 650–723 K) [33].

In this paper, we present the results of a study of phase equilibria in the Cu_2SnSe_3-Cu_3SbSe_4-Se system over the entire concentration range. This region plays an important role in determining the complete picture of phase equilibria in the Cu_2Se-$SnSe_2$-Sb_2Se_3-Se system. The ternary compound Cu_2SnSe_3 melts with an open maximum at 968 K and undergoes a polymorphic transition at 948 K [35, 36]. The high-temperature cubic phase of this compound has a lattice parameter a = 5.6877 Å [35, 37]. Below the polymorphic transition point, the monoclinic phase (Sp. Gr.*Cc*) crystallizes with the following unit cell parameters: a = 6.9670±3 Å, b = 12.0493 ± 7 Å, c = 6.9453 ± 3 Å, β = 109.19(1)°; z = 4 [38, 39]. The compound Cu_3SbSe_4 melts congruently at 755 K and has a tetragonal crystal structure (Sp. Gr. *I*42*m*) with the lattice parameters: $a = b$ = 5.6609 (8) Å; c = 11.280 (5) Å [40].

Both boundary side Cu_2SnSe_3-Se and Cu_3SbSe_4-Se of the studied Cu_2SnSe_3-Cu_3SbSe_4-Se quasi-ternary system are quasi-binary. The Cu_2SnSe_3-Se system is characterized by presence of the monotectic and eutectic equilibria [36]. At the monotectic temperature (910 K), the region of immiscibility of the two liquid phases covers the composition range of 37–95 at. % elemental Se (these numbers refer to the scale of $1/6Cu_2SnSe_3$-Se, i.e., 1 g-atomic amounts of the compound and elemental selenium). The eutectic point is degenerate near the selenium corner of the concentration triangle. The character of the phase equilibria of the $1/8Cu_3SbSe_4$-Se system is qualitatively identical to the previous $1/6Cu_2SnSe_3$-Se system. At the monotectic temperature, the immiscibility region extends over a wide composition range of ~ 10–97 at. % Se, and the eutectic is also degenerate near Se [36]. In [41], the formation of solid solutions with Sn-Sb substitution in the Cu_2SnSe_3-Cu_3SbSe_4 system at 673 K was established, and their thermoelectric properties were studied. However, there is no information in the literature on the phase diagram of this system.

2. Experimental

2.1. Synthesis

High-purity (⩾ 99.999 %) primary components from EVOCHEM Advanced Materials GmbH (Germany) were used for the synthesis. Ternary compounds of the studied system were obtained by melting simple substances in stoichiometric ratios corresponding to the Cu_2SnSe_3 and

Cu_3SbSe_4 formulas. The synthesis was carried out in evacuated (~10^{-2} Pa) quartz ampoules at temperatures 50 °C above the melting points of the ternary compounds [36]. After synthesis, the furnace was shut off and the ampoules were slowly cooled to room temperature and then annealed at 700 K for 50 hours to obtain a homogeneous stoichiometric composition.

The individuality of the synthesized ternary compounds was controlled using differential thermal analysis (DTA) and powder X-ray diffraction (XRD). The determined melting point and crystal lattice parameters for the two synthesized compounds were similar to the literature data given above within the margin of error (± 3 K and ± 0.0003 Å) [35–40].

To conduct the experiments, 32 samples were prepared along the 1/6Cu_2SnSe_3-[B], [A]-1/8 Cu_3SbSe_4, and [C]-Se cross-sections, as well as some additional alloys outside these cross-sections, by melting the initial compounds in a vacuum. According to the DTA of cast non-homogenized samples, their crystallization from melts is complete at 500 K. Therefore, to achieve a state as close to equilibrium as possible, the obtained cast alloys were annealed at 450 K for 400 h.

2.2. Research methods

DTA and XRD were used for the studies. Equilibrium samples were heated in evacuated quartz ampoules using a NETZSCH 404 F1 Pegasus system differential scanning calorimeter at a heating rate of 10 °C/min. The results were processed using NETZSCH Proteus software. The temperature measurement accuracy was ± 2 K.

X-ray diffraction patterns of the annealed homogenized alloys were obtained at room temperature using a Bruker D2 PHASER diffractometer with CuKα1 radiation. Topaz V3.0 software, provided by Bruker, was used to index the powder diffraction patterns of the studied alloys.

3. Results and discussion

A combination of the DTA and XRD data for three internal sections of the studied system, along with literature data on phase equilibria in boundary quasi-binary systems [34, 39], allowed us to determine the phase equilibria in the Cu_2SnSe_3-Cu_3SbSe_4-Se system. The phase diagram of the Cu_2SnSe_3-Cu_3SbSe_4 boundary system, the solid-phase equilibria diagram of the system at 300 K, the liquidus surface projection, and three polythermal sections of the phase diagram are presented below.

3.1. The Cu_2SnSe_3-Cu_3SbSe_4 quasi-binary section

Powder diffraction patterns of selected intermediate alloys of the studied Cu_2SnSe_3-Cu_3SbSe_4 system are shown in Fig. 1. As can

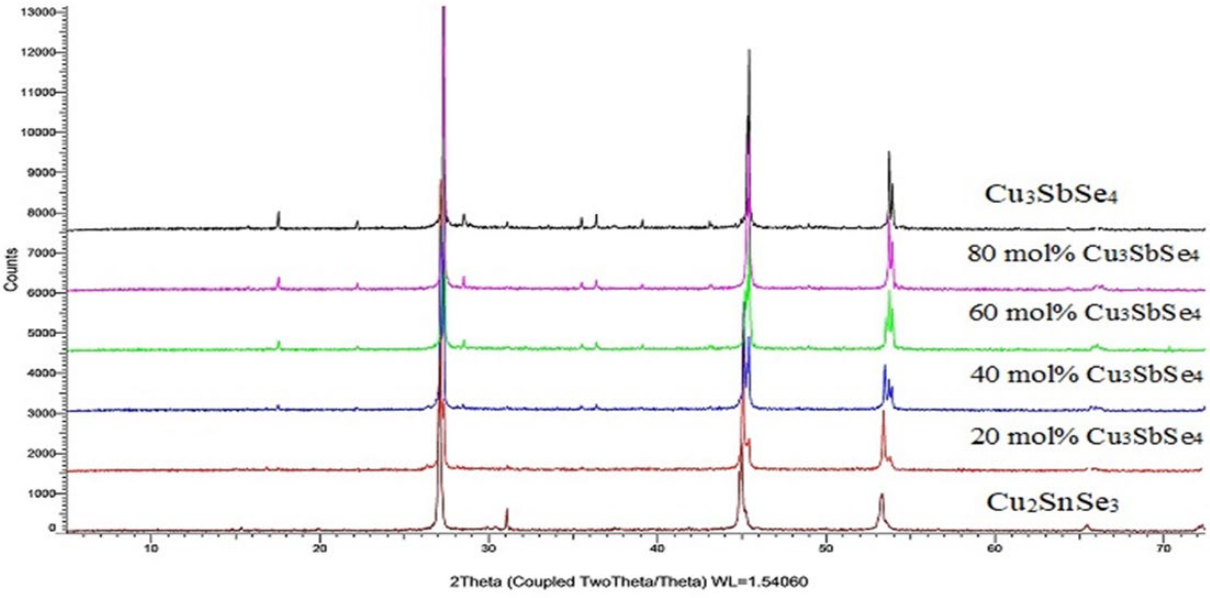

Fig. 1. Powder XRD patterns of alloys of the Cu_2SnSe_3-Cu_3SbSe_4 system

be seen, the diffraction patterns of alloys with compositions of 20 and 80 mol % Cu_3SbSe_4 are qualitatively identical to the diffraction patterns of the initial Cu_2SnSe_3 and Cu_3SbSe_4 compounds, respectively. This indicates the existence of wide solubility regions based on these compounds. Alloys with compositions of 40 and 60 mol % Cu_3SbSe_4 consist of a two-phase mixture of Cu_2SnSe_3+Cu_3SbSe_4 compounds.

Based on DTA and XRD data, a phase diagram of the Cu_2SnSe_3-Cu_3SbSe_4 system was constructed (Fig. 2). It was established that this system is quasi-binary, forms a eutectic-type *T-x* diagram, and is characterized by the formation of wide solid solutions (α- and β-phases) based on both initial components. The liquidus of the system consists of the primary crystallization curves of the α- and β solid solutions. At room temperature, the solubility of Cu_2SnSe_3 and Cu_3SbSe_4 reaches ~30 and ~25 mol %, respectively. The eutectic equilibrium point corresponds to 68 mol % Cu_3SbSe_4 and 727 K. Below the solidus, co-crystallization of the α- and β-phases occurs.

3.2. Isothermal Section at 300 K

According to the solid-phase equilibria diagram (Fig. 3), the Cu_2SnSe_3-Cu_3SbSe_4-Se system consists of two two-phase regions (α + Se and β + Se) and a three-phase region (α + β + Se) separating them.

XRD data of alloys from various regions confirmed their phase composition. As can be seen from Fig. 4, the powder diffractograms of alloys No. 1 and No. 2, shown in Fig. 3, are the sum of the diffraction patterns of the Cu_2SnSe_3 + Se and Cu_3SbSe_4+Se phases, respectively, while the XRD pattern of sample No. 3 contains a set of diffraction lines corresponding to a mixture of α + β + Se.

3.3. Liquidus surface projection (Fig. 5)

The liquidus surface of the studied quasi-ternary system consists of two wide fields of primary crystallization of the α- and β-phases. The immiscibility region that forms on the boundary Cu_2SnSe_3-Se and Cu_3SbSe_4-Se systems penetrates the concentration triangle and forms a wide region of immiscibility of the two liquid phases (L_1 +L_2). The eutectic curve emanating from e_1, corresponding to the eutectic equilibrium of the boundary Cu_2SnSe_3-Cu_3SbSe_4 system, intersects this immiscibility region. As a result, the monovariant eutectic equilibrium $Le_1 \leftrightarrow \alpha+\beta$ is transformed into the nonvariant monotectic equilibrium $L_1 \leftrightarrow L_2 + \alpha + \beta$ (T = 710 K). The compositions of the liquid phases in this equilibrium correspond to points M_1 and M_2. Another nonvariant equilibrium in the system degenerates near the corner of the elementary Se of the concentration triangle. This part of the phase diagram is shown in Fig. 5 at an enlarged scale. At point E, which corresponds to the composition of the ternary eutectic mixture, a

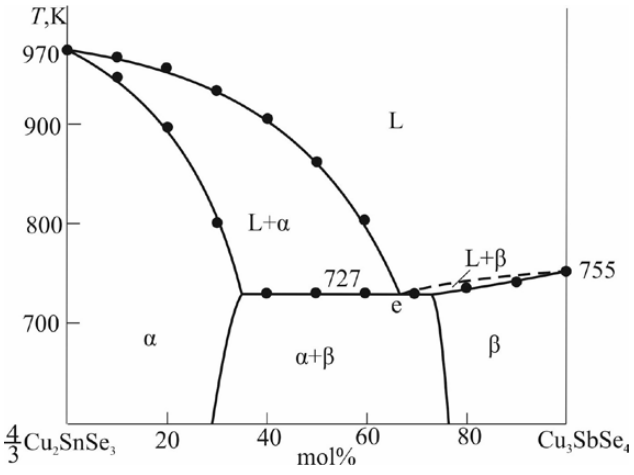

Fig. 2. Phase diagram of the Cu_2SnSe_3-Cu_3SbSe_4 system

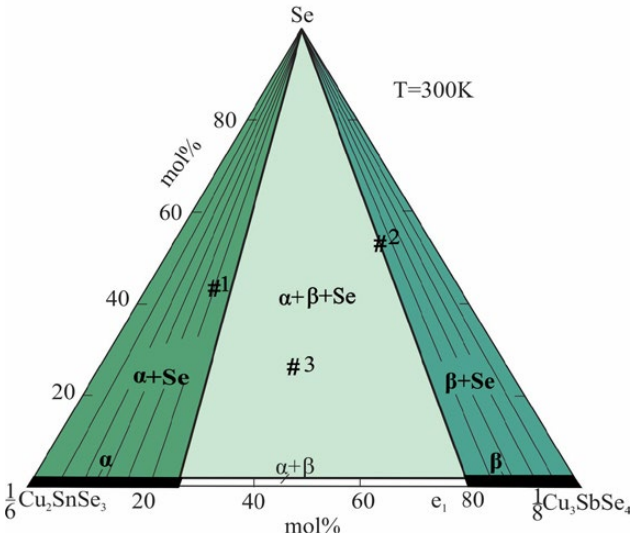

Fig. 3. Solid-phase equilibria diagram of the Cu_2SnSe_3-Cu_3SbSe_4-Se system at 300 K. The composition of the mentioned phases is shown in Fig. 4

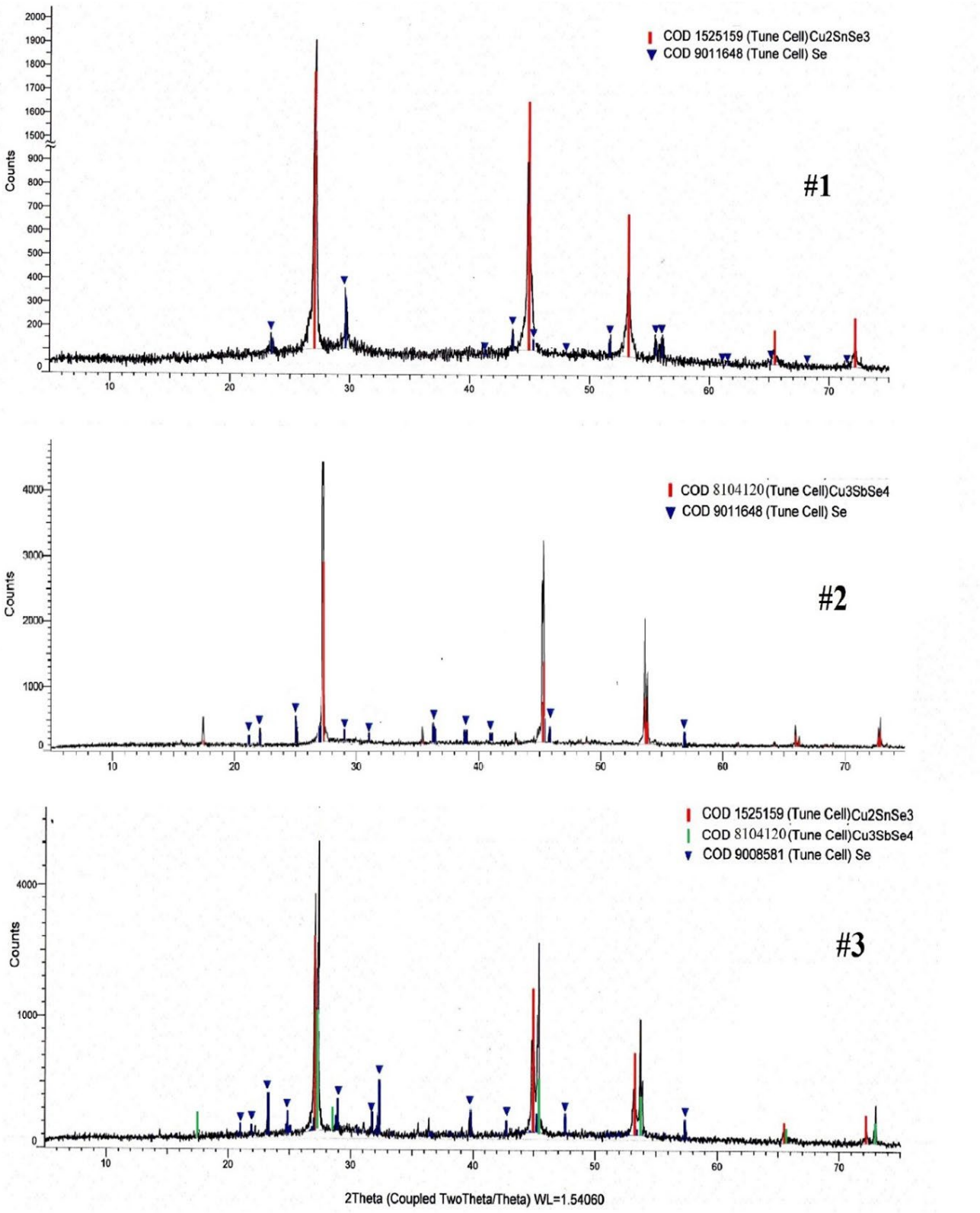

Fig. 4. X-ray powder diffraction patterns of the alloys #1 (50 % Cu_2SnSe_3-50 % Se), #2 (45 % Cu_3SnSe_4-55 % Se), and #3 (40 % Cu_2SnSe_3-30 % Cu_3SnSe_4-30 % Se) in Fig. 3

four-phase eutectic equilibrium L ↔ α + β + Se occurs at 490 K. The conjugate curves (e_2E and e_3E) at the eutectic point (E) degenerate into the following equilibria:

$Le_{2E} \leftrightarrow \alpha + Se$

$Le_{3E} \leftrightarrow \beta + Se$

The immiscibility regions are bounded by the conjugate curves m_1M; $m_1'M'$ и m_2M; $m_2'M'$, which reflect the monovariant monotectic equilibria $L_1 \leftrightarrow L_2 + \alpha$ and $L_1 \leftrightarrow L_2 + \beta$, respectively. The curves e_1M and M'E reflect monovariant eutectic equilibria $L_1 \leftrightarrow \alpha + \beta$ and $L_2 \leftrightarrow \alpha + \beta$ (Fig. 5).

3.4. Polythermal Sections

Polythermal sections of the *T-x-y* phase diagram are important for visualizing crystallization processes in the system.

Section 1/6Cu_2SnSe_3-[B] (Fig. 6). ([B] is an alloy of the 1/8Cu_3SbSe_4-Se side system, corresponding to a 1:1 composition). This region passes through the immiscibility region and the liquidus surface of the α- and β-phases. From left to right, the α-phase crystallizes from the liquid in the range < 55 mol % [B]: L ↔ α. In the 55-85 mol % [B] composition range, the α-phase initially crystallizes from the immiscibility region via the monovariant monotectic reaction $L_1 \leftrightarrow L + \alpha$; and the β-phase crystallizes in the concentration range > 85 mol % [B]. After the primary crystallization of the α-phase based on Cu_2SnSe_3 in the range of ~2–55 mol % [B], crystallization continues via a monotectic reaction. As a result of these processes, the region $L_2 + \alpha$ (L_2 is a liquid based on elemental Se) is formed in Fig. 6. The horizontal line (M) at 710 K in the phase diagram reflects the monovariant equilibrium $L_1 \leftrightarrow L_2 + \alpha + \beta$. This reaction ends with the formation of a three-phase region $L_2 + \alpha + \beta$.

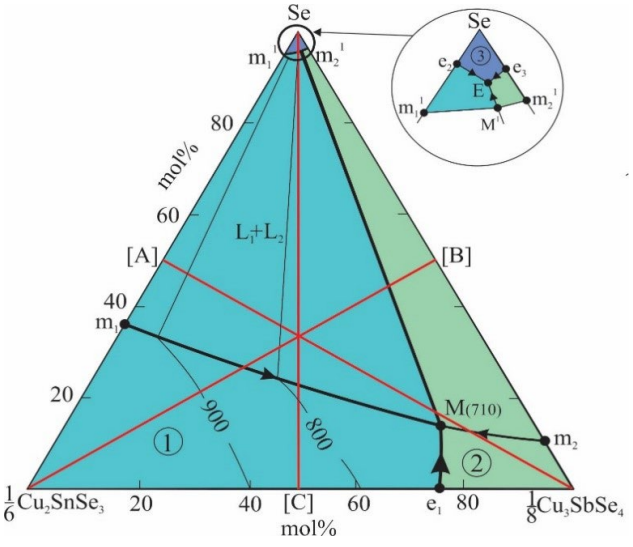

Fig. 5. Liquidus surface of the Cu_2SnSe_3-Cu_3SbSe_4-Se system. Primary crystallization fields: *1* – α (solid solution based on Cu_2SnSe_3); *2* – β (solid solution based on Cu_3SbSe_4); *3* – Se. Red lines are the studied polythermal sections

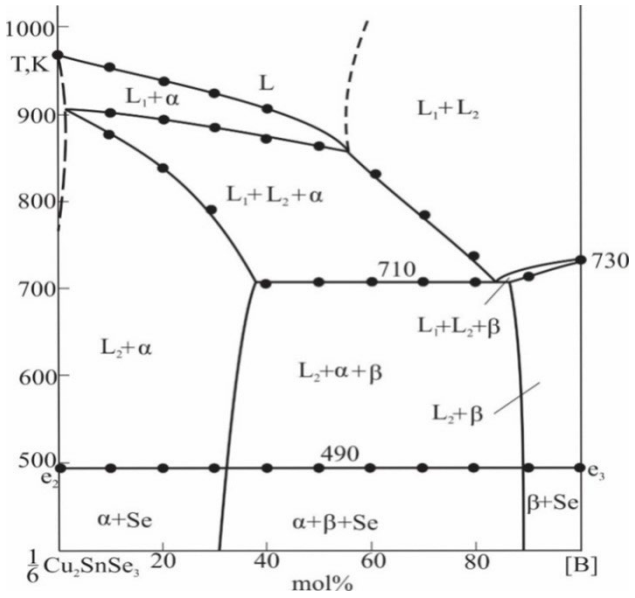

Fig. 6. Polythermal section 1/6Cu_2SnSe_3-[B] system. [B] is alloy of the 1/8 Cu_3SbSe_4-Se boundary system with the composition ratio 1:1

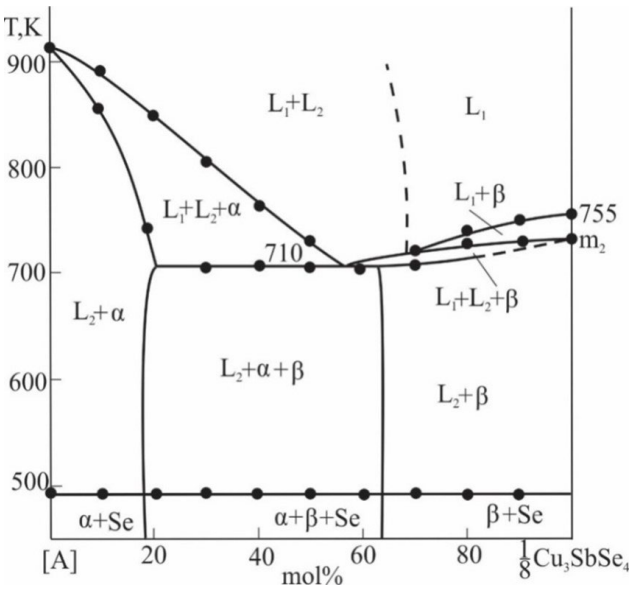

Fig. 7. Polythermal section [A]-1/8Cu_3SbSe_4 system. [A] is an alloy of the 1/6Cu_2SnSe_3-Se boundary system with the composition ratio 1:1

Crystallization is completed by degenerate non- and monovariant eutectic reactions (E, e_2E, e_3E, and M′E) at ~ 490 K, and heterogeneous regions of α + Se, β + Se, and α + β + Se are formed in the subsolidus.

Section [A]-1/8 Cu_3SbSe_4 (Fig. 7). ([A] is an alloy of the $1/6Cu_2SnSe_3$-Se boundary system, corresponding to a 1:1 composition). The crystallization process in this section is somewhat different. Here, the α-phase crystallizes from immiscible liquid phases in the 0–58 mol % 1/8 Cu_3SbSe_4 compositions range. In the ~58–70 mol % 1/8 Cu_3SbSe_4 compositions range, the β-phase initially crystallizes from the L_1+L_2 region, whereas at compositions > 70 mol % 1/8 Cu_3SbSe_4, it crystallizes from the liquid phase L_1. In the composition range of 10-63 mol % 1/8 Cu_3SbSe_4, the system undergoes a nonvariant monotectic equilibrium M, and in the Cu_3SbSe_4-rich region (63–100 mol %), the reaction $L_1 \leftrightarrow L_2$+ β occurs, leading to the formation of the region L_2+ β (Fig. 7).

Thus, the regions L_2+ α, L + α + β, and L_2 + β exist along this section before the crystallization of elemental selenium. As in the previously considered polythermal section, complete crystallization in this section occurs through eutectic reactions, and two-phase mixtures of α + Se, β + Se, and α + β + Se are formed in the solid state.

Section [C]-Se (Fig. 8). (here [C] is an alloy of the boundary system $1/6Cu_2SnSe_3$-$1/8Cu_3SbSe_4$ with a composition of 1:1). This section completely intersects the region of primary crystallization of the α-phase. In the concentration range of ~ 0–23 at. % elemental Se, the α-phase primarily crystallizes from liquid L_1, and in the range of > 95 at. % Se (el.), from liquid L_2. In intermediate compositions, the primary crystallization of the α-phase proceeds according to the monovariant eutectic reaction $L_1 \leftrightarrow L_2$ + α in the L_1 + L_2 immiscibility region. It should be noted that the initial temperature of this process is constant (790 K), indicating that the direction of the L_1-L_2 tie line in the immiscibility region coincides with the plane of this region. Below the liquidus, in the concentration range of 0–10 at. % Se (el.), crystallization continues via the monovariant eutectic reaction $L_1 \leftrightarrow$ α + β, and at 710 K, the system undergoes a four-phase transition reaction: L_1+ α ↔ L_2+ β. Crystallization is completed via the invariant eutectic process L ↔ α + β + Se.

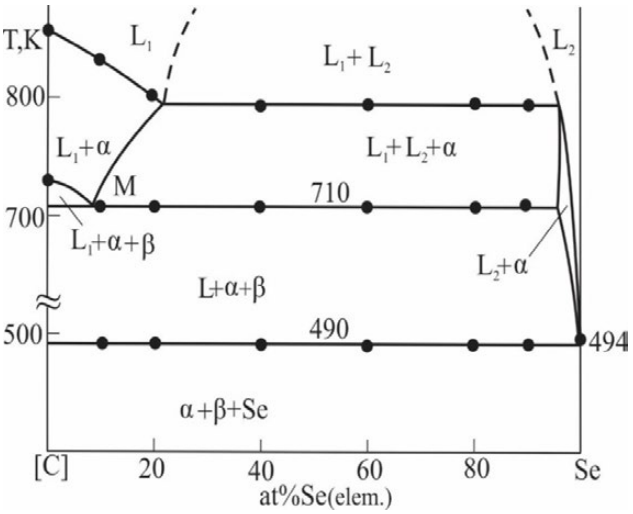

Fig. 8. Polythermal section [C]-Se system. [C] is an alloy of the $1/6Cu_2SnSe_3$-$1/8Cu_3SbSe_4$ boundary system with the composition ratio 1:1

These research results provide the scientific basis for the synthesis and growth of single crystals of selenium-enriched solid solutions based on Cu_2SnSe_3 and Cu_3SbSe_4 compounds.

4. Conclusion

Thus, this study presents a complete picture of phase equilibria in the Cu_2SnSe_3-Cu_3SbSe_4-Se system based on experimental results obtained by differential thermal analysis and X-ray diffraction. It was established that it is a quasi-ternary plane corresponding to the quaternary system. A projection of the liquidus surface and a solid-phase equilibria diagram at 300 K are presented, and a series of polythermal sections is constructed. It is established that the liquidus surface of the phase diagram of the studied quasi-ternary system consists of three primary crystallization fields. The crystallization fields of the α- and β-solid solutions based on Cu_2SnSe_3 and Cu_3SbSe_4 are the most extensive. The region of elemental selenium is degenerate in the corresponding corner of the concentration triangle. A wide region of immiscibility of the two liquid phases is observed in the system, which appears as a continuous band between the corresponding regions of the Cu_2SnSe_3-Se and Cu_3SbSe_4-Se boundary systems.

Author contributions

Ismailova E. N. – study concept, carry out the investigation, compounds synthesis, article writing, and results discussion. Mashadeva L. F. – literature analysis, results discussion. Bakhtiyarly I. B. – results discussion, final conclusions. Gasymov V. A. – XRD results discussion. Huseynova I. F. – compounds synthesis. Dzhafarov Ya. I. – literature review, results discussion.

Conflict of interests

The authors declare that they have no known competing financial interests or personal relationships that could have influenced the work reported in this paper.

References

1. Liu W., Hu J., Zhang S., Deng M., Han C.-G., Liu Y. New trends, strategies and opportunities in thermoelectric materials: a perspective. *Materials Today Physics*. 2017;1: 50–60. https://doi.org/10.1016/j.mtphys.2017.06.001

2. He J., Tritt T. M. Advances in thermoelectric materials research: looking back and moving forward. *Science*. 2017; 357(6358). https://doi.org/10.1126/science.aak9997

3. Jia N., Cao J., Tan X. Y., … Suwardi A.Thermoelectric materials and transport physics. *Materials Today Physics*. 2021;21: 100519. https://doi.org/10.1016/j.mtphys.2021.100519

4. Mukherjee M., Srivastava A., Singh A. K. Recent advances in designing thermoelectric materials *Journal of Materials Chemistry C*. 2022;10: 12524–12555. https://doi.org/10.1039/D2TC02448A

5. Du Y., Xu J., Paul B., Eklund P. Flexible thermoelectric materials and devices. *Applied Materials Today*. 2018;12: 366–388. https://doi.org/10.1016/j.apmt.2018.07.004

6. Qiu P., Shi X., Chen L. Cu-based thermoelectric materials. *Energy Storage Materials*. 2016;3: 85-97. https://doi.org/10.1016/j.ensm.2016.01.009

7.Mikuła A., Mars K., Nieroda P., Rutkowski P. Copper chalcogenide-copper tetrahedrite composites – a new concept for stable thermoelectric materials dased on the chalcogenide system. *Materials*. 2021;14(10): 2635. https://doi.org/10.3390/ma14102635

8. Mulla R., Rabinal M. H. K. Copper sulfides: earth-abundant and low-cost thermoelectric materials. *Energy Technology*. 2019;7(7): 1800850. https://doi.org/10.1002/ente.201800850

9. Jaldurgam F. F., Ahmad Z., Touati F., … Altahtamouni T. Enhancement of thermoelectric properties of low-toxic and earth-abundant copper selenide thermoelectric material by microwave annealing. *Journal of Alloys and Compounds*. 2022;904: 1654131. https://doi.org/10.1016/j.jallcom.2022.164131

10. Wei T.-R., Qin Y., Deng T., … Chen L. Copper chalcogenide thermoelectric materials . *Science China Materials*. 2018;62: 8–24. https://doi.org/10.1007/s40843-018-9314-5

11. Alonso-Vante N. Chalcogenide materials for energy conversion. In: *Nanostructure Science and Technology*. Springer International Publishing; 2018. 226p. https://doi.org/10.1007/978-3-319-89612-0

12. Hu H., Ju Y., Yu J., … Li J.-F. Highly stabilized and efficient thermoelectric copper selenide. *Nature Materials*. 2024;23: 527–534. https://doi.org/10.1038/s41563-024-01815-1

13. Sanghoon X. L., Tengfei L. J., Zhang L. Y-H. *Chalcogenide. From 3D to 2D and beyond*. Elsevier; 2019. 398 p.

14. Wei J., Yang L., Ma Z., … Wang X. Review of current high-ZT thermoelectric materials. *Journal of Materials Science*. 2020;55: 12642–12704 . https://doi.org/10.1007/s10853-020-04949-0

15. Chetty R., Balia A., Mallik R. C. Tetrahedrites as thermoelectric materials: an overview. *Journal of Material Chemistry C*. 2015;3: 12364–12378. https://doi.org/10.1039/C5TC02537K

16. Suekun K., Takabatake T. Research update: Cu–S based synthetic minerals as efficient thermoelectric materials at medium temperatures. *APL Materials*. 2016;4:104503. https://doi.org/10.1063/1.4955398

17. Liu Y., Kretinin A. V., Liu X., … Freer R. Thermoelectric performance of tetrahedrite ($Cu_{12}Sb_4S_{13}$) thin films: the influence of the substrate and interlayer. *ACS Applied Electronic Materials*. 2023;6(5): 2900–2908. https://doi.org/10.1021/acsaelm.3c00909

18. Palchoudhury C. S., Ramasamy K., Gupta A. Multinary copper-based chalcogenide nanocrystal systems from the perspective of device applications. *Nanoscale Advances*. 2020;2(8): 3069–3082. https://doi.org/10.1039/d0na00399a

19. Zhang D., Yang J., Bai H., Yubo L. Significant average ZT enhancement in Cu_3SbSe_4-based thermoelectric material via softening p-d hybridization. *Journal of Materials Chemistry A*. 2019;10: 1039–1048. https://doi.org/10.1039/c9ta05115e

20. Studenyak I. P., Pogodin A. I., Studenyak V. I., … Kúš P. Electrical properties of copper- and silver-containing superionic $(Cu_{1-x}Ag_x)_7SiS_5I$ mixed crystals with argyrodite structure. *Solid State Ion*. 2020;345: 115183–115186. https://doi.org/10.1016/j.ssi.2019.115183

21. Bayramova U. R., Babanly K. N., Ahmadov E. I., Mashadiyeva L. F., Babanly M. B. Phase equilibria in the Cu_2S-Cu_8SiS_6-Cu_8GeS_6 system and thermodynamic functions of phase transitions of the $Cu_8Si_{(1-X)}GeXS_6$ argyrodite phases. *Journal of Phase Equilibria and Diffusion*. 2023;44: 509–519. https://doi.org/10.1007/s11669-023-01054-y

22. Babanly M. B., Yusibov Y. A., Imamaliyeva S. Z., Babanly D. M., Alverdiyev I. J. Phase diagrams in the development of the argyrodite family compounds and solid solutions based on them. *Journal of Phase Equilibria and Diffusion*. 2024;45(12): 228-255. https://doi.org/10.1007/s11669-024-01088-w

23. Babanly M. B., Mashadiyeva L. F., Imamaliyeva S. Z., Babanly D. M., Tagiyev D. B., Yusibov Yu. A. Complex copper-based chalcogenides: a review of phase equilibria and thermodynamic properties Russ. *Condensed Matter and Interphases*. 2024;26(4): 579–619. https://doi.org/10.17308/kcmf.2024.26/12367

24. Mammadov F. M., Babanly D. M., Amiraslanov I. R., Tagiev D. B., Babanly M. B. System FeS–Ga_2S_3–In_2S_3. *Russian Journal of Inorganic Chemistry*. 2021;66(10): 1533–1543. https://doi.org/10.1134/S0036023621100090

25. Abdullayeva Sh. S, Bakhtiyarly I. B, Kurbanova R. J, Mukhtarova Z. M. The quasi-binary $Cu_3In_5S_9$-$FeIn_2S_4$ section. *Condensed Matter and Interphases*. 2022;24(2): 182–186. https://doi.org/10.17308/kcmf.2022.24/9257

26. Mammadov S. H., Mammadov A. N., Kurbanova R .C. Quasi-binary section Ag_2SnS_3–$AgSbS_2$. *Russian Journal of Inorganic Chemistry*. 2020;65(2): 217–221. https://doi.org/10.1134/S003602362001012X

27. Mashadiyeva L. F., Babanly D. M., Hasanova Z. T., Usibov Y. A., Babanly M. B. Phase relations in the Cu-As-S system and thermodynamic properties of copper-arsenic sulfides. *Journal of Phase Equilibria and Diffusion*. 2024:45; 567–582. https://doi.org/10.1007/s11669-024-01115-w

28. Abdullaeva Sh. S., Mammadov F. M., Bakhtiyarly I. B. Quasi-binary section $CuInS_2$–$FeIn_2S_4$. *Russian Journal of Inorganic Chemistry*. 2020;65: 100–105. https://doi.org/10.1134/S0036023619110020

29. Orujlu E. N., Aliev Z. S., Babanly M. B. The phase diagram of the MnTe–SnTe–Sb_2Te_3 ternary system and synthesis of the iso- and aliovalent cation-substituted solid solutions. *Calphad*. 2022;76: 102398. https://doi.org/10.1016/j.calphad.2022.102398

30. Mammadov F. M. New version of the phase diagram of the MnTe- Ga_2Te_3 system. *New Materials*, *Compounds and Applications*. 2021;5(2): 116–121. Available at: http://jomardpublishing.com/UploadFiles/Files/journals/NMCA/V5N2/MammadovF.pdf

31. Ismailova E. N., Mashadieva L. F., Bakhtiyarly I. B., Gasymov V. A., Gurbanova R. J., Mammadova F. M. Phase equilibria in the Cu_2Se - Cu_3SbSe_4 - Cu_2SnSe_3 system. *Chemical Problems*. 2025;23(1): 36–46. https://doi.org/10.32737/2221-8688-2025-1-36-46

32. Ismayilova E. N., Mashadieva L. F., Bakhtiyarly I. B, Babanly M. B. Phase equilibria in the Cu_2SnSe_3–Sb_2Se_3–Se system. *Condensed Matter and Interphases*. 2023;25(1): 47-54. https://doi.org/10.17308/kcmf.2023.25/10973

33. Ismailova E. N., Mashadieva L. F.,Bakhtiyarly I. B, Babanly M. B. Phase equilibria in the Cu_2Se–SnSe–Sb_2Se_3 system. *Azerbaijan Chemical Journal*. 2022;1: 73-82. https://doi.org/10.32737/0005-2531-2022-1-73-82

34. Ismayilova E. N., Baladzhayeva A. N., Mashadiyeva L. F. Phase equılıbrıa along the Cu_3SbSe_4-$GeSe_2$ sectıon of the Cu-Ge-Sb-Se system. *New Materials, Compounds and Applications*. 2021;5(1): 52–58. Available at: https://jomardpublishing.com/UploadFiles/Files/journals/NMCA/V5N1/Ismayilova_et_al.pdf

35. Parasyuk O. V., Olekseyuk I. D., Marchuk O. V. The Cu_2Se–HgSe–$SnSe_2$ system. *Journal of Alloys and Compounds*. 1999;287(1-2): 197–205. https://doi.org/10.1016/S0925-8388(99)00047-X

36. Babanly M. B., Yusibov Yu. A., Abishov V. T. *Three-component chalcogenides based on copper and silver**. Baku: BSU Publ.; 1993. 342 p. (In Russ.).

37. Sharma B. B., Ayyar R., Singh H. Stability of the tetrahedral phase in the $A^I_2B^{IV}C^{VI}_3$ group of compounds. *Physica Status Solidi A*. 1977;40(2): 691–697. https://doi.org/10.1002/pssa.2210400237

38. Marcano G., Chalbaud L., Rincón C., Sánchez P. G. Crystal growth and structure of the semiconductor Cu_2SnSe_3. *Materials Letters*. 2002;53(3): 151–154. https://doi.org/10.1016/s0167-577x(01)00466-9

39. Delgado G. E., Mora A. J., Marcano G., Rincon C. Crystal structure refinement of the semiconducting compound Cu_2SnSe_3 from X-ray powder diffraction data. *Materials Research Bulletin*. 2003;38: 1949–1955. https://doi.org/10.1016/j.materresbull.2003.09.017

40. Pfitzner A. Crystal structure of tri-copper tetraselenoantimonate Cu_3SbSe_4. *Zeitschrift für Kristallographie-Crystalline Materials*. 1994;209(8): 685–685. https://doi.org/10.1524/zkri.1994.209.8.685

41. Fan Y., Xie S., Sun J., Tang X., Tan G. Quasi-isostructural alloying of Cu_2SnSe_3–Cu_3SbSe_4 toward higher thermoelectric performance. *ACS Applied Energy Materials*. 2021;4 (6): 6333–6339. https://doi.org/10.1021/acsaem.1c01155

* *Translated by author of the article*

Information about the authors

Elnara N. Ismayilova, postgraduate student, Researcher, Institute of Catalysis and Inorganic Chemistry of the Ministry of Science and Education of Azerbaijan (Baku, Azerbaijan).

https://orcid.org/0000-0002-1327-1753

eismayilova672@gmail.com

Leyla F. Mashadiyeva, PhD in Chemistry, Senior Researcher, Institute of Catalysis and InorganicChemistry of the Ministry of Science and Education of Azerbaijan (Baku, Azerbaijan).

https://orcid.org/0000-0003-2357-6195

leylafm76@gmail.com

Ikhtiyar B. Bakhtiyarly, Dr. Sci. (Chem.), Professor, Head of Laboratory, Institute of Catalysis and Inorganic Chemistry of the Ministry of Science and Education of Azerbaijan (Baku, Azerbaijan).

https://orcid.org/0000-0002-7765-0672

ibbakhtiarli@mail.ru

Vagif A. Gasymov, Cand. Sci. (Chem.), Associate Professor, Institute of Catalysis and Inorganic Chemistry of the Ministry of Science and Education of Azerbaijan (Baku, Azerbaijan).

https://orcid.org/0000-0001-6233-5840

vgasymov@rambler.ru

Ilahe F. Huseynova, PhD in Chemistry, Institute of Catalysis and Inorganic Chemistry of the Ministry of Science and Education of Azerbaijan (Baku, Azerbaijan).

https://orcid.org/0000-0002-1106-0207

mehdiyeva.ilahe2@gmail.com

Yasin Isa Jafarov, Dr. Sci. (Chem.), Associate Professor, Baku State University (Baku, Azerbaijan).

https://orcid.org/0000-0002-3968-8725

yasin_cafarov@mail.ru

Received March 6, 2025; approved after reviewing April 2, 2025; accepted for publication May 15, 2025; published online December 25, 2025.

ISSN 1606-867X (Print)
ISSN 2687-0711 (Online)
Condensed Matter and Interphases
Kondensirovannye Sredy i Mezhfaznye Granitsy
https://journals.vsu.ru/kcmf/

Original articles

Research article
https://doi.org/10.17308/kcmf.2025.27/13300

Hydration properties of heterogeneous ion exchange membranes after their long-term use in the electrodialysis treatment of wastewater from the production of mineral fertilizers

O. A. Kozaderova✉, **I. A. Saranov**

Voronezh State University of Engineering Technologies
Revolution ave., 19, Voronezh 394036, Russian Federation

Abstract

Objectives: In this paper, the evolution of the hydration characteristics of heterogeneous cation- and anion-exchange membranes during the electrodialysis treatment of multicomponent salt solutions is studied.

Experimental: The objects of research are heterogeneous RalexCMH-Pes (sulfocation exchange) and RalexAMH-Pes (anion exchange with quaternary ammonium groups) membranes, which have been used with different durations in an industrial electrodialyzer for the concentration/desalination of liquid waste from the production of complex mineral fertilizers. The hydration characteristics of the membranes were determined using synchronous thermal analysis. The morphology of the surface of the studied membranes was investigated by scanning electron microscopy. X-ray phase analysis of the ash residue after annealing of the membranes was carried out using the diffractometric method.

Conclusions: The moisture content and specific heat of dehydration of the studied membranes increase during long-term electrodialysis processing of liquid waste from the production of complex mineral fertilizers. For cation-exchange and anion-exchange membranes, the moisture content increases by 74 and 68 %, respectively. The predominant type of kinetically unequal water in membranes is weakly and moderately bound water. Strongly bound water molecules involved in ion-dipole interactions with active functional groups are least represented in membranes, and during operation in an electrodialyzer, their proportion increases by 1.35 times in the case of cation-exchange membranes and decreases by 1.3 times in anion-exchange membranes. The increase in moisture content and the redistribution of water fractions of different degrees of binding can be explained by the degradation of membranes caused by their morphological changes (an increase in the number of defects and the size of macropores filled with solution or water), as well as the stretching of the membrane matrix due to the presence of large and highly hydrated ions in the processed liquid waste. In addition, hydrophilic inorganic precipitates accumulate in the nanopores of anion-exchange membranes.

Keywords: Heterogeneous ion exchange membranes, Degradation, Electrodialysis, Hydration characteristics, Synchronous thermal analysis

Funding: The study was supported by the Russian Science Foundation (RSF), project No. 25-29-00557, https://rscf.ru/en/project/25-29-00557/

Acknowledgements: Synchronous thermal analysis was performed on the equipment of the Test Center of the Voronezh State University of Engineering Technologies. The studies using scanning electron microscopy and X-ray diffractometry were performed on the equipment of the Center for Collective Use of Scientific Equipment of the Voronezh State University

For citation: Kozaderova O. A., Saranov I. A. Hydration properties of heterogeneous ion exchange membranes after their long-term use in the electrodialysis treatment of wastewater from the production of mineral fertilizers. *Condensed Matter and Interphases*. 2025;27(4): 615–629. https://doi.org/10.17308/kcmf.2025.27/13300

Для цитирования: Козадерова О. А., Саранов И. А. Гидратационные свойства гетерогенных ионообменных мембран после их длительного использования в электодиализной переработке сточных вод производства минеральных удобрений. *Конденсированные среды и межфазные границы*. 2025;27(4): 615–629. https://doi.org/10.17308/kcmf.2025.27/13300

✉ Olga A. Kozaderova, e-mail: kozaderova-olga@mail.ru

1. Introduction

The first commercial electrodialyzer was manufactured in the 1950s and was used to desalinate brackish water [1]. Currently, electrodialysis (ED) is widely used in the chemical [2], pharmaceutical [3], and food [4] industries. At the same time, special attention should be paid to the use of this electromembrane method for the extraction of useful components from industrial and municipal wastewater [5-7] and the creation of waste-free production of organic products [8–11]. In particular, the use of electrodialysis technology for the treatment of wastewater from the production of mineral fertilizers [12–14], which are multicomponent solutions and/or mixtures of inorganic and organic compounds, is quite promising.

During the electrodialysis processing of such media containing a wide range of different components, under conditions of direct current, elevated temperature and pH changes, the degradation of ion exchange membranes (IEM) used in electrodialyzers occurs [15]. Due to the presence of polluting components in the treated media and/or due to the initiation of undesirable processes in the membranes, such as precipitation accumulation, changes in morphology, and linear pore sizes, the physico-chemical, electrochemical, and transport characteristics of IEM deteriorate and the efficiency of the electrodialysis process as a whole decreases [16]. The problem of IEM degradation is encountered during the electrodialysis treatment of municipal wastewater [12,17], natural waters [18,19], food industry solutions [20-22], and pharmaceutical industry [23], as well as of IEM artificially aged in the laboratory [24,25]. At the same time, ED technology is being actively implemented in a number of enterprises for the production of mineral fertilizers, including JSC "Minudobreniya" and JSC "Kuibyshevazot", as part of projects for processing steam condensate [26]. It is planned to put ED equipment into operation at JSC NAK Azot, JSC TAIF-NK, and JSC Achinsk Oil Refinery [26]. However, despite the active introduction of this technology, there are few studies on the degradation of IEM during the electrodialysis of waste from the production of mineral fertilizers [10, 27]. This makes it difficult to predict the duration of effective and useful use of IEM in ED installations, which significantly depend on the degree of membrane degradation. This negative process is accompanied by changes in the structure and chemical composition of the membranes [15, 16, 28], which largely determine their selectivity and transport characteristics.

In turn, the structure, transport, and physico-chemical properties of ion-exchange membranes depend significantly on their interaction with water. Membranes function effectively only in the hydrated state, when they are capable of separation and ion exchange due to a significant weakening of the electrostatic interaction between counterions and fixed ions [29]. Deterioration of the transport properties of membranes in conditions of low humidity is one of the main problems limiting the practical application of ion exchange membranes. It was shown in [30] that an increase in moisture content is possible due to modification of the membrane by doping with inorganic nanoparticles, which, at low humidity, participate in ion transport, and the water molecules sorbed by them participate in the hydration of alkali metal cations in the membranes.

High moisture content is one of the main conditions for the formation of an optimal hydrophilic/hydrophobic balance of the ion surface, which, in turn, significantly affects the efficiency parameters of the separation process during electrodialysis, including the intensity of electroconvection and the generation of H^+ and OH^- ions occurring at the membrane/solution interface [31]. For example, it was shown in [32] that hydrophobic amino acids adsorbed on the membrane surface contribute to an increase in its hydrophobicity, which leads to a greater contribution of electroconvection to mass transfer during intensive current modes of electrodialysis.

Heterogeneous IEM are characterized by a higher moisture content, lower temperatures of the onset of dehydration, and a higher relative rate of water release compared to ion-exchange resins, on the basis of which they are manufactured [33]. The features of the interaction of such IEM with a solvent are largely determined by pores of different sizes. Porometric analysis of domestic heterogeneous MK-40 and MA-41

membranes showed [34, 35] that the thinnest pores (mainly with a radius of 3.5 and 13 nm) are located in ion exchanger grains, whereas pores with a radius of 100 nm are formed at the contact points of ion exchange resin and polyethylene particles, and the largest pores with an effective radius of 3 microns are formed between the reinforcing fabric and the ion exchanger/polyethylene composite. Depending on the different levels of membrane structural organization (molecular, supramolecular, macroscopic), several structural, kinetically unequal types of water in the membranes are distinguished: "bound", "intermediate", and "free" [36]. When the nature of the counterion changes, the water content and state inside the ion exchange membrane change [36]. Thus, an urgent task is to determine the hydration characteristics of ion exchangers depending on the type of membrane and the duration of use in electrodialysis plants.

To solve this problem, thermal analysis methods are used: thermogravimetry (TG) and differential thermal analysis (DTA), based on recording the parameters of the system under study, which change under conditions of programmed temperature exposure [33]. The thermogravimetry method consists in measuring the mass loss of the test material as the temperature changes. With the help of differential thermal analysis, the thermal effects of transformations occurring in the test sample under temperature influence are recorded. Synchronization of TG and DTA measurements makes it possible not only to determine the range of thermal stability of the ion exchange materials under study, but also to obtain information about the physico-chemical properties of the water contained in them, as well as to establish the main characteristics of the dehydration process of ion exchangers [33]. The experimental results obtained in this work using several complementary methods (thermal analysis, scanning electron microscopy, and X-ray diffraction) make it possible to reasonably establish the role of morphological changes and precipitation accumulation as the most likely causes of the evolution of hydration characteristics of heterogeneous ion-exchange membranes observed during electrodialysis treatment of multicomponent salt solutions (waste products of complex mineral fertilizers), which is the **purpose** of this study.

2. Experimental

2.1. Membranes

The research objects were RalexCMH-Pes (sulfocation exchange) and RalexAMH-Pes (anion exchange with quaternary ammonium groups) membranes manufactured by Mega JSC (Czech Republic) [37]. They are heterogeneous and contain an ion exchanger, plasticizer (polyethylene), and reinforcing fabric (polyester).

The membranes were operated in an industrial electrodialyzer with alternating cation- and anion-exchange membranes separated by flow turbulator grids in the mode of concentration/desalination of multicomponent salt solutions, such as waste from the production of complex mineral fertilizers for different periods of time. The membranes separated the concentrate/dilute chambers and did not come into contact with the solutions of the electrode chambers. The process was carried out in pre-limit current modes. The composition of treated wastewater is as follows (mg/dm^3): Ca^{2+} 0.9–6.7; Cl^- 1.3–16.9; Mg^{2+} 0.2–3.8; SO_4^{2-} 2.2–39.8; Na^+ 0.10; F^- 3.2–92.3; K^+ 0.15; NO_3^- 15.4–312.1; $Fe^{2(3)+}$ 0.01–0.17; PO_4^{3-} 0.6–2.3; NH_4^+ 15.9–258.5 [27, 38]. After removing the membranes from the electrodialyzer, they were washed in distilled water, the surface was cleaned with a soft sponge and placed in distilled water. The characteristics of the used membranes were compared with similar characteristics of the initial samples that were not involved in the electrodialysis process.

The conditioning of the initial membranes was carried out in accordance with the methods given in [39]. First, salt treatment was performed in NaCl solutions of different concentrations, then the cation exchange membranes were treated with acid, and the anion exchange membranes with alkali. After conditioning, the cation exchange samples were converted to the Na^+ form, and the anion exchange samples were converted to the Cl^- form and stored in distilled water.

In this paper, the pristine conditioned samples have the index "prist", the membranes for one

year of use are "1", five years are "2". CEM and AEM are the designations of cation- and anion-exchange membranes, respectively. The main characteristics of the studied membranes are given in Table 1.

2.2. Methods

The morphology of the surface of the studied IEM was studied using scanning electron microscopy (SEM) on a JSM-6380 LV device (Japan). The preparation of the membranes for analysis was as follows. The membranes (AEM_{prist}, AEM_1, AEM_2, CEM_{prist}, CEM_1, CEM_2) stored in distilled water were dried in a drying cabinet to a constant weight at 70 °C, 5×5 mm samples were cut out, and an electrically conductive carbon layer was sprayed on them.

X-ray phase analysis of the ash residue after IEM annealing at 600 °C was performed using an ARL X'TRA diffractometer (Thermo Scientific, Switzerland). The particle size of the mineral components present in the membrane was calculated from the width of the diffraction maximum using the Scherrer formula [40].

Experimental studies of the membrane dehydration process were carried out using a NETZSCH STA 449 F3 Jupiter synchronous thermal analysis device combining high-precision thermal weights and a differential scanning calorimeter. The device allows one to simultaneously obtain a set of several interrelated thermoanalytical curves: two integral curves (the mass loss curve (TG) and the thermal effects curve (DSC)), as well as their corresponding two differential curves (the mass loss rate curve (DTG) and the curve of the rate of change of the thermal effect (dDSC)). Swollen samples of IEM, previously soaked in distilled water for at least 7 days, were studied. Temperature research program: heating from 298 to 523 K at a rate of 5 K/min. Research conditions: aluminum crucibles, nitrogen atmosphere, purge gas consumption at 15 cm^3/min. The received thermograms were processed using NETZSCH Proteus and MS Excel software.

3. Results and discussion

Typical experimental thermoanalytical curves are shown in Fig. 1 using a CEM_{prist} membrane sample as an example. Similar thermograms in the form of a set of TG, DTG, DSC, and dDSC curves were obtained for the five other membranes studied in the work (AEM_{prist}, AEM_1, AEM_2, CEM_1, CEM_2). The experimental thermoanalytical curves were rearranged and shown in Fig. 2 and 3 in a modified temperature-time format used in works on the thermal analysis of ion-exchange materials [33, 41]. This format for representing thermal curves allows not only to identify, but also to visually compare the integral TG, DSC, and differential DTG effects observed when samples are heated, which makes it possible, among other things, to detect the difference between the original and spent membranes.

It is important to note that for all studied IEM samples, regardless of the type of membranes (cation or anion exchange) and the duration of their use in an electrodialysis unit, the change in mass Δm, determined by the integral thermogravimetric TG curve, is consistent with the deviation of the differential thermal DSC curve from the baseline in the temperature range of 300-430 K. In addition, the highest rate of mass loss of the membrane sample, determined by the minimum on the DTG curve, is observed at a temperature close to the temperature of the DSC maximum (for example, at $T_{max}^{\Delta m}$ = 67.5 °C for the CEM_{prist} membrane sample). This agreement of the TG, DTG, and DSC curves can be explained by the fact that the changes observed on them are due to a single process, the removal of water (dehydration) from the membrane sample when it is heated. Indeed, according to [33], the decrease in the mass of ion-exchange material in the temperature range of 300–430 K, in which the most significant change in Δm for the studied membranes is observed on

Table 1. Characteristics of ion exchange membranes

Parameter	CEM_{prist}	CEM_1	CEM_2	AEM_{prist}	AEM_1	AEM_2
Exchange capacity, mmol/g of dry membrane	1.6±0.1	1.7±0.1	1.6±0.1	1.5±0.1	1.5±0.1	1.2±0.1
Thickness, mm	508±2	511±1	513±2	507±1	510±1	512±2

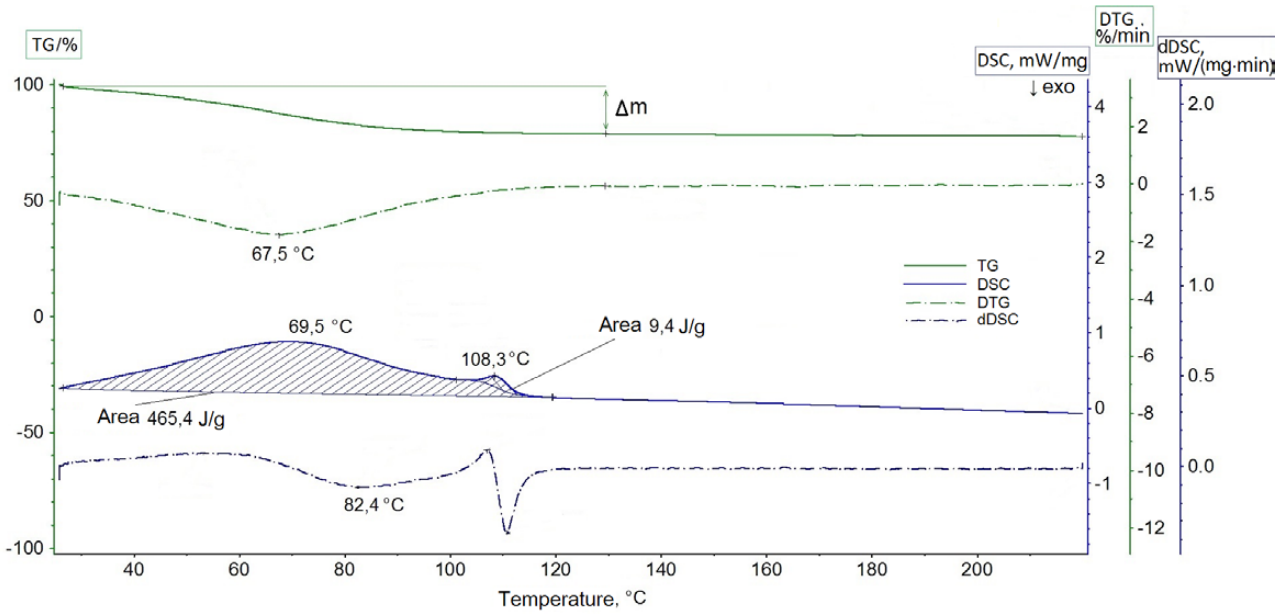

Fig. 1. Experimental thermoanalytical curves obtained for the CEM_{prist} membrane sample. Notation: TG is the mass loss curve, DSC is the thermal effects curve, DTG is the curve of the mass loss rate, dDSC is the curve of the rate of the thermal effect change

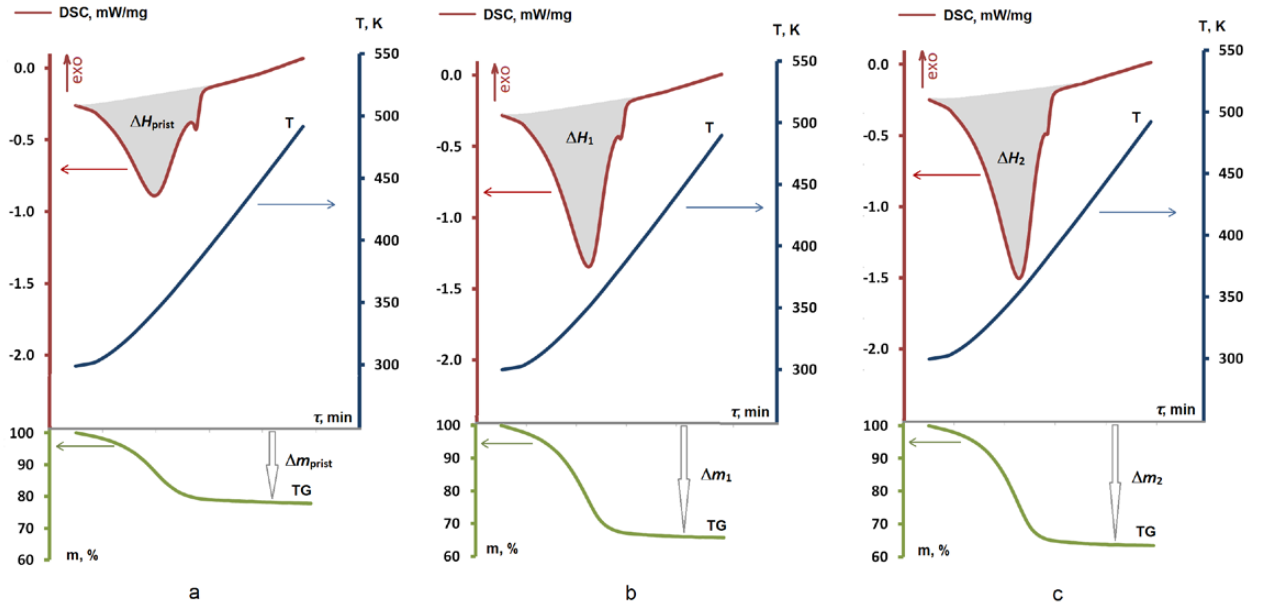

Fig. 2. Thermal curves of cation exchange membranes: CEM_{prist} (a), CEM_1 (b), CEM_2 (c). Notation: T is the temperature change curve, TG is mass loss curve, DSC is the thermal effects curve; Δm_{prist}, Δm_1, Δm_2 – mass change, ΔH_{prist}, ΔH_1, ΔH_2 – specific heat of dehydration (J/g) for samples CEM_{prist} (a), CEM_1 (b), CEM_2 (c) respectively

all the obtained thermoanalytical curves, is due precisely to the removal of water from them. Thus, a comparative assessment of the moisture content of the studied membranes can be carried out by the value of Δm. The specific moisture capacity n_W (mol H_2O/mol functional group) was calculated using the formula:

$$n_W = \frac{\Delta m}{M_{H_2O} \cdot EC} \cdot 100\,\%.$$

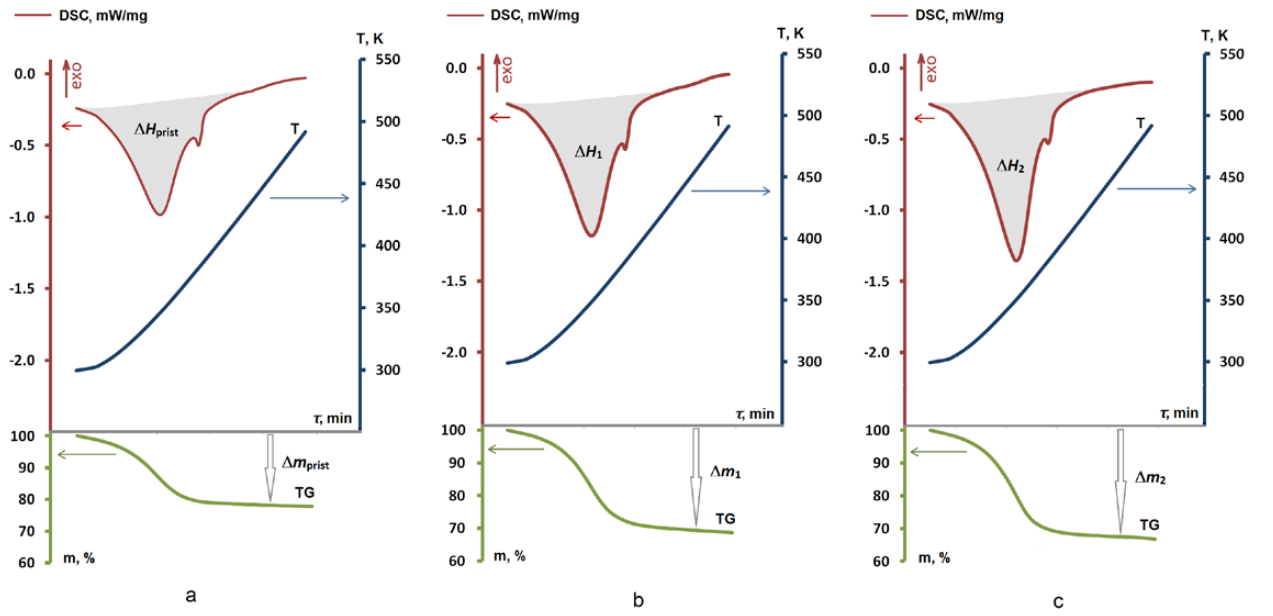

Fig. 3. Thermal curves of anion exchange membranes: AEM_{prist} (a), AEM_1 (b), AEM_2 (c). Notation: T is the temperature change curve, TG is mass loss curve, DSC is the thermal effects curve; Δm_{prist}, Δm_1, Δm_2 – mass change, ΔH_{prist}, ΔH_1, ΔH_2 – specific heat of dehydration (J/g) for samples AEM_{prist} (a), AEM_1 (b), AEM_2 (c) respectively

Here M_{H_2O} is a molar mass of water, *EC* is an exchange capacity of the membrane (Table 1). In turn, the specific thermal effect of the endothermic dehydration process ΔH (the so-called "endoeffect" [33]) is determined by the area of the maximum observed on the DSC dependence. Using the example of a CEM_{prist} membrane sample, it can be seen (Fig. 1) that such a maximum with a peak at T_{max} = 69.5 °C is quite extensive, and its area, equal to ΔH = 465.4 J/g, corresponds to the thermal effect of dehydration of this IEM, normalized by the mass of the initial membrane sample, i.e. represents the heat of dehydration. A small maximum at 108.3 °C can be attributed to the melting of an inert binder of heterogeneous IEM, polyethylene [43].

On the modified temperature-time dependences (Figs. 2 and 3), the minimum area on the DSC curve corresponds to the thermal effect. The complete set of quantitative characteristics of the dehydration process (Δm, $T_{max}^{\Delta m}$, T_{max}, ΔH), found from modified thermoanalytical curves, is given in Table 2 for all studied CEM and AEM samples. It follows from these data that the mass loss Δm increases with increasing duration of use of CEM and AEM membranes. This indicates an increase in the moisture content of both cation and anion exchange membranes during operation of the electrodialysis unit. The specific heat of dehydration increases naturally, which is consistent with an increase in the moisture content of the membrane. It should be emphasized that the heat of dehydration, calculated per mole of removed water, practically does not depend on the type of membrane and the duration of its use, and averages 39.0±1.8 and 35.8±1.2 kJ/mol for CEM and AEM, respectively. According to [33], the values of the molar heat of dehydration in the range of 35-39 kJ/mol correspond to the formation of associates of 2-4 water molecules.

It is important to note the increase in temperature $T^{\Delta m}_{max}$, which corresponds to the highest rate of mass loss of the membrane sample: from 341 to 351 K in the range CEM_{prist} < CEM_1 < CEM_2, and from 343 to 348 K in the range AEM_{prist} < AEM_1 < AEM_2. A similar effect of $T^{\Delta m}_{max}$ growth found for the MF-4-SK membrane in [42] is explained by the effect of an inorganic dopant (polysuric acid particles) on the system of pores and channels, the introduction of which into the volume of MF-4-SK leads to an increase in moisture content. Thus, an increase in the

Table 2. Quantitative characteristics of the membrane dehydration process

Ion exchange membrane	Δm, %	$T_{max}^{\Delta m}$, K	T_{max}, K	ΔH, J/g	ΔH, kJ/mol
CEM_{prist}	20.73	67.5	69.5	465.4	40.5
CEM_1	33.43	74.9	77.5	693.8	37.3
CEM_2	35.51	78.0	80.4	774.9	39.3
AEM_{prist}	24.73	70.2	72.8	476.8	34.7
AEM_1	29.73	73.2	75.7	592.6	35.9
AEM_2	32.08	75.4	77.5	654.5	36.8

temperature of the maximum water removal rate correlates with data on an increase in the parameters Δm and ΔH.

According to [33], the analysis of thermoanalytical curves, along with the determination of the membrane moisture content, makes it possible to quantify the total and relative content of kinetically unequal (weakly, moderately, and strongly bound) water molecules in the membranes. This assessment is based on the representation of the dehydration process of ion-exchange membranes as a sequential release of kinetically unequal water molecules characterized by different degree of binding [33]. In accordance with the procedure for processing TG dependencies described in [33], the thermoanalytical curves of the studied cation and anion exchange membranes are presented in the $\lg \alpha - T^{-1}$ coordinates, where $\alpha = \Delta m_i(T_i)/\Delta m$ is the ratio of the mass change of the membrane sample $\Delta m_i(T_i)$, corresponding to the amount released water at a temperature of T_i, to a total loss of mass. The slope of the $\lg \alpha - T^{-1}$ curve depends on the nature and energy of the interaction of water molecules in the membrane. As a result, the corresponding dependencies are characterized by the presence of three linear sections with different slopes, each of which corresponds to a specific stage of water removal. The removal of weakly bound water (dehydration stage I) is carried out by a low-temperature section based on the logarithmic dependence of the relative mass change of the membrane sample on T^{-1}. In this case, we are talking about H_2O molecules bound to each other by the weakest hydrogen bonds characteristic of the bulk phase of the solvent in the region of "long-range hydration" [33]. The intermediate medium–temperature section of the $\lg \alpha - T^{-1}$ curve corresponds to the stage of dehydration II, the removal of water, in which intermolecular interactions, compared with weakly bound water, are enhanced due to the influence of membrane functional groups [33], as a result of which the slope of the $\lg \alpha$ dependence on T^{-1} decreases. Finally, the high–temperature section of the dependence of the relative change in the mass of the IEM sample on temperature, characterized by the lowest slope, corresponds to stage III of dehydration, that is the removal of water molecules involved in the strongest ion-dipole interactions with the functional groups of the membrane, Fig. 4.

The quantitative characteristics of water molecules of various degrees of binding, found by the dependence of $\lg \alpha$ on T^{-1} of the studied CEM and AEM membranes, are shown in Tables 3 and 4. A comparison of these data shows that all the studied ion exchange membranes are characterized by the highest content of weakly and also moderately bound water, while strongly bound water is represented to the least extent. The values of moisture capacity found are consistent with the data obtained in [33, 44–46]. In this case, the analysis of the relative distribution of the water content of various degrees of binding revealed differences for cation- and anion-exchange membranes in the change of their moisture content during long-term operation in an electrodialysis unit.

Thus, during the transition from CEM_{prist} to CEM_1 and CEM_2, cation exchange membranes are characterized by an increase in the fraction of strongly bound water molecules. Indeed, if this parameter is 9.6 % for the initial sample of a cation exchange membrane, then after one year and five years of use it increases to 12 and 13 %, respectively (Table 3). In the case of anion exchange membranes, the transition from

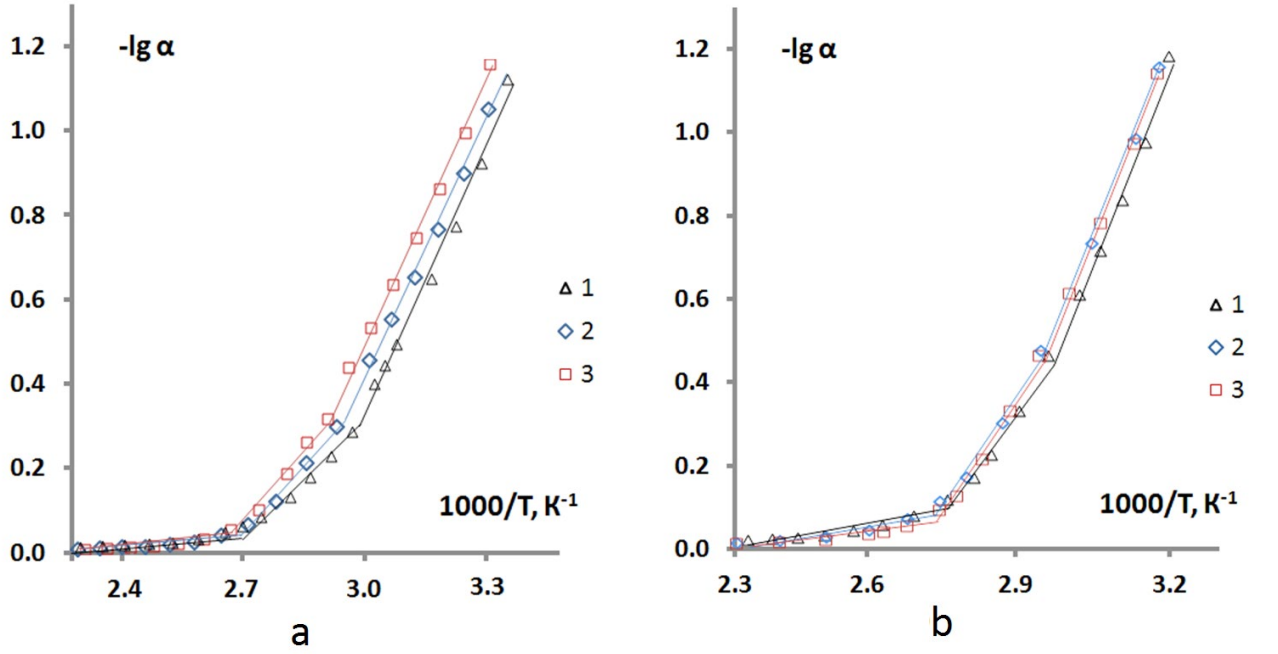

Fig. 4. Dependences of the relative change (α) in the mass of the membrane sample on temperature for cation exchange CEM (a) and anion exchange AEM (b) membranes: *1* - CEM_{prist}, AEM_{prist}; *2* – CEM_1, AEM_1; *3* – CEM_2, AEM_2

Table 3. Quantitative characteristics of kinetically unequal water in cation exchange membranes at maximal swelling

Membrane	Stage of dehydration	ΔT, K	% H_2O	Specific moisture capacity n_W, mol H_2O /mol functional groups	
CEM_{prist}	I	298–331	39.7	3.7	Σ = 9.3
	II	331–369	50.5	4.7	
	III	369–402	9.6	0.9	
CEM_1	I	298–337	43.0	6.8	Σ = 15.8
	II	337–365	44.9	7.1	
	III	365–401	12.0	1.9	
CEM_2	I	298–340	40.1	6.5	Σ = 16.2
	II	340–365	46.9	7.6	
	III	365–410	13.0	2.1	

Table 4. Quantitative characteristics of kinetically unequal water in anion exchange membranes at maximal swelling

Membrane	Stage of dehydration	ΔT, K	% H_2O	Specific moisture capacity n_W, mol H_2O /mol functional groups	
AEM_{prist}	I	298–329	33.3	3.8	Σ = 11.4
	II	329–359	47.4	5.4	
	III	359–419	19.3	2.2	
AEM_1	I	298–336	40.1	5.6	Σ = 14.0
	II	336–359	39.2	5.5	
	III	359–432	20.7	2.9	
AEM_2	I	298–337	40.4	7.8	Σ = 19.3
	II	337–362	44.6	8.6	
	III	362–429	15.0	2.9	

AEM_{prist} to AEM_2 is accompanied, on the contrary, by a decrease in the fraction of strongly bound water molecules from 19.3 to 15.0 % (Table 4). Accordingly, the fraction of weakly bound water in the internal solution of the anion exchange membrane increases from 33.3 to 40.4 %, which is consistent with the results of the analysis of the transport and structural characteristics of the studied IEM, for which, according to electrical conductivity data, an increase in the contribution of the internal solution to conductivity was found [47].

The discovered effects of increasing the moisture content of cation- and anion-exchange membranes during their long-term operation during electrodialysis of multicomponent solutions of mineral salts, as well as the revealed redistribution of water fractions of different degree of connectivity, may be due to a number of reasons.

One of the possible factors causing a change in both the moisture content and the redistribution of water of different degree of binding is the accumulation of precipitation in the pores of the membrane. It is known [30] that the introduction of inorganic dopants into the membrane matrix leads to an increase in the moisture content of the ion-exchange material. In this case, the immobilized nanoparticles replace part of the electroneutral solution in the inter-gel spaces of the membrane, which leads to an increase in their volume fraction and a simultaneous decrease in the fraction of the electroneutral solution in the membrane [48]. For cation exchange membranes, diffractometric analysis of calcination residues failed to detect significant differences between new (CEM_{prist}) and spent (CEM_1, CEM_2) samples. Consequently, sedimentation in cation exchange membranes during their long-term operation in an electrodialysis unit most likely does not occur. A similar effect of an increase in moisture content unrelated to precipitation was observed in [24] during prolonged exposure to temperature and pH variation of the solution.

A feature of the studied anion exchange membranes, on the contrary, is the formation of precipitation during operation in an ED installation. Despite the fact that mineral deposits formed during the use of AEM during the concentration/desalination of wastewater from the production of complex mineral fertilizers are not visually detected during SEM analysis (Fig. 5), diffractometric analysis of the calcined residue of anion exchange membranes after one and five years of use showed the presence of the following substances in IEM: $CaSO_4$, $Ca(H_2PO_4)_2$, Fe_2O_3, Na_3PO_4 (AEM_1); $Ca(OH)_2$, Fe_2O_3, and Na_3PO_4 (AEM_2). The ash residue weights were 0.4 and 0.8 mg/g for AEM_1 and AEM_2, respectively, which indicates an increase in the proportion of mineral deposits in the volume of IEM during the operation of the membranes. The calculation of the particle size of the mineral components in the ash residue according to diffractometry data [40] showed that they have a diameter from 9 to 45 nm. This allows us to make an assumption about the localization of precipitation in IEM nanopores, which is consistent with the results of [40, 49]. The calculation of the relative moisture capacity leads to higher values for AEM_2 compared to CEM_2, which also correlates with the accumulation of precipitation in anion-exchange membranes and is consistent with data on an increase in moisture content in membranes doped with hydrated metal oxides [30]. In contrast to [48], in the present work, the appearance of sediment nanoparticles in the pores of the anion exchange membrane leads to a decrease in the proportion of strongly bound rather than weakly bound water. Considering that the moisture content of membranes is determined by complex internal interactions between water molecules, functional groups, and the hydrophobic matrix, it is difficult to expect an unambiguous dependence of this value on only one factor (precipitation) while changing others at the same time. Moreover, in the case of both types of membranes, the main factor in the increase in moisture content appears to be an increase in the number and size of pores and/or defects in the heterogeneous sample due to membrane degradation during prolonged operation in an electrodialysis unit.

To confirm this assumption, we analyzed the SEM images of the surface of the studied membranes shown in Figs. 5 and 6. The main surface material of the IEM is a composite: polyethylene with ion exchange resin particles fairly evenly distributed in it. In addition, cavities (voids) are visible on the surface for all

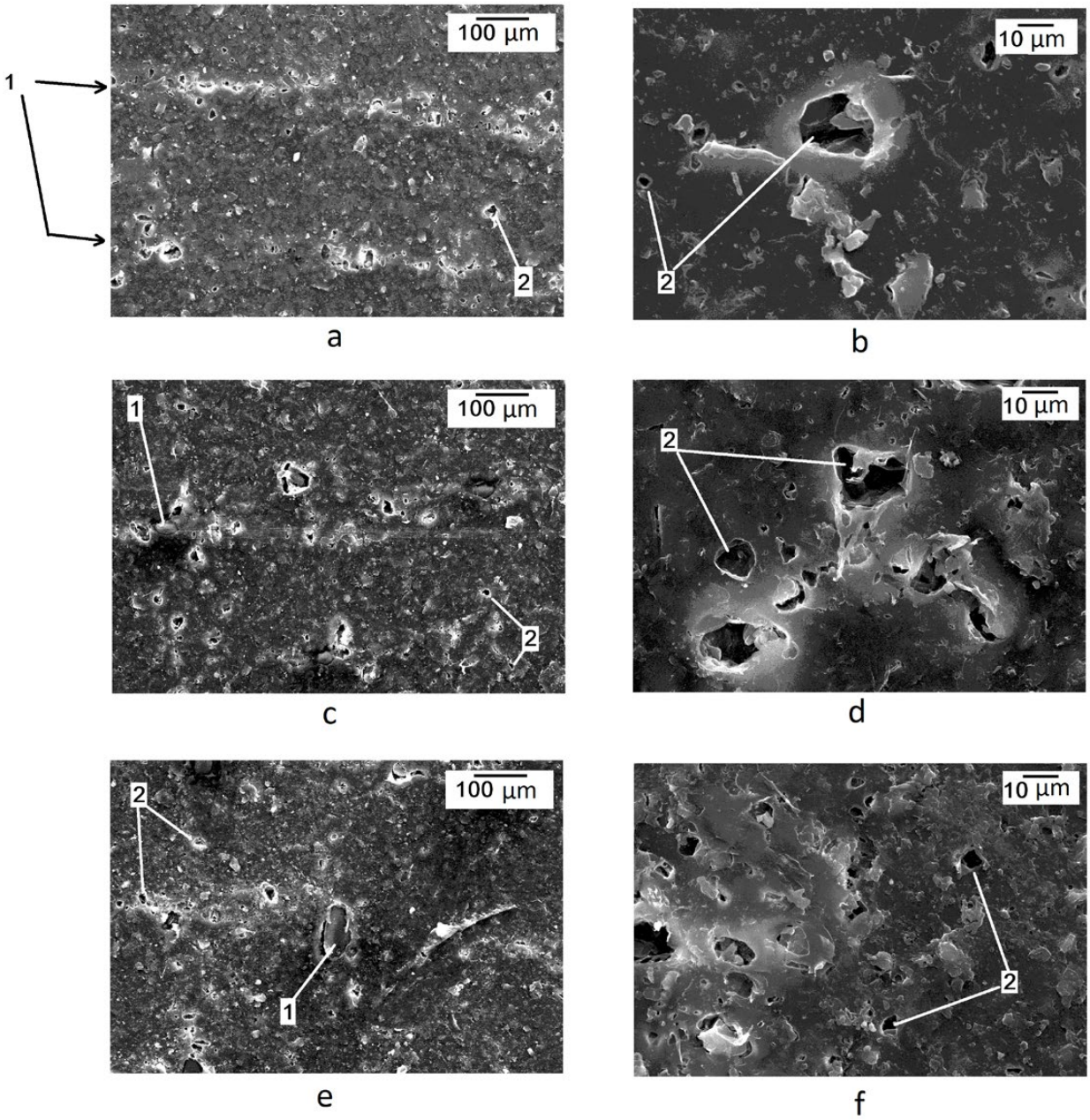

Fig. 5. SEM images of the surface of the anion exchange membranes under study: a, b – AEM_{prist}; c, d – AEM_1; e, f – AEM_2 ; a, c, e – magnification ×150; b, d, f – magnification ×1000

anion–exchange membranes, and fragments of reinforcing tissue are also visible for AEM_1 and AEM_2. For AEM_{prist} (Fig. 5a) the reinforcing fabric is not explicitly detected on the surface, however, there is a noticeable violation of the uniformity of distribution of the polyethylene/ion exchanger composite over the threads of the reinforcing fabric. As the time of using AEM in the electrodialyzer increases, the reinforcing fabric reaches the surface (Fig. 5, c, e): polyester fragments up to 60×40 microns in size for AEM_1, enlarging to 160×60 microns for AEM_2, are visualized on the SEM images. An increase in the size of the sections of reinforcing fabric extending to the surface naturally leads to an increase in the gaps between the reinforcement strands and the polyethylene/ion exchanger composite material. To assess the changes in the state of the cavities and walls, the membrane sections located between the strands of the reinforcing

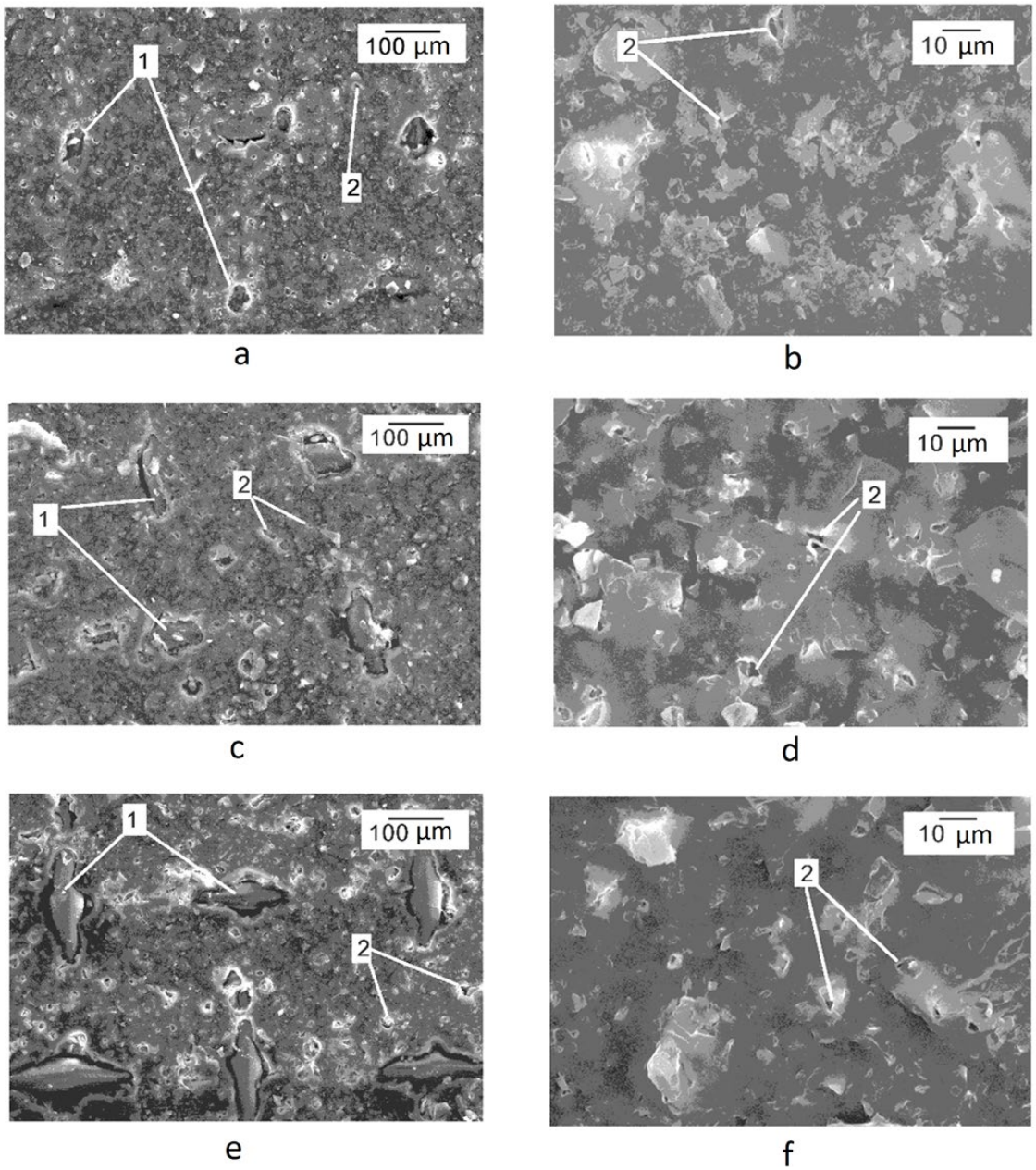

Fig. 6. SEM images of the surface of the cation exchange membranes under study: a, b – CEM_{prist}; c, d – CEM_1; e, f – CEM_2 ; a, c, e - magnification ×150; b, d, f – magnification ×1000

mesh were examined at a higher magnification (Fig. 5b, d, e). For AEM_{prist}, the size of the voids reaches 24 microns. As the operating time of the IEM increases, the size of the caverns does not increase, however, there is an increase in their number. In the case of cation exchange membranes (Fig. 6), a larger (compared to AEM) fraction of the surface is occupied by reinforcing tissue. The main change found during the operation of cation exchange membranes in the electrodialyzer is the appearance of reinforcing fabric on the surface: the size of polyester filaments found on the SEM images of IEM increases in the $CEM_{prist} < CEM_1 < CEM_2$ range and amounts to (microns): 4×3, 13×6, and 15×6, respectively.

Thus, the analysis of the SEM images shows that, compared with the conditioned CEM_{prist} and AEM_{prist} samples, prolonged operation led to a more noticeable manifestation of defects caused

by the formation of cavities and the appearance of reinforcing tissue on the surface. Both cationic (CEM_1, CEM_2) and anion-exchange (AEM_1, AEM_2) membranes are characterized by an increase in the content of macropores formed between the reinforcing fabric and the ion exchanger + polyethylene composite.

In addition, the presence of large [50, 51] and highly hydrated [50, 52, 53] ions in the processed solutions can lead to stretching of the IEM matrix and, consequently, an increase in the size of the pores filled with solution or water. The latter is supported by the observed increase in the thickness of the initial and spent membranes, which swelled under the same conditions (Table 1). In turn, an increase in the content of strongly bound water may be due to an increase in the distance between fixed groups of the ion-exchange material during the degradation of the crosslinking agent, as was shown by the example of the KU-2 sulfocation ion exchanger with different divinylbenzene content [33].

4. Conclusion

The moisture content and thermal effect of dehydration of cation exchange (RalexCMH-Pes) and anion exchange (RalexAMH-Pes) membranes were thermogravimetrically determined before and after their long-term use in industrial electrodialysis plants during the concentration/desalination of multicomponent salt solutions, waste products from the production of complex mineral fertilizers. It was found that the moisture capacity of the membranes and the specific heat of dehydration, regardless of the type of membrane, increase with increasing duration of operation of the electrodialyzer. The molar thermal effect is practically independent of the type of membrane and the duration of its use and averages 39.0±1.8 and 35.8±1.2 kJ/mol for cation-exchange and anion-exchange membranes, respectively, which corresponds to the formation of associates of 2–4 water molecules.

The estimation of the total and relative content of kinetically unequal water molecules in the membranes showed the highest fraction of weakly and moderately bound water, which ranges from 87.0 to 90.2 % for cation exchange membranes and 79.3 to 85.0 % for anion exchange membranes. The contribution of water molecules involved in the strong ion-dipole interaction with the functional groups of the membrane is the smallest. The nature of changes in the content of water molecules with different degree of binding depends on the type of membrane depending on the time of use: if for cation exchange membranes during operation the proportion of strongly bound water increases from 9.6 to 13.0 %, then in the case of anion exchange membranes, on the contrary, it decreases from 19.3 to 15.0 %.

The discovered effects of an increase in moisture content and a redistribution of water fractions of different degree of binding can be explained by an increase in the number of defects (cavities) and the release of reinforcing tissue onto the membrane surface, as well as an increase in the size of macropores filled with solution or water. These changes in membrane morphology may be caused by membrane degradation during prolonged operation in an electrodialysis unit. A feature of anion exchange membranes is the diffractometrically confirmed formation of inorganic precipitation, the hydrophilic particles of which are localized in the nanopores of the membrane, which probably contributes to an additional increase in the moisture content of the anion exchange material.

Contribution of the authors

Kozaderova O. A. – head of the grant, idea, scientific guidance, research concept, development of methodology, conducting research, writing a paper. Saranov I. A. – conducting research.

Conflict of interests

The authors declare that they have no known competing financial interests or personal relationships that could have influenced the work reported in this paper.

References

1. Al-Amshawee S., Yunus M. Y. B. M., Azoddein A. A. M., Hassell D. G., Dakhil I. H., Hasan H. A. Electrodialysis desalination for water and wastewater: a review. *Chemical Engineering Journal*. 2020;380: 122231. https://doi.org/10.1016/j.cej.2019.122231

2. Fadillah G., Hidayat R., Saputra A., ... Ohira S.-I. Advanced electrodialysis techniques for analytical separation: a comprehensive review. *Analytica Chimica Acta*. 2025: 344637. https://doi.org/10.1016/j.aca.2025.344637

3. Konarev A. Use of electrodialysis in the pilot- and commercial-scale production of pharmaceutical substances.

Russian Journal of Electrochemistry. 2015;51: 1124–1134. https://doi.org/10.1134/S1023193515110051

4. Wang M., Kuang S., Wang X., ... Zhang Y. Transport of amino acids in soy sauce desalination process by electrodialysis. *Membranes*. 2021;11: 408. https://doi.org/10.3390/membranes11060408

5. Mohammadi R., Tang W., Sillanpää M. A systematic review and statistical analysis of nutrient recovery from municipal wastewater by electrodialysis. *Desalination*. 2021;498: 114626. https://doi.org/10.1016/j.desal.2020.114626

6. Xie M., Shon H. K., Gray S. R., Elimelech M. Membrane-based processes for wastewater nutrient recovery: technology, challenges, and future direction. *Water Research*. 2015;89: https://doi.org/10.1016/j.watres.2015.11.045

7. Ferrari F., Pijuan M., Molenaar S., ... Radjenovic J. Ammonia recovery from anaerobic digester centrate using onsite pilot scale bipolar membrane electrodialysis coupled to membrane stripping. *Water Research*. 2022;218: 118504. https://doi.org/10.1016/j.watres.2022.118504

8. Vineyard D., Hicks A., Karthikeyan K., Davidson Ch., Barak Ph. Life cycle assessment of electrodialysis for sidestream nitrogen recovery in municipal wastewater treatment. *Cleaner Environmental Systems*. 2021;2: 100026. https://doi.org/10.1016/j.cesys.2021.100026

9. Mondor M., Masse L., Lamarche F., Massé D. Use of electrodialysis and reverse osmosis for the recovery and concentration of ammonia from swine manure. *Bioresource technology*. 2008;99: 7363-8. https://doi.org/10.1016/j.biortech.2006.12.039

10. Pismenskaya N. D., Rybalkina O. A., Tsygurina K. A., ... Bazinet L. Production of cheap phosphorus-ammonium fertilizers using electrodialysis. Problems and solutions. In: *Membrane process modeling: abstracts of the international conference dedicated to the 60th anniversary of Professor A. N. Filippov. December 3-4, 2020, Moscow.* Moscow: Logos Publ.; 2020. P. 68–69. Available at: https://kvm.gubkin.ru/Abstracts_RGU.pdf

11. Huang Ch., Xu T., Zhang Y., Xue Y., Chen G. Application of electrodialysis to the production of organic acids: State-of-the-art and recent developments. *Journal of Membrane Science*. 2007;288: 1. https://doi.org/10.1016/j.memsci.2006.11.026

12. Bagastyo A. Y., Anggrainy A. D., Nindita C. S., Warmadewanthi. Electrodialytic removal of fluoride and calcium ions to recover phosphate from fertilizer industry wastewater, *Sustainable Environment Research*. 2017;27(5): 230–237. https://doi.org/10.1016/j.serj.2017.06.002

13. Hikmawati D., Bagastyo A., Warmadewanthi I. Electrodialytic recovery of ammonium and phosphate ions in fertilizer industry wastewater by using a continuous-flow reactor. *Journal of Ecological Engineering*. 2019;20: 255. https://doi.org/10.12911/22998993/109461

14. Niftaliev S. I., Kozaderova O. A., Kim K. B., Malyavina Yu. M., Electrodialysis in the treatment of nitrogen-containing wastewater of a mineral fertilizer manufacturing enterprise*. *Chemical Industry Developments*. 2014;7: 52. (in Russ.). Available at: https://elibrary.ru/item.asp?id=22017822

15. Bokhary A., Tikka A., Leitch M., Liao B.Q. Membrane fouling prevention and control strategies in pulp and paper industry applications: a review. *Membrane*. 2018;4(4): 181. https://doi.org/10.22079/jmsr.2018.83337.1185

16. Apel P. Yu., Velizarov S., Volkov A. V., Yaroslavtsev A. B. Fouling and membrane degradation in electromembrane and baromembrane processes. *Membranes and Membrane Technologies*. 2022;4: 69–92. https://doi.org/10.1134/S2517751622020032

17. Gally C. R., Benvenuti T., Trindade C. M., ... Bernardes A. M. Electrodialysis for the tertiary treatment of municipal wastewater: Efficiency of ion removal and ageing of ion exchange membranes. *Journal of Environmental Chemical Engineering*. 2018;6(5): 5855–5869. https://doi.org/10.1016/j.jece.2018.07.052

18. Vasil'eva V. I., Akberova E. M., Kostylev D. V., Tzkhai A. A. Diagnostics of the structural and transport properties of an anion-exchange membrane MA-40 after use in electrodialysis of mineralized natural waters. *Membranes and Membrane Technologies*. 2019;1(3): 153–167. https://doi.org/10.1134/S2517751619030077

19. Vasil'eva V. I., Akberova E. M., Goleva E. A., Yatsev A. M., Tzkhai A. A. Changes in the microstructure and operational characteristics of the MK-40 sulfocation-exchange membrane during the electrodialysis of natural waters. *Journal of Surface Investigation: X-Ray, Synchrotron and Neutron Techniques*. 2017;11(2): 429–436. https://doi.org/10.1134/S1027451017020367

20. Pasechnaya E. L., Ponomar M. A., Klevtsova A. V., Korshunova A. V., Sarapulova V. V., Pismenskaya N. D. Characteristics of aliphitic and aromatic ion-exchange membranes after electrodialysis tartrate stabilization of wine materials *Membranes and Membrane Technologies*. 2024;14(4): 317–332. https://doi.org/10.31857/S2218117224040079

21. Ghalloussi R., Garcia-Vasquez W., Bellakhal N., ... Grande D. Ageing of ion-exchange membranes used in electrodialysis: Investigation of static parameters, electrolyte permeability and tensile strength. *Separation and Purification Technology*. 2011;80(2): 270-275. https://doi.org/10.1016/j.seppur.2011.05.005

22. Ghalloussi R., Chaabane L., Dammak L., Grande D. Ageing of ion-exchange membranes used in an electrodialysis for food industry: SEM, EDX, and limiting current investigations. *Desalination and Water Treatment*. 2015;56(10): 2561–2566. https://doi.org/10.1080/19443994.2014.968908

23. Kharina A. Yu., Charushina O. E., Eliseeva T. V. Organic fouling of anion-exchange and bipolar membranes during the separation of amino acid and sucrose by electrodialysis. *Condensed Matter and Interphases*.. 2023;25(2): 268–276. https://doi.org/10.17308/kcmf.2023.25/11107

24. Vasil'eva V. I., Akberova E. M., Shaposhnik V. A., Malykhin M. D. Electrochemical properties and structure of ion-exchange membranes upon thermochemical treatment. *Russian Journal of Electrochemistry*. 2014;50(8): 789–797. https://doi.org/10.1134/S102319351408014X

25. Vasil'eva V. I., Akberova E. M., Pismenskaya N. D., Nebavskaya K. A. Effect of thermochemical treatment on the surface morphology and hydrophobicity of heterogeneous ion-exchange membranes. *Russian Journal of Physical Chemistry A*. 2014;88(8): 1293-1299. https://doi.org/10.1134/S0036024414080317

26. Volodin D. N., Magomedova N. V., Voropayev A. N. The use of electromembrane technology in wastewater treatment. *Vodoochistka. Vodopodgotovka. Vodosnabzhenie.*

2015;92(8): 32–36. (In Russ.). Available at: https://elibrary.ru/item.asp?id=24146800

27. Kozaderova O. A., Kim K. B., Niftaliev S. I. Changes of physicochemical and transport characteristics of ion exchange membranes in the process of operation under demineralization of wastewater water production of nitrogen-containing mineral fertilizers *Sorbtsionnye I Khromatograficheskie Protsessy*. 2018;18(6): 875–885. (in Russ.). https://doi.org/10.17308/sorpchrom.2018.18/616

28. Han L. Aging and degradation of ion-exchange membranes. In: *Zhang Z., Zhang W., Chehimi M.M. (eds.) Membrane technology enhancement for environmental protection and sustainable industrial growth. Advances in Science, Technology & Innovation*. 2021. Springer, Cham. https://doi.org/10.1007/978-3-030-41295-1_3

29. Shaposhnik V. A. The role of hydration in ion exchange separations. Kinetics and dynamics of metabolic processes✉. *In: Fundamental problems of Separation Science: Abstracts of the VIII All-Russian Symposium with international participation, November 18–22, 2019, Moscow*. Moscow: Publishing House "Frontier"; 2019. p. 34–36. (in Russ.). Available at: https://elibrary.ru/item.asp?id=44353630&selid=44353758

30. Safronova E. Y., Yaroslavtsev A. B., Volkov V. I., Pavlov A. A., Chernyak A. V., Volkov E. V. Hydration of the H^+, Li^+, Na^+, and Cs^+ ions in MF-4SK perfluorinated sulfonic acid cation-exchange membranes modified with inorganic dopants. *Russian Journal of Inorganic Chemistry*. 2011;56(2): 156–162. https://doi.org/10.1134/S0036023611020240

31. Zyryanova S., Mareev S., Gil V., ... Dammak L. How electrical heterogeneity parameters of ion-exchange membrane surface affect the mass transfer and water splitting rate in electrodialysis. *International Journal of Molecular Sciences*. 2020;21(3): 973. https://doi.org/10.3390/ijms21030973

32. Kharina A. Yu., Eliseeva T. V. Cation-exchange membrane MK-40 characteristics in electrodialysis of mixed solutions of mineral salt and amino acid. *Sorbtsionnye I Khromatograficheskie Protsessy*. 2017;17(1): 148–155. (in Russ.). https://doi.org/10.17308/sorpchrom.2017.17/364

33. Kotova D. L., Selemenev V. F. *Thermal analysis of ion-exchange matherials**. Moscow: Nauka Publ.; 2002. 157 p. (in Russ.)

34. Kononenko N., Nikonenko V., Grande D., ... Volfkovich Yu. Porous structure of ion exchange membranes investigated by various techniques *Advances in Colloid and Interface Science*. 2017;246: 196–216. https://doi.org/10.1016/j.cis.2017.05.007

35. Sarapulova V. V., Titorova V. D., Nikonenko V. V., Pismenskaya N. D. Transport characteristics of homogeneous and heterogeneous ion-exchange membranes in sodium chloride, calcium chloride, and sodium sulfate solutions. *Membranes and Membrane Technologies*. 2019;1(3): 168–182. https://doi.org/10.1134/S2517751619030041

36. Krisilova E. V., Eliseeva T. V., Oros G. Y. Effect of amino acid sorption on formation of water clusters in ion-exchange membranes. *Colloid Journal*. 2011;73(1): 72–75. https://doi.org/10.1134/S1061933X11010091

37. https://www.mega.cz/membranes/#what-we-do

38. Niftaliyev S. I., Kouznetsova I. V., Peregoudov Yu. S., Okshin V. V., Melnik A. V. Prospects for utilization of sewage from the "FERTILIZERS" open joint-stock company. *Ecology and Industry of Russia*. 2012;(5): 36–39. (In Russ.). https://doi.org/10.18412/1816-0395-2012-5-36-39

39. Kononenko N. A., Demina O. A., Loza N. V., Falina I. V., Shkirskaya S. A. *Membrane electrochemistry**. Krasnodar: Kubanskii gosudarstvennyi universitet Publ.; 2015. 290 p. (In Russ.)

40. Kozaderova O. A. Electrochemical characterization of an MB-2 bipolar membrane modified by nanosized chromium(III) hydroxide. *Nanotechnologies in Russia*. 2018;13(9-10): 508–515. https://doi.org/10.1134/S1995078018050075

41. Astapov A. V., Peregudov Y. S., Kopylova V. D. The state of water in different forms of sulfo ion-exchange fiber. *Russian Journal of Physical Chemistry A*. 2011;85(7): 1253–1256. https://doi.org/10.1134/S0036024411070028

42. Yaroshenko F. A. *Proton conductivity of composite materials based on polymers modified with polysuric acid**. Cand. chem. sci. diss. Chelyabinsk: 2020. 131 p. Available at: https://www.dissercat.com/content/protonnaya-provodimost-kompozitsionnykh-materialov-na-osnove-polimerov-modifitsirovannykh/read

43. Vainertova K., Krshivchik I., Nedela D., ... Movsumzade E. M. Polymer binders for ion-exchange membranes with improved mechanical strength. *Industrial Production and Use Elastomers*. 2016;2: 33–42. (In Russ.). Available at: https://www.elibrary.ru/item.asp?id=26599727

44. Eliseeva T. V., Zyablov A. N., Kotova D. L., Selemenev V. F. Hydration of ion-exchange membranes saturated with amino acids. *Russian Journal of Physical Chemistry A*. 1999;73(5): 783–785. Available at: https://www.elibrary.ru/item.asp?id=13321063

45. Zyablov A. N. Hydration of amino acids and ion-exchange membranes in amino acid forms and its effect on diffusion transport*. Cand. chem. sci. diss. Voronezh: 1999. 162 p. Available at: https://www.dissercat.com/content/gidratatsiya-aminokislot-i-ionoobmennykh-membran-v-aminokislotnykh-formakh-i-ee-vliyanie-na-

46. Zyablov A.N., Eliseeva T.V., Kotova D.L. Thermal analysis as a method for studying the hydration of ion-exchange membranes in amino acid forms*. *Teoriya i praktika sorbtsionnykh protsessov*. 1999;24: 57–58. (In Russ.)

47. Kozaderova O. A., Sinyaeva L. A., Khukharkina Y. S. Contact-difference method for measuring electrical conductivity in determination of the transport characteristics of heterogeneous ion-exchange membranes of different service life in an industrial electrodialyzer. *Sorbtsionnye I Khromatograficheskie Protsessy*. 2025;25(3): 316–327. (in Russ.). https://doi.org/10.17308/sorpchrom.2025.25/13043

48. Porozhny M. V. Electrochemical characteristics of ion-exchange membranes with organic and inorganic immobilized nanoparticles*. Cand. chem. sci. diss. Krasnodar: 2018. 112 p. (in Russ.)

49. Yurova P. A., Karavanova Y. A., Stenina I. A., Yaroslavtsev A. B. Synthesis and studies on the diffusion properties of MK-40 cation-exchange membranes modified with ceria. *Nanotechnologies in Russia*. 2016;11(11-12): 761–765. https://doi.org/10.1134/S1995078016060215

50. Helfferich F. G. *Ionenaustauscher. Band 1: Grundlagen. Struktur - Herstellung – Theorie*. Weinheim: Verlag Chemie; 1959.

51. Pismenskaya N., Sarapulova V., Nevakshenova E., Kononenko N., Fomenko M., Nikonenko V. Concentration

dependencies of diffusion permeability of anion-exchange membranes in sodium hydrogen carbonate, monosodium phosphate, and potassium hydrogen tartrate solutions. *Membranes*. 2019;9: 170. https://doi.org/10.3390/membranes9120170

52. Kononenko N. A., Berezina N. P. Research methods and characterization of synthetic polymer membranes. In: *Membranes and Membrane technologies**. Moscow: Nauchny Mir Publ., 2013. p. 402–455. (in Russ.)

53. Koga Y., Kondo T., Miyazaki Y., Inaba A. The effects of sulphate and tartrate ions on the molecular organization of water: towards understanding the hofmeister series (VI). *Journal of Solution Chemistry*. 2012;41: 1388–1400. https://doi.org/10.1007/s10953-012-9880-x

* *Translated by author of the article*

Information about the authors

Olga A. Kozaderova, Professor, Dr. Sci. (Chem.), Professor at the Department of Inorganic Chemistry and Chemical Technology, Voronezh State University of Engineering Technologies (Voronezh, Russian Federation).

https://orcid.org/ 0000-0002-8135-5801

kozaderova-olga@mail.ru

Igor A. Saranov, Cand. Sci. (Tech.), Associate Professor at the Department of Information Security, Voronezh State University of Engineering Technologies (Voronezh, Russian Federation).

https://orcid.org/ 0000-0002-9510-5168

mr.saranov@mail.ru

Received August 11, 2025; accepted after reviewing November 13, 2025; accepted for publication November 17, 2025; published online December 25, 2025.

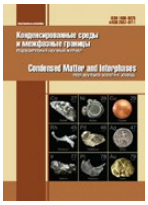

ISSN 1606-867X (Print)
ISSN 2687-0711 (Online)
Condensed Matter and Interphases
Kondensirovannye Sredy i Mezhfaznye Granitsy
https://journals.vsu.ru/kcmf/

Original articles

Research article
https://doi.org/10.17308/kcmf.2025.27/13320

Synthesis and anticorrosive properties of 2-alkyl-5-methyl-4,5,6,7-tetrahydro-[1,2,4]triazolo[1,5-a]pyrimidin-7-ols

A. A. Kruzhilin✉, D. S. Shevtsov, I. A. Dmitriev, M. A. Potapov, Kh. S. Shikhaliev

Voronezh State University,
1 Universitetskaya pl., Voronezh 394018, Russian Federation

Abstract

Objectives: The aim of the study is to synthesize a series of 2-alkyl-5-methyl-4,5,6,7-tetrahydro-[1,2,4]triazolo[1,5-a]pyrimidin-7-ols, to investigate their inhibitory properties and the regularities of their interaction with a steel surface, in order to create a new generation of efficient and environmentally friendly acid corrosion inhibitors.

Experimental: The paper presents the results of synthesis and investigation of the anticorrosion properties of new 2-alkyl-5-methyl-4,5,6,7-tetrahydro-[1,2,4]triazolo[1,5-a]pyrimidin-7-ol derivatives obtained from individual fatty acids and vegetable oils. The reaction of aminotriazoles with crotonaldehyde in an amphoteric surfactant medium made it possible to develop a method for producing the target compounds with high yield and purity. The anticorrosion properties of the synthesized triazolopyrimidinol derivatives were studied with respect to St3 steel in 24% HCl using both direct methods (GOST 9.905-82, 9.907-83) and electrochemical techniques (potentiodynamic polarization and polarization resistance method according to Mansfeld). Electrochemical tests by potentiodynamic polarization and direct corrosion measurements in 24% HCl showed that all investigated compounds exhibited a pronounced inhibiting effect on St3 steel.

Conclusions: It has been established that all investigated compounds act as mixed-type inhibitors. The most effective ones were the derivatives obtained from coconut oil, providing protection efficiencies up to 98.5% at concentrations of 1–2 g/L. Comparison of gravimetric and polarization data revealed that the high instantaneous protection efficiencies determined by electrochemical methods correspond to intensive physical adsorption of inhibitor molecules immediately after their introduction. However, during prolonged exposure in direct gravimetric tests, a decrease in protection efficiency was observed for compounds with alkyl substituents of C13 and longer, which is attributed to the partial instability and desorption of the protective films under extended acid exposure. This leads to localized corrosion on certain surface areas and a reduction in the overall protection efficiency. The results confirm the promise of synthesizing 4,5,6,7-tetrahydro-[1,2,4]triazolo[1,5-a]pyrimidin-7-ols from renewable plant-based feedstocks for the development of biodegradable acid corrosion inhibitors.

Keywords: Corrosion, Steel, Hydrochloric acid, Corrosion inhibitors, Heterocyclic compounds, Vegetable oils, Aminotriazoles, Tetrahydrotriazolopyrimidinols, Physicochemical research methods

Funding: The study was supported by Russian Science Foundation (project No. 24-23-00457, https://rscf.ru/project/24-23-00457/).

For citation: Kruzhilin A. A., Shevtsov D. S., Dmitriev I. A., Potapov M. A., Shikhaliev Kh. S. Synthesis and anticorrosive properties of 2-alkyl-5-methyl-4,5,6,7-tetrahydro-[1,2,4]triazolo[1,5-a]pyrimidin-7-ols. *Condensed Matter and Interphases*. 2025;27(4): 630–638. https://doi.org/10.17308/kcmf.2025.27/13320

Для цитирования: Кружилин А. А., Шевцов Д. С., Дмитриев И. А., Потапов М. А., Шихалиев Х. С. Синтез и антикоррозионные свойства 2-алкил-5-метил-4,5,6,7-тетрагидро-[1,2,4]триазоло[1,5-a]пиримидин-7-олов. *Конденсированные среды и межфазные границы*. 2025;27(4): 630–638. https://doi.org/10.17308/kcmf.2025.27/13320

✉ Alexey A. Kruzhilin, e-mail: kruzhilin.alexey@gmail.com

1. Introduction

In modern technologies of acid treatment of oil and gas wells, inhibited acids are widely used to protect the steel components of equipment from intense acid corrosion [1–3]. Their composition is primarily based on organic compounds capable of adsorbing on the metal surface and forming a protective film that prevents direct contact of the acid with the metal. The most studied and commonly applied classes of such compounds are nitrogen- and sulfur-containing inhibitors, as well as composite systems based on them with the addition of surfactants [4].

Nitrogen-containing heterocycles, such as benzotriazole and its derivatives, are characterized by high efficiency in hydrochloric acid and by the stability of their adsorption layer at moderate temperatures. Their advantages include low volatility, compatibility with acid solutions, and the ability to form complexes with iron ions. However, as temperature increases, their protective performance may decrease, which necessitates either structural modification of the molecule or the use of synergistic additives. Sulfur-containing compounds, such as thiourea and certain benzothiazole derivatives, demonstrate good activity under harsher conditions, but their effectiveness is often limited by instability in oxidative environments and by high sensitivity to the composition of formation waters.

The most stable protection is provided by combined systems in which nitrogen- and sulfur-containing compounds are complemented by cationic or nonionic surfactants. Such compositions are characterized by strong adsorption capacity and uniform distribution over the metal surface. However, their multicomponent nature complicates the optimization of their formulation and may reduce environmental acceptability. In this regard, new generations of inhibitors based on biodegradable and renewable sources are of particular interest, as they combine the efficiency of traditional organic inhibitors with environmental safety and the availability of raw materials. This is especially relevant for modern reservoir treatment technologies oriented toward the principles of "green chemistry" [5].

In light of these considerations, one of the most promising areas is the synthesis of corrosion inhibitors derived from plant-based raw materials, particularly fatty acids and vegetable oils. The authors have previously shown [6–7] that derivatives of certain triazolopyrimidines obtained from vegetable oils exhibit high inhibition efficiency toward acid corrosion of steel in 24% HCl. These compounds contain active centers (N atoms and OH groups) capable of strong coordination with the steel surface and formation of stable protective layers.

Another class of structurally related inhibitors is represented by 2-alkyl-5-methyl-4,5,6,7-tetrahydro-[1,2,4]triazolo[1,5-a]pyrimidin-7-ols. The development of a method for their synthesis, along with an investigation of their inhibitory properties and interaction mechanisms with the steel surface, represents an important task for creating a new generation of efficient and environmentally friendly acid corrosion inhibitors.

2. Experimental

Spectral analysis method

Chromatographic analysis of the purity of the obtained compounds was performed using an Agilent 1260 Infinity chromatograph with UV and mass detection (Agilent 6230 TOF LC/MS detector, electrospray ionization). Chromatographic conditions were as follows: column Gemini C18 (4.6×50 mm); sorbent particle diameter 5 μm; linear gradient elution; mobile phase: eluent A – MeCN–H_2O, 2.5 : 97.5, 0.1 % CF_3COOH, eluent B – MeCN, 0.1 % CF_3COOH, mobile phase flow rate 3.75 ml/min; column oven temperature 40 °C; injection volume 1.5 μL.

*General procedure for the synthesis of 3-substituted 5-amino-1H-1,2,4-triazoles (**1a-c**)*

To a solution of 0.1 mol of the corresponding carboxylic acid in 100 mL of butanol, 0.1 mol (13.6 g) of aminoguanidine bicarbonate was added in portions. The mixture was heated to 90–95 °C (evolution of carbon dioxide was observed) and then refluxed using a Dean–Stark apparatus equipped with a reflux condenser fitted with a calcium chloride drying tube for approximately 20 hours. After this period, 2 g of sodium hydroxide was added to the reaction mixture, and refluxing was continued for an additional 5 hours to induce cyclization of the intermediate 1a–c*. Completion of the reaction was monitored by the amount of water collected in the Dean–Stark trap

(~3.5 cm^3). The reaction mixture was then cooled, and the resulting mixture of triazoles was washed with water and extracted using a butanol–water system, removing the aqueous phase three times. The organic layer was dried over sodium sulfate, and the solvent was subsequently removed under reduced pressure using a rotary evaporator.

*General procedure for the synthesis of 3-substituted 5-amino-1H-1,2,4-triazoles (**1d-f**)*

For the synthesis based on vegetable oils, a solution of approximately 0.1 mol of vegetable oil in 100 mL of butanol was treated dropwise with 1 mL of sulfuric acid, followed by the portionwise addition of 0.3 mol (40.8 g) of aminoguanidine bicarbonate. The subsequent procedure was carried out according to the method described above.

*General procedure for the synthesis of 2-alkyl-5-methyl-4,5,6,7-tetrahydro-[1,2,4] triazolo[1,5-a]pyrimidin-7-ol derivative (**2a-f**)*

A mixture of 0.1 mol of cinnamaldehyde and ~ 0.1 mol of the aminotriazole mixture **1a-f** in the presence of an amphoteric surfactant (40 wt.% of the total reagent weight) was kept at 80–85 °C for 15 minutes. The mixture was then cooled down and analyzed without extraction or further treatment.

Electrochemical studies

The obtained 2-alkyl-5-methyl-4,5,6,7-tetrahydro-[1,2,4]triazolo[1,5-a]pyrimidin-7-ol derivatives were analyzed with regard to their anticorrosive activity towards acid corrosion on St3 steel in a 24% HC solution using gravimetric direct corrosion tests and potentiodynamic polarization method.

Gravimetric direct corrosion tests were performed according to GOST 9.907-83 "Methods for the removal of corrosion products after corrosion tests".

Corrosion tests were carried out on steel plates (20×40 mm, thickness 1.2 mm). Each sample was preliminarily polished with K1000 fine-grained sandpaper, after which it was washed with distilled water, ethanol, and dried with filter paper. The experiments were carried out in a 24% HCl solution (for 7 days) under natural aeration without stirring for three samples in parallel (for each inhibitor concentration). After testing, the plates were washed with distilled water and treated with compositions in accordance with GOST 9.907-83.

The corrosion rate was determined according to the mass loss of the samples and was calculated using the formula:

$$k_{inh} = \frac{\Delta m}{S \times t},$$

where $\Delta m = m_0 - m$ (m_0 is the mass of the sample before the start of the experiment, m – is the mass of the sample after the test, g), S – is the total surface area of the plate, m^2.

For each solution, the corrosion rate k_0 without an inhibitor additive was determined (k_0(avg) ≈ 16.9 g/m^2·day). The inhibitory effect of aminotriazine derivatives was evaluated according to the value of the inhibition coefficient:

$$\gamma = \frac{k_0}{k_{\text{inh}}}$$

and the degree of protection:

$$Z = \left[\frac{k_0 - k_{inh}}{k_0}\right] \times 100\,\%,$$

where k_0 and k_{inh} are the corrosion rates in the blank solution and in the solution with the inhibitor, respectively.

Calculation of the corrosion rate using the polarization resistance method

Polarization curves were obtained on an electrode made of St3 steel (with an area of 1.0 cm^2) in an electrochemical cell with undivided electrode chambers using an IPC-PRO potentiostat. The working electrode was preliminarily cleaned with K2000 sandpaper and degreased with ethyl alcohol. Electrode potentials (E) were measured relative to the silver chloride electrode, connecting the space of the electrochemical cell and the reference electrode through an electrolytic bridge based on agar-agar and sodium nitrate, and recalculated to the scale of a standard hydrogen electrode (potential was +202 mV relative to SHE). The auxiliary electrode was a platinum mesh.

The test substances were introduced into the acid until the required concentration was obtained. The electrodes were placed in the prepared solution and kept until the onset of a stationary state for 30 min. After the corrosion potential (E_{cor}) was established, polarization curves with a potential scan rate of 0.2 mV/s in the anode and cathode directions were obtained.

Polarization curves were recorded until the current density (i) reached 0.1 A cm^{-2}.

The rate of corrosion in current units was determined by the polarization resistance technique as summarized by Mansfeld [8].

The studies were carried out using a three-electrode cell with undivided cathode and anode spaces without stirring under natural aeration conditions. The reference electrode was silver chloride (potential +202 mV relative to SHE), and the auxiliary electrode was a platinum mesh. The reference electrode was separated from the cell by an electrolytic bridge based on agar-agar and $NaNO_3$.

The working electrode was preliminarily cleaned with P2000 sandpaper, degreased with ethyl alcohol (96%), and washed with distilled water. The electrodes were placed in the prepared solution and kept until the onset of a stationary state for 30 min. When the stationary state was reached, the electrode was polarized in the range of ±30 mV from the E_{cor} value in potentiodynamic mode with a scanning rate of 0.2 mV/s.

Polarization resistance R_p was determined as the slope of the polarization curve at the point E_{cor} in the coordinates $\Delta E - I$, where ΔE is the difference between the current electrode potential and the corrosion potential (E-E_{cor}), and I is the electric current in the measuring circuit. Next, the dependence was replotted with the coordinates $2.3R_pI - \Delta E$. Coefficients b_a and b_c (anodic and cathodic Tafel slopes of the polarization curve) were determined using the TableCurve 2D software as the approximation parameters of the equation:

$$2.3R_pI = \frac{b_a b_c}{b_a + b_c}\left[\exp\left(\frac{E - E_{cor}}{b_a}\right) - \exp\left(-\frac{E - E_{cor}}{b_c}\right)\right].$$

The corrosion current was calculated taking into account the obtained coefficients according to the equation:

$$I_{cor} = \frac{B}{R_p},$$

where B is the Stern-Geary coefficient calculated using the formula:

$$B = \frac{b_a b_c}{2.3(b_a + b_c)}.$$

For the comparison of the data obtained in various studies, the values of the corrosion current density (i_{cor}) calculated using the expression will be presented further:

$$i_{cor} = \frac{I_{cor}}{S},$$

where S is the geometric area of the electrode. For the convenience of further comparison of the obtained data, the ratio of the corrosion current density of each test sample to the current density of the control experiment was calculated ($i^0_{cor} \approx 6.8$ mA/cm^2):

$$Z_i = \frac{i_{cor}}{i^0_{cor}} \times 100\,\%.$$

Measurements for each concentration of the substance were made at least 5 times until reproducible data was obtained with subsequent statistical processing of the measurement results.

3. Results and discussion

1,2,4-Aminotriazoles 1a–c, derived from individual fatty acids (capric, myristic, and stearic acids), as well as mixtures of 1,2,4-aminotriazoles **1d–f** obtained from vegetable oils (coconut, palm, and sunflower), were synthesized via the reaction of aminoguanidine bicarbonate with the corresponding fatty acid or oil according to the previously described procedure [6] (Fig. 1).

The composition of the aminotriazole mixtures **1a-f** was determined by HPLC/MS and was found to be greater than 95 %.

The resulting 3-alkyl-1H-5-amino-1,2,4-triazoles were subjected to further transformation with crotonaldehyde according to a previously reported method [7]. For this purpose, a mixture of 0.1 mol of crotonaldehyde and approximately 0.1 mol of the aminotriazole mixture **1a-f** in an amphoteric surfactant medium was maintained at 80–85 °C for 15 minutes.

During this process, 1,2,4-triazoles underwent a transformation that proceeded in two stages: the first stage involved a Michael addition of the exocyclic amino group to the double bond, followed by a second stage of intramolecular cyclization via nucleophilic attack on the carbonyl group. As a result, derivatives of 2-alkyl-5-methyl-4,5,6,7-tetrahydro-[1,2,4]triazolo[1,5-a] pyrimidin-7-ols (**2a-f**) were formed (Fig. 2).

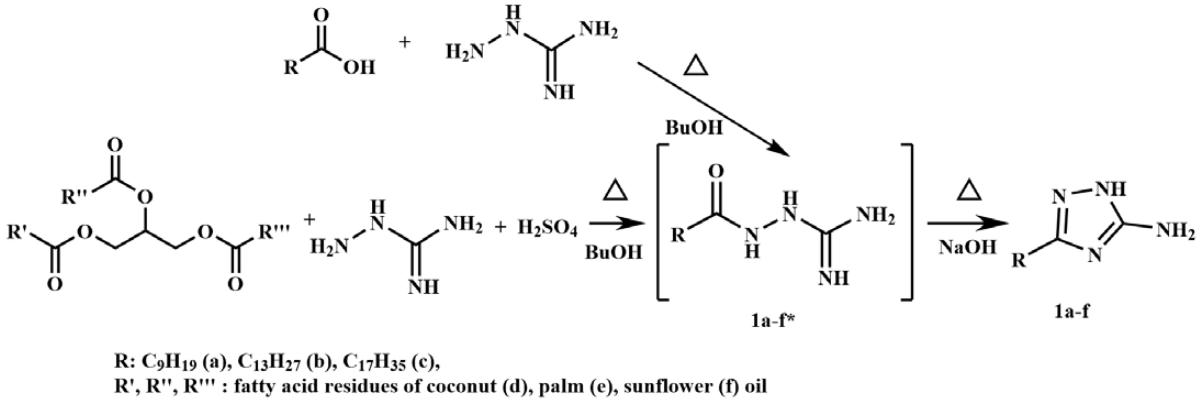

Fig. 1. Scheme for the synthesis of 3-alkyl-1H-5-amino-1,2,4-triazoles

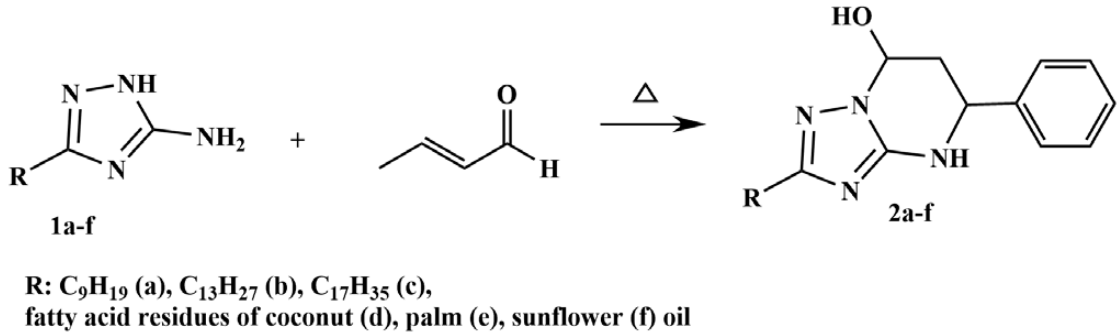

Fig. 2. Reaction of 3-alkyl-1H-5-amino-1,2,4-triazoles with crotonaldehyde

Table 1. Anti-corrosion activity indicators based on the results of direct corrosion tests in 24% HCl

Inhibitor	C_{inh}, g·dm^{-3}	Corrosion rate. k_{inh}, g/(m^2·h)	Inhibition coefficient. γ, %	Protection degree. Z, %
without inhibitor	–	16.90	–	–
2a	1	1.02	9.60	94.05
	2	0.85	11.50	95.03
2b	1	4.46	2.18	73.84
	2	4.32	2.26	74.72
2c	1	7.29	1.34	57.31
	2	4.98	1.96	70.84
2d	1	0.32	30.23	98.11
	2	0.25	38.41	98.51
2e	1	5.25	3.25	69.24
	2	1.92	8.90	88.77
2f	1	10.19	1.67	40.28
	2	9.93	1.72	41.85

The results of direct corrosion tests in 24% HCl (Table 1) showed that all **2a-f** compounds reduced the corrosion rate of St3 steel compared to the uninhibited solution. The most pronounced inhibitory effect was observed for the derivative obtained from coconut oil (**2d**) – the protection efficiency Z reached 98.1–98.5 % at concentrations of 1-2 g/L, corresponding to an inhibition coefficient γ ≈ 30–38, which significantly exceeds the values obtained for other analogues. In

comparison, the derivative **2a**, obtained from an individual carboxylic acid (capric acid), provided 94.0-95.0% protection.

This level of efficiency correlates with the average fatty acid composition of coconut oil, where derivatives with C7–C13 alkyl substituents predominate. A similar relationship between inhibitor structure and protective efficiency was observed for the other triazolopyrimidinol derivatives studied: as the alkyl chain length exceeded 9-10 carbon atoms, a significant decrease in protective performance was noted. This trend is consistent with the known influence of hydrocarbon chain length on surface activity and molecular adsorption ability at the metal-acid interface: excessive chain elongation reduces solubility and, consequently, decreases the packing density of the inhibitor film on the steel surface.

According to polarization measurements of derivatives **2a-c**, a set of anodic and cathodic polarization curves was obtained (Fig. 3). Electrochemical measurements by the potentiodynamic polarization method (Table 2) confirmed the high inhibitory activity of all investigated compounds. The addition of all inhibitors caused a shift of the corrosion potential (E_{cor}) toward the cathodic region by 90–120 mV relative to the blank, accompanied by suppression of both anodic and cathodic reactions, indicating a mixed inhibition mechanism. The shape of the anodic and cathodic branches of the polarization curves remained unchanged, but the current density decreased substantially, suggesting blocking of active corrosion sites without alteration of the iron dissolution mechanism.

The polarization resistance (R_p) increased by tens to hundreds of times (up to 1124 kΩ·cm^2 for compound **2d** at 2 g/L), accompanied by a reduction of the corrosion current density (icor) to 0.021-0.055 mA·cm^{-2}. For comparison, in the absence of an inhibitor, i_{cor} ≈ 6.8 mA·cm^{-2}. The protection degree determined by electrochemical methods (Z_i) ranged from 94–98 %. The high inhibitory activity of the compounds is likely due to their multicenter adsorption character. The molecules contain several donor-acceptor centers (nitrogen atoms of the pyrimidine ring and hydroxyl groups) capable of complex formation with iron ions, probably resulting in the formation of chelate-like surface complexes that produce a dense protective layer preventing the penetration of H^+ and Cl^- ions to the metal surface.

The nature of adsorption, as indicated by the high protection efficiencies and their dependence on concentration, follows the Langmuir adsorption isotherm, suggesting monomolecular surface coverage.

Despite the high protection degrees calculated from potentiodynamic polarization and polarization resistance data (Z_i > 90 %), noticeably lower protection values Z were obtained by gravimetric measurements for certain samples (**2b-2c** and **2e-2f**). This discrepancy

Table 2. Data from electrochemical tests of mixtures of 2-alkyl-5-methyl-4,5,6,7-tetrahydro-[1,2,4] triazolo[1,5-a]pyrimidin-7-ols **2a-f**

Inhibitor	C_{inh}, g·dm^{-3}	E_{cor}, mV	R_p, kΩ·cm^2	i_{cor}, mA·cm^{-2}	Z_i, %
Blank	–	–188	4.2±0.5	6.8±0.3	–
2a	1.0	–297	574±18	0.054±0.014	94.0
	2.0	–301	487±25	0.077±0.011	92.3
2b	1.0	–293	715±11	0.046±0.003	95.4
	2.0	–303	692±19	0.0046±0.004	95.4
2c	1.0	–291	523±21	0.060±0.014	94.0
	2.0	–291	637±19	0.048±0.004	95.2
2d	1.0	–293	262±14	0.10±0.03	90.3
	2.0	–301	1124±42	0.034±0.013	96.6
2e	1.0	–293	865±19	0.040±0.008	96.0
	2.0	–310	1080±48	0.021±0.005	97.9
2f	1.0	–301	827±22	0.037±0.008	96.3
	2.0	–306	640±14	0.055±0.009	94.5

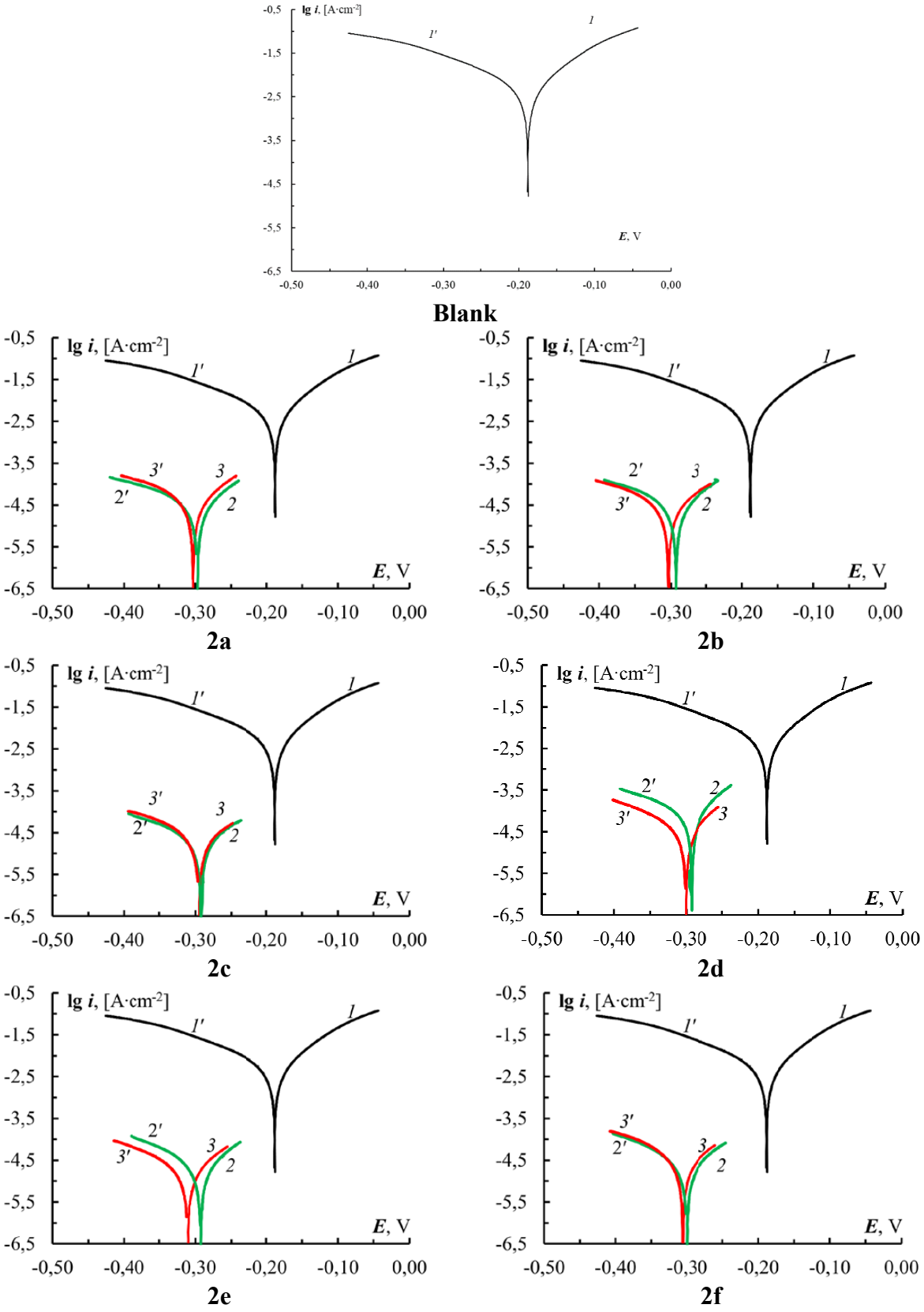

Fig. 3. Anodic (*1-3*) and cathodic (*1′–3′*) polarization curves of St3 steel electrodes in a 24% HCl solution without inhibitor additives (blank), with additives **2a-f** at concentrations of 1 g/L (*2-2′*) and 2 g/L (*3-3′*)

is explained by the fundamental differences in the nature and time scale of the applied methods. Electrochemical techniques assess the instantaneous adsorption effect and suppression of electrochemical currents within the first tens of minutes after inhibitor introduction; they are sensitive to rapid blocking of active corrosion sites and provide a localized, short-term efficiency profile over a small electrode area. Gravimetric testing, on the other hand, reflects integrated mass loss during prolonged (7-day) exposure and captures subsequent processes: restructuring or degradation of the adsorbed layer, inhibitor leaching, interactions with corrosion products, and development of localized corrosion sites.

4. Conclusions

A series of new 2-alkyl-5-methyl-4,5,6,7-tetrahydro-[1,2,4]triazolo[1,5-a]pyrimidin-7-ol derivatives was obtained from aminotriazoles and crotonaldehyde in an amphoteric surfactant medium. Gravimetric tests in 24% HCl showed that all investigated compounds reduce the corrosion rate of St3 steel at inhibitor concentrations of 1–2 g/L. The highest efficiency was achieved for compound **2d**, derived from coconut oil, with a protection degree of 98.5%. Potentiodynamic polarization data indicate that all inhibitors act as mixed-type compounds, affecting both anodic and cathodic processes. The polarization resistance (R_p) increased by an order of magnitude (up to 1124 kΩ·cm^2), while the corrosion current density (icor) decreased by more than two orders of magnitude, corresponding to protection degrees of 94–98 %. For samples **2b–2c** and **2e–2f**, discrepancies were observed between electrochemical and gravimetric data: high instantaneous efficiency (Z_i > 90 %) did not translate into long-term stability of the inhibitor film. This behavior is explained by partial desorption and leaching of the adsorbed inhibitor layer during prolonged exposure of the metal in hydrochloric acid. It was demonstrated that inhibitor efficiency is determined by the optimal length of the alkyl radical (C9-C10): excessive chain elongation reduces compound solubility and the uniformity of surface coverage, leading to decreased protective performance. The results highlight the high potential of 4,5,6,7-tetrahydro-[1,2,4] triazolo[1,5-a]pyrimidin-7-ol derivatives, including those synthesized from vegetable oils, as environmentally safe and effective acid corrosion inhibitors for steel in the oil, gas, and chemical industries.

Contribution of the authors

The authors contributed equally to this article.

Conflict of interests

The authors declare that they have no known competing financial interests or personal relationships that could have influenced the work reported in this paper.

References

1. Fredd C. N., Fogler H. S. Alternative stimulation fluids and their impact on carbonate acidizing. *SPE Journal*. 1998;3(1): 34–41. https://doi.org/10.2118/31074-PA

2. Iqbal M. I., Kudapa V. K. *Oil well production mechanism*. New York: River Publishers; 2025. 484 p. https://doi.org/10.1201/9781003605706

3. Al-Moubaraki A. H., Obot I. B. Corrosion challenges in petroleum refinery operations: Sources, mechanisms, mitigation, and future outlook. *Journal of Saudi Chemical Society*. 2021;25(12): 101370. https://doi.org/10.1016/j.jscs.2021.101370

4. Avdeev Y. G., Kuznetsov Y. I. Physicochemical aspects of inhibition of acid corrosion of metals by unsaturated organic compounds. *Russian Chemical Reviews*. 2012;81(12): 1133–1145. https://doi.org/10.1070/RC2012v081n12ABEH004292

5. Swathi P. N., Rasheeda K., Samshuddin S., Alva V. D. Fatty acids and its derivatives as corrosion inhibitors for mild steel-an overview. *Journal of Asian Scientific Research*. 2017;7(8): 301–308. https://doi.org/10.18488/journal.2.2017.78.301.308

6. Kruzhilin, A. A., Shevtsov, D. S., Dmitriev, I. A., Potapov, M. A., & Shikhaliev, K. S. Synthesis of 2-Alkyl-5-phenyl-4,5,6,7-tetrahydro-[1,2,4]triazolo[1,5-a]pyrimidin-7-ol derivatives from vegetable oils and their efficiency as inhibitors of hydrochloric acid corrosion of steel. *Condensed Matter and Interphases*. 2025; 27(3): 409-416. https://doi.org/10.17308/kcmf.2025.27/13017

7. Kruzhilin A. A., Shevtsov D. S., Potapov A. Yu., ... Kasatkin V. E. Novel inhibitory compositions based on 4,5,6,7-tetrahydro-[1,2,4]triazolo[1,5-a]pyrimidin-7-ol derivatives for steel acid corrosion protection. *International Journal of Corrosion and Scale Inhibition*. 2022;11(2): 774-795. https://doi.org/10.17675/2305-6894-2022-11-2-22

8. Mansfeld F. Tafel slopes and corrosion rates obtained in the pre-Tafel region of polarization curves. *Corrosion Science*. 2005; 47(12): 3178-3186. https://doi.org/10.1016/j.corsci.2005.04.012

Information about the authors

Alexey A. Kruzhilin, Cand. Sci. (Chem.), Head of Laboratory of Organic Additives for the Processes of Chemical and Electrochemical Deposition of Metals and Alloys Used in the Electronics Industry, Voronezh State University (Voronezh, Russian Federation).

https://orcid.org/0000-0003-2262-0131
kruzhilin.alexey@gmail.com

Dmitry S. Shevtsov, Cand. Sci. (Chem.), Researcher of Laboratory of Organic Additives for the Processes of Chemical and Electrochemical Deposition of Metals and Alloys Used in the Electronics Industry, Voronezh State University (Voronezh, Russian Federation).

https://orcid.org/0000-0003-4480-787X
shevtsov@chem.vsu.ru

Ivan A. Dmitriev, student of the Department of Organic Chemistry, Voronezh State University (Voronezh, Russian Federation).

Mikhail A. Potapov, Cand. Sci. (Chem.), Leading Chemical Engineer of the Department of Biochemistry and Cell Physiology of the Faculty of Medical Biology, Voronezh State University (Voronezh, Russian Federation).

https://orcid.org/0000-0002-1795-7605
amidines@mail.ru

Khidmet S. Shikhaliev, Dr. Sci. (Chem.), Professor, Head of the Department of Organic Chemistry, Voronezh State University (Voronezh, Russian Federation).

https://orcid.org/0000-0002-6576-0305
chocd261@chem.vsu.ru

Received February 28, 2025; approved after reviewing September 10, 2025; accepted for publication October 15, 2025; published online December 25, 2025.

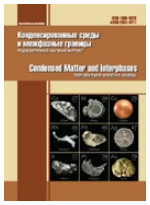

ISSN 1606-867X (Print)
ISSN 2687-0711 (Online)
Condensed Matter and Interphases
Kondensirovannye Sredy i Mezhfaznye Granitsy
https://journals.vsu.ru/kcmf/

Original articles

Research article
https://doi.org/10.17308/kcmf.2025.27/13322

Phase equilibria in the GeTe-Sb_2Te_3-Te system

E. R. Nabiyev[1], E. N. Orujlu[2]✉, A. A. Hasanov[2], A. I. Aghazade[3], S. H. Aliyeva[4], Yu. A. Yusibov[1]

[1]*Ganja State University,*
429 H. Aliyev ave., Ganja AZ-2001, Azerbaijan

[2]*Azerbaijan State Oil and Industry University,*
16/21 Azadlıq ave., Baku AZ-1010, Azerbaijan

[3]*Institute of Catalysis and Inorganic Chemistry,*
113 H. Javid ave., Baku AZ-1143, Azerbaijan

[4]*Nakhchivan State University,*
1 H. Aliyev ave., Nakhchivan AZ-7000, Azerbaijan

Abstract

Objectives: Germanium-antimony tellurides are of considerable practical interest as thermoelectrics with low thermal conductivity, topological insulators and phase memory materials. In this paper, the results of a study of phase equilibria in the region of GeTe-Sb_2Te_3-Te compositions of the Ge-Sb-Te system using the DTA, X-ray diffraction and SEM methods are we presents.

Experimental: The studied samples were synthesized using a special technique that allows them to be obtained in a state as close to equilibrium as possible.

Conclusions: A diagram of solid-phase equilibria at 300 K, a projection of the liquidus surface and some polythermal sections of the phase diagram are constructed. The fields of primary crystallization of phases are outlined, non- and monovariant equilibria are determined. According to the obtained picture of phase equilibria, the curves of monovariant equilibria originating from the peritectic and eutectic points of the boundary system GeTe-Sb_2Te_3 undergo transformations at certain transition points. In the region of compositions rich in tellurium, a number of invariant transition reactions occur, corresponding to the joint crystallization of two-phase mixtures of telluride phases and elemental tellurium.

Keywords: Layered germanium-antimony tellurides, Phase memory materials, Topological insulator, Phase diagram

Funding: The work was partially supported by the Azerbaijan Science Foundation - Grant No AEF-MCG-2022-1(42)-12/10/4-M-10.

For citation: Nabiyev E. R., Orujlu E. N., Hasanov A. A., Aghazade A. I., Aliyeva S. G., Yusibov Yu. A. Phase equilibria in the GeTe-Sb_2Te_3-Te system. *Condensed Matter and Interphases*. 2024;26(4): 639–650. https://doi.org/10.17308/kcmf.2025.27/13322

Для цитирования: Набиев Э. Р., Оруджлу Э. Н., Гасанов А. А., Агазаде А. И., Алиева С. Г., Юсибов Ю. А. Фазовые равновесия в системе GeTe-Sb_2Te_3-Te. *Конденсированные среды и межфазные границы*. 2025;26(4), 639–650. https://doi.org/10.17308/kcmf.2025.27/13322

✉ Elnur N. Orujlu, e-mail: elnur.oruclu@yahoo.com

1. Introduction

Ternary compounds of the A^{IV}-B^V-Te systems (A^{IV}-Ge, Sn, Pb; B^V-Sb, Bi) with layered tetradymite-like structures have long been in the focus of researchers as thermoelectric materials with anomalously low thermal conductivity [1-6]. The discovery at the beginning of our century of a new quantum state of matter - a topological insulator [7, 8] gave a new powerful impetus to the study of these compounds and phases based on them. It turned out that compounds of the homologous series $A^{IV}Te{\cdot}mB^V_2Te_3$($A^{IV}B^V_2Te_4$, $A^{IV}B^V_4Te_7$, $A^{IV}B^V_6Te_{10}$, etc.) and solid solutions based on them are 3D topological insulators and are very promising for use in various areas of high technology, including spintronics, quantum computers, scanning devices used in security systems and medicine, etc. [9-17].

Recently, the special attention of researchers has been attracted by compounds and alloys of the GeTe-Sb_2Te_3 system with a reversible phase transition between the crystalline and amorphous states caused by very short (only a few tens of nanoseconds) laser radiation. These alloys, called phase memory materials, are already used as memory materials in rewritable optical disks and have great potential for creating a non-volatile alternative based on them to traditional flash memory [18–24].

At the initial of research stage on the development of new complex inorganic materials, particularly chalcogenide materials, it is essential to have reliable data on phase equilibria in the corresponding systems [25-29]. In the review article [26], based on a critical analysis of the available literature, it was shown that the data on the phase diagrams of most $A^{IV}Te$-$B^V_2Te_3$ type systems are contradictory and need to be clarified. Taking this into account, we have undertaken repeated detailed studies of phase equilibria in some $A^{IV}Te$-$B^V_2Te_3$ type systems using a specially developed technique for synthesizing equilibrium samples, as well as the thermodynamic properties of intermediate phases [30–37].

Numerous works [38–46] are devoted to the study of phase equilibria in the Ge–Sb–Te system, some of which are summarized in [43]. According to the data of [38], in the GeTe-Sb_2Te_3 quasi-binary system, ternary compounds $Ge_2Sb_2Te_5$, $GeSb_2Te_4$, $GeSb_4Te_7$ are formed, melting with decomposition according to peritectic reactions at 903, 888, and 875 K, respectively, as well as wide regions of solid solutions based on both initial compounds. The results of the study of phase equilibria in the GeTe– Sb_2Te_3–Te compositions region are presented in [39], and in [40, 41] in the Ge–GeTe–Sb_2Te_3–Sb compositions region. The results of the thermodynamic study of some ternary compounds of the GeTe– Sb_2Te_3 system by the calorimetric method are presented in [42].

The papers [44, 45], published at the beginning of our century, present the results of repeated studies of solid-phase equilibria in the Ge-Sb-Te system and crystal structures of germanium-antimony tellurides. The authors of [44] presented a compilation phase diagram of the GeTe- Sb_2Te_3 system, constructed based on the data of [38] with the addition of compositions of other known and suspected ternary compounds without specifying the nature and temperatures of their melting (Fig. 1a). Taking into account the compilation nature of this diagram, a new detailed study of this system was undertaken in [46]. It was shown that it is characterized by the presence of six ternary compounds: $Ge_4Sb_2Te_7$, $Ge_3Sb_2Te_6$ $Ge_2Sb_2Te_5$, $GeSb_2Te_4$, $GeSb_4Te_7$, and $GeSb_6Te_{10}$. The first two melt with decomposition by a solid-phase reaction, and the rest - by peritectic reactions at 863, 854, 848, and 843 K, respectively (Fig. 1). In addition, in [46] the refined parameters of the crystal lattices of all the indicated compounds are presented.

New data obtained in [46] for the key section GeTe- Sb_2Te_3 of the ternary system Ge-Sb-Te indicate the need to revise its complete T-x-y diagram and determine the primary crystallization fields of all identified ternary compounds.

Taking into account the above, we have undertaken a re-examination of phase equilibria in the Ge-Sb-Te system. In this paper, a new refined picture of phase equilibria of the indicated system in the GeTe -Sb_2Te_3-Te compositions range is presented, including the liquidus surface projection, the isothermal section at 300 K, and some polythermal sections of the phase diagram.

2. Experimental

2.1. Synthesis

The alloys for the study were prepared in 2 stages. At the first stage, the initial binary tellurides GeTe and Sb_2Te_3 were synthesized

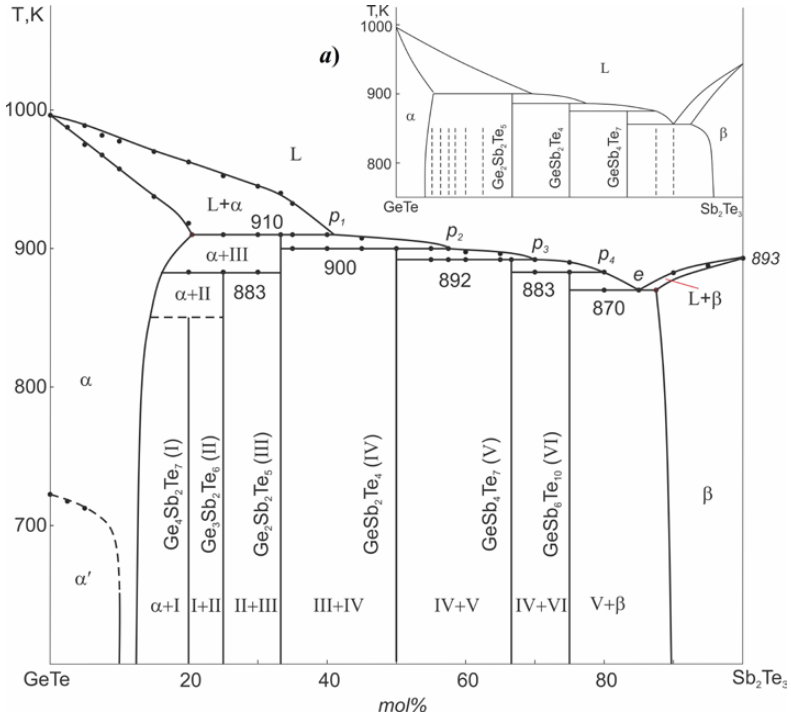

Fig. 1. Phase diagram of the GeTe-Sb_2Te+ system [46]. a) Compilation phase diagram according to [44, 45]

and identified by DTA and X-ray diffraction techniques. The synthesis was carried out by melting high-purity elemental components in quartz ampoules evacuated to a residual pressure of ~10^{-2} Pa. At the second stage, intermediate alloys of the GeTe-Sb_2Te_3-Te system were obtained by fusing the obtained tellurides, as well as elemental tellurium in various stoichiometric ratios, also under vacuum conditions.

At the second stage of synthesis, the results of works [46–48] were taken into account, which showed that even long-term (up to 3000 h) thermal annealing of bulk samples of layered tetradymite-like phases obtained by the traditional method of alloying does not lead to reaching the equilibrium state. According to the authors of the mentioned works, this is due to weak diffusion between the layers in the layered structure of the phases. Taking into account the results of these works, the alloys after alloying were quenched by throwing them into ice water with subsequent homogenizing annealing. Quenching was carried out in the temperature range of 900-1050 K depending on the composition, and homogenizing annealing was carried out at 620 K for 1000 h. Then the alloys were cooled in the switched-off furnace mode.

2.2. Methods

Differential thermal analysis (DTA), X-ray diffraction analysis (XRD), and scanning electron microscopy (SEM) were used for the alloys investigations.

Thermal heating curves were recorded on a differential scanning calorimeter DSC NETZSCH 404 F1 Pegasus system and on a multichannel DTA setup assembled based on an electronic data recorder “TC-08 Thermocouple Data Logger”. Powder diffraction patterns were obtained on a Bruker D8 diffractometer with CuK_α radiation, and SEM images were collected on a Tescan Vega 3 SBH scanning electron microscope.

3. Results and discussion

Analysis of the set of obtained experimental results of annealed samples along different sections of the GeTe-Sb_2Te_3-Te concentration triangle using literature data on the системам GeTe-Te [49, 50], Sb_2Te_3-Te [50] and GeTe-Sb_2Te_3 [46] boundary systems allowed to obtain a mutually consistent picture of phase equilibria in the studied system (Fig. 2-8, Table). In the text, figures and table we have adopted the following designations of phases: α- and α′-solid solutions based on high-temperature (HT) and low-temperature (RT) modifications of GeTe,

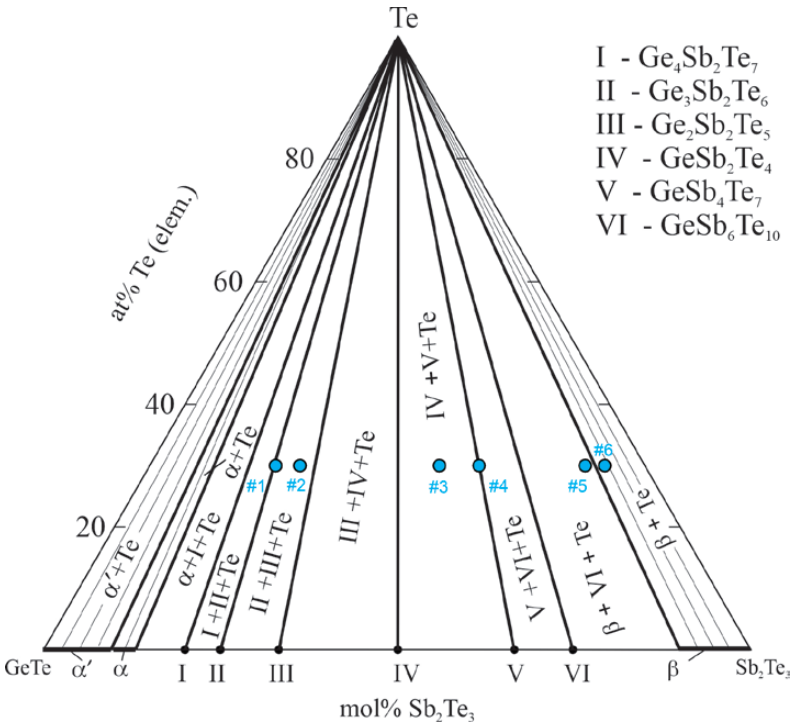

Fig. 2. Solid-phase equilibria diagram of the GeTe-Sb_2Te_3-Te system at 300 K

β-solid solutions based on Sb_2Te_3, I-VI – ternary compounds $Ge_4Sb_2Te_7$, $Ge_3Sb_2Te_6$, $Ge_2Sb_2Te_5$, $GeSb_2Te_4$, $GeSb_4Te_7$ and $GeSb_6Te_{10}$, respectively (Fig. 2).

3.1. Solid-phase equilibria diagram

Fig. 2 shows an isothermal section of the phase diagram at 300 K. As can be seen, it is characterized by the presence of stable tie-lines between elemental tellurium and all crystalline phases of the GeTe-Sb_2Te_3 side system. The two-phase regions α′+Te and β+Te occupy a significant part of the area of the concentration triangle. Other possible two-phase regions are practically degenerated into tie-lines between ternary compounds and elemental tellurium, which is due to the insignificance of their homogeneity regions.

All phase regions in Fig. 2 are confirmed by X-ray diffraction and SEM methods. As can be seen from Fig. 3, the powder diffraction patterns of alloys, which are on the tie-lines in composition, consist of reflection lines of the corresponding ternary compounds and elemental tellurium, and the diffraction patterns of alloys from the $Ge_3Sb_2Te_6$-$Ge_2Sb_2Te_5$-Te and $GeSb_2Te_4$-$GeSb_4Te_7$-Te three-phase regions contain diffraction reflections of the corresponding three phases.

The SEM patterns were also in accordance with the solid-phase equilibria diagram. As an example, Fig. 4 shows the SEM patterns of two alloys (samples 5 and 6 in Fig. 2), which clearly show the interface between the β+Te and $GeSb_6Te_{10}$+β+Te phase regions.

3.2. Liquidus surface

Fig. 5 shows the projection of the liquidus surface of the GeTe-Sb_2Te_3-Te system. As can be seen, it consists of the fields of primary crystallization of seven phases: α- and β-solid solutions, ternary compounds $Ge_2Sb_2Te_5$, $GeSb_2Te_4$, $GeSb_4Te_7$, $GeSb_6Te_{10}$, and elemental tellurium. All liquidus surfaces of telluride phases have the form of stripes from the GeTe-Sb_2Te_3 side system towards the tellurium angle of the concentration triangle.

The primary crystallization fields of phases are delimited by a series of curves of monovariant equilibria, which originate from various points of nonvariant equilibria of the boundary systems. The indicated curves, intersecting near the tellurium angle of the concentration triangle, form a series of points with nonvariant transition (U_1-U_4) and eutectic (E) equilibria. The types and temperatures of all non- and monovariant equilibria are given in Table.

Table. Non- and monovariant equilibria in the GeTe-Sb_2Te_3-Te system

Points and curves in Fig. 5	Equilibrium	*T*, K
p_1	$L + \alpha \leftrightarrow Ge_2Sb_2Te_5$	910
p_2	$L + Ge_2Sb_2Te_5 \leftrightarrow GeSb_2Te_4$	900
p_3	$L + GeSb_2Te_4 \leftrightarrow GeSb_4Te_7$	892
p_4	$L + GeSb_4Te_7 \leftrightarrow GeSb_6Te_{10}$	883
e_1	$L \leftrightarrow GeSb_6Te_{10} + \beta$	873
e_2	$L \leftrightarrow \alpha' + Te$	653
e_3	$L \leftrightarrow \beta + Te$	695
U_1	$L + \beta \leftrightarrow GeSb_6Te_{10} + Te$	688
U_2	$L + GeSb_6Te_{10} \leftrightarrow GeSb_4Te_7 + Te$	677
U_3	$L + GeSb_4Te_7 \leftrightarrow GeSb_2Te_4 + Te$	665
U_4	$L + GeSb_2Te_4 \leftrightarrow Ge_2Sb_2Te_5 + Te$	651
E	$L \leftrightarrow \alpha' + Ge_2Sb_2Te_5 + Te$	640
p_1K_1	$L + \alpha_1 \leftrightarrow Ge_2Sb_2Te_5$	910–825
p_2K_2	$L + Ge_2Sb_2Te_5 \leftrightarrow GeSb_2Te_4$	900–830
p_3K_3	$L + GeSb_2Te_4 \leftrightarrow GeSb_4Te_7$	892–840
p_4K_4	$L + GeSb_4Te_7 \leftrightarrow GeSb_6Te_{10}$	883–850
e_1K_5	$L \leftrightarrow GeSb_6Te_{10} + \beta$	873–855
K_5U_1	$L + \beta \leftrightarrow GeSb_6Te_{10}$	855–688
K_4U_2	$L + GeSb_6Te_{10} \leftrightarrow GeSb_4Te_7$	850–677
K_3U_3	$L + GeSb_4Te_7 \leftrightarrow GeSb_2Te_4$	840–665
K_2U_4	$L + GeSb_2Te_4 \leftrightarrow Ge_2Sb_2Te_5$	830–651
K_1E	$L \leftrightarrow \alpha_1(\alpha_2) + Ge_2Sb_2Te_5$	835–640
e_3U_1	$L \leftrightarrow \beta + Te$	695–688
U_1U_2	$L \leftrightarrow GeSb_6Te_{10} + Te$	688–677
U_2U_3	$L \leftrightarrow GeSb_4Te_7 + Te$	677–665
U_3U_4	$L \leftrightarrow GeSb_2Te_4 + Te$	665–651
U_4E	$L \leftrightarrow Ge_2Sb_2Te_5 + Te$	651–640
e_2E	$L \leftrightarrow \alpha_2 + Te$	653–640

According to Fig. 5, the curves emanating from the peritectic (P_1-P_4) and eutectic (e_1) points of the GeTe-Sb_2Te_3 boundary system undergo transformations at certain transition points K_1-K_5. These transformations can be explained based on phase diagrams of the boundary components of the studied system. Thus, in the side system GeTe- Sb_2Te_3, the temperatures of the peritectic (P_1-P_4) and eutectic (e_1) equilibria decrease in the direction from germanium telluride to Sb_2Te_3, i.e. from left to right in Fig. 5. At the same time, in the side system GeTe-Te, the temperature of the eutectic e_2 (653 K) is significantly lower than that of the eutectic e_3 (695 K) in the other boundary system Sb_2Te_3-Te, i.e. in this part of the phase diagram, the temperatures of the invariant equilibria decrease in the opposite direction. The

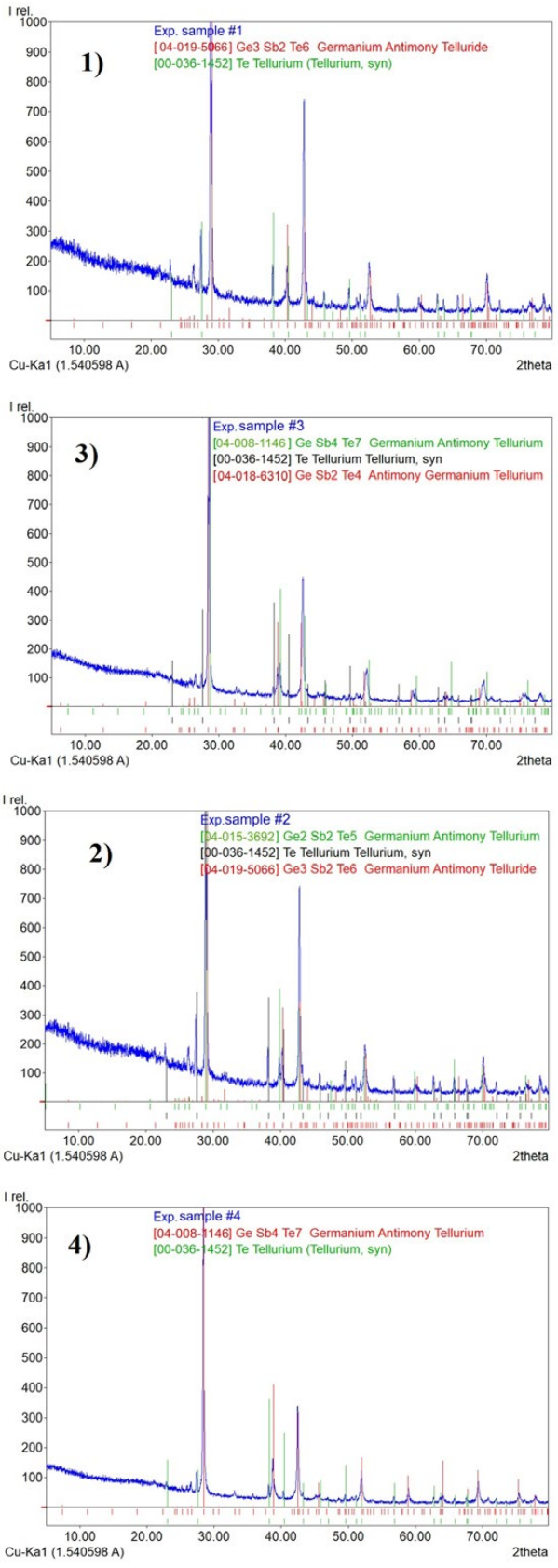

Fig. 3. Powder diffraction patterns of alloys 1-4, shown in Fig. 2

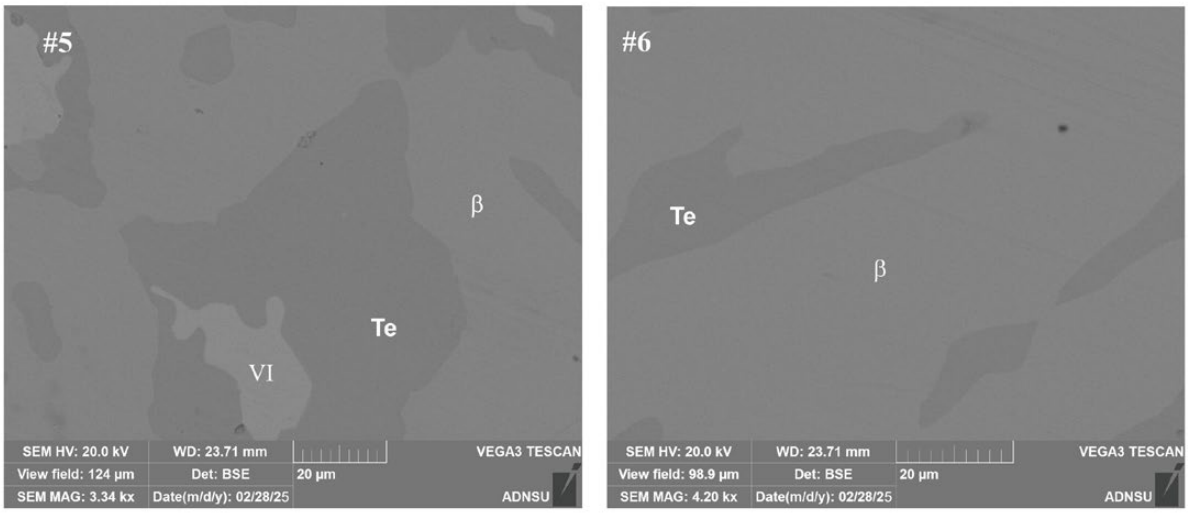

Fig. 4. SEM patterns of alloys 5 and 6, shown in Fig. 2

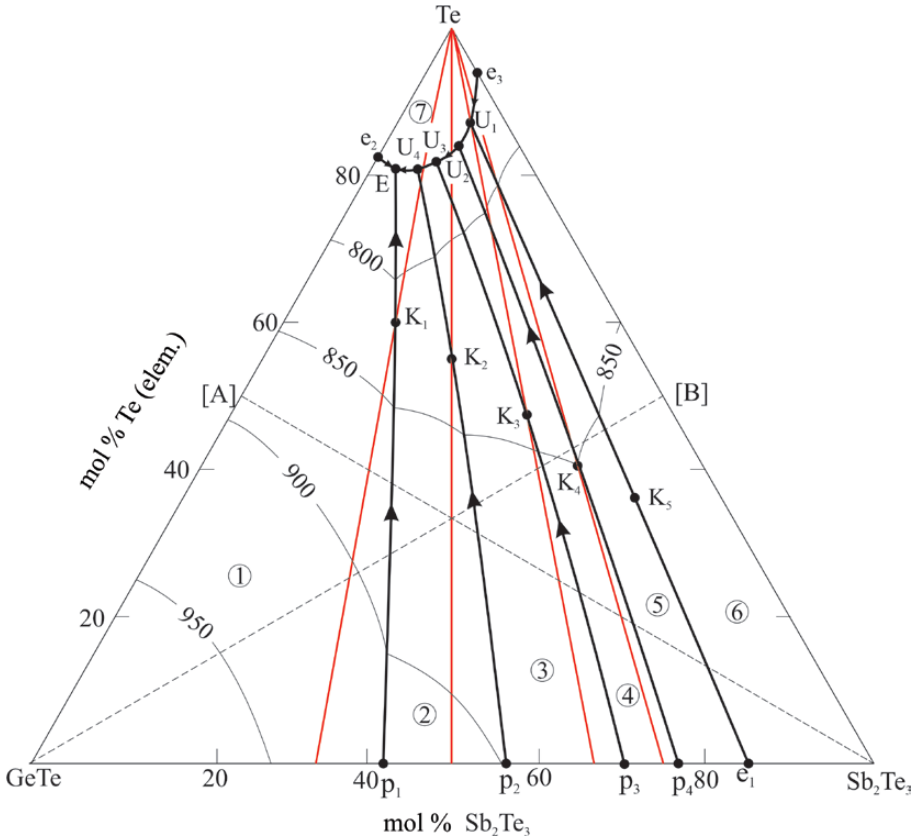

Fig. 5. Projection of the liquidus surface of the GeTe-Sb_2Te_3-Te system. Primary crystallization fields: 1 – α; 2 – $Ge_2Sb_2Te_5$; 3 – $GeSb_2Te_4$; 4 – $GeSb_4Te_7$; 5 – $GeSb_6Te_{10}$; 6 – β; 7 – Te

experimental DTA data obtained by us showed that the temperatures of nonvariant transition equilibria (U_1-U_4) also decrease in the direction from the eutectic e_3 to the ternary eutectic point E (640 K) (Fig. 5, Table). Similar opposite directions of changes in the temperatures of nonvariant equilibria in the boundary system GeTe- Sb_2Te_3 and in the regions of compositions rich in tellurium lead to the transformation of the above-mentioned monovariant equilibria [51, 52]. In the case of peritectic equilibrium curves, similar transformations occur at the intersection points (K_1-K_4) of the pointed curves with the corresponding stable sections of the "ternary compound-elementary tellurium" type (Fig. 5). Therefore, in the Table, the pointed curves are

presented as two series, transforming into each other at the transition points K_1-K_5 (Fig. 5).

Using the curve P_1E as an example, we will consider one of the above transformations. This curve, before intersecting with the stable section $Ge_2Sb_2Te_5$-Te (P_1K_1), reflects the peritectic equilibrium L + α ↔ III. At the intersection point (K_1), this equilibrium is transformed into the eutectic L ↔ α + III (curve K_1E). Similar transformations take place on the P_2U_4, P_3U_3, P_4U_2 and e_1U_1 curves.

3.3. Polythermal sections of the phase diagram

Below some polythermal sections of the *T*-*x*-*y* phase diagram of the GeTe-Sb_2Te_3-Te system (Fig. 6–8) are presented, which reflect the crystallization processes in more detail and made it possible to clarify the location of the curves of monovariant equilibria and the coordinates of the invariant points.

Four ($Ge_2Sb_2Te_5$-Te, $GeSb_2Te_4$-Te, $GeSb_4Te_7$-Te and $GeSb_6Te_{10}$-Te) of the six polythermal sections considered are stable in the subsolidus. Two other

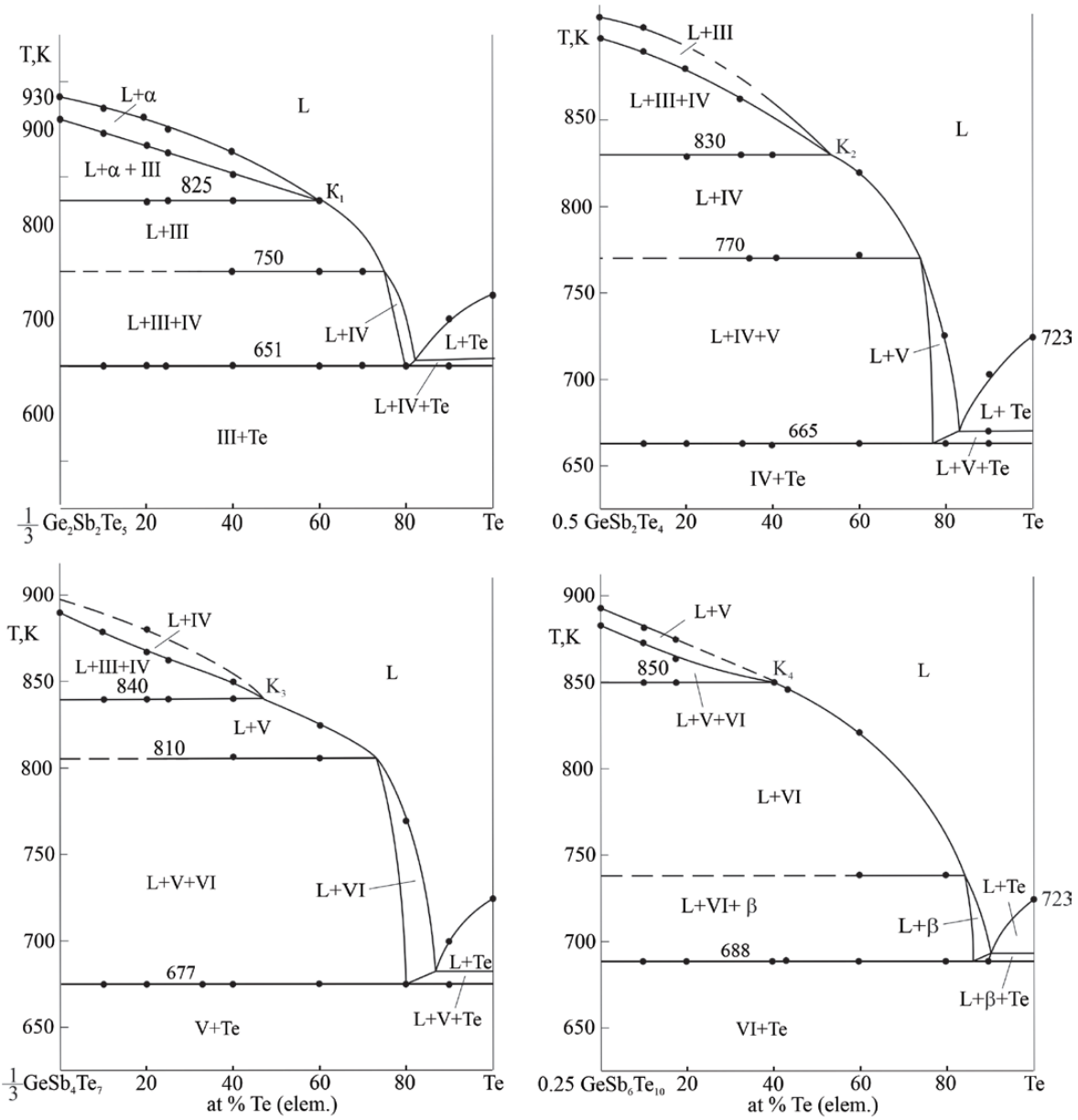

Fig. 6. Polythermal sections of $Ge_2Sb_2Te_5$-Te, $GeSb_2Te_4$-Te, $GeSb_4Te_7$-Te и $GeSb_6Te_{10}$-Te of the phase diagram of the GeTe-Sb_2Te_3-Te system

sections GeTe-[B] and [A]-Sb_2Te_3 ([A] and [B] are alloys with equimolar ratios of components of the boundary systems GeTe-Te and Sb_2Te_3-Te, respectively) intersect almost all fields of primary crystallization of phases and reflect most heterogeneous equilibria.

$Ge_2Sb_2Te_5$-Te section (Fig. 6) passes through the fields of primary crystallization of the α-phase, $Ge_2Sb_2Te_5$ and $GeSb_2Te_4$ compounds as well as elemental tellurium. Below the α-phase liquidus, crystallization proceeds according to the L + α ↔ $Ge_2Sb_2Te_5$ peritectic reaction (Fig. 5, curve P_1K_1), resulting in the formation of a three-phase field L + α + $Ge_2Sb_2Te_5$. In this reaction, the α-phase is completely consumed and at 825 K the system passes into a two-phase state L + $Ge_2Sb_2Te_5$. Starting from 750 K, crystallization continues according to the peritectic reaction L + $GeSb_2Te_4$ ↔ $Ge_2Sb_2Te_5$ (Fig. 5, curve K_2U_4), as a result of which a three-phase region L+$Ge_2Sb_2Te_5$+$GeSb_2Te_4$ is formed.

Near the tellurium angle, tellurium crystallizes primarily from the melt, then the monovariant eutectic process L ↔ $GeSb_2Te_4$+Te begins (Fig. 5, curve U_3U_4). Complete crystallization of the alloys of this section occurs at 651 K according to the invariant transition reaction U_4 and a two-phase mixture $GeSb_2Te_4$+Te is formed. The crystallization processes along the other three sections connecting the compositions of ternary compounds with elemental tellurium (Fig. 6) can be followed by comparing them with Figs. 2 and 5. As can be seen from the T-diagrams, despite the stability of these sections below the solidus, the crystallization processes in them are complex and multi-stage.

The GeTe-[B] section (Fig. 7) passes through the fields of primary crystallization of all phases except elemental tellurium (Fig. 5). In the subsolidus it crosses all phase regions of the system (Fig. 2). In this diagram, the liquidus curves of different phases are marked taking into account Fig. 5. Pairs of conjugate curves emanating from the intersection points of the liquidus lines reflect the beginning and the

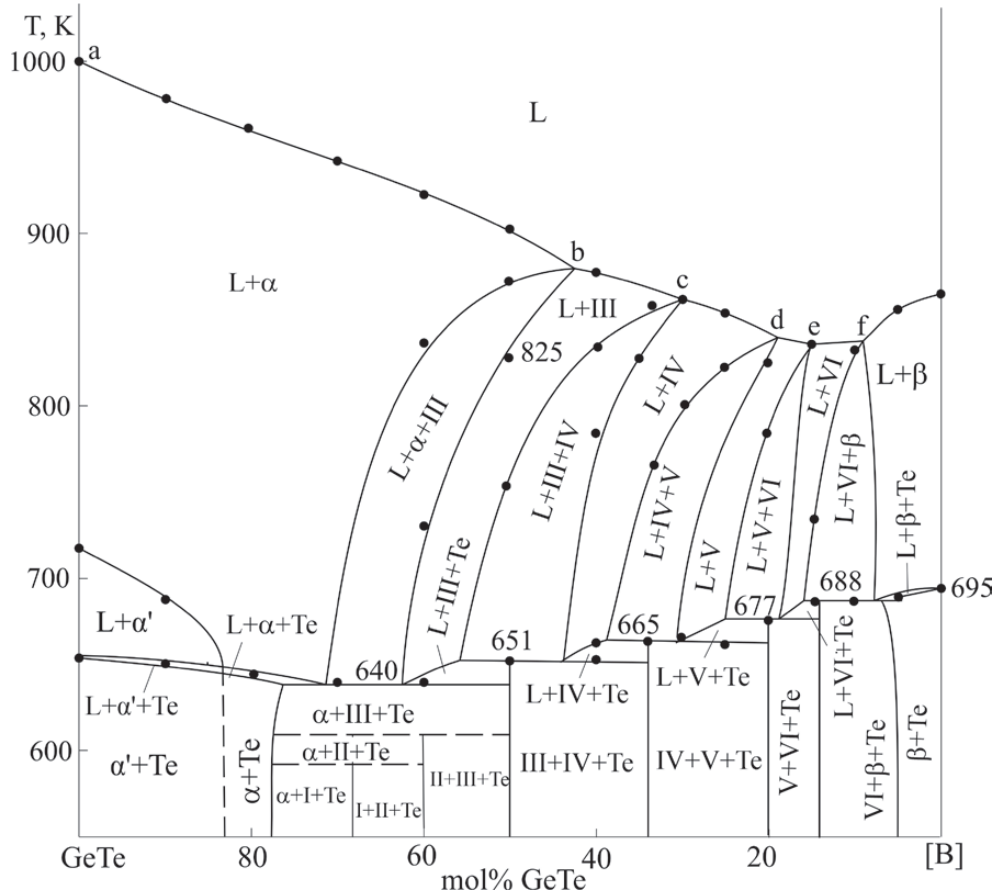

Fig. 7. Polythermal section of GeTe-[B] of the phase diagram of the GeTe-Sb_2Te_3-Te system

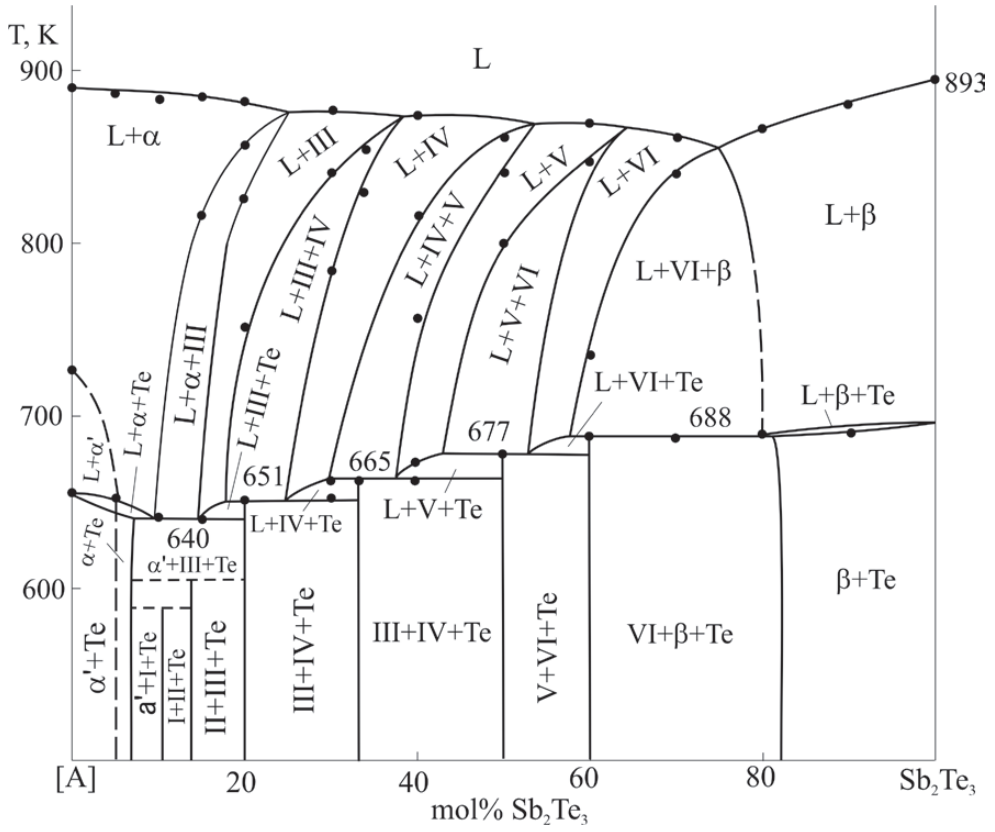

Fig. 8. Polythermal section of [A]-Sb_2Te_3 of the phase diagram of the GeTe-Sb_2Te_3-Te system

end of monovariant equilibria along the curves P_1K_1E (*b*), $P_2K_2U_4$ (*c*), $P_3K_3U_3$ (*d*), $P_4K_4U_2$ (*e*), $P_1K_5U_1$ (*f*). The fields between the indicated pairs of curves correspond to the two-phase areas L+III (IV, V, VI) and L + β. These pairs of curves in the temperature range of 640-688 K reach the curves of monovariant equilibria originating from the eutectic points e_2 and e_3 of the side systems and form a series of transition points (U_1, U_2, U_3, U_4) and eutectic (E) equilibria (Fig. 5). The horizontals at 688, 677, 665, 651 and 640 K in Fig. 7 reflect these nonvariant equilibria.

Section [A]-Sb_2Te_3 (Fig. 8). Phase equilibria along this section are qualitatively similar to those in Fig. 7 and differ from them only in temperature-concentration intervals.

4. Conclusion

Based on the experimental data obtained by studying carefully homogenized equilibrium alloys using the DTA, XRD and SEM methods, a new refined picture of phase equilibria in the GeTe-Sb_2Te_3-Te system was obtained, which significantly differs from the previously known one. A solid-phase equilibria diagram at 300 K and a projection of the liquidus surface, as well as a number of polythermal sections of the phase diagram, were constructed. The fields of primary crystallization of seven phases, including ternary compounds $Ge_2Sb_2Te_5$, $GeSb_2Te_4$, $GeSb_4Te_7$ and $GeSb_6Te_{10}$ were determined, non- and monovariant equilibria were established. It was shown that monovariant equilibria on the curves of monovariant equilibria undergo transformations at certain transition points. The interaction of the indicated curves with the eutectic curves emanating from the lateral systems GeTe-Te and Sb_2Te_3-Te leads to a cascade of invariant transition reactions characterizing the joint crystallization of two-phase mixtures III(IV, V, VI)+Te.

The results obtained in the work can be used to obtain poly- and single crystals of the above-mentioned ternary compounds, which are promising as topological insulators, thermoelectrics and materials with phase memory.

Contribution of the authors

The authors contributed equally to this article.

Conflict of interests

The authors declare that they have no known competing financial interests or personal relationships that could have influenced the work reported in this paper.

References

1. Shevelkov A. V. Chemical aspects of the design of thermoelectric materials. *Russian Chemical Reviews*. 2008;77: 1–19. https://doi.org/10.1070/rc2008v077n01abeh003746

2. Sootsman J. R., Chung D. Y., Kanatzidis M. G. New and old concepts in thermoelectric materials. *Angewandte Chemie International Edition*. 2009;48: 8616–8639. https://doi.org/10.1002/anie.200900598

3. Ma W., Record M., Tian J., Boulet P. Strain effects on the electronic and thermoelectric properties of n(PbTe)-m(Sb_2Te_3) system compounds. *Materials*. 2021;*14*(15): 4086–4095. https://doi.org/10.3390/ma14154086

4. Xu B., Feng T., Li Z., Zhou L., Pantelides S. T., Wu Y. Creating zipper-like van Der Waals gap discontinuity in low-temperature-processed nanostructured $PbSb_{2n}Te_{1+3n}$. enhanced phonon scattering and improved thermoelectric performance. *Angewandte Chemie International Edition*. 2018;57: 10938–10943. https://doi.org/10.1002/anie.201805890

5. Xiao Y., Xianli S., Yonggao Y., Xinfeng T. Structures and thermoelectric properties of $(GeTe)_nBi_2Te_3$. *Journal of Inorganic Materials*. 2021;36(1): 75–80. https://doi.org/10.15541/jim20200252

6. Kihoi S. K., Shenoy U. S., Kahiu J. N., Kim H., Bhat D. K., Lee H. S. Tailoring the thermoelectric performance of the layered topological insulator $SnSb_2Te_4$ through Sb positional doping at the Sn and Sb cation sites. *ACS Applied Electronic Materials*. 2023;5(8): 4504–4513. https://doi.org/10.1021/acsaelm.3c00685

7. Kane C. L., Moore J. E. Topological insulators. *Physics World*. 2011;24(2): 32–36. https://doi.org/10.1088/2058-7058/24/02/36

8. Moore J. E., The birth of topological insulator. *Nature*. 2010;464: 194–198. https://doi.org/10.1038/nature08916

9. Heremans J. P., Cava R. J., Samarth N. Tetradymites as thermoelectrics and topological insulators. *Nature Reviews Materials*. 2017;2: 17049. https://doi.org/10.1038/natrevmats.2017.49

10. Politano A., Caputo M., Nappini S., … Chulkov E. Exploring the surface chemical reactivity of single crystals of binary and ternary bismuth chalcogenides. *Journal of Physical Chemistry C*. 2014;118: 21517–-21522. https://doi.org/10.1021/jp506444f

11. Shvets I. A., Klimovskikh I. I., Aliev Z. S., … Chulkov E. V. Impact of stoichiometry and disorder on the electronic structure of the $PbSb_2Te_{4-x}Se_x$ topological insulator. *Physical Review B*. 2017;96: 235124–235127. https://doi.org/10.1103/physrevb.96.235124

12. Pacilè D., Eremeev S. V., Caputo M., … Papagno M. Deep insight into the electronic structure of ternary topological insulators: a comparative study of $PbBi_4Te_7$ and $PbBi_6Te_{10}$. *Physica Status Solidi. Rapid Research Letters*. 2018; 1800341–1800348. https://doi.org/10.1002/pssr.201800341

13. Shvets I. A., Klimovskikh I. I., Aliev Z. S., … Chulkov E. V. Surface electronic structure of the wide band gap topological insulator $PbBi_4Te_4Se_3$. *Physical Review B*. 2019;100(19): 195127. https://doi.org/10.1103/PhysRevB.100.195127

14. Jahangirli Z. A., Alizade E. H., Aliev Z. S., … Chulkov E. V. Electronic structure and dielectric function of Mn-Bi-Te layered compounds. *Journal of Vacuum Science & Technology B, Nanotechnology and Microelectronics: Materials, Processing, Measurement, and Phenomena*. 2019;37: 062910. https://doi.org/10.1116/1.5122702

15. Wu Z., Liang G., Pang W. … Guo Z. Coupling topological insulator $SnSb_2Te_4$ nanodots with highly doped graphene for high-rate energy storage. *Advanced Material*. 2019;32(2): 1905632. https://doi.org/10.1002/adma.201905632

16. Klimovskikh I., Otrokov M. M., Estyunin D. Tunable 3D/2D magnetism in the $(MnBi_2Te_4)(Bi_2Te_3)_m$ topological insulators family. *npj Quantum Mater*. 2020;5: 54. https://doi.org/10.1038/s41535-020-00255-9

17. Hattori Y., Tokumoto Y., Kimoto K. Evidences of inner Se ordering in topological insulator $PbBi_2Te_4$-$PbBi_2Se_4$-$PbSb_2Se_4$ solid solutions. *Science Reports*. 2020;10: 7957. https://doi.org/10.1038/s41598-020-64742-6

18. Tominaga J. Topological memory using phase-change materials. *MRS Bulletin*. 2018;43(5): 347–351. https://doi.org/10.1557/mrs.2018.94

19. Jones R. O. Phase change memory materials: rationalizing the dominance of Ge/Sb/Te alloys. *Physical Review B*. 2020;101(2): 024103. https://doi.org/10.1103/PhysRevB.101.024103

20. Cao T., Wang R., Simpson R. E., Li G. Photonic Ge-Sb-Te phase change metamaterials and their applications. *Progress in Quantum Electronics*. 2020;74: 100299. https://doi.org/10.1016/j.pquantelec.2020.100299

21. Wang D., Zhao L., Yu S., … Zhang W. Non-volatile tunable optics by design: from chalcogenide phase-change materials to device structures. *Materials Today*. 2023;68: 334–355. https://doi.org/10.1016/j.mattod.2023.08.001

22. Sun C. W., Youm M. S., Kim Y.T. Crystallization behavior of non-stoichiometric Ge–Bi–Te ternary phase change materials for PRAM application. *Journal of Physics: Condensed Matter. 2007;*19: 446004. https://doi.org/10.1088/0953-8984/19/44/446004

23. Cui Y., Zhang Y., Cheng Z. Nonvolatile displays based on phase change materials. *Advanced Optical Materials*. 2023;11(21): 2300481. https://doi.org/10.1002/adom.202300481

24. Gavdush A. A., Komandin G. A., Bukin V. V., … Shi Q. Terahertz-infrared spectroscopy of $Ge_2Sb_2Te_5$ films on sapphire: evolution of broadband electrodynamic response upon phase transitions. *Journal of Applied Physics*. 2023;134: 085103. https://doi.org/10.1063/5.0160772

25. West D. R. F. *Ternary phase diagrams in materials science*. 3rd edn. London: CRC Press; 2020. 240 p. https://doi.org/10.1201/9781003077213

26. Babanly M. B., Chulkov E. V., Aliev Z. S., Shevel'kov A. V., Amiraslanov I. R. Phase diagrams in materials science of topological insulators based on metal

chalkogenides. *Russian Journal of Inorganic Chemistry*. 2017;62(13): 1703–1729. https://doi.org/10.1134/S0036023617130034

27. Babanly M. B., Yusibov Y. A., Imamaliyeva S. Z., Babanly D. M., Alverdiyev I. J. Phase diagrams in the development of the argyrodite family compounds and solid solutions based on them. *Phase Equilibria and Diffusion*. 2024;45: 228–255. https://doi.org/10.1007/s11669-024-01088-w

28. Babanly M. B., Mashadieva L. F., Imamalieva S. Z., Babanly D. M., Tagiev D. B., Yusibov Yu. A. Complex copper-based chalcogenides: a review of phase equilibria and thermodynamic properties. *Condensed Matter and Interphases*. 2024;26(4): 579–619. https://doi.org/10.17308/kcmf.2024.26/12367

29. Cantor B. Exploring multicomponent phase space to discover new materials. *Journal Phase Equilibria and Diffusion*. 2024;45: 188–218. https://doi.org/10.1007/s11669-024-01131-w

30. Seidzade A. E., Orujlu E. N., Doert T., Babanly M. B. An updated phase diagram of the SnTe-Sb_2Te_3 system and the crystal structure of the new compound $SnSb_4Te_7$. *Journal Phase Equilibria and Diffusion*. 2021;42: 373–378. https://doi.org/10.1007/s11669-021-00888-8

31. Gojayeva I. M., Babanly V. I., Aghazade A. I., Orujlu E. N. Experimental reinvestigation of the PbTe–Sb_2Te_3 pseudo-binary system. *Azerbaijan Chemical Journal*. 2022;2: 47-53. https://doi.org/10.32737/0005-2531-2022-2-47-53

32. Orujlu E. N., Seidzade A. E., Babanly D. M., Amiraslanov I. R., Babanly M. B. New insights into phase equilibria of the SnTe–Sb_2Te_3 pseudo-binary system: synthesis and crystal structure of new tetradymite-type compound $Sn_3Sb_2Te_6$. *Journal of Solid State Chemistry*. 2024;330: 124494. https://doi.org/10.1016/j.jssc.2023.124494

33. Alakbarova T. M., Meyer H.-J., Orujlu E. N., Amiraslanov I. R., Babanly M. B. Phase equilibria of the GeTe–Sb_2Te_3 quasi-binary system in the range 0–50 mol % Sb_2Te_3. *Phase Transitions*. 2021;94(5): 366–375. https://doi.org/10.1080/01411594.2021.1937625

34. Alakbarova T. M. Meyer H.-J., Orujlu E. N. A refined phase diagram of the GeTe-Sb_2Te_3 system. *Condensed Matter and Interphases*. 2022;24(1): 11–18. https://doi.org/10.17308/kcmf.2022.24/9050

35. Alakbarova T. M., Orujlu E. N., Babanly D. M. Solid-phase equilibria in the $GeSb_2Te_4$-Sb_2Te_3-Te system and thermodynamic properties of compounds of the GeTe·mSb_2Te_3 homologous series. *Physics and Chemistry of Solid State*. 2022;23(1): 25–33. https://doi.org/10.15330/pcss.23.1.25-33

36. Orujlu E. N., Babanly D. M., Alakbarova T. M., Orujov N. I., Babanly M. B. Study of the solid-phase equilibria in the GeTe-Sb_2Te_3-Te system and thermodynamic properties of GeTe-rich germanium bismuth tellurides. *The Journal of Chemical Thermodynamics*. 2024;196: 107323. https://doi.org/10.1016/j.jct.2024.107323

37. Orujlu E. N., Alakbarova T. M., Babanly M. B. The GeTe-Bi_2Te_3-Te system. *Russian Journal of Inorganic Chemistry*. 2024;68(8): 1144–1154. https://doi.org/10.31857/S0044457X24080079

38. Abrikosov N. X., Danilova-Dobryakova G. T. Study of the GeTe-Sb_2Te_3 phase diagram*. *Izvestiya Akademii Nauk SSSR, Neorganicheskie Materialy*. 1965;2: 204–207. (in Russ.)

39. Legendre B., Hancheng C., Bordas S., Clavaguera-Mora M. T. Phase diagram of the ternary system Ge-Sb-Te. I. The subternary GeTe-Sb_2Te_3-Te. *Thermochimica Acta*. 1984;78: 141–157. https://doi.org/10.1016/0040-6031(84)87142-7

40. Abrikosov N. Kh., Danilova-Dobryakova G. T. System Ge-Sb-Te*. *Izvestiya Akademii Nauk SSSR, Neorganicheskie Materialy*. 1970; 6(3): 475–481. (in Russ.)

41. Bordas S., Clavaguera-Mora M. T. Legendre B., Hancheng C. Phase diagram of the ternary system Ge-Sb-Te. II. The subternary Ge-GeTe-Sb_2Te_3-Sb. *Thermochimica Acta*. 1986;107: 239–265. https://doi.org/10.1016/0040-6031(86)85051-1

42. Skoropanov A. S., Valevsky B. L., Skums V. F., Samal G. I., Vecher A. A. Physico-chemial study of Ge(Pb) Te-$Sb_2(Sb_2)Te_3$ system ternary compounds. *Thermochimica Acta*. 1985;90: 331–334. https://doi.org/10.1016/0040-6031(85)87110-0

43. Shelimova L. E., Tomashik V. N., Grytsiv V. I. *State diagrams in semiconductor materials science: systems based on Si, Ge, Sn, Pb**. Moscow: Nauka Publ.; 1991. 368 p. (in Russ.)

44. Shelimova L. E., Karpinsku O. G., Zemskov V. S., Konstantinov P. P. Structural and electrical properties of layered tetradymite-like compounds in the GeTe-Bi_2Te_3 and GeTe--Sb_2Te_3 systems. *Inorganic Materials*. 2000;36(3): 235–242. https://doi.org/10.1007/BF02757928

45. Shelimova L. E., Karpinskii O. G., Konstantinov P. P., Avilov, E. S., Kretova M. A., Zemskov V. S. Crystal structures and thermoelectric properties of layered Compounds in the ATe–Bi_2Te_3(A = Ge, Sn, Pb) Systems. *Inorganic Materials*. 2004;40: 451–460. https://doi.org/10.1023/B:INMA.0000027590.43038.a8

46. Orujlu E. N., Izzatli S. B., Jafarov Y. I., Babanly M. B. Reinvestigation of the GeTe-Sb2Te3 pseudobinary phase diagram. Azerbaijan Chemical Journal. 2025;2: 95–103. https://doi.org/10.32737/0005-2531-2025-2-95-103

47. Hasanova G. S., Aghazade A. I., Imamaliyeva S. Z., Yusibov Y. A., Babanly M. B. Refinement of the phase diagram of the Bi-Te system and the thermodynamic properties of lower bismuth tellurides. JOM. 2021;73(5): 1511–1521. https://doi.org/10.1007/s11837-021-04621-1

48. Hasanova G. S., Aghazade A. I., Babanly D. M., Imamaliyeva S. Z, Yusibov Y. A., Babanly M. B. Experimental study of the phase relations and thermodynamic properties of Bi-Se system. Journal of Thermal Analysis Calorimetry. 2021;147: 6403–6414. https://doi.org/10.1007/s10973-021-10975-0

49. Bletskan D. I. Phase equilibrium in the systems AIV–BVI. Journal of Ovonic Research. 2005;1(5): 53-60. Режим доступа: https://www.chalcogen.ro/Bletskan1.pdf

50. *Binary alloy phase diagrams*. T. B. Massalski (ed.). second edition. ASM International. Ohio: Materials Park; 1990. 3589 p.

51. Lutsyk V. I., Vorob'eva V. P., Shodorova S. Ya. Determining the conditions for changes of the three-phase reaction type in a V–Zr–Cr system. *Russian Journal Physical Chemistry A*. 2015;89: 2331. https://doi.org/10.1134/S0036024415130245

52. Lutsyk V. I., Vorob'eva V. P. 3D computer models of *T*–*x*–*y* diagrams, forming the Fe–Ni–Co–FeS–NiS–CoS subsystem. *Russian Journal Physical Chemistry A*. 2017;91(13): 2593-2599. https://doi.org/10.1134/s0036024417130131

* *Translated by author of the article*

Information about the authors

Elnur R. Nabiyev, PhD student, Ganja State University (Ganja, Azerbaijan).
https://orcid.org/0009-0006-1907-3957
azechemist@gmail.com

Elnur N. Orujlu, PhD in Chemistry, Head of "Nanomaterials and Nanotechnologies" Science-Research Laboratory, Azerbajan State Oil and Industry University (Baku, Azerbaijan).
https://orcid.org/0000-0001-8955-7910
elnur.oruclu@yahoo.com

Alekper A. Hasanov, Dr. Sci. (Tech.), Professor, Azerbajan State Oil and Industry University (Baku, Azerbaijan).
elekber.hasanov@asoiu.edu.az

Aytan I. Aghazade, PhD student, Researcher at the Institute of Catalysis and Inorganic Chemistry (Baku, Azerbaijan).
https://orcid.org/0000-0002-6072-1075
aytenagazade94@gmail.com

Sevda H. Aliyeva, PhD student, Nakhchivan State University (Nakhchivan, Azerbaijan).
https://orcid.org/0009-0007-7737-0578
sevdaeliyeva@gdu.edu.az

Yusif A. Yusibov, Dr. Sci. (Chem.), Professor, Rector of the Ganja State University (Ganja, Azerbaijan).
https://orcid.org/0000-0003-4081-6170
yusifyusibov1951@gmail.com

Received May 29, 2025; approved after reviewing June 16, 2025; accepted for publication July 15, 2025; published online December 25, 2025.

ISSN 1606-867X (Print)
ISSN 2687-0711 (Online)
Condensed Matter and Interphases
Kondensirovannye Sredy i Mezhfaznye Granitsy
https://journals.vsu.ru/kcmf/

Original articles

Research article
https://doi.org/10.17308/kcmf.2025.27/13329

Study of the influence of the microstructure of Pt/C materials on the electrochemical characteristics of PtCo/C electrocatalysts based on them

A. K. Nevelskaya[1,2]✉, S. V. Belenov[1], A. A. Gavrilova[1], K. O. Paperzh[1], N. V. Lyanguzov[3], I. V. Pankov[4], A. A. Kokhanov[1]

[1]Southern Federal University, Faculty of Chemistry, 7 ul. Sorge, Rostov-on-Don 344090, Russian Federation

[2]Federal Research Center Southern Scientific Center of the Russian Academy of Sciences (SSC RAS), 41 pr. Chekhov, Rostov-on-Don 344006, Russian Federation

[3]Southern Federal University, Faculty of Physics, 5 ul. Sorge, Rostov-on-Don 344090, Russian Federation

[4]Southern Federal University, Research Institute of Physical and Organic Chemistry, 194/2 pr. Stachki, Rostov-on-Don 344090, Russian Federation

Abstract

Objectives: The paper studies the effect of the uniformity of spatial distribution of Pt nanoparticles over the support surface in Pt/C materials on the microstructure and electrochemical behavior of PtCo/C catalysts obtained on their basis. PtCo/C catalysts are synthesized by the impregnation of Pt/C followed by heat treatment in an Ar/H_2 atmosphere. The use of a Pt/C material with a platinum mass fraction of about 20% and a uniform distribution of Pt nanoparticles over the surface of the carbon support makes it possible to obtain a PtCo/C catalyst, the activity of which in the oxygen reduction reaction at 0.90 V is 1215 A/g (Pt), which is 4.8 times higher than a similar figure for a commercial Pt/C catalyst. In this case, the use of a Pt/C material with an ununiform distribution of nanoparticles leads to the production of a PtCo/C catalyst with large particle size and low active surface area, which significantly worsens its activity in oxygen reduction reactions. The purpose of this article is to study the effect of the uniformity of the spatial distribution of Pt nanoparticles over the support surface in Pt/C materials on the microstructure and electrochemical behavior of the PtCo/C catalysts obtained from them.

Experimental: PtCo/C catalysts were synthesized by impregnation with Pt/C followed by heat treatment in an Ar/H_2 atmosphere.

Conclusions: The use of a Pt/C material with a platinum content of approximately 20% and a uniform distribution of Pt nanoparticles over the carbon support surface allows the production of a PtCo/C catalyst with an oxygen reduction reaction (ORR) activity of 1215 A/g (Pt) at 0.90 V, which is 4.8 times higher than that of a commercial Pt/C catalyst. The use of a Pt/C material with a non-uniform distribution of nanoparticles results in a PtCo/C catalyst with a large particle size and a low active surface area, which significantly reduces its ORR activity.

Keywords: Platinum-based electrocatalysts, Bimetallic nanoparticles, High-temperature synthesis, Heat treatment, Oxygen electroreduction reaction

Funding: This research conducted at the Southern Federal University was financially supported by the Russian Science Foundation (Grant No. 24-79-00279).

Acknowledgement: The authors are also grateful to the Shared Use Center "High-Resolution Transmission Electron Microscopy" (SFedU) for conducting the TEM studies.

For citation: Nevelskaya A. K., Belenov S. V., Gavrilova A. A., Paperzh K. O., Lyanguzov N. V., Pankov I. V., Kokhanov A. A. Study of the influence of the microstructure of Pt/C materials on the electrochemical characteristics of PtCo/C electrocatalysts based on them. *Condensed Matter and Interphases*. 2025;27(4): 651–660. https://doi.org/10.17308/kcmf.2025.27/13329

✉ Alina K. Nevelskaya, e-mail: alina_nevelskaya@mail.ru

Для цитирования: Невельская А. К., Беленов С. В., Гаврилова А. А., Паперж К. О., Лянгузов Н. В., Панков И. В., Коханов А. А. Изучение влияния микроструктуры Pt/C материалов на электрохимические характеристики полученных на их основе PtCo/C электрокатализаторов. *Конденсированные среды и межфазные границы*. 2025;27(4): 651–660. https://doi.org/10.17308/kcmf.2025.27/13329

1. Introduction

Finding ways to enhance the activity and stability of platinum-based electrocatalysts is a critical task for advancing various areas of hydrogen energy, such as low-temperature fuel cells (LTFCs) [1-4]. One effective approach involves doping platinum with d-metals (e.g., Co, Ni, Fe, Cu) [5–7]. By varying the composition and structure of the resulting nanoparticles, this strategy can improve the functional characteristics of the catalyst [8–14] while reducing its cost.

It is known that a catalyst's performance is largely determined by its morphology, including the distribution of metal nanoparticles on the carbon support, as well as their shape, composition, structure, average size, and size distribution [15–18]. Furthermore, catalysts incorporating bimetallic nanoparticles often exhibit enhanced stability due to stronger metal-support interactions. Therefore, for bimetallic systems, these factors must be carefully considered when developing an optimal synthesis strategy.

Among various candidates, PtCo/C catalysts are regarded as the most promising for LTFCs, combining high activity in the oxygen reduction reaction (ORR) with outstanding stability [4, 19, 20]. The high practical relevance of research on PtCo/C catalysts is underscored by their application in commercial systems, such as the Toyota Mirai fuel cell [21].

The functional properties of bimetallic catalysts are determined by the chemical composition and structure of their nanoparticles, as well as by the distribution of these particles on the carbon support. For instance, achieving a high degree of alloying in PtCo/C catalyst nanoparticles is crucial. Cobalt atoms that are not incorporated into the platinum lattice can dissolve during operation and poison the polymer electrolyte membrane, thereby degrading the performance of the LTFC [22]. However, incorporating Co atoms into the Pt nanoparticles during synthesis is challenging. In many cases, subsequent heat treatment is required, which can lead to particle agglomeration (coarsening), a reduction in active surface area, and consequently, a loss of catalytic activity. Furthermore, forming bimetallic PtCo nanoparticles with an ordered alloy structure (an intermetallic phase) can significantly enhance the catalyst's stability compared to materials with a disordered alloy structure [22, 24].

High-temperature synthesis in a reducing atmosphere is a promising route for producing platinum-based electrocatalysts for low-temperature fuel cells, offering advantages such as high-performance characteristics. Several methods exist for the high-temperature synthesis of bimetallic platinum catalysts.

The first approach involves impregnating a high-surface-area carbon support with precursors of platinum and a d-metal in the required ratio, followed by carbothermic reduction in an inert atmosphere with hydrogen [25–27]. The uniformity of the final product depends heavily on the properties of the carbon support and the high-temperature reduction conditions. Another method utilizes a pre-synthesized Pt/C catalyst (often commercial), which is impregnated with a d-metal precursor. Subsequent heat treatment in an inert atmosphere with a small amount of hydrogen reduces the metal oxide/hydroxide and facilitates its "fusion" with platinum nanoparticles [28, 29]. In this case, the properties of the resulting bimetallic catalyst are determined not only by the temperature and atmosphere but also by the microstructure of the initial Pt/C material.

While several studies have investigated the effects of temperature and atmosphere on the properties of PtM/C catalysts prepared by this method, systematic studies on the influence of the Pt/C precursor's microstructure are lacking. This includes the role of the average size and size distribution of platinum nanoparticles, as well as their dispersion on the carbon support, on the structural characteristics

and electrochemical performance of the final bimetallic catalysts.

Therefore, the aim of this work was to prepare a series of PtCo/C catalysts via high-temperature treatment in a reducing atmosphere using Pt/C precursors with varying microstructures, and to conduct a comparative study of the composition, structure, and catalytic activity of the resulting materials in the oxygen reduction reaction.

2. Experimental

2.1. Deposition of $Co(OH)_2$ on a Pt/C catalyst

The development of highly efficient catalysts containing non-precious metals is an important and promising area of hydrogen energy research. The synthesis method described herein allows for the production of catalysts exhibiting high activity in ORR and enhanced stability.

A sample of a Pt/C catalyst (with a Pt loading of approximately 20 wt. %) was placed in a beaker, and 60 mL of ethylene glycol (reagent grade, AO "EKOS-1", Moscow, Russia) measured with a cylinder was added. A magnetic stir bar was placed into the resulting suspension, and it was stirred on a magnetic stirrer for 2–3 minutes. Subsequently, the mixture was subjected to ultrasonic dispersion twice for 2 minutes each (using an Ultrasonic Processor FS-1200N) and then returned to the magnetic stirrer. A calculated volume of the cobalt precursor, $CoSO_4 \cdot 7H_2O$, as an aqueous solution with a concentration of 0.071 M, was added via a dispenser, and stirring was continued for 1 hour [30].

Following this, a calculated amount of NaOH, dissolved in 20 mL of bidistilled water, was introduced to precipitate cobalt hydroxide. The mixture was stirred on a magnetic stirrer for another hour. The catalyst suspension was filtered using a Büchner funnel with "Blue Ribbon" filter paper and washed sequentially with water, ethanol, and again with water, each for at least three cycles. The catalyst on the filter was then dried at 80 °C in a vacuum oven. After drying, the catalyst was separated from the filter paper, and the resulting powder was subjected to thermal treatment in a tube furnace at 700 °C for 1 hour under a flow of inert gas containing 5 % hydrogen.

Two types of Pt/C catalysts were used to prepare the bimetallic catalysts: (1) a catalyst with a uniform distribution of nanoparticles on the Vulcan XC-72 carbon support (Fig. 1a), designated as Pt/C-u, which is characterized by a high electrochemical active surface area (ECSA) of 80 m^2/g(Pt); and (2) a catalyst with a non-uniform distribution, a high fraction of agglomerates (Fig. 1b), and an ECSA of 25 m^2/g(Pt), designated as Pt/C-n. After thermal treatment at 700 °C, the samples were labeled as PtCo/C-u and PtCo/C-n, respectively, according to the type of Pt/C material used.

2.2. *Investigation of the composition and structure of PtCo/C catalysts*

The phase composition of the obtained materials was studied on an ARL X'TRA diffractometer (Cu$K\alpha$) in the 2θ range from 15° to 55° with a step of 0.04° and a recording rate of 2° per minute. The elemental composition of the materials was studied by X-ray fluorescence analysis on an RFS-001 spectrometer with total internal reflection (TXRF). The average size, shape, and spatial distribution of nanoparticles on the surface of the carbon support were studied using a JEM-F200 transmission electron microscope (TEM) (JEOL). A JEOL EM-01361RSTHB beryllium sample holder with a double tilt was used for TEM measurements. TEM images were obtained at magnifications from 30000× to 600000×.

2.3. Electrochemical characterization

The electrochemical behavior of the electrocatalysts was studied using a three-electrode cell and a rotating disk electrode (RDE) in a 0.1 M $HClO_4$ electrolyte [31]. Catalytic ink was prepared by dispersing 0.006 g of the catalyst in a mixture of 2000 μL isopropyl alcohol and 40 μL of a 5 wt. % Nafion solution via 30-minute ultrasonication to form a homogeneous suspension. A calculated aliquot of the ink was drop-cast onto a glassy carbon disk electrode to achieve a uniform Pt loading of 19–21 μg/cm^2.

Standardization of the electrode surface and recording of cyclic voltammograms (CVs) to determine the ECSA were performed according to the procedure described in [31]. The activity of

the synthesized catalysts in ORR was evaluated by voltammetry with a linear potential sweep on a rotating disk electrode. The kinetic current was calculated at a potential of 0.90 V using the Koutecky–Levich equation [31]. All potentials in this work are given relative to a reversible hydrogen electrode (RHE).

3. Results and discussion

Two Pt/C materials with distinct microstructures were selected for cobalt doping: (1) Pt/C-u with a uniform distribution of nanoparticles on the carbon support surface (Fig. 1) and an average crystallite size of approximately 2.3 nm (Table 1); and (2) Pt/C-n, a material with a non-uniform nanoparticle distribution, pronounced agglomeration, and a slightly larger average crystallite size of 3.0 nm, as determined by X-ray diffraction (XRD) analysis.

It should be noted that despite using the same amount of cobalt precursors (calculated for a Pt:Co atomic ratio of 1:1) deposited on the Pt/C materials, the composition of the resulting PtCo/C materials differed depending on the synthesis methodology. When cobalt precursors were deposited onto the Pt/C-u material using an alkali, the composition of the resulting catalyst was Pt_1Co_1, which corresponds to the atomic ratio of the precursors used in the synthesis. In contrast, for the PtCo/C-n catalyst derived from the Pt/C-n material, the composition corresponded to $PtCo_{1.6}$. This indicates that the PtCo/C-n catalyst contained a lower proportion of Pt compared to the PtCo/C-u material, which may be attributed to specific features of the synthesis procedure and metal losses during the process. The platinum mass fraction in the PtCo/C-n material was 14 % (Table 1), which is lower than expected from the precursor loading and supports the assumption of metal losses during synthesis.

During the deposition of cobalt onto a Pt/C support followed by thermal treatment in an inert atmosphere, two primary processes can occur: the formation of bimetallic PtCo nanoparticles via atomic diffusion, and the coarsening of metal nanoparticles through agglomeration.

The formation of bimetallic nanoparticles after the deposition of cobalt precursors on Pt/C materials and subsequent thermal treatment is

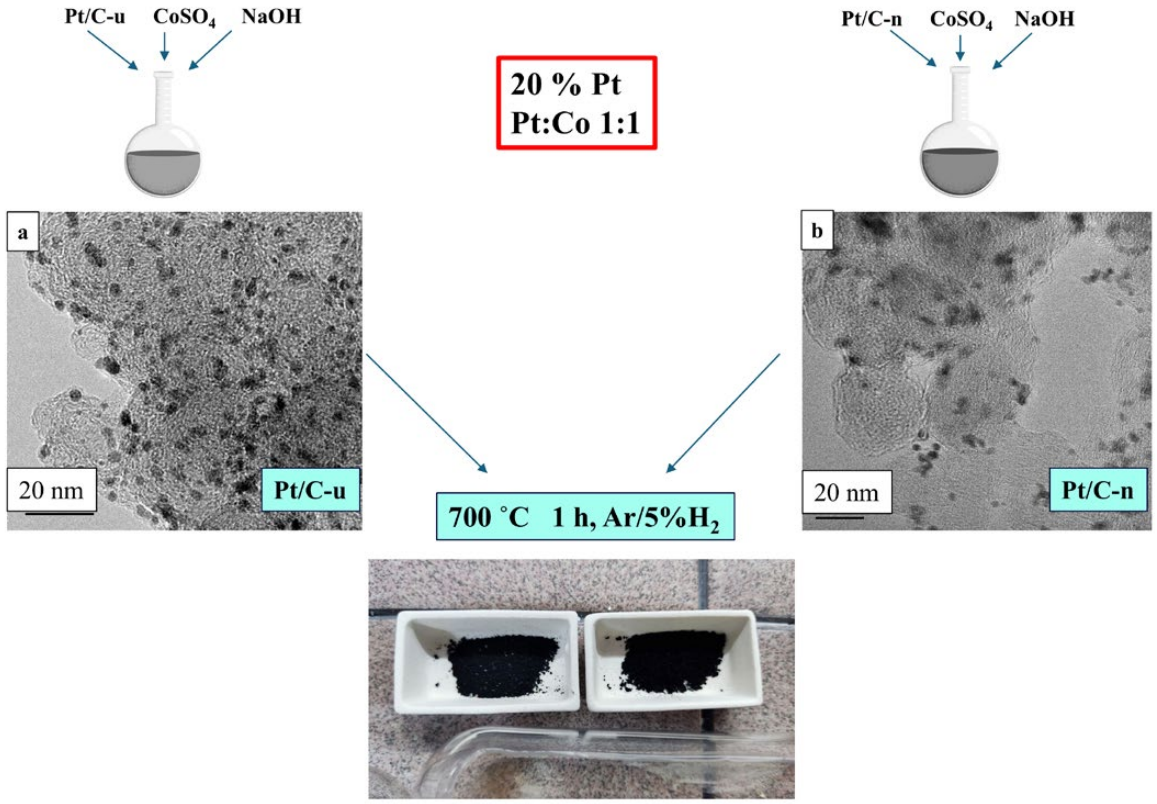

Fig. 1. Synthesis scheme of PtCo/C catalysts on various Pt/C materials

Table 1. Structural characteristics of PtCo/C catalysts obtained on the basis of various Pt/C materials

Sample	ω(Pt), %	Composition TXRF	Lattice parameter, Å	Composition XRD	Average crystallite size, nm
Pt/C-p	21±1	Pt	3.94(6)	–	2.3±0.2
Pt/C-н	18±1	Pt	3.93(3)	–	3.0±0.2
PtCo/C-p	18±1	$PtCo_{1.0}$	3.85(3)	$PtCo_{0.23}$	4.5±0.2
PtCo/C-н	14±1	$PtCo_{1.6}$	3.86(6) 3.81(1)	$PtCo_{0.18}$ $PtCo_{0.44}$	30±3 10±1

confirmed by XRD data. A shift of the reflections corresponding to the face-centered cubic (fcc) structure of platinum towards higher 2θ angles was observed (Fig. 2a). This indicates a decrease in the crystal lattice parameter (Table 1) due to the formation of an alloy of platinum with cobalt. The extent of the peak shift and the phase composition of the resulting PtCo/C catalysts depend on the type of Pt/C material used. For the PtCo/C-u catalyst, derived from the uniformly distributed Pt/C material, a single PtCo phase with a lattice parameter of 3.853 Å was formed. In contrast, XRD analysis of the PtCo/C-n catalyst revealed two distinct metallic phases (Table 1). The composition of the Pt-Co alloy can be estimated from the lattice parameter using Vegard's law. For the PtCo/C-n material, the compositions are $PtCo_{0.18}$ and $PtCo_{0.44}$ for the phases with lower and higher cobalt content, respectively. A discrepancy was noted between the composition of the bimetallic phases determined by XRD and the bulk composition from elemental analysis. This suggests that not all cobalt is incorporated into the platinum lattice to form an alloy. The cobalt not alloyed with platinum may exist in the material as a separate phase, likely an X-ray amorphous cobalt oxide or hydroxide. Analysis of the average crystallite size in the bimetallic catalysts using the Scherrer equation [31] showed that thermal treatment leads to different structural changes in the materials. For the PtCo/C-u catalyst, a slight increase in nanoparticle size to 4.5 nm was observed. Conversely, the PtCo/C-n material exhibited more significant particle coarsening, with sizes reaching 10–30 nm.

Furthermore, additional reflections appeared on the XRD pattern of the PtCo/C-n material after thermal treatment. The presence of these reflections may indicate the formation of Pt-Co intermetallic compounds. However, their low intensity makes precise identification

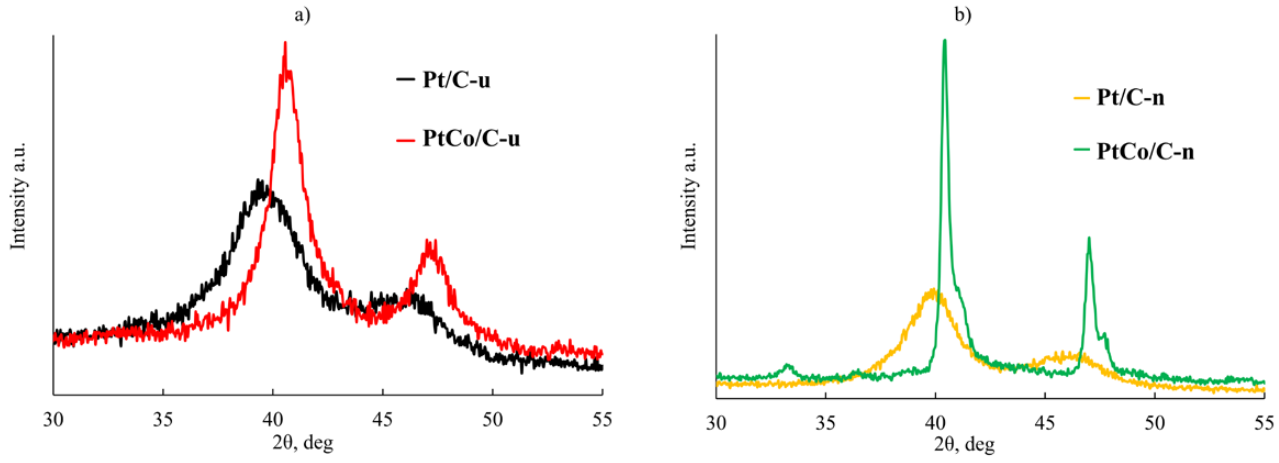

Fig. 2. X-ray diffraction patterns of Pt/C materials and PtCo/C catalysts obtained on their basis with uniform (a) and non-uniform (b) distribution of nanoparticles over the surface of the carbon support

difficult.

According to TEM data (Fig. 3), the PtCo/C-u catalyst is characterized by a uniform distribution of metal nanoparticles on the carbon support surface. TEM results also revealed that the material contains nanoparticles with a size range of 2 to 8 nm (Fig. 3b), as well as large nanoparticle agglomerates up to 30 nm in size (Fig. 3b). A particle size distribution histogram was constructed based on the analysis of TEM images (Fig. 3c), and the average size of the metal nanoparticles was calculated to be 4.7 nm. The histogram shows a wide dispersion, indicating the presence of both small nanoparticles (around 2 nm) and larger ones exceeding 8 nm. It is important to note that the large nanoparticle agglomerates were not included in the calculation of the average particle size or in the construction of the histogram due to methodological constraints in their accurate accounting. The average nanoparticle size for the PtCo/C-u material, as determined by TEM, closely matches the average crystallite size of PtCo calculated using the Scherrer equation (Table 1). Thus, the bimetallic catalyst derived from the uniform Pt/C material exhibits a uniform distribution of nanoparticles across the carbon support surface but simultaneously possesses a very broad particle size distribution and the presence of agglomerates, which is a detrimental factor for developing highly efficient catalysts. Consequently, further optimization of the cobalt precursor deposition method and thermal treatment conditions is likely required to obtain a catalyst with a narrower size distribution.

Evaluation of the ECSA by cyclic voltammetry (Fig. 4) revealed significant differences between the PtCo/C materials derived from Pt/C precursors with different uniformities. The ECSA for the PtCo/C-u material was about 50 m^2/g(Pt) (Table 2), which is somewhat lower than that of the commercial Pt/C analogue (ECSA = 84 m^2/g(Pt)). This decrease is likely associated with the larger size and broader size distribution of the nanoparticles in the bimetallic material. Notably, the deposition of cobalt followed by thermal treatment led to a reduction in the ECSA for the PtCo/C-u material compared to the original Pt/C-u (Table 2), which can be attributed to particle growth during the high-temperature synthesis of the bimetallic catalyst. The ECSA for the PtCo/C-n material, derived from the non-uniform Pt/C precursor, was significantly lower than that of PtCo/C-u. This can be explained both by the lower initial ECSA of the Pt/C-n precursor and the larger metal particle size in the final PtCo/C-n material (Table 1).

The polarization curves in Fig. 4 exhibit a typical shape for platinum-based catalysts. From 1.10 V to an onset potential of about 0.98 V for PtCo/C-n and Pt/C, and about 1.00 V for PtCo/C-u (Fig. 4c, Region I; Fig. 4d), the current is zero, indicating that the ORR does not proceed. Upon reaching the onset potential, the cathodic current increases as the potential decreases. This region is independent of the

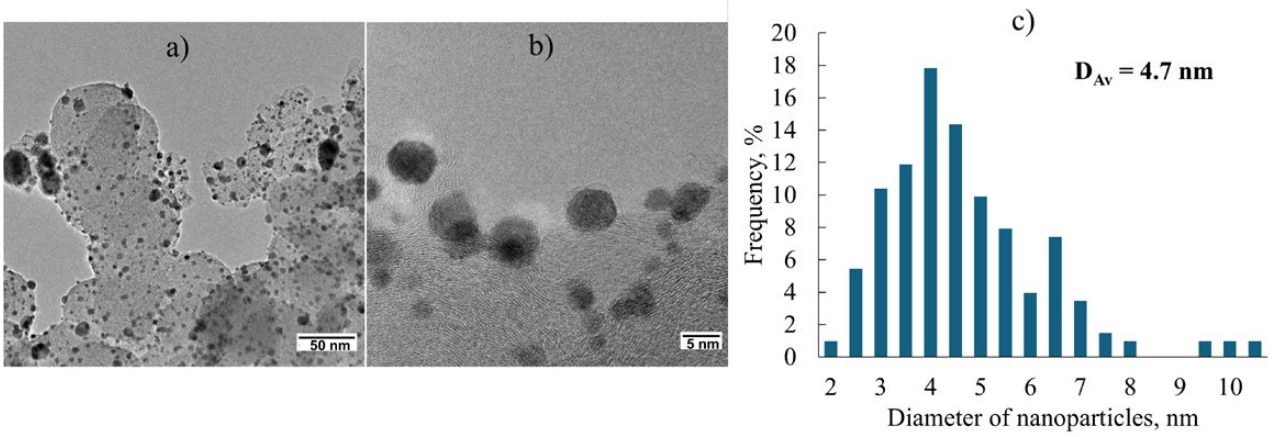

Fig. 3. TEM images (a, b) and histogram of the size distribution of nanoparticles (c) of PtCo/C-u catalyst obtained on the basis of Pt/C catalyst with uniform distribution of nanoparticles

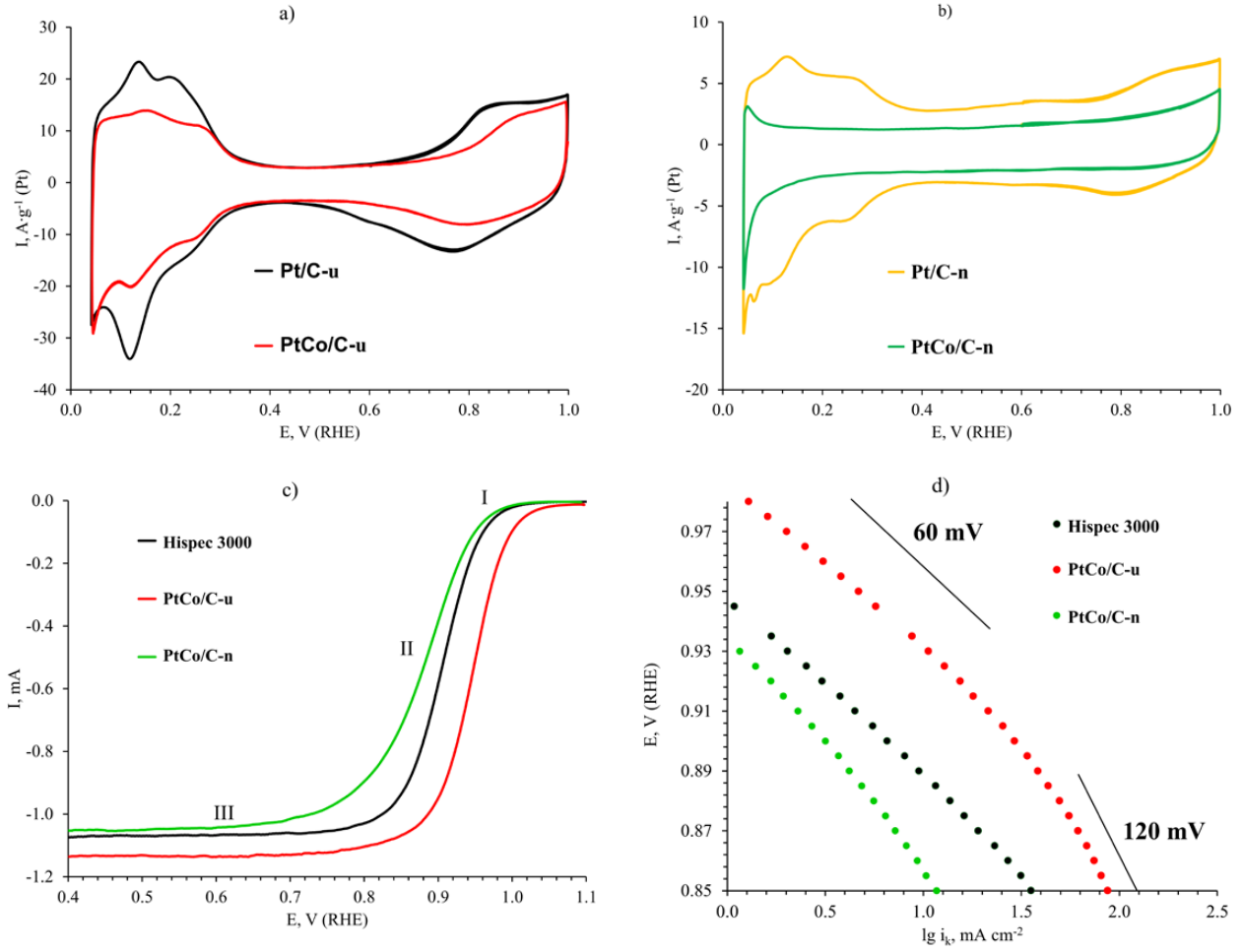

Fig. 4. Cyclic voltammograms of PtCo/C catalysts obtained using various Pt/C catalysts (a, b); linear potential sweep voltammograms (c) and Tafel dependence for the obtained PtCo/C catalysts, as well as the commercial Pt/C catalyst Hispec 3000 (d)

Table 2. Electrochemical characteristics of the obtained PtCo/C catalysts, as well as the commercial Pt/C catalyst Hispec 3000

Sample	ECSA, m^2/g (Pt)	I_k, mA	I_m, A/g (Pt) (at 0.90 V)	I_s, A/m^2 (Pt) (at 0.90 V)	$E_{1/2}$, V
PtCo/C-p	50±5	5.0±0.5	1215±122	24.3±2.4	0.94±0.01
PtCo/C-н	< 3	0.6±0.1	192±19	–	0.88±0.01
Hispec 3000	84±8	1.2±0.1	254±25	3.0±0.3	0.91±0.01

electrode rotation rate, and the reaction rate is governed solely by the sluggish kinetics of the ORR. With a further decrease in potential, oxygen diffusion to the electrode surface begins to contribute. This region (Fig. 4c, Region II) is characterized by mixed kinetic-diffusion control. At even lower potentials, the cathodic current becomes independent of the applied potential as it becomes limited solely by the rate of oxygen supply to the electrode surface – this is the region of the limiting diffusion current (Fig. 4c, Region III).

The catalytic activity at 0.90 V, normalized both to the mass of Pt (mass activity, I_m), and to the ECSA (specific activity, I_s), demonstrates the superior performance of the PtCo/C-u material. Its mass activity of 1215 A/g(Pt) and specific activity of 24.3 A/m^2(Pt) far exceed those of the

commercial Pt/C analogue (254 A/g(Pt)), despite its lower ECSA (Table 2). In contrast, the PtCo/C-n material shows significantly lower activity compared to the commercial Pt/C, which can be attributed to its extremely low ECSA. Based on the half-wave potential ($E_{1/2}$), the studied samples can be ranked in the following order of increasing activity: PtCo/C-n < Pt/C < PtCo/C-u. The half-wave potential serves as a key indicator of activity, alongside kinetic current values. Thus, it is confirmed that the PtCo/C-u catalyst, possessing the highest half-wave potential of 0.94 V among all samples, exhibits the greatest activity in the ORR.

4. Conclusions

A study on model Pt/C samples with uniform and non-uniform distributions of platinum nanoparticles demonstrated the decisive influence of this parameter on the performance of the resulting bimetallic PtCo/C catalysts. It was found that the PtCo/C catalyst derived from the uniformly distributed Pt/C precursor exhibits a larger electrochemical surface area and a mass activity more than six times higher than that of the catalyst obtained from the non-uniform Pt/C material. Furthermore, the mass activity of the most active PtCo/C catalyst exceeded that of a commercial Pt/C catalyst by a factor of 4.8.

Thus, the presented high-temperature synthesis method for PtCo/C electrocatalysts has proven to be both promising and scalable for producing highly efficient bimetallic materials. Future work will focus on synthesizing catalysts with varying metal loadings and testing their performance in membrane-electrode assemblies of low-temperature fuel cells.

Contribution of the authors

A. K. Nevelskaya: Investigation, Data curation, Writing - original draft. S. V. Belenov: Supervision, Conceptualization, Writing - review & editing, Project administration. A. A. Gavrilova: Investigation. K. O. Paperzh: Investigation. N. V. Lyanguzov: Investigation. I. V. Pankov: Investigation, TEM analysis. A. A. Kokhanov: Investigation.

Conflict of interests

The authors declare that they have no known competing financial interests or personal relationships that could have influenced the work reported in this paper.

References

3. Peng Z, Yang H. Designer platinum nanoparticles: control of shape, composition in alloy, nanostructure and electrocatalytic property. *Nano Today*. 2009;4: 143–164. https://doi.org/10.1016/j.nantod.2008.10.010

4. Xu G., Yang L., Li J., Liu C., Xing W., Zhu J. Strategies for improving stability of Pt-based catalysts for oxygen reduction reaction. *Advanced Sensor and Energy Materials*. 2023;2: 100058. https://doi.org/10.1016/j.asems.2023.100058

5. Xiao F., Wang Y., Wu Z., ...Shao M. Recent advances in electrocatalysts for proton exchange membrane fuel cells and alkaline membrane fuel cells. *Advanced Materials*. 2021;33: 2006292. https://doi.org/10.1002/adma.202006292

6. Wu D., Shen X., Pan Y., Yao L., Peng Z. Platinum alloy catalysts for oxygen reduction reaction: advances, challenges and perspectives. *ChemNanoMat*. 2020;6: 32–41. https://doi.org/10.1002/cnma.201900319

7. Wang X. X., Swihart M. T., Wu G. Achievements, challenges and perspectives on cathode catalysts in proton exchange membrane fuel cells for transportation. *Nature Catalysis*. 2019;2: 578–589. https://doi.org/10.1038/s41929-019-0304-9

8. Glüsen A., Dionigi F., Paciok P., ... Stolten D. Dealloyed PtNi-core–shell nanocatalysts enable significant lowering of Pt electrode content in direct methanol fuel cells. *ACS Catalysis*. 2019;9: 3764–3772. https://doi.org/10.1021/acscatal.8b04883

9. Jeyabharathi C., Hodnik N., Baldizzone C., ... Mayrhofer K. J. J. Time evolution of the stability and oxygen reduction reaction activity of PtCu/C nanoparticles. *ChemCatChem*. 2013;5: 2627–2635. https://doi.org/10.1002/cctc.201300287

10. Koh S., Strasser P. Electrocatalysis on bimetallic surfaces: modifying catalytic reactivity for oxygen reduction by voltammetric surface dealloying. *Journal of the American Chemical Society*. 2007;129: 12624–12625. https://doi.org/10.1021/ja0742784

11. Lopez-Haro M., Dubau L., Guétaz L., ... Maillard F. Atomic-scale structure and composition of Pt_3Co/C nanocrystallites during real PEMFC operation: a STEM–EELS study. *Applied Catalysis B: Environmental*. 2014;152–153: 300–308. https://doi.org/10.1016/j.apcatb.2014.01.034

12. Gan L., Heggen M., O'Malley R., Theobald B., Strasser P. Understanding and controlling nanoporosity formation for improving the stability of bimetallic fuel cell catalysts. *Nano Letters*. 2013;13: 1131–1138. https://doi.org/10.1021/nl304488q

13. Lyu X., Jia Y., Mao X., ... Yao X. Gradient-concentration design of stable core-shell nanostructure for acidic oxygen reduction electrocatalysis. *Advanced Materials*. 2020;32: 2003493. https://doi.org/10.1002/adma.202003493

14. Gan L., Yu R., Luo J., Cheng Z., Zhu J. Lattice strain distributions in individual dealloyed Pt–Fe catalyst nanoparticles. *The Journal of Physical Chemistry Letters*. 2012;3: 934–938. https://doi.org/10.1021/jz300192b

15. Paperzh K. O., Alekseenko A. A., Safronenko O. A., Volochaev V. A., Pankov I. V., Guterman V. E. Stability and activity of platinum nanoparticles in the oxygen electroreduction reaction: is size or ordering of primary importance? 2021: 593–606. https://doi.org/10.3762/bxiv.2021.27.v1

16. Paperzh K. O., Pavlets A. S., Alekseenko A. A., Pankov I. V., Guterman V. E. The integrated study of the morphology and the electrochemical behavior of Pt-based ORR electrocatalysts during the stress testing. *International Journal of Hydrogen Energy*. 2023;48: 22401–22414. https://doi.org/10.1016/j.ijhydene.2023.01.079

17. Paperzh K., Moguchikh E., Pankov I., Belenov S., Alekseenko A. Effect of AST atmosphere on Pt/C electrocatalyst degradation. *Inorganics (Basel)*. 2023;11: 237. https://doi.org/10.3390/inorganics11060237

18. Paperzh K., Alekseenko A., Danilenko M., Pankov I., Guterman V. E. Advanced methods of controlling the morphology, activity, and durability of Pt/C electrocatalysts. *ACS Applied Energy Materials*. 2022;5: 9530–9541. https://doi.org/10.1021/acsaem.2c01151

19. Wen Y.-H., Zhang L.-H., Wang J.-B., Huang R. Atomic-scale insights into thermal stability of Pt_3Co nanoparticles: a comparison between disordered alloy and ordered intermetallics. *Journal of Alloys and Compounds*. 2019;776: 629–635. https://doi.org/10.1016/j.jallcom.2018.10.274

20. Jung W. S., Popov B. N. Effect of pretreatment on durability of fct-structured Pt-based alloy catalyst for the oxygen reduction reaction under operating conditions in polymer electrolyte membrane fuel cells. *ACS Sustainable Chemistry and Engineering*. 2017;5: 9809–9817. https://doi.org/10.1021/acssuschemeng.7b01728

21. Konno N., Mizuno S., Nakaji H., Ishikawa Y. Development of compact and high-performance fuel cell stack. *SAE International Journal of Alternative Powertrains*. 2015;4: 2015-01–1175. https://doi.org/10.4271/2015-01-1175

22. Yan W., Sun P., Luo C., ... Du F. PtCo-based nanocatalyst for oxygen reduction reaction: Recent highlights on synthesis strategy and catalytic mechanism. *Chinese Journal of Chemical Engineering*. 2023;53: 101–123. https://doi.org/10.1016/j.cjche.2022.03.024

23. Tong L., Fan L., Liang H.-W. Platinum intermetallic nanoparticle cathode catalysts for proton-exchange-membrane fuel cells: Synthesis and ordering effect. *Current Opinion in Electrochemistry*. 2023;39: 101281. https://doi.org/10.1016/j.coelec.2023.101281

24. Liu X., Liang J., Li Q. Design principle and synthetic approach of intermetallic Pt-M alloy oxygen reduction catalysts for fuel cells. *Chinese Journal of Catalysis*. 2023;45: 17–26. https://doi.org/10.1016/S1872-2067(22)64165-2

25. Yang B., Yu X., Hou J., Xiang Z. Secondary reduction strategy synthesis of Pt–Co nanoparticle catalysts towards boosting the activity of proton exchange membrane fuel cells. *Particuology*. 2023;79: 18–26. https://doi.org/10.1016/j.partic.2022.11.010

26. Wan K., Wang J., Zhang J., ... Zhang C. Ligand carbonization in-situ derived ultrathin carbon shells enable high-temperature confinement synthesis of PtCo alloy catalysts for high-efficiency fuel cells. *Chemical Engineering Journal*. 2024;482: 149060. https://doi.org/10.1016/j.cej.2024.149060

27. Lima F. H. B., de Castro J. F. R., Santos L. G. R. A., Ticianelli E. A. Electrocatalysis of oxygen reduction on carbon-supported Pt–Co nanoparticles with low Pt content. *Journal of Power Sources*. 2009;190: 293–300. https://doi.org/10.1016/j.jpowsour.2008.12.128

28. Mai Y., XIE X, Wang Z., Yan C., Liu G. Effect of heat treatment temperature on the Pt3Co binary metal catalysts for oxygen reduced reaction and DFT calculations. *Journal of Fuel Chemistry and Technology*. 2022;50: 114–121. https://doi.org/10.1016/S1872-5813(21)60099-3

29. Koh S., Hahn N., Yu C., Strasser P. Effects of composition and annealing conditions on catalytic activities of dealloyed Pt–Cu nanoparticle electrocatalysts for PEMFC. *Journal of The Electrochemical Society*. 2008;155: B1281. https://doi.org/10.1149/1.2988741

30. Belenov S., Mauer D., Moguchikh E…Alekseenko A. New approach to synthesizing cathode PtCo/C catalysts for low-temperature fuel cells. *Nanomaterials*. 2024;14: 856. https://doi.org/10.3390/nano14100856

31. Belenov S., Nevelskaya A., Nikulin A., Tolstunov M. The effect of pretreatment on a PtCu/C catalyst's structure and functional characteristics. *International Journal of Molecula*. 2023;24: 2177. https://doi.org/10.3390/ijms24032177

Information about the authors

Alina K. Nevelskaya, Cand. Sci. (Chem.), Researcher at the Department of Electrochemistry, Southern Federal University (Rostov-on-Don, Russian Federation); Junior Researcher at the Federal Research Center Southern Scientific Center of the Russian Academy of Sciences (SSC RAS) (Rostov-on-Don, Russian Federation).

https://orcid.org/0000-0001-5799-9925

alina_nevelskaya@mail.ru

Sergey V. Belenov, Cand. Sci. (Chem.), Leading Researcher at the Department of Electrochemistry, Faculty of Chemistry, Southern Federal University (Rostov-on-Don, Russian Federation).

https://orcid.org/0000-0003-2980-7089

serg1986chem@mail.ru

Anna A. Gavrilova, student, Research Intern, Southern Federal University (Rostov-on-Don, Russian Federation).

https://orcid.org/0009-0006-7596-6821

ganna2800@mail.ru

Kirill O. Paperzh, Junior Researcher at the Department of Electrochemistry, Southern Federal University (Rostov-on-Don, Russian Federation).

https://orcid.org/0000-0003-4878-9728

paperzh@sfedu.ru

Nikolay V. Lyanguzov, Cand. Sci. (Chem.), Associate Professor of the Nanotechnology Department, Southern Federal University (Rostov-on-Don, Russian Federation).

https://orcid.org/0000-0001-9802-9335

nvlyanguzov@sfedu.ru

Ilya Pankov, Cand. Sci. (Chem.), Lead Engineer of the Shared Use Center "High-Resolution Transmission Electron Microscopy".
https://orcid.org/0000-0001-5302-4792
ipankov@sfedu.ru

Andrey A. Kokhanov, student, Southern Federal University (Rostov-on-Don, Russian Federation).
https://orcid.org/0009-0003-6546-0710
akokhanov@sfedu.ru

Received February 6, 2025; approved after reviewing March 11, 2025; accepted for publication March 17, 2025; published online December 25, 2025.

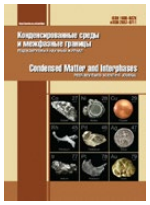

ISSN 1606-867X (Print)
ISSN 2687-0711 (Online)
Condensed Matter and Interphases
Kondensirovannye Sredy i Mezhfaznye Granitsy
https://journals.vsu.ru/kcmf/

Original articles

Research article
https://doi.org/10.17308/kcmf.2025.27/13325

Formation of oxide films on manganese silicide-germanides of various compositions during anodic polarization in an aqueous sodium sulfate solution

I. L. Rakityanskaya[1]✉, D. A. Myasnikov[1]

[1]Perm State University,
Bukireva st., 15, Perm 614990, Russian Federation

Abstract

Objectives: Manganese silicide-germanides, with the general formula composition $Mn_5(Si,Ge)_3$, different in the quantitative ratio of silicon and germanium with the formula $Mn_5Si_{2.40}Ge_{0.60}$, $Mn_5Si_{0.60}Ge_{2.40}$, and $Mn_5Si_{0.15}Ge_{2.85}$, were subjected to anodic polarization in an aqueous sodium sulfate solution. The main objective of the study was the determination of the products of their anodic transformation in a non-oxidizing neutral medium and the identification of regularities of the formation of oxide films on their surface.

Experimental: The cyclic voltammetry method showed that the anodic oxidation process is not reversible. Polarization measurements were accompanied by subsequent monitoring of changes in the surface state using electron microscopy. The micro-X-ray spectral analysis was used for the determination of the ratio of elements on the surface before polarization of the sample and in the corrosion products.

Conclusions: The results of the study demonstrated that during the anodic transformation process for all materials, the fraction of manganese in the samples decreased, the fraction of germanium increased, and the fraction of silicon changed insignificantly. It was concluded that the dissolution of the material components occurs selectively: manganese was predominantly ionized from the solid phase of manganese germanide into the solution, and its content on the surface was reduced to insignificant amounts. Silicon and germanium formed loose oxide layers without good adhesion to a hard, manganese-depleted surface and did not provide a serious protective effect. Germanium (II) oxide and partially hydrated germanium (IV) oxide $GeO_2 \times H_2O$ were the main products of anodic oxidation that remained on the surface. Silicon oxide was also present in anodic oxidation products, but in lower quantities, and was not sufficient for the provision of the protective effect of the material.

Keywords: Silicide-germanide, Manganese, Germanium, Oxide films, Anodic oxidation, Sodium sulfate

For citation: Rakityanskaya I. L., Myasnikov D. A. Formation of oxide films on manganese silicide-germanides of various compositions during anodic polarization in an aqueous sodium sulfate solution. *Condensed Matter and Interphases*. 2025;27(4): 661–668. https://doi.org/10.17308/kcmf.2025.27/13325

Для цитирования: Ракитянская И. Л., Мясников Д. А. Формирование оксидных плёнок на силицидо-германидах марганца различного состава при анодной поляризации в водном растворе сульфата натрия. *Конденсированные среды и межфазные границы*. 2025;27(4): 661–668. https://doi.org/10.17308/kcmf.2025.27/13325

✉ Irina L. Rakityanskaya, e-mail: irisa@yandex.ru

1. Introduction

The rapid development of modern technologies inevitably dictates the need to create and investigate the properties of new materials, which often represent a complex composition of components with significantly different properties. At the same time, modeling the electrochemical behavior of multicomponent and multiphase systems is a complex and non-trivial task, requiring a comprehensive approach and a wide range of methods. These methods should allow us to evaluate not only the final change in the material surface under the influence of an aggressive medium but also provide information about the kinetics of cathodic and anodic processes. The combination of cyclic voltammetry (allowing to assess the rate and reversibility of electrode processes) with electron microscopy and micro-X-ray spectral analysis (enabling to visually evaluate changes in the structure, qualitative and quantitative composition of the surface of the material) allows examining the various aspects of dissolution process of the material and to form a comprehensive view of the changes occurring on its surface. Manganese silicide-germanides, which have different ratios of silicon and germanium are suitable objects for such studies, since their individual components, manganese, silicon and germanium, have significantly different electrochemical behavior [1].

It is known that all individual components of manganese silicide-germanides are capable for oxidation in both acidic and alkaline media, forming products with various thermodynamic stability on the surface of the sample. Thus, during the oxidation of manganese, compounds in various oxidation states can be formed, none of which is capable to form the strong film with protective properties: in an acidic medium, soluble salts of divalent manganese are formed, and in an alkaline medium, manganese is in a passive state due to the formation of $Mn(OH)_2$ and at higher potentials, MnO_2 on the surface [2–5]. Silicon, due to the formation of poorly soluble SiO_2, protects the surface well from dissolution in acidic media, while in alkaline media its protective properties are not so significant [2, 6–8]. Germanium, despite its structure and some chemical properties like silicon, cannot form protective surface compounds in any of the previously studied media [2, 10].

Manganese silicide-germanides are two-phase structures consisting of silicide, silicide-germanide, and manganese germanide phases, with the amount of one or the other phase varying depending on the silicon or germanium content of the material [11].

It is known that Mn_5Si_3 and Mn_5Ge_3 "limiting" phases with respect to silicide-germanides during anodization form layers of oxidation products, which, in the case of manganese silicide, protect the surface of the sample from further destruction [9, 12]. In the case of manganese germanide, a defective layer of anodic transformation products, unable to protect the sample is formed [10, 12]. To date, there is no systematic data on the qualitative and quantitative composition of the products of anodic oxidation of manganese silicide-germanides with different ratios of germanium and silicon in neutral media. Nevertheless, data on the influence of the ratio of elemental silicon and germanium, as well as the phases formed in the material, on the formation of surface compounds can be used both for modeling the behavior of such three-component metal + two-non-metal systems and for practical use in the creation of semiconductor structures.

This work aims to compare the anodic behavior of manganese silicide-germanides with different ratios of silicon and germanium in the sample and to analyze changes in the surface microstructure of the materials and the products of their anodic oxidation.

2. Experimental

Manganese silicide-germanides with the following compositions: $Mn_5Si_{3-2.85}Ge_{2.85}$, $Mn_5Si_{3-2.40}Ge_{2.40}$, and $Mn_5Si_{3-0.60}Ge_{0.60}$, obtained according to the method described in [13], were subjected to multiple cyclic anodic polarization from the open circuit potential to the potential of thermodynamically possible oxygen evolution, followed by a return to the original potential. The surface of the sample was then examined microscopically using micro-X-ray spectral analysis. The methods of sample preparation and their study are described in detail in the study [13, 15]. The phase composition of the samples was confirmed by X-ray structural analysis [11].

With an increase in the fraction of germanium atoms in the sample, the phase composition of the material changes from a predominant content of the manganese silicide phase Mn_5Si_3 to the predominant content of the manganese germanide phase, Mn_5Ge_3.

3. Results and discussion

3.1. Polarization measurements and data from microscopic and micro-X-ray spectral studies of manganese silicide-germanides

Anodic CVA curves for $Mn_5Si_{3-0.60}Ge_{0.60}$ are shown in Fig. 1. From E = +0.2 V, the current density started to increase noticeably, which indicates active dissolution of the material. However, it was impossible to isolate a separate maximum on the curve; the peaks were not separated, and the oxidation processes of the components occurred at close potentials. At a potential of +1.6 V, a state of passivity occurred, and the process of active dissolution was suspended. The anodic oxidation process is irreversible, since the reverse scan curve also had oxidation peaks accompanied by current oscillations, while reduction peaks were absent. Current oscillations were detected at potentials of thermodynamic possibility of oxygen release. It can be assumed that the released gas promoted the detachment of the oxide layer formed during direct unfolding, characterized by weak adhesion to the surface of the material.

After anodic polarization on the surface of the $n_5Si_{3-0.60}Ge_{0.60}$ electrode there was no visible layer of transformation products (Fig. 2). At magnifications of 370× and 1000×, it became clear that the most developed areas of the surface were cracks, where the manganese content was noticeably lower than in smooth areas, and the percentages of germanium and oxygen were higher. This allowed us to assume that the manganese silicide phase in this medium was stable and was not subjected to anodic destruction, while in the cracks, the transformation of manganese germanide with the ionization of manganese into a solution and the accumulation of insoluble germanium oxides occurred (Table 1).

The $Mn_5Si_{3-2.40}Ge_{2.40}$ material, containing a higher amount of germanium in the sample, was subjected to destruction at a significantly higher anodic current in the active dissolution region compared to $Mn_5Si_{3-0.60}Ge_{0.60}$ (Fig. 3). The process was also irreversible; the reverse curves for all cycles were above the forward curves, since

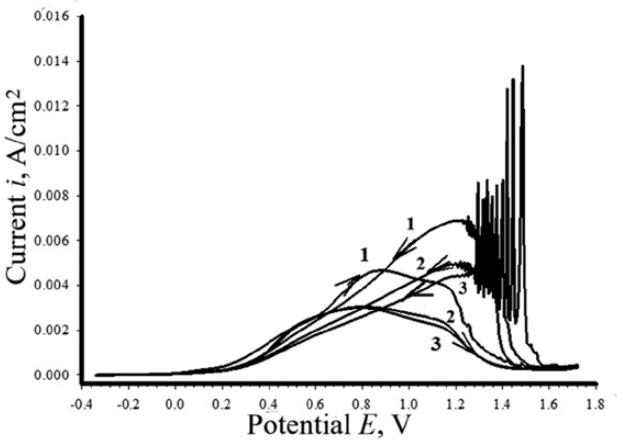

Fig. 1. Anodic CVA-curves for $Mn_5Si_{3-0.60}Ge_{0.60}$ in an 0.5M Na_2SO_4 solution, potential change rate is 5 mV/s; the number of the cycle is shown by a number near the curve

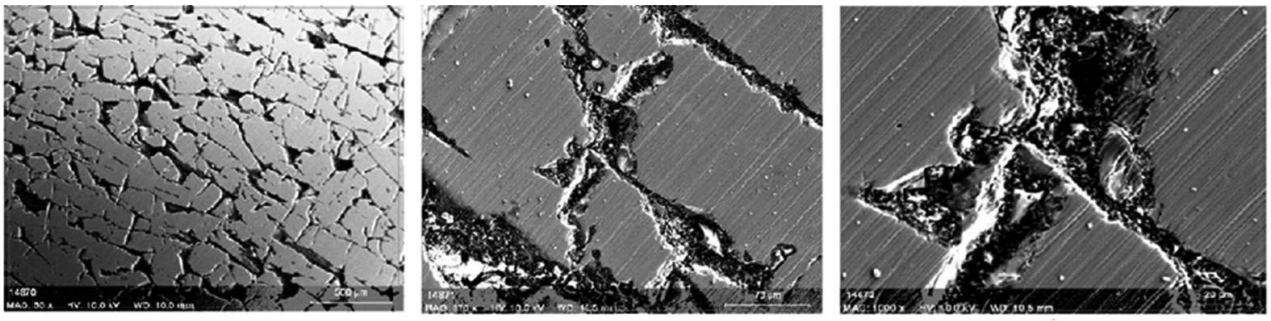

a b c

Fig. 2. Micrographs of the $Mn_5Si_{3-0.60}Ge_{0.60}$ surface after 3 cycles of anodic polarization in an 0.5M Na_2SO_4 solution at the following magnifications: (a) 50×, (b) 370×, (c) 1000×

Table 1. Content of elements on $Mn_5Si_{3-0.60}Ge_{0.60}$ surface before and after anodic polarization

	ω_{at} Mn, %	ω_{at} Si, %	ω_{at} Ge, %	ω_{at} O, %
Surface before the polarization	60.25±2.55	31.24±1.87	6.16±0.83	2.35±0.51
On the surface	56.85±2.15	34.93±1.88	2.81±0.54	5.41±0.64
In the cracks	15.78±1.23	31.28±1.87	12.83±1.12	40.11±1.85

during reverse scanning, additional oxidation of components occurred on a more developed surface.

A yellow-brown oxide layer formed on manganese silicide germanide $Mn_5Si_{3-2.40}Ge_{2.40}$ during anodic polarization was clearly visible. Microscopic examination also showed the presence of a well-developed layer of anodic transformation products (Fig. 4). The layer was not continuous, it was loose, and easily detachable from the surface of the material. Uneven film formation led to current oscillations in the CVA curves (Fig. 3): during detachment, the current increased sharply and then decreased as a new portion of the product accumulated on the surface.

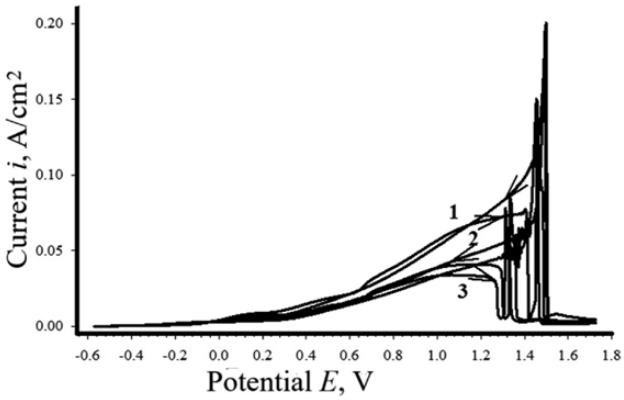

Fig. 3. Anodic CVA-curves for $Mn_5Si_{3-2.40}Ge_{2.40}$ in an 0.5 M Na_2SO_4 solution, potential change rate is 5 mV/s; the number of the cycle is shown by a number near the curve

Micro-X-ray spectral analysis of the surface showed that after anodic polarization the silicon content decreased slightly, the percentage of the manganese component decreased, and the germanium component increased. This suggested that the manganese silicide phase was still resistant to anodic destruction, manganese was actively removed into solution, and germanium remained on the surface in the form of yellow germanium oxide with complex composition GeO_X. In cracks, the composition of the anodic dissolution products differed from that on the sample surface, with a further depletion of manganese and enrichment of the germanium component.

The $Mn_5Si_{3-2.85}Ge_{2.85}$ sample consisted of 91 % of manganese germanide Mn_5Ge_3 phase, less thermodynamically stable during anodic oxidation in electrolyte solutions [11, 14]. Therefore, the currents in the active dissolution region were even higher than for $Mn_5Si_{3-0.60}Ge_{0.60}$ and $Mn_5Si_{3-2.40}Ge_{2.40}$ samples (Fig. 5). Oscillations associated with the detachment of anodic oxidation products were expressed less strongly; the reverse curve showed a sharp increase in current in active dissolution potentials, followed by a decrease. The process, just like in the previous samples, was not reversible; there was no symmetrical recovery peak.

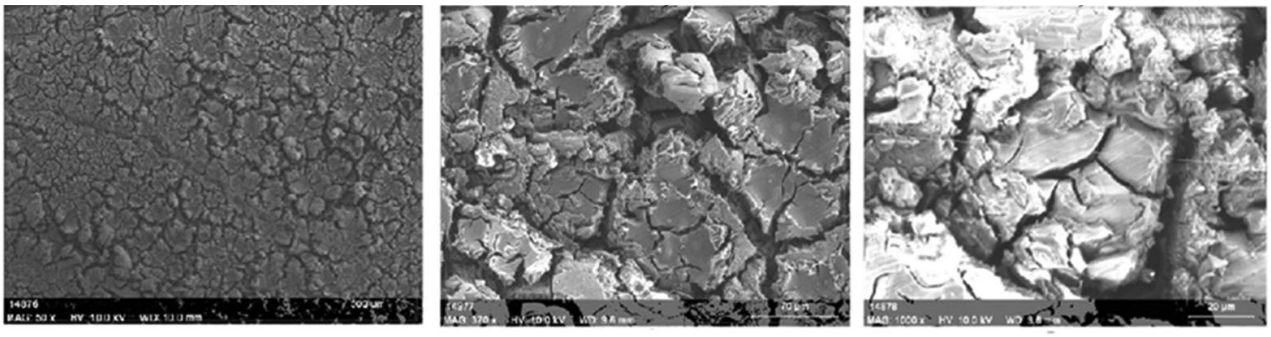

a b c

Fig. 4. Micrographs of the $Mn_5Si_{3-2.40}Ge_{2.40}$ surface after 3 cycles of anodic polarization in an 0.5M Na_2SO_4 solution at the following magnifications: (a) 50×, (b) 370×, (c) 1000×

After anodic polarization in 0.5 M sodium sulfate solution on the surface of $Mn_5Si_{3-2.85}Ge_{2.85}$ similarly as on the surface of $Mn_5Si_{3-2.40}Ge_{2.40}$, the yellow-brown oxide layer was clearly visible. Surface microscopy demonstrated that this layer was even looser. At 2000x magnification, the smallest parts of the layer, represented by structures twisted into tubes became visible. The size of the particles that composed the oxide layer did not exceed several tens of micrometers (Fig. 6).

Micro-X-ray spectral analysis showed a significant decrease in the content of manganese and silicon in the layer of anodic oxidation products and a simultaneous increase in the germanium and oxygen (Table 3). Apparently, the less thermodynamically stable phase of manganese germanide was destroyed with the transition of manganese into solution, leaving germanium oxide on the surface, characterized by poor adhesion to the surface and, consequently, a low protective effect.

The dried layer of anodic transformation products was easily separated from the sample

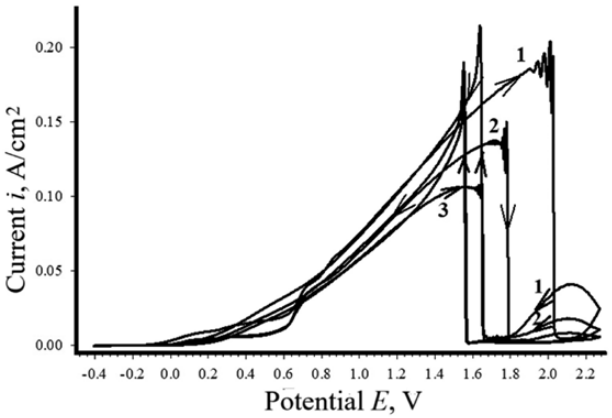

Fig. 5. Anodic CVA-curves for $Mn_5Si_{3-2.85}Ge_{2.85}$ in an 0.5 M Na_2SO_4 solution, potential change rate is 5 mV/s; the number of the cycle is shown by a number near the curve

by lightly tapping of the electrode on any hard surface. Micrographs of the cleaned surface are shown in Fig. 7. Surface relief of the $Mn_5Si_{3-2.85}Ge_{2.85}$ sample was quite developed, and areas affected by corrosion, where selective etching of manganese and the formation of oxides, primarily germanium

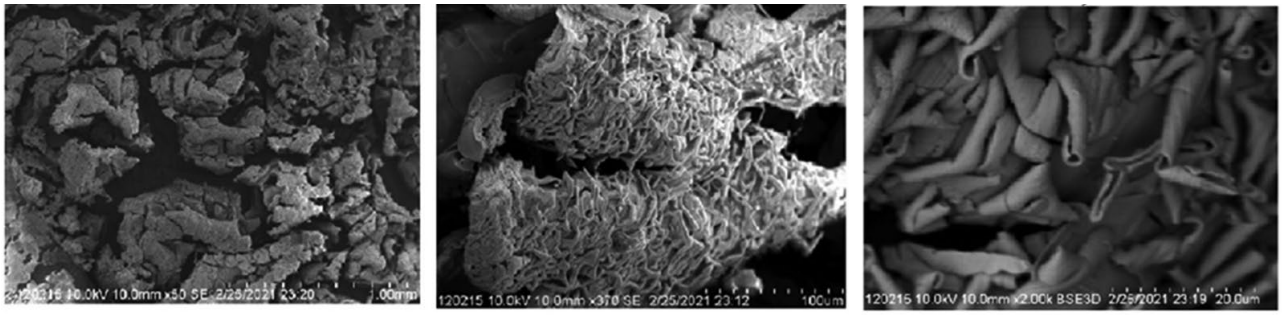

a b c

Fig. 6. Micrographs of the $Mn_5Si_{3-2.85}Ge_{2.85}$ surface after 3 cycles of anodic polarization in an 0.5M Na_2SO_4 solution at the following magnifications: (a) 50×, (b) 370×, (c) 2000×

Table 2. Content of elements on the $Mn_5Si_{3-2.40}Ge_{2.40}$ surface before and after anodic polarization

	ω_{at} Mn, %	ω_{at} Si, %	ω_{at} Ge, %	ω_{at} O, %
Surface before the polarization	57.78±2.14	6.16±0.81	30.34±2.03	5.72±0.66
On the surface	20.13±1.93	5.97±0.79	47.07±2.12	26.83±1.64
In the cracks	11.79±2.25	5.65±1.79	53.49±3.34	29.07±2.73

Table 3. Content of elements on the $Mn_5Si_{3-2.85}Ge_{2.85}$ surface

	$\omega_{at.}$ % Mn	ω_{at} % Si	ω_{at} % Ge	ω_{at} % O
Surface before the polarization	61.34±2.15	3.27±0.08	30.51±1.75	4.88±0.53
The layer of the corrosion products	10.17±1.24	2.18±0.12	40.30±2.05	47.35±4.36
Cleaned surface	58.53±2.08	4.69±0.12	36.77±2.64	0

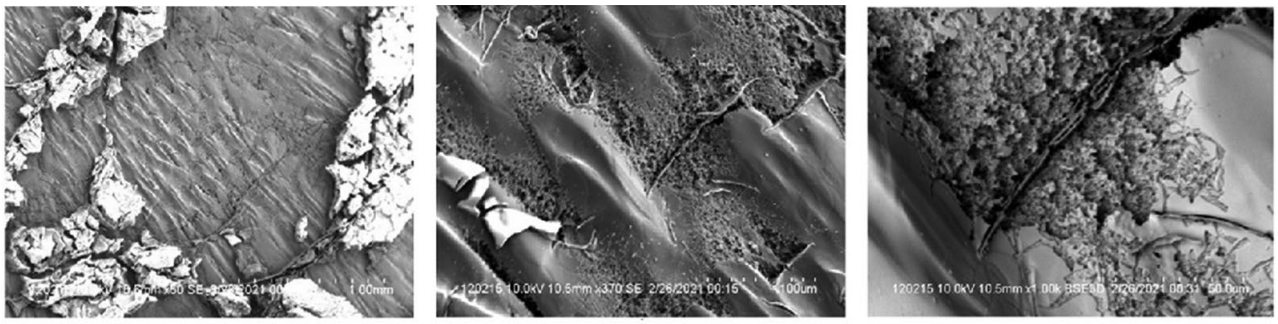

a b c

Fig. 7. Micrographs of the $Mn_5Si_{3-2.85}Ge_{2.85}$ surface after 3 cycles of anodic polarization in an 0.5M Na_2SO_4 solution, purified from anodic oxidation products at the following magnifications: (a) 50×, (b) 370×, (c) 2000×

oxides, occurred, were clearly visible. Micro-X-ray spectral analysis of the surface freed from oxidation products showed that quantitatively its composition was very close to the composition of the $Mn_5Si_{3-2.85}Ge_{2.85}$ surface before anodic polarization in a sodium sulfate solution (Table 3). A small increase in the fraction of silicon may indirectly indicate some enrichment of the surface with the manganese silicide phase Mn_5Si_3, while the upper surface layer of the manganese germanide phase Mn_5Ge_3 was completely transformed and removed.

3.1. X-ray phase and thermal analysis of anodic oxidation products

For more accurate determination of the composition of the corrosion products of germanium-containing phases, X-ray phase and thermal analysis methods were used. From among all materials studied, the powder detached from the $Mn_5Si_{3-2.85}Ge_{2.85}$ sample with the highest number of germanium atoms was chosen for further study.

The diffraction pattern of the anodic oxidation products removed from the surface of the sample is shown in Fig. 8. The absence of peaks and a large halo at small angles was characteristic for the presence of a large amount of amorphous phase and the absence of crystallites. This indicated the amorphous nature of the oxide layer formed during the corrosion process.

The results of thermal analysis of anodic oxidation products, thermogravimetric (TG) and differential scanning (DSC) curves are presented in Fig. 9.

On the TG curve, two processes of mass loss in the range of 100–600 °C and 650–1000 °C

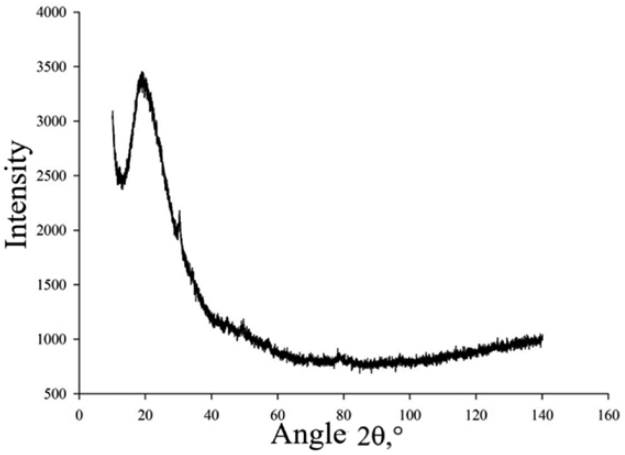

Fig. 8. Diffraction pattern of $Mn_5Si_{3-2.85}Ge_{2.85}$ anodic oxidation products

and the beginning of the melting process at 1137 °C were clearly visible. Mass spectrometric analysis revealed the presence of one water molecule in the compound, which evaporated during the first mass loss process. The second mass loss process corresponded to the phase transition of germanium monoxide GeO into germanium dioxide GeO_2. The DSC curve clearly showed the oxidation peak of GeO into GeO_2 at 1056 °C. The process involved the absorption of oxygen, as was indicated by the readings of the mass spectrometer. The onset of melting of the substance was recorded at 1137 °C. Considering that the melting of germanium dioxide is a relatively high-temperature process occurring at temperatures above 1137 °C, sublimation of the oxide onto the surface of the crucible can occur simultaneously, followed by the formation of refractory compounds [16]. After the analysis, it was noticed that the lid of the platinum crucible was tightly adhered to the crucible. When the

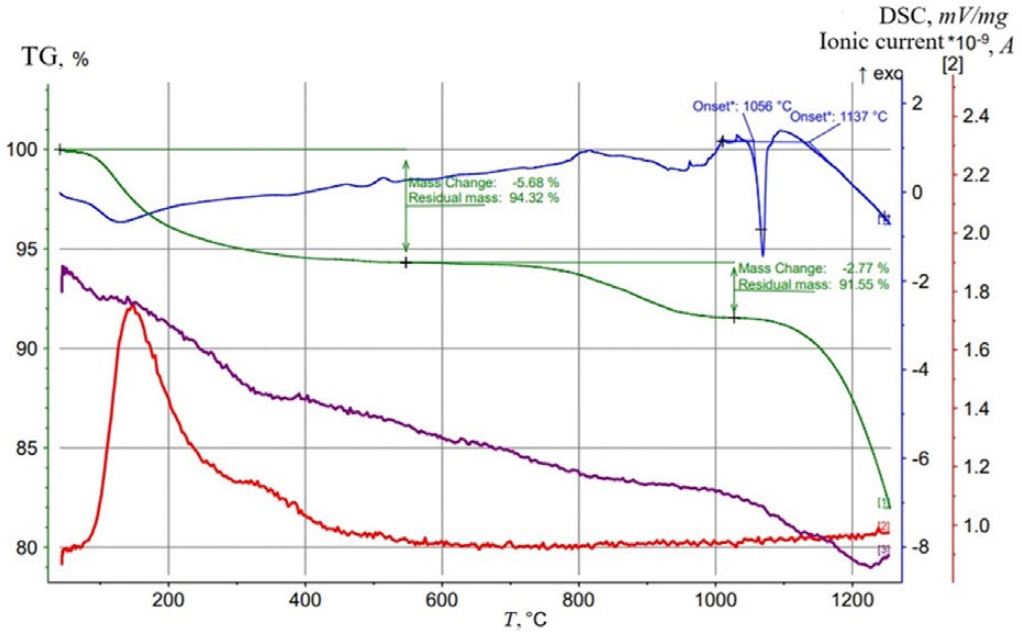

Fig. 9. Thermogravimetric and DSC curves for $Mn_5Si_{3-2.85}Ge_{2.85}$ anodic oxidation products

lid was removed, a thin film of reaction products could be detected. The weight of the crucible was also changed after thermal analysis. Thus, the corrosion products of the samples were predominantly oxygen-containing germanium compounds. Possible formulas of anodic oxidation products are GeO, GeO_2, and $Ge(OH)_x$.

4. Conclusions

Analysis of the CVA curves, the surface microstructure of the samples and their elemental composition after anodic oxidation showed that anodic destruction occurs selectively and predominantly affects the manganese germanide phase. In this case, manganese ionizes and passes into solution, and germanium forms an oxide layer containing GeO, GeO_2, and their hydrated form $Ge(OH)_x$ on the surface.

A comparison of changes in surface composition showed that with an increase in the fraction of germanium in manganese silicide-germanides, the ability of the material to resist anodic oxidation decreased. Thus, in the $Mn_5Si_{3-0.60}Ge_{0.60}$ sample with a high silicon and a low germanium content, after polarization, the fraction of the manganese component on the surface decreased by 6 %, while the germanium content decreased by half, and the fraction of silicon increased by 12 %. Corrosion products, mostly germanium oxides, accumulated in cracks. There was no visible oxide layer on the surface. This sample contained predominantly the Mn_5Si_3 phase, resistant to anodic oxidation in a wide range of aggressive media, and its behavior, including the absence of an abundant layer of products, was determined by it.

When the fraction of silicon in the sample decreased and the fraction of germanium increased to a composition of $Mn_5Si_{3-2.85}Ge_{2.85}$, the total amount of corrosion products increased, and they formed a developed layer of structures resembling microtubes, enriched in germanium oxide, which could be easily removed from the surface. Since this material contained predominantly the Mn_5Ge_3 phase, which did not exhibit high resistance to anodic destruction, its behavior was close to the behavior of the individual substance Mn_5Ge_3. In corrosion products, the fraction of manganese decreased by more than 80 %, silicon by 33 %, and the fraction of germanium increased by 32 %. The surface under the product layer also underwent changes: manganese was selectively etched from it, its fraction decreased by 5 %, while the fraction of germanium increased by 20 %, and silicon by 43 %.

Changes in the content of components the sample of intermediate $Mn_5Si_{3-2.40}Ge_{2.40}$ composition was due to the behavior of both

phases: Mn_5Si_3, and Mn_5Ge_3. The product layer was sufficiently formed, but it was bound to the surface more strongly than in the case of $Mn_5Si_{3-2.85}Ge_{2.85}$. The manganese content in the products was 65 % lower than in the original material, and the germanium content increased by 5 5%. The fraction of silicon changed insignificantly. Most of the oxidation products were contained in cracks, where the fraction of germanium was 76 % higher than on the original surface.

Thus, the active transition of the manganese germanide phase into solution enriches the surface of the sample with a silicide phase that is more resistant to anodic oxidation.

Contribution of the authors

The authors contributed equally to this article.

Conflict of interests

The authors declare that they have no known competing financial interests or personal relationships that could have influenced the work reported in this paper.

References

1. Knyajeva V. M., Babich S. G., Kolotyrkin V. I., Kojevnikov V. B. Metal-like compounds of transition metals. A new class of corrosion-resistible materials and protective coatings. *Protection of Metals*. 1991;27(4): 470-480. Available at: https://elibrary.ru/item.asp?id=31104641

2. Takeno N. "Atlas of Eh-pH diagrams," Geological survey of Japan open file report. 2005. Available at: https://www.nrc.gov/docs/ML1808/ML18089A638.pdf

3. Hurlen T., Våland T., Electrochemical behaviour of manganese: Dissolution, deposition, hydrogen evolution. *Electrochimica Acta*. 1964;9(8): 1077–1085. https://doi.org/10.1016/0013-4686(64)80077-3

4. Messaoudy B. Anodic behavior of manganese in alkaline medium. *Electrochimica Acta*. 2001;46: 2487-2498. https://doi.org/10.1016/S0013-4686(01)00449-2

5. Polkovnikov I. S., Shaidullina A. R., Panteleeva V. V., Shein A. B. Anodic processes on the manganese monosilicide in sodium hydroxide solutions. *Vestnik Permskogo universiteta. Seria: Bulletin of Perm University. Series: Chemistry*. 2018;8(3): 325-341. (In Russ.). https://doi.org/10.17072/2223-1838-2018-3-325-341

6. Efimov E. A. Features of the electrochemical dissolution of *n*-type silicon. *Doklady Akademii Nauk SSSR*. 1960;130(2): 353-355. (In Russ.)

7. Dubrovsky L. A., Mel'nik V. G., Odynets L. L. Anodic oxidation of silicon in pure water. *Russian Journal of Physical Chemistry A*. 1962;36(10): 2199–2204. (In Russ.)

8. Lehmann, V., *Electrochemistry of silicon: instrumentation, science, materials and applications*. Wiley-VCH Verlag GmbH; 2003. 283 p. https://doi.org/10.1002/3527600272

9. Zhang X., *Electrochemistry of silicon and its oxide*. Boston: Springer, MA; 2001. 510 p.

10. Zhang, L., Zhang, B., Pan, B., Wang, C. Germanium electrochemical study and its CMP application. *Applied Surface Science*. 2017;422: 247–256. https://doi.org/10.1016/j.apsusc.2017.05.220

11. Rakityanskaya I. L., Myasnikov D.A. The anodic behavior of manganese silicide-germanides in aqueous sodium sulfate solutions: the effect of the germanium content. *Russian Journal of Electrochemistry*. 2024;60: 623–632. https://doi.org/10.1134/S1023193524700228

12. Popov U. A. *Theory of the interaction of metals and alloys with corrosion-aggressive medium**. Moscow: Nauka Publ., 1995. 200 p. (In Russ.)

13. Shein A. B. *Electrochemistry of silicides and germanides of transition metals**. Perm: Perm State Univ. Publ., 2009. 209 p. (In Russ.)

14. Rakityanskaya I. L., Myasnikov D. A., Shein A. B. Anodic behaviour of manganese germanide Mn_5Ge_3 in a sodium sulphate aqueous solution. *Condensed Matter and Interphases*. 2021;23(4): 535–542. https://doi.org/10.17308/kcmf.2021.23/3672

15. Shein A. B. Corrosian-electrochemical behaviour of Mn_5Si_3, Mn_5Ge_3 and $Mn_5(Ge_{1-x}Si_x)_3$ in sulphuric acid electrolyte. *Polzunov's bulletin*. 2009;3: 247–252. (In Russ.). Available at: https://journal.altstu.ru/media/f/old2/pv2009_03/pdf/247shein.pdf

16. Atabaev I. G., Hajiev M. U., Matchanov N. A., Saliev T. M., Bobojonov K. A. Effect of surface chemical treatments on Ti–*p*-$Si_{1-x}Ge_x$ and Ni–*p*-$Si_{1-x}Ge_x$ contact properties. *Semiconductors*. 2010;44(12): 1606–1610. https://doi.org/10.1134/s1063782610120134

* *Translated by author of the article*

Information about the authors

Irina L. Rakityanskaya, Cand. Sci. (Chem.), Associate Professor at the Department of Physical Chemistry, Perm State National Research University (Perm, Russian Federation).

https://orcid.org/0000-0001-9963-2937

irisa@yandex.ru

Danil A. Myasnikov, Assistant Lecturer at the Department of Inorganic Chemistry, Chemical Technology and Technosphere Safety, Perm State National Research University (Perm, Russian Federation).

https://orcid.org/0000-0001-8889-9580

bzhendzhishchchakevich@mail.ru

Received January 14, 2025; approved after reviewing September 25, 2025; accepted for publication October 15, 2025; published online December 25, 2025.

ISSN 1606-867X (Print)
ISSN 2687-0711 (Online)
Condensed Matter and Interphases
Kondensirovannye Sredy i Mezhfaznye Granitsy
https://journals.vsu.ru/kcmf/

Original articles

Research article
https://doi.org/10.17308/kcmf.2025.27/13327

Phase composition and texture of palladium (II) oxide thin films on SiO_2/Si

A. M. Samoylov[1], A. I. Dontsov[1], A. S. Prizhimov[1]✉, S. Yu. Vakhmin[2]

[1]*Voronezh State University,*
Universitetskaya pl., 1, Voronezh 394018, Russian Federation

[2]*Military Air Academy named after Professor N. E. Zhukovsky and Yu. A. Gagarin,*
54a Starye Bolshevikov ul., Voronezh 394064, Russian Federation

Abstract

The objects of the study are nanostructures based on palladium (II) oxide of various elemental compositions and morphological organization.

The aim of the work is to establish the influence of synthesis conditions on the phase composition and texture of thin films of palladium (II) oxide synthesized by oxidation in an oxygen atmosphere of initial ultrafine layers of metallic palladium of various thicknesses on SiO_2/Si(100) substrates.

Conclusions: It has been established that the oxidation of the initial ultrafine layers of metallic palladium with thicknesses of ~ 95, ~ 190, and ~ 290 nm in an oxygen atmosphere in the temperature range T_{ox} = 873 - 1123 K leads to the formation of homogeneous polycrystalline films of palladium (II) oxide on SiO_2/Si (100) substrates. It is shown that the surface layers of PdO/SiO_2/Si (100) films have a pronounced texture (001), the degree of which increases with increasing oxidation temperature.

Keywords: Palladium (II) oxide, Phase composition, X-ray phase analysis, High-energy electron diffraction, Gas sensors

Funding: The work was carried out with the support of the Ministry of Science and Higher Education of the Russian Federation as part of the state assignment for universities in the field of scientific activity for 2023-2025 (project no.FZGU-2023-006).

Acknowledgments: The research was carried out using the equipment of the VSU Center for Collective Use of Scientific Equipment

For citation: Samoylov A. M., Dontsov A. I., Prizhimov A. S., Vakhmin S. Yu. Phase composition and texture of palladium (II) oxide thin films on SiO_2/Si. *Condensed Matter and Interphases*. 2025;27(4): 669–675. https://doi.org/10.17308/kcmf.2025.27/13327

Для цитирования: Самойлов А. М., Донцов А. И., Прижимов А. С., Вахмин С. Ю. Фазовый состав и текстура тонких пленок оксида палладия (II), синтезированных на SiO2/Si. *Конденсированные среды и межфазные границы*. 2025;27(4): 669–675. https://doi.org/10.17308/kcmf.2025.27/13327

✉ Andrey S. Prizhimov, e-mail: rnileme@mail.ru

1. Introduction

Currently, various types of binary, ternary, and more complex metal oxide semiconductors are being intensively studied as materials suitable for detecting gases with oxidizing properties. In most cases, n-type conduction semiconductors such as SnO_2 [1–3], ZnO [4, 5], In_2O_3 [6], and TiO_2 [7] are traditionally used for this purpose. However, in the last decade, the study of the sensory properties of wide-band metal oxide semiconductors with p-type conductivity and composites based on them has begun [8]. Sensor materials based on Cu_2O [9], NiO [10] nanostructures, porous NiO microspheres [11], and nanostructures based on copper (II) oxide [12] have been synthesized. Nanocomposites with a p-n heterojunction are considered the most promising for the detection of oxidizing gases [13]. Research by scientists of Voronezh State University has proved the effectiveness of using nanocrystalline and thin films of palladium (II) oxide characterized by p-type conductivity [14]. Studies of the physical and chemical properties of n-type metal oxide semiconductors have led to the creation of sufficiently efficient gas sensors based on them [15]. The enormous success in using tin dioxide SnO_2 gas sensors is not least due to accurate information about the nature of point defects (oxygen vacancies), as well as about chemical and physical processes involving adsorbed oxygen molecules and analyzing gases. To date, gas sensors of the resistive type are produced in two ways: thick-film and thin-film technologies. It should be emphasized that thick-film gas sensors are formed by various methods from pre-synthesized nanocrystalline powders. As a result, thick-film polycrystalline structures can be considered isotropic in the first approximation. Therefore, nonstoichiometry, crystallite sizes, and specific surface area are critical physical and chemical parameters that determine the functional properties of sensors. For gas sensors based on thin films, another important criterion is the morphology and orientation of the surface layers, which play an important role in the detection of toxic or explosive gases [15]. Despite the widespread use of palladium (II) oxide in various fields of science and technology, many fundamental properties of this material have not been sufficiently studied, including the formation of thin and nanocrystalline films. Therefore, the purpose of this work is to establish the influence of synthesis conditions on the phase composition and texture of thin films of palladium (II) oxide synthesized by oxidation in an oxygen atmosphere of initial ultrafine layers of metallic palladium of various thicknesses on SiO_2/Si(100) substrates.

2. Experimental methodology

A two-stage process was used to synthesize thin films of palladium (II) oxide. During the first stage, thin films of metallic palladium were formed by open evaporation in a vacuum. The method of open evaporation in vacuum is the simplest way to produce films of various materials. A freshly prepared powder of the sprayed substance is placed in a crucible made of graphite or refractory metal, the substrate is fixed in a heated holder, and the entire system is evacuated. The substrate is heated until its temperature is equal to the required value, and then the temperature of the evaporator is increased. When the time of the spraying process reaches the required value, the flap separating the evaporator and the substrate is closed, after which the substrate with the film cools down in vacuum. In addition, an upgraded film production technology is often used, which uses additional evaporators. In this work, tungsten heaters were used to produce thin films of metallic Pd by thermal evaporation in high vacuum, which were used to heat palladium foil with a basic component content of 99.99 at. %. A high vacuum at a residual pressure level of ~ 10^{-8} mmHg in the working chamber was created using a turbomolecular pump. To establish the modes of the palladium film formation process, its vapor pressure was calculated using the equation:

$$\lg P(\mathrm{Pd}^{S}, \mathrm{Pa}) = \\ = -\frac{20150}{T} + 13{,}670 - 0{,}419 \lg T - 0{,}302 \cdot 10^{-3} T, \quad (1)$$

where T is the absolute temperature, K.

Palladium metal films were formed on SiO_2/Si (100) substrates. The thickness of the SiO_2 buffer layer was ~ 300 nm. The SiO_2 buffer layer is necessary in order to prevent direct interaction of the palladium metal with the substrate material. The oxidation of palladium metal films in the

temperature range T = 970–1070 K grown on Si(100) substrates without a SiO_2 buffer layer led to the formation of palladium silicide Pd_2Si [14].

Metallic Pd films were grown on a SiO_2/Si(100) substrate without heating in order to obtain ultrafine layers with Pd crystallite sizes from 2 to 6 nm. Such crystallite sizes ensure uniform oxidation to form palladium (II) oxide. The thickness of the initial palladium metal films, determined by scanning electron microscopy during the study of chips of Pd/SiO_2/Si (100) heterostructures, ranged from 95±8 to 300±15 nm. When choosing the modes of oxidation of ultradisperse palladium layers, we were guided by the conditions under which films of lower thickness were oxidized in an oxygen atmosphere. The modes of oxidation of the initial palladium metal films in air are shown in Table 1.

The Pd/SiO_2/Si (100) heterostructures were placed in a tubular furnace at room temperature and then the furnace was heated at a rate of ~ 250 degrees per hour to the desired temperature. After reaching the required temperature, isothermal exposure was carried out for 360 and 480 minutes. As shown in Table 1, in several cases, in particular, at oxidation temperatures of T_{ox} = 773 K and T_{ox} = 973 K, the durations of oxidation in air were 360 and 480 minutes, respectively.

3. Results and discussion

Thin PdO films on SiO_2/Si(100) substrates obtained by thermal oxidation in an oxygen atmosphere of the initial ultrafine layers of metallic palladium with a thickness from 95±5 to 290±15 nm were studied by X-ray phase analysis (XFA). In order to increase the accuracy of calculations of the parameters of the tetragonal lattice of thin PdO films, CoKα radiation was used during X-ray studies. In addition, for the same purpose, thin PdO films were synthesized on SiO_2/Si(100) substrates with a thickness from 95±5 nm to 290±15 nm (Table 1). An increase in the thickness of thin PdO films on SiO_2/Si(100) substrates should lead to a change in the ratio of the reflection intensities of palladium (II) oxide and silicon.

For X-ray studies, PdO/SiO_2/Si(100) heterostructures were selected, thermally oxidized under conditions that allowed the synthesis of homogeneous polycrystalline films of palladium (II) oxide. The experimental

Table 1. Modes of thermal oxidation in an oxygen atmosphere of ultrafine metallic Pd films of various thicknesses and phase composition of samples (according to XRD data) after heat treatment

The thickness of the initial films Pd d_{Pd}, nm	Duration of annealing t, min	Annealing temperature		Phase composition of the samples
		T_{ox}, °C	T_{ox}, K	
95 ± 5	480	400	673	PdO + Pd*
95 ± 5	480	500	773	PdO
95 ± 5	480	600	873	PdO
95 ± 5	480	700	973	PdO
95 ± 5	480	800	1073	PdO
95 ± 5	480	850	1123	PdO
190 ± 10	480	400	673	Pd + PdO**
190 ± 10	480	500	773	PdO + Pd*
190 ± 10	480	600	873	PdO
190 ± 10	480	700	973	PdO
190 ± 10	480	800	1073	PdO
190 ± 10	480	850	1123	PdO
290 ± 15	480	400	673	Pd + PdO**
290 ± 15	480	500	773	PdO + Pd*
290 ± 15	480	600	873	PdO
290 ± 15	480	700	973	PdO
290 ± 15	480	800	1073	PdO
290 ± 15	480	850	1123	PdO

* Intense PdO reflexes and weak Pd reflexes.
** Intense Pd reflexes and a few weak PdO reflexes.

data obtained in the form of bar diagrams of PdO/SiO_2/Si (100) samples obtained by oxygen oxidation of the initial palladium metal layers of various thicknesses are shown in Fig. 1–3. Since the intensity of the Si(400) reflex from the silicon substrate in some cases exceeds the intensity of the strongest reflexes of the palladium (II) oxide film by two or three orders of magnitude, the intensity of the X-ray reflexes is represented in logarithmic coordinates.

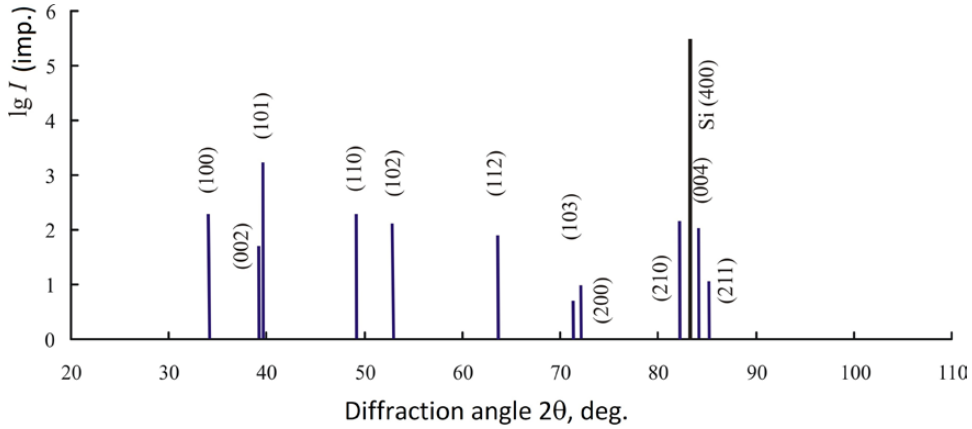

Fig. 1. X-ray diffraction pattern of a nanocrystalline PdO film on a SiO_2/Si (100) substrate obtained by thermal oxidation in oxygen of the initial palladium layer with a thickness of ~ 35 nm at T_{ox} = 1073 K

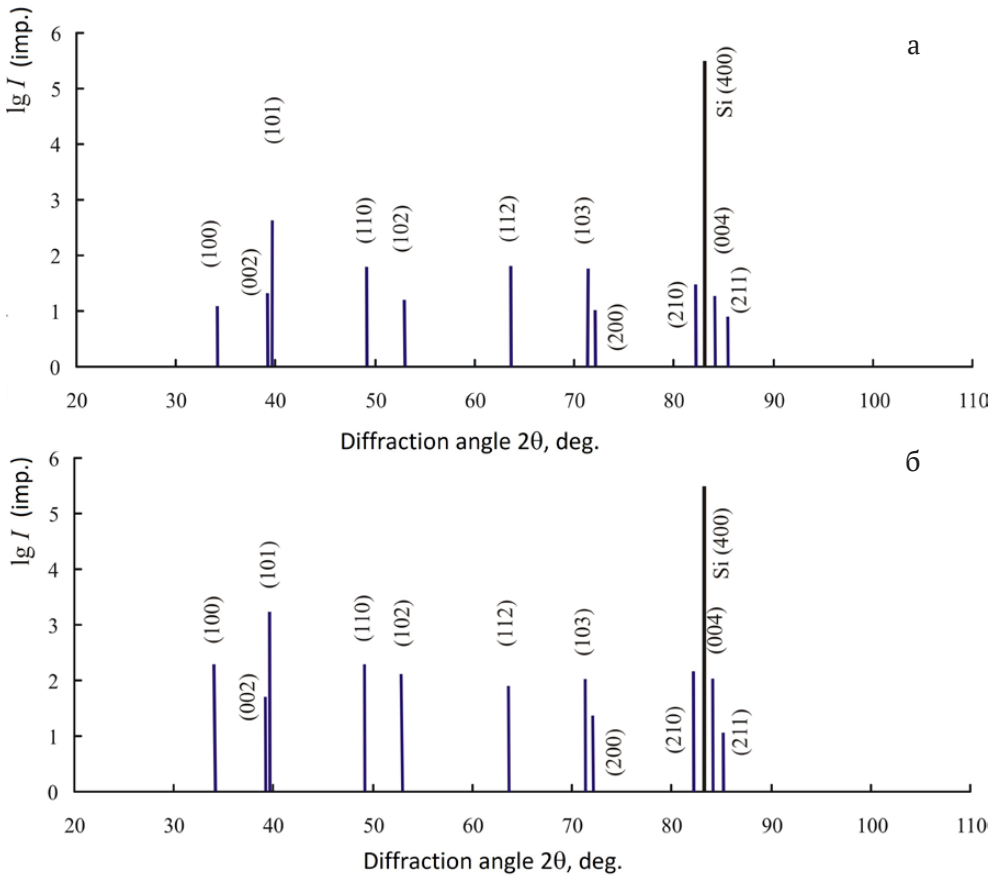

Fig. 2. X-ray diffraction pattern of thin PdO films on a SiO_2/Si(100) substrate obtained by thermal oxidation in oxygen in the initial palladium layer with a thickness of 190 ± 10 nm: a) T_{ox} = 873 K; b) T_{ox} = 973 K

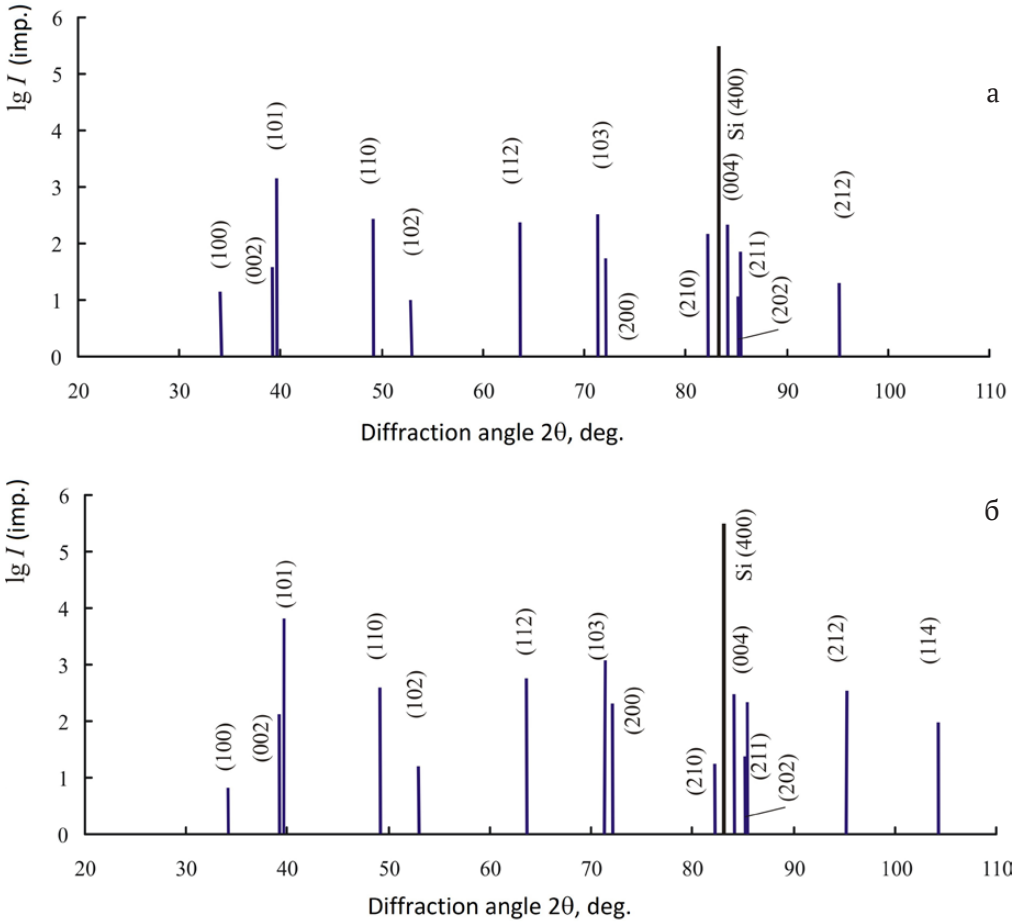

Fig. 3. X-ray diffraction pattern of thin PdO films on a SiO_2/Si (100) substrate obtained by thermal oxidation in oxygen of the initial palladium layer with a thickness of 190±10 nm: a) T_{ox} = 1073 K; b) T_{ox} = 1123 K

When comparing Figures 1 and 2, it becomes obvious that with increasing thickness of the initial ultrafine palladium layers, the intensity of X-ray reflections of palladium (II) oxide films on SiO_2/Si(100) substrates increases. In addition, as can be seen when comparing Fig. 1 and Fig. 3, for palladium (II) oxide films obtained by the thermal oxidation of initial palladium layers with a thickness of ~ 190 nm at T_{ox} = 1073 K, X-ray reflections were recorded at the far diffraction angles, for example, (202) and (212), which did not appear on diffractograms of films synthesized by the thermal oxidation of initial palladium layers with a thickness of ~ 35 nm. Diffractograms of PdO/SiO_2/Si (100) samples synthesized at T_{ox} = 1123 K reveal another long-range reflex (114).

A general analysis of X–ray diffraction patterns of PdO/SiO_2/Si(100) heterostructures obtained by the thermal oxidation of initial palladium layers with a thickness of ~ 190 nm in the temperature range T_{ox} = 873–1123 K allows us to conclude that the synthesized palladium (II) oxide films are single-phase and polycrystalline without signs of any texture. This is evidenced by the ratio of X-ray reflex intensities, which in most cases correspond to similar characteristics of the ASTM standard for a powdered palladium (II) oxide sample [42].

Nevertheless, it should be noted that an increase in the oxidation temperature leads to an increase in the degree of structural perfection of palladium (II) oxide films. This fact is confirmed not only by an increase in the intensity of the corresponding X-ray peaks, but also by the appearance of additional reflections at distant diffraction angles with large values of the Miller indices, for example, peaks (212) and (114).

In order to determine the orientation of the surface layers, PdO/SiO_2/Si(100) samples were

studied by high-energy electron diffraction (HEED), which allows obtaining information from layers several nanometers thick. The electron diffraction patterns obtained during the study of some SiO_2/Si(100) heterostructures are shown in Fig. 4.

A comparison of experimental X-ray diffraction data on the crystal structure over the entire volume of thin films of PdO/SiO_2/Si(100) and the results obtained by the HEED method from near-surface layers allows us to draw the following conclusions. The XRD method captures all reflexes, while the HEED method does not register a number of mixed reflexes (*hkl*) characteristic of a homogeneous polycrystalline palladium (II) oxide film. In addition, with an increase in the oxidation temperature from T_{ox} = 873 K and T_{ox} = 1073 K, along with the disappearance of mixed reflexes (*hkl*), reflexes (002) and (004) become the most intense on electronograms. All this indicates that, unlike the entire volume of thin polycrystalline films of palladium (II) oxide, the surface layers with a thickness of several nanometers acquire a pronounced orientation (001).

The crystallographic planes (001) and (002) in the unit cell of palladium (II) oxide are formed exclusively by palladium atoms, which allows us to conclude that there is a preferential orientation (001) of the surface layers of thin PdO films with increasing oxidation temperature and may be important for the formation of gas sensors with increased selectivity.

4. Conclusion

1. By the X-ray method has been established that the oxidation of the initial ultrafine layers of metallic palladium with thicknesses of ~ 95, ~ 190, and ~ 290 nm in an oxygen atmosphere in the temperature range T_{ox} = 873–1123 K leads to the formation of homogeneous polycrystalline films of palladium (II) oxide on SiO_2/Si (100) substrates.

2. Through the use of the HEED method it has been established that the surface layers of PdO/SiO_2/Si (100) films have a pronounced texture (001), the degree of which increases with increasing oxidation temperature.

Contribution of the authors

The authors contributed equally to this article.

Conflict of interests

The authors declare that they have no known competing financial interests or personal relationships that could have influenced the work reported in this paper.

References

1. Korotcenkov G., Brinzar, V., Cho B. K. In_2O_3- and SnO_2-based thin film ozone sensors: fundamentals. *Journal of Sensors*. 2016;2016: 1-31. https://doi.org/10.1155/2016/3816094

2. Oros C., Horprathumb M., Wisitsoraat A., ... Chindaudom P. Ultra-sensitive NO_2 sensor based on vertically aligned SnO_2 nanorods deposited by DC reactive magnetron sputtering with glancing angle deposition technique. *Sensors and Actuators B*. 2016;223: 936–945. https://doi.org/10.1016/j.snb.2015.09.104

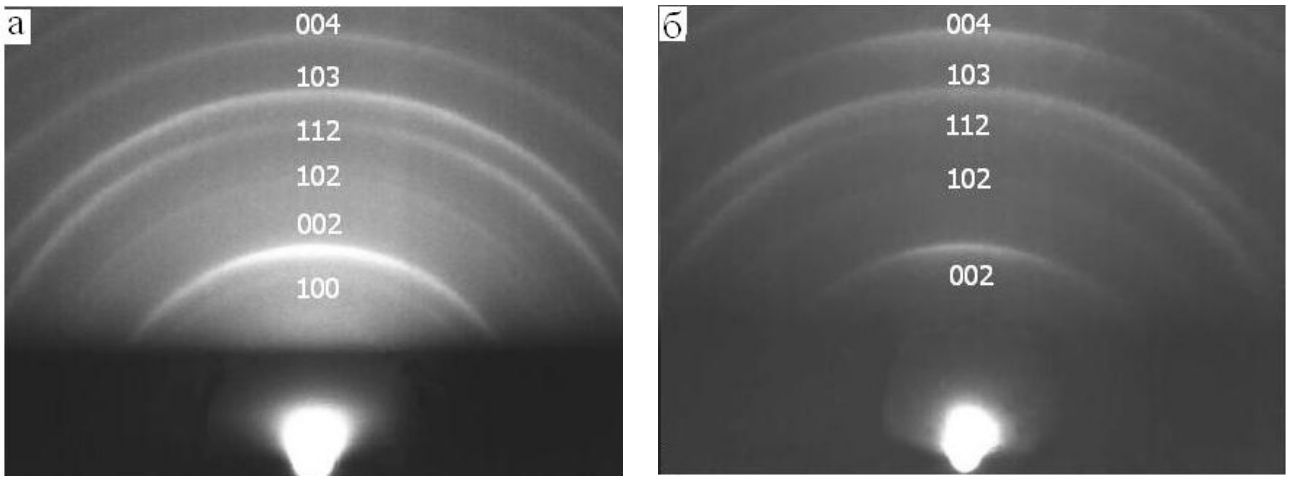

Fig. 4. Electron diffraction patterns obtained with the RHEED method on palladium (II) oxide films synthesized by oxidation in an oxygen atmosphere of the initial ultrafine layers of metallic Pd with a thickness of ~ 190±10 nm: a) T_{ox} = 873 K; b) T_{ox} = 1073 K

3. Stanoiu A., Somacescu S., Calderon-Moreno J. M., … Simion C. E. Low level NO_2 detection under humid background and associated sensing mechanism for mesoporous SnO_2. *Sensors and Actuators B*. 2016;231: 166–174. https://doi.org/10.1016/j.snb.2016.02.137

4. Jiao M., Chien N. V., Duy N. V., … Nguyen H. On-chip hydrothermal growth of ZnO nanorods at low temperature for highly selective NO_2 gas sensor. *Materials Letters*. 2016;169: 231–235. https://doi.org/10.1016/j.matlet.2016.01.123

5. Katoch A., Sun G.–J., Choi S., Byun J., Kim S. S. Competitive influence of grain size and crystallinity on gas sensing performances of ZnO nanofibers. *Sensors and Actuators B: Chemical*. 2013;185: 411–416. https://doi.org/10.1016/j.snb.2013.05.030

6. Ilin A., Martyshov M., Forsh E., … Kashkarov P. UV effect on NO_2 sensing properties of nanocrystalline In_2O_3. *Sensors and Actuators B: Chemical*. 2016;231: 491–496. https://doi.org/10.1016/j.snb.2016.03.051

7. Navale S. T., Tehare K. K., Shaikh S. F., … Mane R. S. Hexamethylenetetramine-mediated TiO_2 films: facile chemical synthesis strategy and their use in nitrogen dioxide detection. *Materials Letters*. 2016;173: 9–12. https://doi.org/10.1016/j.matlet.2016.02.140

8. Kim H.-J., Lee J.-H. Highly sensitive and selective gas sensors using *p*- type oxide semiconductors: overview. *Sensors and Actuators B: Chemical*. 2014;192: 607–627. https://doi.org/10.1016/j.snb.2013.11.005

9. Cao S., Chen H., Han T., Zhao C., Peng L. Cu_2O nanoflowers via hydrothermal synthesis and their gas sensing properties. *Materials Letters*. 2016;180: 135–139. https://doi.org/10.1016/j.matlet.2016.05.105

10. Choia J.-M., Byun J.-H., Kim S. S. Influence of grain size on gas- sensing properties of chemiresistive *p*-type NiO nanofibers. *Sensors and Actuators B: Chemical*. 2016;227: 149–156. https://doi.org/10.1016/j.snb.2015.12.014

11. Tian K., Wang X. X., Li H. Y., Nadimicherla R., Guo X. Lotus pollen derived 3-dimensional hierarchically porous NiO microspheres for NO_2 gas sensing. *Sensors and Actuators B: Chemical*. 2016;227: 554–560. https://doi.org/10.1016/j.snb.2015.12.104

12. Kneer J., Wöllenstein J., Palzer S. Manipulating the gas–surface interaction between copper (II) oxide and mononitrogen oxides using temperature. *Sensors and Actuators B: Chemical*. 2016;229: 57–62. https://doi.org/10.1016/j.snb.2016.01.104

13. Srivastava V., Jain K. At room temperature graphene/SnO_2 is better than MWCNT/SnO_2 as NO_2 gas sensor. *Materials Letters*. 2016:169: 28–32. https://doi.org/10.1016/j.matlet.2015.12.115

14. Ryabtsev S. V., Ievlev V. M., Samoylov A. M., Kuschev S. B., Soldatenko S. A. Microstructure and electrical properties of palladium oxide thin films for oxidizing gases detection. *Thin Solid Films*. 2017;636: 751–759. https://doi.org/10.1016/j.tsf.2017.04.009

15. Marikutsa A. V., Rumyantseva M. N., Gaskov A. M., Samoylov A. M. Nanocrystalline tin dioxide: Basics in relation with gas sensing phenomena. Part II. Active centers and sensor behavior. *Inorganic Materials*. 2016;52:1311–1338. https://doi.org/10.1134/s002016851513004x

Information about the authors

Aleksander M. Samoylov, Dr. Sci. (Chem.), Senior Researcher at the Department of Materials Science and Industry of Nanosystems, Voronezh State University (Voronezh, Russian Federation).

https://orcid.org/0000-0003-4224-2203

rnileme@mail.ru

Alexey I. Dontsov, Cand. Sci. (Phys.–Math.), Associate Professor, Department of Materials Science and Industry of Nanosystems, Voronezh State University (Voronezh, Russian Federation).

https://orcid.org/0000-0002-3645-1626

dontalex@mail.ru

Andrey S. Prizhimov, Cand. Sci. (Phys.-Math.), Associate Professor, Department of Materials Science and Industry of Nanosystems, Voronezh State University (Voronezh, Russian Federation).

https://orcid.org/0000-0003-0052-0826

rnileme@mail.ru

Sergey Yu. Vakhmin, Cand. Sci. (Phys.-Math.), Associate Professor, Military Air Academy named after Professor N. E. Zhukovsky and Yu. A. Gagarin (Voronezh, Russian Federation).

vax_serg@mail.ru

Received March 21, 2025; approved after reviewing April 10, 2025; accepted for publication May 15, 2025; published online December 25, 2025.

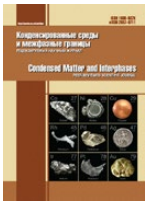

ISSN 1606-867X (Print)
ISSN 2687-0711 (Online)
Condensed Matter and Interphases
Kondensirovannye Sredy i Mezhfaznye Granitsy
https://journals.vsu.ru/kcmf/

Original articles

Research article
https://doi.org/10.17308/kcmf.2025.27/13326

Composition, structure, and electrophysical properties of natural zeolite clinoptilolites subjected to mechanical activation with potassium hydrosulfate

T. P. Soloboeva[1], O. N. Dabizha[1,2]✉, A. G. Batukhtin[1]

[1]Transbaikal State University,
30 ul. Aleksandro-Zavodskaya, Chita 672039, Russian Federation

[2]I. V. Grebenshchikov Institute of Silicate Chemistry of NRC "Kurchatov Institute",
2 emb. Makarova, Saint Petersburg 199034, Russian Federation

Abstract

Objectives: The mechanochemical modification of zeolites with the addition of acidic salts causes an increase in the defectiveness of their structure, a change in the dispersion of the powder, and the conductivity of tableted samples. The aim of the study was to obtain mineral samples with improved conductivity using a mechanochemical method from air-dry mixtures of clinoptilolite-stilbite, clinoptilolite rocks and, potassium hydrosulfate in different ratios.

Experimental: The shape and size of particles, chemical and phase composition of powders, and their physical properties were studied using electron microscopy, energy-dispersive X-ray spectrometry, X-ray phase analysis, differential scanning calorimetry, infrared spectroscopy, sieve analysis, gravimetry, and air permeability. The electrical conductivity of the tableted samples was measured using a three-electrode circuit in the temperature range from 25 to 100 °C.

Conclusions: The results of the study demonstrated that mechanical treatment of mixtures of zeolites with an acidic salt leads to the amorphization of stilbite and feldspar, polymorphic transformations of quartz into cristobalite and tridymite, and an increase in structural defects. The interaction of components occurs via the silanol groups of clinoptilolite and hydrosulfate groups through the formation of hydrogen bonds and with the involvement of water molecules. It was also established that the electrical conductivity of a mineral tablet sample based on clinoptilolite rock and potassium hydrosulfate in an equimass ratio, subjected to shock-shear action with a mechanical energy dose of 2.16 kJ/g, amounted to $4.26 \cdot 10^{-4}$ S·m^{-1} at 100 °C. Electrical conductivity values of the same order were obtained earlier for the mechanochemical activation of natural zeolites with potassium hydrophosphates. Consequently, the hydrosulfate anion does not make a significant contribution to the conductivity of zeolite samples compared to the hydrophosphate anion.

Keywords: Natural zeolites, Clinoptilolite, Stilbite, Mechanochemical activation, Electrical conductivity, Potassium hydrosulfate

Funding: The study was carried out within the framework of the state assignment of the Ministry of Science and Higher Education of the Russian Federation - topic No. 123102000012-2. The electrical properties of the samples were determined in accordance with the state assignment at the branch of the National Research Center "Kurchatov Institute" - B.P. Konstantinov St. Petersburg Nuclear Physics Institute - I. V. Grebenshchikov Institute of Silicate Chemistry of the Russian Academy of Sciences, research theme 1023033000122-7-1.4.3.

For citation: Soloboeva T. P., Dabizha O. N., Batukhtin A. G. Composition, structure, and electrophysical properties of natural zeolite clinoptilolites subjected to mechanical activation with potassium hydrosulfate. *Condensed Matter and Interphases*. 2025;27(4): 676–688. https://doi.org/10.17308/kcmf.2025.27/13326

Для цитирования: Солобоева Т. П., Дабижа О. Н., Батухтин А. Г. Состав - структура - электрофизические свойства природных цеолитов клиноптилолитов, подвергнутых механической активации с гидросульфатом калия. *Конденсированные среды и межфазные границы*. 2025;27(4): 676–688. https://doi.org/10.17308/kcmf.2025.27/13326

✉ Olga N. Dabizha, e-mail: dabiga75@mail.ru

1. Introduction

Zeolites are used as adsorbents, catalysts, and ion exchangers [1–4], in electrochemical devices, for example, for lithium-ion batteries due to the unique microporous structure and ion-exchange properties [5–7]. Low ionic conductivity limits the use of natural zeolites as solid electrolytes [8, 9]. The ionic conductivity can be increased by chemical modification, thermal treatment, and mechanical activation in high-energy devices [10–13]. Mechanical treatment of a solid substance leads to the reduction and deformation of particles without the use of high temperatures and aggressive chemical reagents [14–16]. The resulting defects and impairments in the crystal lattice create additional vacancies and interstitials and contribute to an increase in the concentration and mobility of charge carrier ions [8, 10]. Moreover, the formation of an amorphous phase can provide higher ionic conductivity compared to the crystalline phase [10, 17, 18].

The mechanical treatment of zeolites in the presence of acidic alkali metal salts leads to complex structural changes [11]. Intense mechanical action causes a decrease in the size of crystallites, an increase in the specific surface area, and the introduction of alkali metal ions from the acid salt into the zeolite structure [19]. The electrical properties of mechanically activated zeolites containing acidic salts of alkali metals differ significantly from the properties of the original materials [11, 19]. Ionic conductivity increases by several orders of magnitude depending on the type of zeolite, acid salt, mechanical activation conditions, and temperature [19]. In mechanically activated zeolites, an increase in the concentration of alkali metal ions and the formation of defects contribute to an increase in ionic conductivity [8, 12]. The control of the amount of defects in zeolites is crucial for energy storage applications [20]. It was demonstrated [19] that the electrical conductivity of pressed samples obtained by joint mechanochemical activation of clinoptilolite-stilbite or clinoptilolite rocks with potassium hydrophosphate is ~ 10^{-5}–10^{-6} S·m^{-1} at 25 ºC. Potassium hydrosulfate is a good ionic conductor (Fig. 1) with the ability to stabilize the amorphous state [21], but it is brittle and not chemically stable. Properties of potassium hydrosulfate in nanocomposite solid electrolytes (1–x) $KHSO_4$-xSiO_2 depend on the particle size and pores of silicon dioxide [21]. Highly porous and microporous zeolites are mechanically and thermally stable and are also suitable matrices for encapsulating conductive components [5, 6]. Guest ions can influence proton conductivity due to the synergistic effect of pore characteristics and ion concentration [7]. The structure, dispersion, morphology, physical, and electrophysical properties of the resulting composite will be affected by the joint mechanical activation of natural zeolite with potassium hydrosulfate.

This study aimed to obtain mineral powders with improved electrophysical properties using short-term mechanical activation of mixtures of natural zeolite clinoptilolites with potassium hydrosulfate in different ratios.

2. Experimental part

2.1. Materials

Natural zeolite rocks [22], clinoptilolite-stilbite (I) and clinoptilolite (II) (Kholinsky and Shivyrtuisky deposits, Russia) were pre-crushed using a crusher, and potassium hydrosulfate (d) (pure for analysis grade, GOST 4223) was used without any processing.

The assignment of absorption bands in the IR spectrum of $KHSO_4$, ν, cm^{-1} was: 2978; 2884; 2834; 2484; 2417 (H_2O; OH in HSO_4); 1767; 1701 (OH bound with HSO_4); 1651; 1620 (H_2O); 1454;

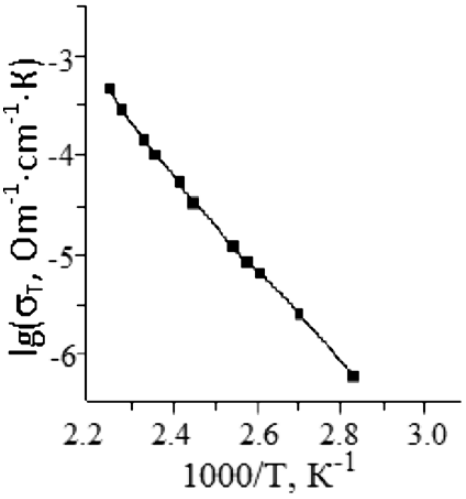

Fig. 1. Temperature dependences of potassium hydrosulfate conductivity (complex impedance method, impedance meter BM-507, *n* = 5 Hz–500 kHz, silver electrodes, cooling mode, air, 2 K/min) [21]

1317; 1284; 1175 (S-O-H); 1071; 1007; 883; 853 (SO_4); 665; 614; 577 (SO_4); 453. The conductivity of tableted mechanically activated samples of clinoptilolite-stilbite and clinoptilolite rocks at 25 °C varied from ~ 10^{-6} to10^{-9} S·m^{-1} [23].

Modified mineral samples were obtained by mixing clinoptilolite powders with a particle size not exceeding 0.5 mm with 25, 33, and 50 wt % potassium hydrosulfate and subsequent mechanical activation for 3, 5, and 7 min in a vibratory bowl grinder IVCh-3 according to the method described in detail in the study [19].

2.2. Research methods

The shapes and sizes of particles were examined using electron microscopy (scanning electron microscope JSM-6510LV JEOL, Japan). The elemental composition was determined using an INCA Energy 350 X-ray energy dispersive spectrometer (Oxford Instruments, UK).

The phase composition was investigated using powder diffraction (DRON-3 diffractometer, CuK_α-radiation, Ni-filter, U = 25 kV, I = 20 mA, 2θ = 3–55°, 1°/min). Semi-quantitative analysis was carried out using the corundum number method. The relative degree of crystallinity of clinoptilolite (k_{rel}) was calculated as described in [19].

Weight changes of 20 mg of mineral samples heated in platinum crucibles in the range of 30 to 850 °C were studied in a dynamic argon atmosphere at a heating rate of 10 °C/min using a synchronous thermal analyzer (STA 449F1, NETZSCH, Germany). The apparent activation energy of dehydration (E_A) in the temperature range from 50 to 150 °C was calculated using the Arrhenius equation according to the study [24].

The specific area was determined using the T-3 (Tovarov) device [14]. The granulometric composition of the powders was studied using sieve analysis, and their bulk density (ρ_b) was measured using gravimetry. True density (ρ_{tr}) was determined by the pycnometric method using TS-1 kerosene as the working fluid. Layer porosity (ε_{la}) was calculated using the equation [19]:

$$\varepsilon_{la} = [1 - (1/\rho_b \cdot \rho_{tr})] \cdot 100\ \%, \quad (1)$$

The mineral structures were analyzed using a SHIMADZU FTIR-8400S Fourier transform infrared spectrometer in the frequency range of 4000–400 cm^{-1} in tablets with KBr.

The samples were prepared in tablet form (diameter 10 mm and thickness 3–4 mm) using the IP-1A-1000 press. The volume conductivity was measured using an E6-13A teraohmmeter (air humidity 26 %, U = 100 V, three-electrode circuit, t = 25–100 °C; error: 5 %) [19]. The activation energy of conductivity (E_{act}) was calculated graphically based on the linear dependence of the natural logarithm of electrical conductivity on the reciprocal temperature.

The parameters and properties of clinoptilolite zeolites modified with potassium hydrosulfate and subjected to mechanical activation were compared with similar characteristics of natural zeolites processed under identical conditions without additives and with potassium hydrophosphate. [19]. The marking of the samples includes the type of rock (I, II), salt content (*dx*, where x = 25, 33, 50), and the exposure time (3, 5, 7 min, corresponding to energy doses equal to 2.16, 3.60, 5.04 kJ/g), with its components separated by a dash.

3. Results and discussion

3.1. Study of morphology and chemical composition

Clinoptilolite-stilbite rocks modified with potassium hydrosulfate were characterized by a complex surface relief formed by polydisperse aggregates of irregularly shaped particles (Fig. 2). After three minutes of mechanical treatment, micron-sized aggregates with the size of 46×23, 44×21, 42×33 (Id33-3), and after seven minutes aggregates with the size of 29×23, 25×21, 24×30 (Id33-7) were revealed on SEM images of the powder surface. The replacement of clinoptilolite-stilbite with clinoptilolite rock in the composition did not have a significant effect on the surface morphology, but the size of the largest aggregates increased to 41×53, 30×27, 26×17 (IId33-7). A doubled increase of salt content had practically no effect on the sizes of particle aggregates – 40×44, 21×25, 17×23 (IId25-5), 45×25, 25×14, 16×22 (IId50-5), without excluding the possibility of the formation of quasi-spherical agglomerates in the case of a potassium hydrosulfate content of 25 wt %. The image of the surface of the Id50-7 powder was significantly different, with large, rounded, agglomerated particle formations measuring 60×95, 57×81, 54×42 μm revealed. Electron microscopy data showed that mechanical

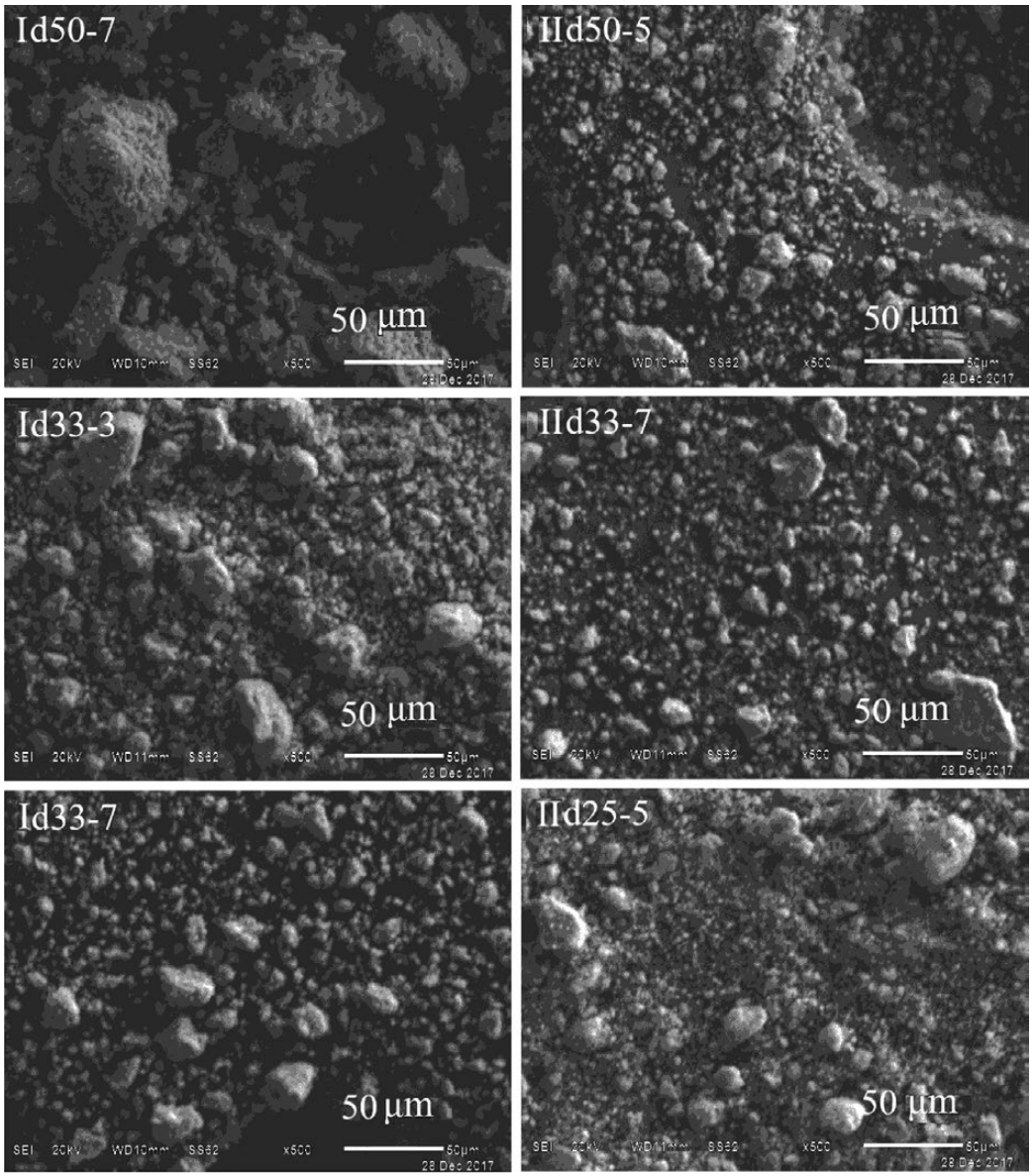

Fig. 2. SEM images of selected samples: I, clinoptilolite-stilbite rock; II, clinoptilolite rock; 25, 33, 50, potassium hydrosulfate (d) content, wt %; 3, 5, 7, duration of mechanical treatment, min

shock-shear action in an air environment promoted both dispersion and the formation of aggregate-agglomerate structures of mineral particles. In order to obtain high-quality powder for pressing, the duration of mechanical processing should be 7 minutes. This time corresponds to an energy dose of 5.04 kJ/g.

The average oxide content in mass percentage and the calculated silicate modulus indicated that natural zeolites belong to the high-silica group (Table 1). The silicate modulus of samples from clinoptilolite-stilbite rock was 10–11, while for samples from clinoptilolite rock it was 8–9. As a result of increasing the energy dose from 2.16 to 5.04 kJ/g (Id33-3 and Id33-7), the silicate modulus increased slightly, indicating that the strength and number of acid centers decreased. An increase in the content of potassium hydrosulfate in the sample compositions expectedly led to an increase in the concentration of K_2O and SO_3, as well as a decrease in the concentration of Na_2O. An increase in the dose of mechanical energy will lead to an increase in the mobility of extra-framework hydrated cations in the aluminum-silicon-oxygen framework system. This is possible not only due to the increase in the concentration of K^+ cations, but also due to changes in the degree of their hydration, caused by the conversion

Table 1. Average oxide content and silicate modulus for selected samples

Samples	Average content of main components in mineral samples, wt %										M_c = Si/Al
	SiO_2	Al_2O_3	Na_2O	CaO	Fe_2O_3	K_2O	SO_3	MgO	CuO	ZnO	
Id33-3	52.2±7.4	8.8±0.9	1.3±0.2	1.2±0.2	0.7±0.2	15.6±2.1	18.4±1.8	0	1.1±0.5	0.8±0.3	10.1
Id33-7	47.1±7.6	7.6±0.4	1.1±0.3	1.0±0.3	0.8±0.5	19.4±5.2	19.6±2.5	0	2.1±1.4	1.2±0.6	10.5
Id50-7	34.3±1.6	6.0±0.4	0.9±0.2	0	0.5±0.1	25.3±2.9	31.5±3.4	0	0.9±0.6	0.6±0.5	9.7
IId25-5	63.8±2.9	13.2±0.7	1.6±0.2	2.2±0.2	2.0±0.4	6.8±1.9	7.6±2.9	1.0±0.1	1.0±0.2	0.7±0.1	8.2
IId33-7	47.9±4.6	9.6±0.7	1.2±0.1	2.1±0.3	1.9±0.2	14.3±1.6	19.5±1.8	0.8±0.1	1.6±0.7	1.1±0.5	8.4
IId50-5	37.3±4.0	7.3±0.6	0.8±0.1	1.7±0.2	1.9±1.1	20.3±2.0	26.1±2.1	0.8±0.1	2.3±2.3	1.5±1.5	8.7

I, clinoptilolite-stilbite rock; II, clinoptilolite rock; 25, 33, 50, potassium hydrosulphate (d) content, wt %; 3, 5, 7, duration of mechanical treatment, min

of mechanical energy into thermal energy as a result of local heating during mechanochemical activation.

3.2. Study of phase composition

X-ray diffraction patterns of mechanically activated (I5, I7, II5, II7) and mechanochemically modified with potassium hydrosulfate clinoptilolite rocks (Id50-7, Id33-7, IId50-5, IId33-7, IId25-7) are shown in Fig. 3. Changes in the intensities and positions of diffraction peaks reflect transformations in the crystal structure of clinoptilolite after mechanical treatment. In the X-ray images of clinoptilolites mechanically activated with acid salt, compared to those mechanically activated without additives, an increase in the intensity of reflections by 1.3–1.9 times was observed. Disorder of the crystal structure was indicated by an amorphous halo in the region 2θ = 10–35° (Id33-7, IId33-7). Mechanochemical treatment of natural zeolites together with salt led to a change in their phase composition (Fig. 3). Thus, in the diffraction patterns of Id50-7, Id33-7, and IId50-5 samples, reflections of high-temperature phases of cristobalite and tridymite were recorded instead of the expected impurity quartz (Table 2). This indicates a polymorphic transition of quartz into cristobalite and is consistent with the data on the products of mechanical activation of quartz raw materials [25]. The relative degree of crystallinity of clinoptilolite increased in Id33-7 and IId25-5 samples and decreased in Id50-7, IId50-5, and IId33-7 samples. It was revealed that salt is present after mechanical activation, together with stilbite-clinoptilolite and clinoptilolite rocks in the form of $K_3H(SO_4)_2$ and $KHSO_4$, respectively. It is known that the disordering of the hydrogen bond system during phase transitions and high proton conductivity is the characteristic feature of the first of the mentioned salts [26]. In addition, the diffraction patterns of clinoptilolite-stilbite samples modified with potassium hydrosulfate did not contain crystalline phases of stilbite and microcline. The increase in electrical conductivity was associated with amorphization, which was confirmed by a decrease in the relative degree of crystallinity of clinoptilolite (Id50-7, IId33-7, IId50-7 samples). At the same time, the crystalline nanoporous structure of clinoptilolite provided channels for the efficient diffusion of metal cations and the necessary mechanical strength. Obviously, the optimal values of the degree of crystallinity of clinoptilolite in the samples, rather than the maximal values, are important.

3.3. Thermal stability study

On the DSC curves of mechanically activated zeolites, endothermic effects were observed in the temperature range of 172–202 °C [22], which are explained by the removal of sorption water. Similar curves of zeolites mechanically activated together with potassium hydrosulfate in equimass ratios contain several endothermic effects (Fig. 4). During thermal decomposition of potassium hydrosulfate, reactions (2)–(4) may occur.

$$2KHSO_4 \xrightarrow{240\ ^\circ C} K_2SO_4 + H_2SO_4, \quad (2)$$

$$2KHSO_4 \xrightarrow{320–340\ ^\circ C} K_2S_2O_7 + H_2O, \quad (3)$$

$$K_2S_2O_7 \xrightarrow{>600\ ^\circ C} K_2SO_4 + SO_3. \quad (4)$$

According to the results of X-ray phase analysis, samples contained crystals of $K_3H(SO_4)_2$ (Table 2). Then the endothermic effects at 386 and 392 °C (IId50-3, Id50-3) can be attributed to the phase transition of $K_3H(SO_4)_2$ into the high-temperature tetragonal phase [26]. The endothermic effects at

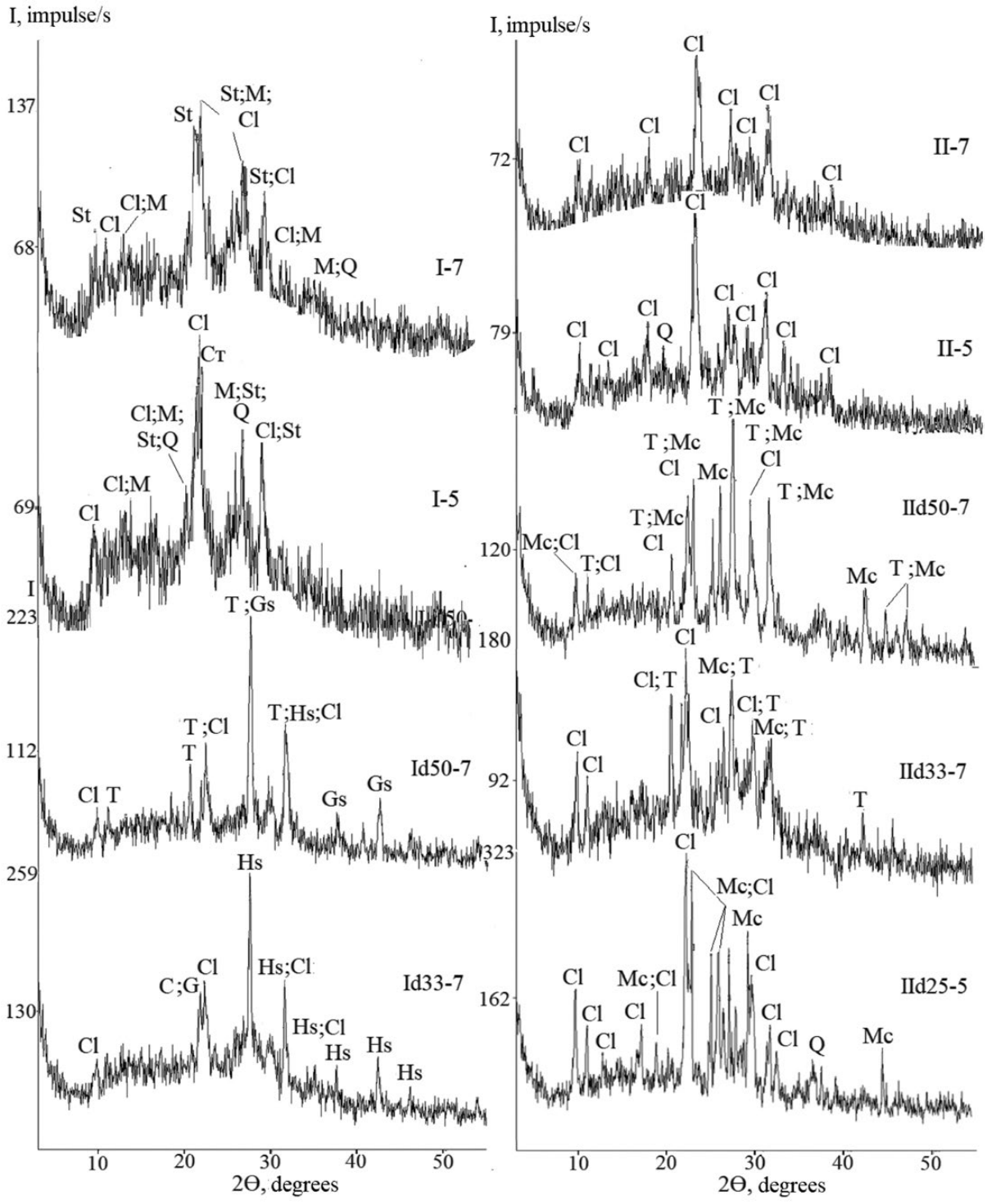

Fig. 3. X-ray diffraction patterns of zeolite samples: I, clinoptilolite-stilbite rock; II, clinoptilolite rock; 25, 33, 50, potassium hydrosulfate (d) content, wt %; 3, 5, 7, duration of mechanical treatment, min.; Cl, clinoptilolite; G, heilandite; St, stilbite; M, microcline; Q, quartz; C, cristobalite; T, tridymite; Ms, mercallite; Hs, potassium hydrosulfate

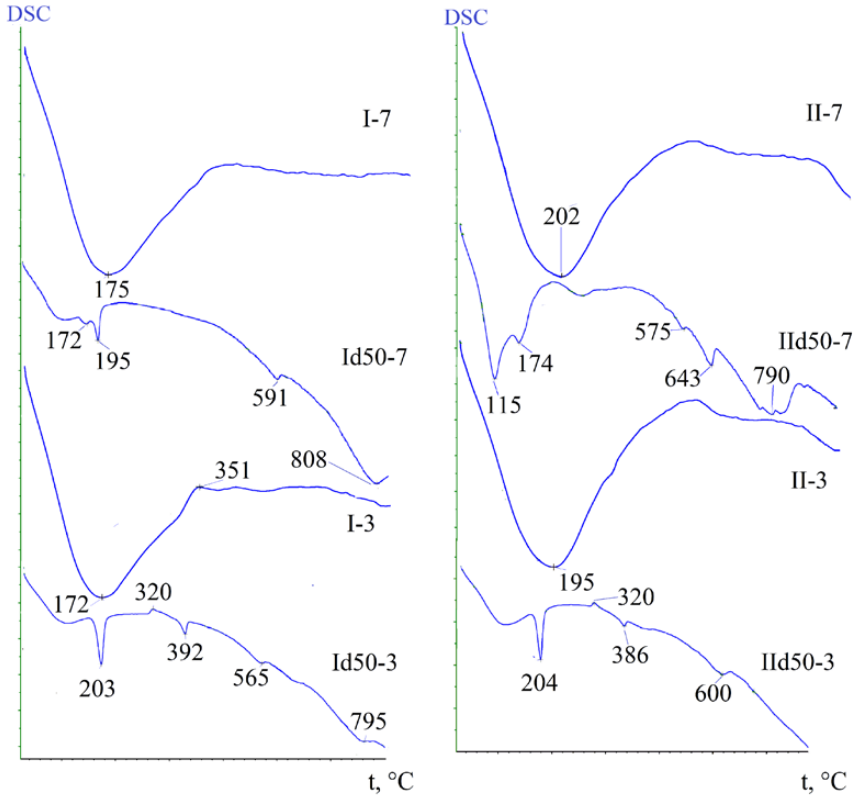

Fig. 4. Differential scanning calorimetry curves of selected samples: I, clinoptilolite-stilbite rock; II, clinoptilolite rock; 50, potassium hydrosulfate (d) content, wt %; 3, 7, duration of mechanical treatment, min

Table 2. Composition of phases, interplanar distances (d) in the region 2θ = 22–26°, relative intensities of diffraction reflections (I/I_0) of clinoptilolite and relative degree of its crystallinity (k_{rel})

Samples	Crystalline phases*	d, Å			I/I_0			k_{rel}, %
I7	St; Cl; M; Q	3.975	3.786	3.427	253	137	171	100
Id33-7	Hs; Cl; G; C	3.974	–	3.320	402	0	268	119
Id50-7	Hs; T; Cl	3.981	3.869	3.426	209	90	49	62
II5	Cl	3.971	3.780	3.419	1000	297	484	100
IId25-5	Cl; Mc; Q	3.979	3.862	3.417	1000	465	427	106
II7	Cl	3.982	–	3.434	1000	0	579	100
IId33-7	Mc; T; Cl	3.962	3.787	3.411	941	202	334	94
IId50-7	Mc; Cl; T	3.972	3.863	3.342	369	169	74	39

Cl: [00-025-1349] $(Na,K,Ca)_6(Si,Al)_{36}O_{72}\times 20H_2O$; [00-019-0211] $CaAl_2Si_7O_{18}\cdot 7.5H_2O$
St: [00-022-0518] $Ca_4Al_9Si_{27}O_{72}\cdot 32H_2O$; M: [00-019-0932] $KAlSi_3O_8$; Q: [01-085-0794] SiO_2; C: [01-082-0512] SiO_2; T: [01-083-1339], [00-016-0152] SiO_2; Mc: [01-072-1247] $KHSO_4$; Hs: [00-052-0406] $K_3H(SO_4)_2$; I, clinoptilolite-stilbite rock; II, clinoptilolite rock; 25, 33, 50, potassium hydrosulphate (d) content, wt %; 5, 7, duration of mechanical treatment, min

195–204 °C with a clear shape were caused by the structural phase transition and disorder in the crystal lattice of $KHSO_4$ [27]. They can be attributed to the process of salt melting in a mechanically activated zeolite matrix. After seven minutes of mechanical treatment, an obvious inclusion of the hydrosulfate anion in the hydrogen bond system was observed, and the indicated endothermic effect in the region of 381–390 °C was no longer recorded. Moreover, endothermic effects were reduced by a factor of 2–3 at 195 °C (Id50-7) and 174 °C (IId50-7) . It should be noted that the endothermic effects were preserved in the temperature range from 560 to 650 °C in all zeolite samples with potassium hydrosulfate additives.

The smooth course of thermogravimetric curves of mechanically activated zeolites is characteristic of the mineral clinoptilolite

[19]. The TG curves of zeolites modified with potassium hydrosulfate, as in the case of modification with potassium hydrophosphate trihydrate [19], had two to three stages of weight loss (Fig. 5). It was found that the residual mass of mechanically activated equimass compositions of clinoptilolites with the addition of acid salt at 850 °C reaches 76–79 % (Table 3). The process of evaporation of sorption water from the studied powders with high determination coefficients ($R^2 \geq 0.94$) can be described by the formal Broido's kinetic equations and diffusion models (Table 3). The apparent activation energy of dehydration in the temperature range of 30–150 °C for samples mechanically activated together with potassium hydrosulfate for 3 and 7 minutes was comparable

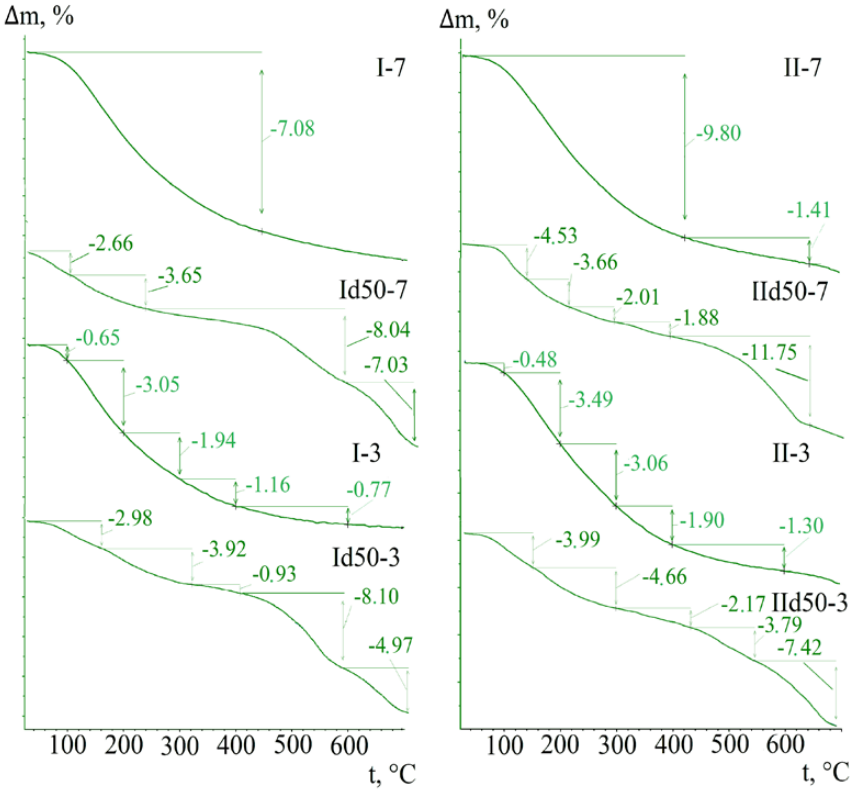

Fig. 5. Thermogravimetric curves of selected samples: I, clinoptilolite-stilbite rock; II, clinoptilolite rock; 50, potassium hydrosulfate (d) content, wt %; 3, 7, duration of mechanical treatment, min

Table 3. Minima of DTG curves, mass loss at 850 °C, apparent activation energy of dehydration in the Arrhenius equation according to selected formal kinetics: models one-dimensional diffusion (D1), Ginstling–Brownstein (D4),

Samples	DTG_{min}, °C	Δm_{850}, %	Model D1		Model D4		Broido*	
			R^2	E_a, kJ·mol^{-1}	R^2	E_a, kJ·mol^{-1}	R^2	E_a, kJ·mol^{-1}
Ic50-3	93; 144; 307	9.95*	0.9688	34.19	0.9774	36.58	0.9883	30.74
Id50-3	119; 218	21.04	0.9936	43.20	0.9932	43.59	0.9994	32.17
Ic50-7	110; 142; 309	8.39*	0.9971	49.49	0.9955	51.27	0.9976	37.42
Id50-7	117; 169	21.40	0.9962	51.12	0.9960	51.60	0.9999	36.25
IIc50-3	140; 303	9.31	0.9983	45.48	0.9971	47.05	0.9978	35.10
IId50-3	121; 207	22.03	0.9760	42.20	0.9751	42.71	0.9938	31.84
IIc50-7	140; 293	10.00	0.9998	43.08	0.9994	44.94	0.9983	34.35
IId50-7	115; 174	23.57	0.9908	55.04	0.9902	55.79	0.9980	38.62

* – mass losses are given at 700 °C [19], activation energy of dehydration of samples with potassium hydrophosphate trihydrate (c) was calculated by us earlier [19]; I, clinoptilolite-stilbite rock; II, clinoptilolite rock; 50, potassium hydrosulphate (d) content, wt %; 3, 7, duration of mechanical treatment, min

to similar indicators for zeolites modified with potassium hydrophosphate trihydrate [19]. In addition, the E_A values were approximately 50 % and 10-17 % lower compared to the same indicators for control samples (I3, I7, II3, II7).

3.4. Analysis of the structure

The IR spectra of the studied samples (Fig. 6) had characteristic absorption bands associated with vibrations of the Si-O-Si, Si-O-Al, and O-H bonds, as well as the presence of water molecules in the zeolite channels [22]. Absorption bands with maxima in the regions of 1283–1287 and ~ 850 and 885 cm^{-1} belong to the stretching vibrations of the S-O and S-O-H groups [27, 28], and deformation vibrations of O-S-O and scissor vibrations of S-O-H groups at 577–579 cm^{-1} [27]. An increase in the acid salt content in the compositions of mineral samples was accompanied by an increase in the number of absorption bands in the region of 3050–2450 cm^{-1}, associated with sulfate groups, and an increase in the intensity of absorption bands belonging to OH groups linked by hydrogen bonds. In the IR spectra of samples from clinoptilolite-stilbite rocks containing 25 wt % potassium hydrosulfate, an increase in the dose of mechanical energy was accompanied by a shift in several absorption bands. A shift to the short-wave region of the bands of the stretching vibrations of OH groups and to the long-wave region of the absorption bands of asymmetric stretching vibrations of SO_4 were observed at 1169 cm^{-1} (Id25-x, where x = 3, 5, 7), and the shift of the absorption bands of the Si-O-Si stretching vibrations (IId25-x, where x = 3, 5, 7) to the long-wave region was also revealed.

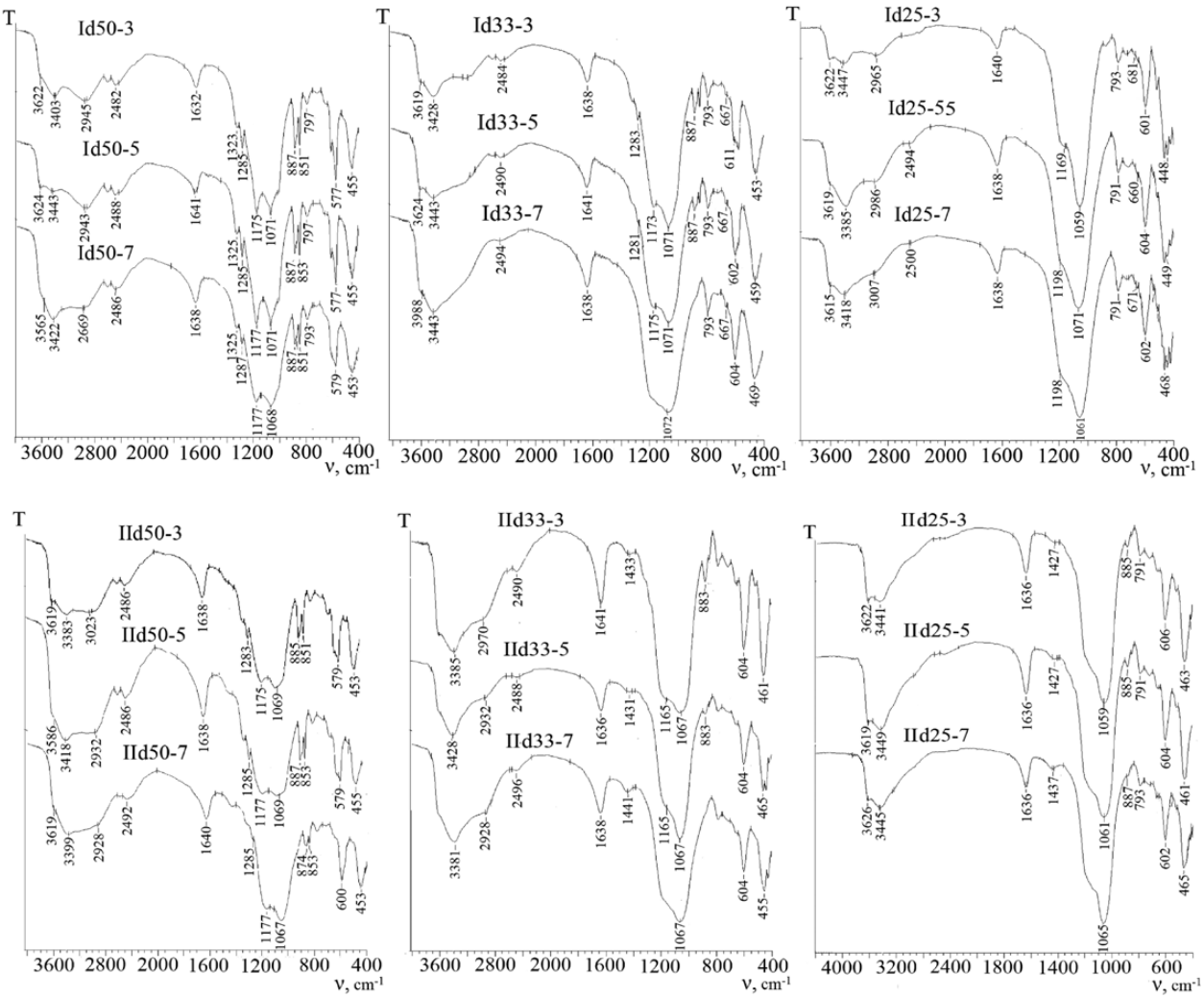

Fig. 6. Infrared spectra of zeolite samples: I, clinoptilolite-stilbite rock; II, clinoptilolite rock; 25, 33, 50, potassium hydrosulfate (d) content, wt %; 3, 5, 7, duration of mechanical treatment, min

In the IR spectra of samples from clinoptilolite rock (II), hydrosulfate absorption bands appeared with a maximum at 885–887 cm^{-1}, and small shifts of absorption bands to the long-wavelength region were observed. An increase in the acid salt content in the zeolite matrix led to significant changes, primarily in the infrared region of OH group vibrations. Hydrogen bonds of the polymer HSO_4^- chain play a significant role in the conductivity process and in the polymorphic behavior of $KHSO_4$ [29]. Doses of mechanical energy of 2.16 and 3.60 kJ/g caused similar structural changes, and already seven minutes of mechanical treatment (D = 5.04 kJ/g) led to more significant shifts of the absorption bands. The highest number of hydrogen-bonded OH groups was found in the IR spectra of powders with an equimass composition of potassium hydrosulfate and zeolite (Id50-x, IId50-x, where x = 3, 5, 7). In these cases, a transformation of the absorption band at 883–887 cm^{-1} into doublets, for example, 887 and 851 cm^{-1} (Id50-3) was observed. Absorption bands belonging to clinoptilolite at 604–601 cm^{-1} gave way to salt absorption bands at 579–577 cm^{-1} (Id50-x, where x =3, 5, 7, IId50-x, where x =3, 5). Considering the proton conductivity of potassium hydrosulfate and the important role of hydrogen bonds in the formation of conductivity channels, improved electrophysical properties can be expected in mineral samples with an equimass composition.

3.5. Study of physical properties

It is known that the presence of water molecules in natural zeolites contributes to an increase in conductivity [30]. When shock-shear mechanical action is applied to air-dry clinoptilolite rocks, local heating, is observed which activates the process of water desorption from the internal pores of zeolites [19]. This explains the decrease in humidity by ~ 9 % for mechanically activated natural zeolites (I3, I7, II3, II7) (Table 4). An increase in the dose of mechanical energy from 2.16 to 3.60 kJ/g causes a change in the crystalline structure of clinoptilolite, in which the constitutional water from the silanol groups, released during their interaction with potassium hydrosulfate, is converted into sorption water. As a result, the moisture content increases (W, %) in all acid salt-modified zeolite samples except Id50-5. With a further increase in the energy dose to 5.04 kJ/g, a decrease in hygroscopic moisture was observed, with the exception of IId50-7. The reduction of the salt concentration from 50 to 25 wt % in modified zeolites increased hygroscopicity, except for IId25-7. This can be explained by the formation of a new system of H-bonding of salt anions and silanol groups with the participation of water molecules, namely: S-O-H...H-O-H...H-O-Si.

Increasing the dose of supplied specific mechanical energy by 2.88 kJ/g contributed to an increase in the bulk density of the samples by ~ 6 % (IId33-7) and 13-14 % (Id50-7, IId50-7, IId25-7). The true density of powders changed or remained practically unchanged (Id25-7, IId50-7, IId25-7), or increased by 5-6 % (Id50-7, Id33-7), or decreased by 12 % (IId33-7). In this case, the porosity of the layer ranged from 40 % (IId25-3) to 64–65 % (IId50-7, Id50-5, Id50-7). Such changes are explained by the dispersion-agglomeration processes, the formation of an amorphous phase, dehydration, and the restructuring of

Table 4. Physical characteristics of modified zeolite samples

Samples	ρ_b, g·cm^{-3}	ρ_{tr}, g·cm^{-3}	ε_{la}, %	W, %	S_{sp}, cm^2·g^{-1}	Samples	ρ_b, g·cm^{-3}	ρ_{tr}, g·cm^{-3}	ε_{la}, %	W, %	S_{sp}, cm^2·g^{-1}
Id50-3	1.16	2.06	44	3.3	4870	IId50-3	1.10	2.18	58	3.4	5410
Id50-5	1.28	2.16	41	3.0	5950	IId50-5	1.19	2.11	60	4.3	3950
Id50-7	1.33	2.17	39	3.0	2630	IId50-7	1.25	2.22	64	4.5	3840
Id33-3	1.15	2.10	45	3.7	4710	IId33-3	0.88	2.37	52	4.8	10140
Id33-5	1.15	1.96	41	4.5	3480	IId33-5	0.98	2.04	50	5.0	6480
Id33-7	1.09	2.23	44	3.7	6200	IId33-7	0.93	2.08	48	5.0	7140
Id25-3	1.05	2.05	49	4.6	6950	IId25-3	0.78	2.14	40	4.7	13300
Id25-5	1.08	2.09	48	5.5	7120	IId25-5	0.81	2.14	42	4.9	13800
Id25-7	1.03	2.09	51	4.2	8500	IId25-7	0.88	2.15	47	4.3	11650

I, clinoptilolite-stilbite rock; II, clinoptilolite rock; 25, 33, 50, potassium hydrosulphate (d) content, wt %; 3, 5, 7, duration of mechanical treatment, min

the pore system as a result of mechanochemical activation. The specific surface area of salt-modified clinoptilolite rocks after 7 minutes of mechanical activation decreased by 1.4 times compared to 3 minutes of such exposure (IIdx-3 and IIdx-7, where x = 25, 33, 50, Table 4). The same characteristic of clinoptilolite-stilbite rocks, on the contrary, increased by 1.2–1.3 times (Id25-7, Id33-7), except for the Id50-7 sample, the specific surface of which decreased by 1.9 times in comparison with Id50-3.

The granulometric composition and electrophysical characteristics of individual mechanically strong potassium hydrosulfate-modified and mechanically activated zeolite samples are presented in Table 5. An increase in the time of mechanical activation exposure predictably led to an increase in the mass fraction of particles with sizes of 71, 80 (Id50-5) and 140, 320 μm (IId50-5).

The dependence of the electrical conductivity of tableted samples on temperature in Arrhenius coordinates is shown in Fig. 7. The highest value of electrical conductivity among the studied samples at 25 and 100 °C was revealed for IId50-3 (Table 5). The activation energies of conductivity for mechanically activated clinoptilolite-stilbite rocks without additives and with potassium hydrosulfate were 0.17–0.18 [19] and 0.70–0.75 eV. For similar samples from clinoptilolite rock, the same characteristics were equal to 0.60–0.63 [19] and 0.66–0.91 eV. The determination

Table 5. Granulometric composition, specific conductivity at 25 and 100 °C, activation energies of conductivity, coefficient of determination of dependence ln (σ) = *f* (1/T)

Samples	Content of micrometer particle fractions, wt. %					Electrical conductivity at different temperatures (°C): $\sigma \cdot 10^6$, S·m^{-1}		E_{act}, эВ	R^2
	≥ 630	320	140	80	≤ 71	25	100		
Id50-3	0.4	5.0	44.3	47.4	2.9	0.25	74.34	0.74	0.9379
Id50-5	1.9	7.9	29.7	50.4	10.1	0.34	88.84	0.75	0.9785
Id33-3	6.1	5.0	25.5	54.7	8.8	0.45	57.94	0.70	0.9280
IId50-3	0.5	4.9	54.6	35.6	4.3	0.85	426.47	0.73	0.8925
IId50-5	0.4	7.1	70.1	21.1	1.3	0.62	145.66	0.66	0.9063
IId33-3	1.1	4.9	81.0	10.3	2.8	0.08	71.48	0.91	0.9027

E_{act} is activation energy of conductivity in temperature ranges of 25–100 °C; R^2 is the coefficient of determination of the linear dependence $\ln\sigma = f(1/T)$; I, clinoptilolite-stilbite rock; II, clinoptilolite rock; 33, 50, potassium hydrosulphate (d) content, wt %; 3, 5, duration of mechanical treatment, min.

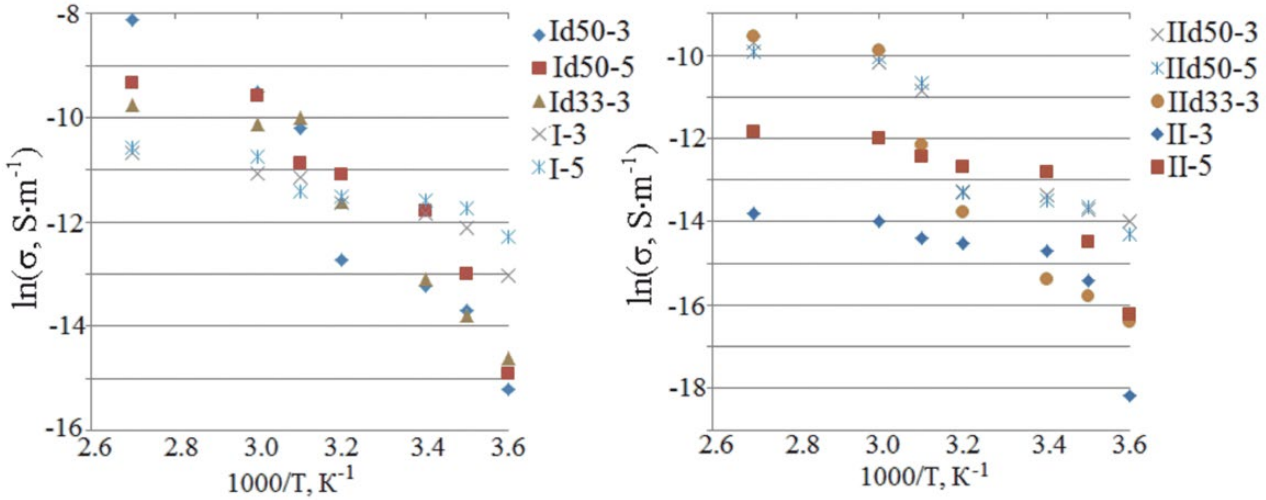

Fig. 7. Dependencies of the logarithm of specific conductivity on the inverse temperature for pressed samples: I, clinoptilolite-stilbite rock; II, clinoptilolite rock; 33, 50, potassium hydrosulfate (d) content, wt %; 3, 5, duration of mechanical treatment, min

coefficients of the linear dependencies $\ln\sigma = f(1/T)$ varied from 0.90 to 0.98. Clinoptilolite rock modified with potassium hydrosulfate in an equimass ratio after mechanical activation with an energy dose of 2.16 kJ/g had the highest specific electrical conductivity $\sigma = 4.26 \cdot 10^{-4}$ S·m^{-1}. This was comparable to the conductivity for a similar sample modified with potassium hydrogen phosphate trihydrate [19]. However, the activation energy of conductivity in the case of potassium hydrosulfate samples is almost 2 times higher.

4. Conclusions

From an air-dry mixture of clinoptilolite-stilbite (clinoptilolite) rocks and potassium hydrosulfate in ratios of 3:1, 2:1, and 1:1, mineral powders were obtained using a vibratory bowl grinder IVCh-3 with impact-shear action and an energy dose of 2.16, 3.60, and 5.04 kJ/g. Pressed samples at 25 ºC had specific electrical conductivity values of about 10^{-6} S·m^{-1}. Short-term mechanical action on clinoptilolite rocks for 3–7 minutes together with salt led to the amorphization of stilbite and microcline, polymorphic transition of quartz into cristobalite and tridymite, as well as different phase states of the salts ($KHSO_4$, $K_3H(SO_4)_2$). The system of silanol groups and proton-containing hydrosulfate anions connected by hydrogen bonds, representing possible conduction channels, was formed with an equimass ratio of components and a dose of mechanical energy of 5.04 kJ/g. At 25 and 100 °C, the electrical conductivity of a sample based on clinoptilolite rock and potassium hydrosulfate of equimass composition with an energy dose of 2.16 kJ/g was ~$8.5 \cdot 10^{-7}$ and $4.3 \cdot 10^{-4}$ S·m^{-1}, respectively. The results obtained earlier indicate that HPO_4^{2-} ions are better integrated into the zeolite structure and transfer charge more efficiently than HSO_4^-. Zeolites with the addition of potassium hydrosulfate, due to the presence of interaction and high hygroscopicity, are less promising for practical use in electrochemical devices compared to zeolites with the addition of potassium hydrogen phosphate trihydrate.

Contribution of the authors

Soloboeva T. P. – research concept, research implementation, writing and editing, and text conclusions. Dabizha O. N. – research concept, methodology development, text editing, conclusions, and scientific supervision. Batukhtin A. G. – research concept, resource provision for the research, participation in the discussion of results, assessment of research prospects.

Conflict of interests

The authors declare that they have no known competing financial interests or personal relationships that could have influenced the work reported in this paper.

References

1. Lesiak P. Zeolites as catalysts: a review of the recent developments. *Jntes*. 2023;2: 065–073. https://doi.org/10.53412/jntes-2023-2-4.

2. Luzanova V. D., Rozhmanova N. B., Lanin S. N., Nesterenko P. N. Application of zeolites in high-performance liquid chromatography. *Sorbtsionnye I Khromatograficheskie Protsessy*. 2023;23(4): 691–704. (In Russ.). https://doi.org/10.17308/sorpchrom.2023.23/11576

3. Stocker K., Ellersdorfer M., Lehner M., Raith J. G. Characterization and utilization of natural zeolites in technical applications. *BHM Berg- Und Hüttenmännische Monatshefte*. 2017;162 (4): 142–147. https://doi.org/10.1007/s00501-017-0596-5

4. Grifasi N., Ziantoni B., Fino D., Piumetti M. Fundamental properties and sustainable applications of the natural zeolite clinoptilolite. *Environmental Science and Pollution Research*. 2024; 32:27805–27840. https://doi.org/10.1007/s11356-024-33656-5

5. Barbosa J. C., Gonçalves R., Costa C. M., … Lanceros-Méndez S. Metal-organic frameworks and zeolite materials as active fillers for lithium-ion battery solid polymer electrolytes. *Materials Advances*. 2021;2(12): 3790–3805. https://doi.org/10.1039/d1ma00244a

6. Li M., Chi X., Yu J. Zeolite-based electrolytes: a promising choice for solid-state batteries. *PRX Energy*. 2022;1(3): 1–16. https://doi.org/10.1103/prxenergy.1.031001

7. Shi H., Zhang J., Li J. The effect of guest cations on proton conduction of LTA zeolite. *RSC Advances*. 2021;11(10): 5393–5398. https://doi.org/10.1039/d0ra09917a

8. Kalogeras J. M., Vassilikou-Dova A. Molecular mobility in microporous architectures: conductivity and dielectric relaxation phenomena in natural and synthetic zeolites. *Crystal Research and Technology*. 1996;31(6): 693–726. https://doi.org/10.1002/crat.2170310602

9. Bolotin O. A., Goncharuk V. P., Bologa M. K., Mitina T. F., Polikarpov, A. A., Kostryukova, N. V. Activation of zeolite in a magnetic fluidized bed. *Electronic Processing of Materials*. 2024;60(3): 50–55. (In Russ.) https://doi.org/10.52577/eom.2024.60.3.50

10. Buzimov A. Y., Kulkov S. N., Gömze L. A., Géber R., Kocserha, I. Effect of mechanical treatment on the structure and properties of natural zeolite. *Perspektivnye Materialy*. 2018;9(5): 031–039. https://doi.org/10.30791/1028-978x-2018-4-31-39

11. Dabizha O. N., Soloboeva T. P., Khamova T. V., Shilova O. A. Mechanical activation of clinoptilolites with

sodium and ammonium hydrophosphates to improve their electrophysical properties. *Glass Physics and Chemistry*. 2023;49(3): 293–305. https://doi.org/10.1134/S1087659623600059

12. Astapova E. S., Pavlov S. S., Astapov I. A. Determination of structure characteristics and conductivity of Na-HS-zeolite with Mo, W and Ni nanopowders. *The Bulletin of the Adyghe State University, the series 4: Natural, Mathematical and Technical Sciences*. 2012;2(4): 31–39. (In Russ.) Available at: https://www.elibrary.ru/item.asp?id=18055827

13. Rainer D. N., Morris R. E. New avenues for mechanochemistry in zeolite science. *Dalton Transactions*. 2021;50(26): 8995–9009. https://doi.org/10.1039/d1dt01440d

14. Nikashina V. A., Streletskii A. N., Kolbanev I. V., … Shumskaya L. G. Effect of mechanical activation on the properties of natural zeolites. *Inorganic Materials*. 2011;47(12): 1341–1346. https://doi.org/10.1134/S0020168511120144

15. Bebiya A. G., Gulyaev P. Y., Milyukova I. V. Change of physical and chemical properties clinoptilolite after mechanical activation. *Yugra State University Bulletin*. 2012;7-8: 7-13. (in Russ.). Available at: https://www.elibrary.ru/item.asp?id=24989138

16. Velichkina L. M., Zaikovskii V. I., Barbashin Ya. E., Ryabova N. V., Perevezentsev S. A., Vosmerikov A. V. Changes in the physicochemical properties of nickel-containing ZSM-5 zeolite under mechanical treatment. *Chemistry for Sustainable Development*. 2020;28 (4): 378–386. (In Russ.). https://doi.org/10.15372/khur2020242

17. Ovsyuk N. N., Goryaĭnov S. V. Amorphous-to-amorphous phase transition in zeolites. *JETP Letters*. 2006;83(3): 138–142. https://doi.org/10.1134/S0021364006030064

18. Buzimov A. Y., Eckl W., Gömze L. A., Kocserha I., Kurovics E., Kulkov A. S., Kulkov S. N. Effect of mechanical treatment on properties of Si-Al-O zeolites. *Epitoanyag - Journal of Silicate Based and Composite Materials*. 2018;70(1): 023–026. https://doi.org/10.14382/epitoanyag-jsbcm.2018.5

19. Dabizha O. N., Soloboeva T. P., Kalinina M. V., Shilova O. A. Structure formation and electrophysical properties of natural zeolites mechanically activated with potassium hydrophosphate to produce solid electrolytes. *Glass Physics and Chemistry*. 2024;50(4): 428–443. https://doi.org/10.1134/S1087659624600996

20. de Izarra A., Coudert F. X., Fuchs A. H., Boutin A. Molecular simulation of the impact of defects on electrolyte intrusion in zeolites. *Langmuir*. 2023;39(51): 19056–19063. https://doi.org/10.1021/acs.langmuir.3c03306

21. Ponomareva V. G., Lavrova G. The investigation of disordered phases in nanocomposite proton electrolytes based on MeHSO4 (Me = Rb, Cs, K). *Solid State Ionics*. 2001;145: 197–204. https://doi.org/10.1016/S0167-2738(01)00957-2

22. Dabizha O. N., Derbeneva T. V., Khamova T. V., Shilova O. A. Controlling the sorption activity of clinoptilolites with mechanical activation. *Inorganic Materials*. 2021;57(4): 399-408. https://doi.org/10.1134/s0020168521040038

23. Soloboeva T. P., Dabizha O. N. Investigation of electrical conductivity of mechanically activated clinoptilolite rocks. In: *Fundamental Bases of Mechanochemical Technologies: VI International conference, 21-24 November 2022, Novosibirsk*. Novosibirsk: ISSCM SB RAS, 2022. p. 46.

24. Rat'ko A. I., Ivanets A. I., Kulak A. I., Morozov, E. A., Sakhar I. O. Thermal decomposition of natural dolomite. *Inorganic Materials*. 2011;47(12): 1372–1377. https://doi.org/10.1134/s0020168511120156

25. Kosenko N. F., Smirnova M. A. Quartz polymorphic transformations stimulated by mechanical treatment. *Refractories and Industrial Ceramics*. 2012;7-8: 7–13. (In Russ.). https://elibrary.ru/item.asp?id=17889319

26. Selezneva E. V., Makarova I. P., Grebenev V. V., … Choundhury R. R. The changes of thermal, dielectric, and optical properties at insertion of small concentrations of ammonium to $K_3H(SO_4)_2$ crystals. *Crystallography Reports*. 2018;63: 553–562. https://doi.org/10.1134/s1063774518040247

27. Swain D., Bhadram V. S., Pradhan G. K., Bhat S. V., Narayana C., Rao C. B. H. Superionic phase transition in $KHSO_4$: a temperature-dependent raman investigation. *Journal of Physical Chemistry A*. 2010;114(37): 10040-10044. https://doi.org/10.1021/jp103005g

28. Periasamy A., Muruganand S., Palaniswamy M. Vibrational studies of Na_2SO_4, K_2SO_4, $NaHSO_4$ and $KHSO_4$ crystals. *RASĀYAN Journal of Chemistry*. 2009;2 (4): 981–989. Available at: https://rasayanjournal.co.in/vol-2/issue-4/34.pdf

29. Payan F., Haser R. On the hydrogen bonding in potassium hydrogensulphate. Comparison with a previous crystal structure determination. *Acta Crystallographica Section B Structural Crystallography and Crystal Chemistry*. 1976;32(6): 1875–1879. https://doi.org/10.1107/s0567740876006572

30. Cura Ö., Ajjaq A., Çağırtekin A., Cavdar S., Acar S. Low-energy ball milling effect on the dielectric response and electrical transport mechanisms of natural clinoptilolite zeolites in a wide temperature range. *Materials Today Communications*. 2021;29: 102964. https://doi.org/10.1016/j.mtcomm.2021.102964

Information about the authors

Tatyana P. Soloboeva, degree candidate, Transbaikal State University, (Chita, Russian Federation).

https://orcid.org/0000-0001-5461-2668

laperdina.lapi@yandex.ru

Olga N. Dabizha, Cand. Sci. (Chem.), Associate Professor, Associate Professor at the Department of Chemistry, Transbaikal State University (Chita, Russian Federation); Senior Researcher, Laboratory of Inorganic Synthesis, I. V. Grebenshchikov Institute of Silicate Chemistry (St. Petersburg, Russian Federation).

https://orcid.org/0000-0002-8633-8082

dabiga75@mail.ru

Andrey G. Batukhtin, Dr. Sci., Associate Professor, dean of the Faculty of Energy, Transbaikal State University (Chita, Russian Federation)

https://orcid.org/0000-0002-9134-0873

batuhtina_ir@mail.ru

Received April 2, 2025; approved after reviewing April 18, 2025; accepted for publication May 15, 2025; published online December 25, 2025

ISSN 1606-867X (Print)
ISSN 2687-0711 (Online)
Condensed Matter and Interphases
Kondensirovannye Sredy i Mezhfaznye Granitsy
https://journals.vsu.ru/kcmf/

Original articles

Research article
https://doi.org/10.17308/kcmf.2025.27/13328

Biotemplate synthesis of In_2O_3-Pd for room temperature sensor of hydrogen

A. V. Shaposhnik[1]✉, O. A. Arefieva[1], A. A. Zviagin[1], N. Yu. Brezhnev[1], E. A. Vysotskaya[1], A. A. Vasiliev[2], S. V. Ryabtsev[3], S. Yu. Turishchev[3]

[1]Voronezh State Agrarian University,
1 Michurina st., Voronezh 394087, Russian Federation

[2]Laboratory of Sensor Systems, University "Dubna",
19 Universitetskaya st., Dubna 141980, Moscow region, Russian Federation

[3]Voronezh State University,
1 Universitetskaya pl., Voronezh 394018, Russian Federation

Abstract

Objective: The solution to the urgent task of creating compact gas analyzers capable of long-term autonomous operation in hard-to-reach places is related to the development of sensors with reduced energy consumption. The aim of this work was to create a room temperature hydrogen sensor, as it is the sensor's heating that contributes significantly to the energy consumption of the entire device.

Experimental: To solve this problem, a new method for the synthesis of a nanomaterial based on In_2O_3 with a 3 % palladium additive was developed, which differs significantly from the common methods of sol-gel synthesis and hydrothermal synthesis. This was due to the fact that at low sensor temperatures, minimizing the effect of humidity is crucial. Performing the synthesis in an aqueous environment leads to the formation of a large number of hydroxyl groups on the surface, which attract water. In our work, the nanomaterial was prepared by sintering a cellulose fiber pre-impregnated with a solution of indium nitrate (+3) and tetraammine palladium nitrate (+2). According to X-ray phase analysis, the powder sintered at a temperature of 500 °C consists mainly of the triclinic phase of indium oxide (+3). According to scanning electron microscopy, the samples largely retained the reproducible characteristic macrostructure of the cellulose template. The electrophysical characteristics of the nanomaterial obtained at room temperature showed the possibility of determining hydrogen in the air. The detection limit is less than 10 ppm.

Conclusions: The sensitivity of our hydrogen sensor at room temperature is higher than that of sensors described in other publications. The effect of humidity on sensor readings is minimized.

Keywords: Metal oxide sensors, Biotemplated synthesis, Hydrogen, Room temperature, Indium oxide, Palladium

Funding: RSV and TSYu acknowledge the grant of the Ministry of Science and Higher Education of the Russian Federation (Project FZGU-2023-0006) in part of material characterization.

Acknowledgements: The SEM studies and X-ray phase analysis were performed on the equipment of the Center for the Collective Use of Scientific Equipment of Voronezh State University.

For citation: Shaposhnik A. V., Arefieva O. A., Zviagin A. A., Brezhnev N. Ya., Vysotskaya E. A., Vasiliev A. A., Ryabtsev S. V., Turishchev S. Ya. Biotemplate synthesis of In_2O_3-Pd for room temperature sensor of hydrogen. *Condensed Matter and Interphases*. 2025;27(4): 689–695. https://doi.org/10.17308/kcmf.2025.27/13328

Для цитирования: Шапошник А. В., Арефьева О. А., Звягин А. А., Брежнев Н. Ю., Высоцкая Е. А., Васильев А. А., Рябцев С. В., Турищев С. Ю. Биотемплатный синтез In_2O_3-Pd для низкотемпературного сенсора водорода. *Конденсированные среды и межфазные границы*. 2025;27(4): 000-000. https://doi.org/10.17308/kcmf.2025.27/13328

✉ Alexey V. Shaposhnik, e-mail: a.v.shaposhnik@gmail.com

1. Introduction

The determination of hydrogen and other combustible explosive gases in hard-to-reach places is an important practical task. Gas sensors are commonly used to solve this problem, including thermocatalytic, electrochemical, and semiconductor sensors. Thermocatalytic sensors are simple and inexpensive, but they have low sensitivity and selectivity. Electrochemical sensors, which are similar to fuel cells, have high sensitivity and selectivity, but they have a limited operational duration due to the consumption of the reactant. High sensitivity and high selectivity can be achieved using semiconductor sensors, but their application usually requires maintaining an operating temperature of around 300 °C. The significant energy consumption makes it difficult to create autonomous gas analyzers based on semiconductor sensors that can operate in remote areas for extended periods.

There are several approaches to solving the problem of reducing energy consumption by semiconductor sensors. One approach is to miniaturize the sensor and use special dielectric substrates with low heat capacity [1]. Another approach is pulse heating, which not only reduces energy consumption but also increases the sensitivity and selectivity of the analysis in some cases [2]. In recent years, there have been many publications that propose a third approach to solving this problem: the synthesis of gas-sensitive materials that can perform gas analysis without heating the sensor. In English literature, this approach is known as a "room temperature sensor." These sensors can be used to detect various gases in the air, including both reducing gases such as ammonia [3–5] and hydrogen sulfide [6-8], and oxidizing gases such as NO_2 [9–11].

Gas-sensitive materials for low-temperature hydrogen sensors have been synthesized. PdO nanoparticles with added palladium allow for the detection of very high hydrogen concentrations, exceeding 1000 ppm at room temperature [12]. A nanomaterial based on WO_3, graphene, and palladium exhibited a response of several percent at a hydrogen concentration of 10000 ppm and a temperature of 50 °C [13]. The response of Ti_2CTx MXene to 1000 ppm of hydrogen was several percent [14]. A material based on TiO_2 nanospheres with palladium additives allowed for the detection of hydrogen at a concentration of 500 ppm [15]. A material based on $NiCo_2O_4$ nanoneedles with an addition of palladium allowed for the confident detection of hydrogen at a concentration of 100 ppm [16]. A nanomaterial based on WO_3 allowed for a sensor response of 12% at a hydrogen concentration of 100 ppm [17]. A nanomaterial based on mixed manganese and cobalt oxides with an addition of reduced graphene had a similar response [18]. A significantly greater response to hydrogen was observed in a tungsten (VI) oxide-based nanomaterial with a palladium additive [19]. Using TiO_2-based nanomaterials, significant responses to hydrogen were obtained at room temperature, but this required the use of UV radiation to activate the sensitive material and impedance measurements [20].

Indium (III) oxide-based nanomaterials are widely used [21, 22]. For example, silver-modified In_2O_3 nanosheets were used to detect 1-butanol under UV light [23]. Thermal spraying of thin-film indium oxide allowed for the detection of NO_2 and H_2S at room temperature [24].

An important problem in the determination of gases by low-temperature ("room temperature") semiconductor sensors is the minimization of the influence of the humidity of the environment. The presence on the surface of metal oxide semiconductors of hydroxyl groups formed during synthesis makes them vulnerable to water sorption, which leads to a significant increase in the contribution of ionic conductivity. The electroconductive response of semiconductor sensors is based on a change in the concentration of electrons and a change in their mobility, so an increase in the contribution of ionic conductivity interferes with the gas analysis. Thus, in order to obtain gas-sensitive materials for low-temperature sensors, it makes sense to choose methods in which the interaction of the reactants does not occur in an aqueous environment. Most studies on "room temperature sensors" do not use either sol-gel synthesis or hydrothermal synthesis.

In this paper, the synthesis of the In_2O_3 nanomaterial was carried out using the biotemplate method, which has been widely used in recent years for the production of biocatalysts, antibiotics, and anti-cancer drugs

[25]. Biotemplate synthesis is also used for the production of gas-sensitive materials. For example, a CeO_2-ZnO hollow-fiber-based material was successfully used to create an ethanol sensor [26]. SnO_2-based nanotubes were used to create an acetone sensor [27].

The purpose of our work was not only to study the gas sensitivity of the obtained material in relation to hydrogen, but also to study the effect of humidity on the background resistance, since this problem is not considered in publications on "room temperature sensors" for unknown reasons.

2. Experimental

2.1. Synthesis

A weighed amount of indium nitrate (CAS: 207398-97-8, InN_3O_9·nHOH, MW: 300.83 g/mol, form: powder and chunks, Sigma-Aldrich, USA), corresponding to 0.05 mol(eq)/L, was mixed with an aqueous solution of acetic acid (pH = 5). The mixture was kept at room temperature until the indium nitrate was completely dissolved.

The sheets of ash-free cellulose filters (red tape) were washed with an eluent, a mixture of butanol and acetic acid in a volume ratio of 1:4. 50 ml of the eluent was poured into a 0.5-liter glass, and the cellulose sheets were immersed in the solution to a depth of 1-2 cm. The glass was covered with glass and left for 5 hours. Next, the sheets were removed from the cup, dried, and after drying, the top 2 cm of the sheets were cut off and removed, and then heated for 3 hours in a drying oven at 105 °C.

50 ml of the solution of indium nitrate was poured into a glass, and sheets of washed and dried filter paper were immersed in it to a depth of 1 cm. The glass was closed and left to stand for 2 hours. After impregnation, the cellulose was removed from the chamber and dried at 105 °C for 3 hours. The material was then calcined at 500 °C for 6 hours to burn off the cellulose and form indium oxide:

$$4In(NO_3)_3 \rightarrow 2In_2O_3 + 12NO_2 + 3O_2 \quad (1)$$

2.2. Sensor fabrication

A gas-sensitive layer based on In_2O_3+Pd (mass fraction of palladium 3%) was created by treating the In_2O_3 material with a solution of tetraammine palladium (II) nitrate. After drying, the material was mixed with terpeniol, which was used as a binding agent, to form a paste. The resulting paste was applied to a dielectric substrate made of aluminum oxide, with platinum electrodes and a heater, and then baked at a temperature of 750 °C, resulting in the burning of the terpeniol and the formation of a semiconductor layer of brittle indium oxide gel on the substrate.

2.3. Material characterization

The structure of the In_2O_3 sample was characterized by X-ray phase analysis using a DRON-4 instrument with a cobalt anode. The resulting diffraction patterns were subsequently analyzed using the ICSD Database 2010-2).

The material was investigated using a JEOL JSM-6380LV scanning electron microscope in secondary electron mode.

2.4. Sensor measurements

Calibration gas mixtures "hydrogen in synthetic air" with concentrations of 10 ppm and 200 ppm were used. To achieve the desired hydrogen concentration, the calibration gas mixtures were diluted with synthetic air. A portion of the synthetic air flow was passed through distilled water for humidification. After mixing the three streams - dry air, humidified air, and the verification gas mixture, the humidity and temperature were measured using a Honeywell HIH-4602-A sensor. A TO-8 sensor in a metal casing was placed in a stainless-steel chamber.

Using a specially designed device, the electrical resistance of the gas-sensitive layer of the sensor was measured at a sampling rate of 40 Hz and recorded as a computer file.

The sensor response S was determined as the relative difference in electrical conductivity in the gas medium σ and in synthetic air σ_0, which is equivalent to the relative difference in electrical resistance in the gas medium R and in synthetic air R_0:

$$S = \frac{\sigma - \sigma_0}{\sigma_0} = \frac{R_0 - R}{R}. \quad (2)$$

3. Results and discussion

3.1. Morphology and structure of the material

Fig. 1 shows images of an indium oxide sample obtained using a scanning electron

microscope. The samples retain the characteristic macrostructure of the cellulose template. In terms of morphology, the studied material consists of agglomerations of fiber-like objects, each of which is curved or "twisted," sometimes multiple times, along its length, which ranges from a few micrometers to several tens of micrometers. The thickness of the relatively flat fibers can be as thin as submicrons, while the width can be several micrometers, forming extended "sheets." In some areas of fiber agglomerations, there are objects of small thickness (size) of ~ 100 nm.

As a result of the deciphering of diffraction patterns, it was found that the studied sample is almost completely (more than 95%) represented by the main modifications of crystalline indium (III) oxide, which is cubic (PG Ia). In addition, the presence of mixed indium oxide-hydroxide InO(OH) (cubic, PG P213, up to 3%) and indium hydroxide $In(OH)_3$ (cubic, PG Im, less than 1%) was detected in small amounts, which can be explained by insufficient thermal treatment in terms of time or temperature. The data on R-factors and the quality factor of the diffraction pattern are also shown in Figure 2.

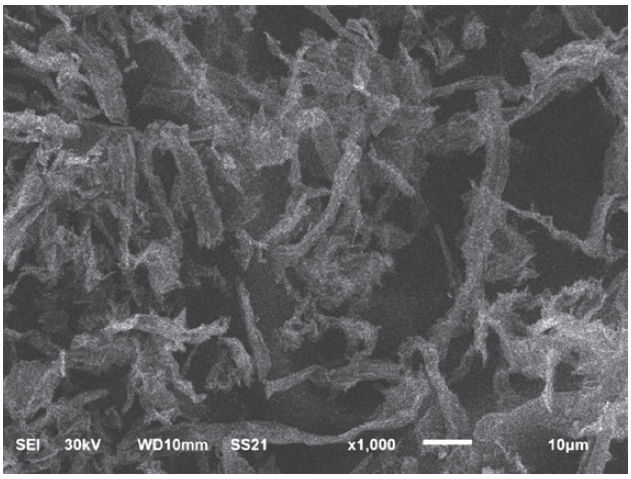

Fig. 1. SEM image of In_2O_3 material obtained by the biotemplate method

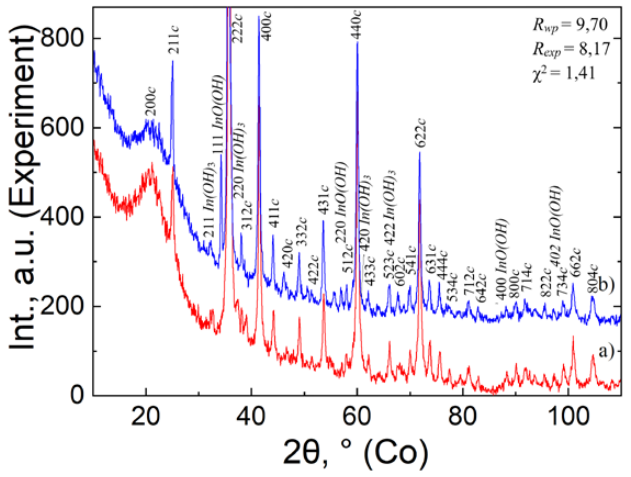

Fig. 2. X-ray diffraction pattern of indium (III) oxide nanopowder, calcinated at 500 °C. Compounds: *c* – In_2O_3 (cubic, SG *Ia*); InO(OH) (cubic, SG $P2_13$), $In(OH)_3$ (cubic, SG *Im*)

3.2. Sensor investigation

Fig. 3 shows the electrical resistance of the sensor when hydrogen is added to the air at a concentration of 10 ppm. As expected, the response is donor-type, resulting in an increase in the electrical conductivity of the sensor. This is because indium oxide is an n-type semiconductor, and hydrogen is a reducing agent. Adding hydrogen increases the concentration of electrons in the semiconductor:

$$H_2 \rightarrow 2H^+ + 2e \quad (3)$$

$$2H_2 + O_2^- \rightarrow 2H_2O + e \quad (4)$$

Fig. 4 shows the calibration dependence of the In_2O_3+Pd sensor at a temperature of 25 °C. The sensitivity of our sensor is higher than in papers [12-18].

3.3. Determining the effect of humidity

As already noted, an important problem of low-temperature sensors is to minimize

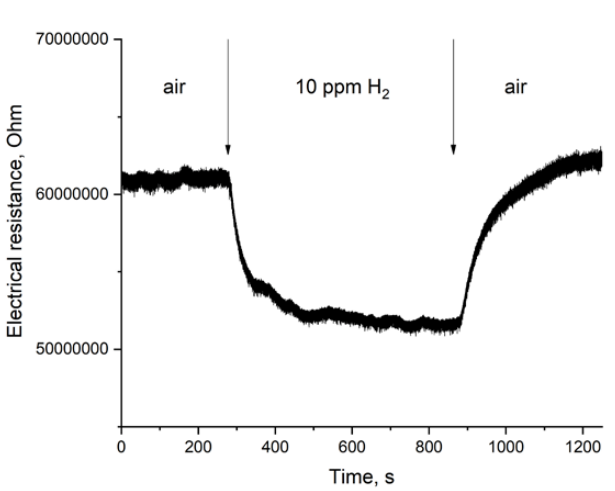

Fig. 3. Electrical resistance of the In_2O_3-Pd sensor when hydrogen is added. Sensor temperature is 25°C, the air humidity is 25 %

the influence of humidity. Fig. 5 shows the dependence of the electrical resistance of the In_2O_3-Pd sensor on humidity at a temperature of 25 °C.

As expected, an increase in humidity leads to a significant decrease in electrical resistance, which is due to the appearance of an additional (ionic) conduction mechanism caused by the sorption of water on the surface of the metal oxide semiconductor [28]. This mechanism is caused by the dissociation of water and the appearance of a significant number of hydrogen cations on the surface. Additionally, charge transfer can also be associated with the transport of hydroxide anions.

4. Conclusion

In_2O_3-Pd nanomaterial samples synthesized by the biotemporal method showed the ability to detect relatively low concentrations of hydrogen at room temperature, which suggests that they can be used to create sensors that do not require energy consumption for heating.

Despite the choice of a non-aqueous synthesis method and the minimal number of hydroxyl groups in the metal oxide semiconductor, the resistance of the resulting sensor is significantly affected by humidity, so the practical application of the corresponding gas analyzer is only possible in combination with a humidity sensor.

Contribution of the authors

The authors contributed equally to this article.

Conflict of interests

The authors declare that they have no known competing financial interests or personal relationships that could have influenced the work reported in this paper.

References

1. Kul O., Vasiliev A., Shaposhnik A. … Simonenko E. Novel screen-printed ceramic MEMS microhotplate for MOS sensors. *Sensors and Actuators A: Physical*. 2024;379(8): 115907. https://doi.org/10.1016/j.sna.2024.115907

2. Shaposhnik A. V., Moskalev P. V., Zviagin A. A. … Vasiliev A. A. Selective determination of hydrogen sulfide using SnO_2–Ag sensor working in non-stationary temperature regime. *Chemosensors*. 2021;9(8): 203. https://doi.org/10.3390/chemosensors9080203

3. Cai S., Huang X., Luo M. … Gao Z. High-performance ammonia sensor at room temperature based on 2D conductive MOF Cu3(HITP)2. *Talanta*. 2025;285(11): 127226 https://doi.org/10.1016/j.talanta.2024.127226

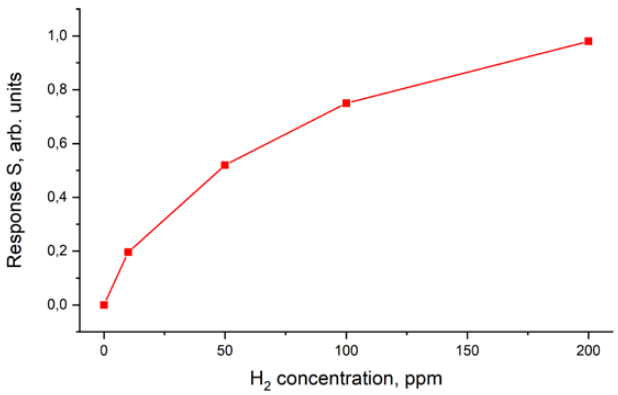

Fig. 4. Dependence of the In_2O_3-Pd sensor response on hydrogen concentration at a temperature of 25 °C

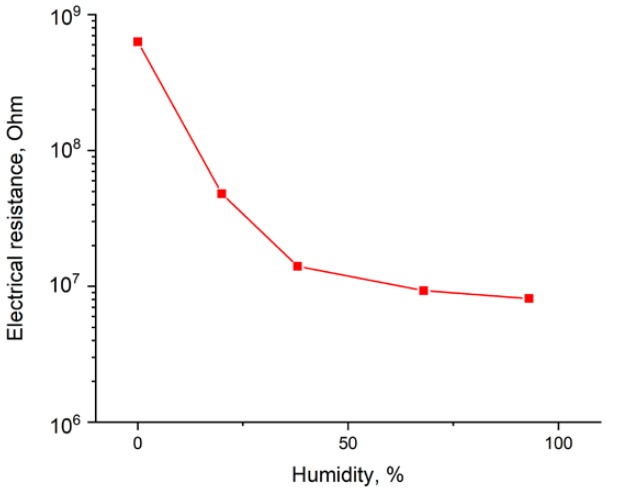

Fig. 5. Dependence of the electrical resistance of the In_2O_3-Pd sensor on air humidity at a temperature of 25 °C

4. Xue L., Zhang F., Dang J. … Wang Q. Room-temperature NH_3 sensor with ppb detection via AACVD of nanosphere WO_3 on IO SnO_2. *Ceramics International*. 2024;50(8): 47991–47999. https://doi.org/10.1016/j.ceramint.2024.09.146

5. Tripathi S., Singh S. P., Tripathi S., Kumar A., Chauhan P. γ-WO_3 decorated MXene: an advanced nanomaterial for room temperature operable enhanced ammonia sensor. *Colloids and Surfaces A: Physicochemical and Engineering Aspects*. 2025;705(P1): 135538. https://doi.org/10.1016/j.colsurfa.2024.135538

6. Zhao W., Yao G., Wu H. … Yu J. Chemiresistive room temperature H_2S sensor based on Cu_nO nanoflowers fabricated by laser ablation. *Sensors and Actuators B: Chemical*. 2025;423: 136732. https://doi.org/10.1016/j.snb.2024.136732

7. Huang C.-W., Wu C.-Y., Hsueh T.-J. Materials science in semiconductor processing a room temperature ZnO : Ga NWs & NSs / MEMS H_2S gas sensor. *Materials Science in Semiconductor Processing*. 2025;187(11): 109149. https://doi.org/10.1016/j.mssp.2024.109149

8. Bai H., Feng C., Chen Y. … Guo F. Chemiresistive room temperature H_2S gas sensor based on MoO_3 nanobelts

decorated with MnO_2 nanoparticles. *Sensors and Actuators B: Chemical*. 2024;420(8): 136468. https://doi.org/10.1016/j.snb.2024.136468

9. Hao X., Xing R. Fabrication of MoS_2-Fe_3O_4 heterostructure as an ultrafast and high-sensitivity NO_2 gas sensor at room temperature. *Materials Letters*. 2024;377(8): 4–7. https://doi.org/10.1016/j.matlet.2024.137387

10. Ge C., Ni M., Liu S., … Liu J. A room-temperature NO_2 gas sensor based on Zn^{2+} doped Cu_2O/CuO composites with ultra-high response. *Ceramics International*. 2025;51 (2): 2194–2203. https://doi.org/10.1016/j.ceramint.2024.11.197

11. Guo Y.-Y., Zheng X.-H., Bo L.-B., Gu Z.-Q., Zhang C., Liu Y.-F. UV-activated gas sensor based on ordered mesoporous ZnO – TiO_2 heterogeneous composites for trace NO_2 detection at room temperature. *Talanta*. 2025;285(10): 127415. https://doi.org/10.1016/j.talanta.2024.127415

12. Yang S., Chen G., Zheng F. … Zhang X. Pd-decorated PdO nanoparticle nanonetworks: a low-cost eye-readable H_2 indicator with reactivation ability. *Sensors and Actuators B: Chemical*. 2022;368(5): 132242. https://doi.org/10.1016/j.snb.2022.132242

13. Wang L., An F., Liu X., Zhang D., Yang Z. Preparation and hydrogen-sensitive property of WO_3/graphene/Pd ternary composite. *Chemosensors*. 2023;11(7). https://doi.org/10.3390/chemosensors11070410

14. Mokrushin A. S., Nagornov I. A., Gorobtsov P. Y. … Kuznetsov N. T. Effect of Ti2CT x MXene oxidation on its gas-sensitive properties. *Chemosensors*. 2023;11(1): 13. https://doi.org/10.3390/chemosensors11010013

15. Thathsara T, Harrison C. J., Hocking R. K., Shafiei M. Pd- and PdO-decorated TiO_2 nanospheres: hydrogen sensing properties under visible light conditions at room temperature. *Chemosensors*. 2023;11(7): 409. https://doi.org/10.3390/chemosensors11070409

16. Kim S.-H., Yun K.-S. Room-temperature hydrogen gas sensor composed of palladium thin film deposited on $NiCo_2O_4$ nanoneedle forest. *Sensors and Actuators B: Chemical*. 2023;376(PA): 132958. https://doi.org/10.1016/j.snb.2022.132958

17. Shrisha Wu, C.-M., Motora K. G., Chen G.-Y., Kuo D.-H., Gultom N. S. Highly efficient reduced tungsten oxide-based hydrogen gas sensor at room temperature. *Materials Science and Engineering: B*. 2023;289: 116285. https://doi.org/10.1016/j.mseb.2023.116285

18. Maji B., Barik B., Sahoo S. J., …Dash P. Shape selective comprehensive gas sensing study of different morphological manganese-cobalt oxide based nanocomposite as potential room temperature hydrogen gas sensor. *Sensors and Actuators B: Chemical*. 2023;380: 133348. https://doi.org/10.1016/j.snb.2023.133348

19. Lee J., Kim S. Y., Yoo H. S., Lee W. Pd-WO_3 chemiresistive sensor with reinforced self-assembly for hydrogen detection at room temperature. *Sensors and Actuators B: Chemical*. 2022;368: 132236. https://doi.org/10.1016/j.snb.2022.132236

20. Peng X., Wang Z., Huang P., Chen X., Fu X., Dai W. Comparative study of two different TiO_2 film sensors on response to H_2 under UV light and room temperature. *Sensors*. 2016;16(8): 1249. https://doi.org/10.3390/s16081249

21. Artamonova O. V., Almjasheva O. V., Mittova I. Y., Gusarov V. V. Zirconia-based nanocrystals in the ZrO_2 – In_2O_3 system. *Inorganic Materials*. 2006;42(10): 1178–1181. https://doi.org/10.1134/s0020168506100049

22. Artamonova O. V., Almyasheva O. V., Mittova I. Ya., Gusarov V. V. Sintering of nanopowders and properties of ceramics in the ZrO_2 – In_2O_3 system*. *Perspektivnye Materialy*. 2009;1: 91–4. (in Russ). Available at: https://elibrary.ru/item.asp?id=11779849

23. Meng F., Li M., Zhang R., Yuan Z. Room temperature n-butanol detection by Ag-modified In_2O_3 gas sensor with UV excitation. *Ceramics International*. 2025;51(2): 1764–1773. https://doi.org/10.1016/j.ceramint.2024.11.152

24. Roopa, Kumar Pradhan B., Kumar Mauraya A., Chatterjee K., Pal P., Kumar Muthusamy S. High-sensitive and fast-responsive In_2O_3 thin film sensors for dual detection of NO_2 and H_2S gases at room temperature. *Applied Surface Science*. 2024;678: 161111. https://doi.org/10.1016/j.apsusc.2024.161111

25. Kahandal A., Chaudhary S., Methe S., Nagwade P., Sivaram A., Tagad C. K. Galactomannan polysaccharide as a biotemplate for the synthesis of zinc oxide nanoparticles with photocatalytic, antimicrobial and anticancer applications. *nternational Journal of Biological Macromolecules*. 2023;253(P3): 126787. https://doi.org/10.1016/j.ijbiomac.2023.126787

26. Yan S., Ma S., Xu X.,… Yang H. Synthesis and gas sensing application of porous CeO_2-ZnO hollow fibers using cotton as biotemplates. *Materials Letters*. 2016;165: 9–13. https://doi.org/10.1016/j.matlet.2015.11.095

27. Song B. Y., Huang J., Cui Z. Q. … Gao S. Temperature-controlled dual-selectivity nitric oxide/acetone sensor constructed from mesoporous SnO_2 tubes doped by biomass-derived graphitic carbon. *Applied Surface Science*. 2023;623(3): 157009. https://doi.org/10.1016/j.apsusc.2023.157009

28. Shaposhnik A. V., Moskalev P. V., Arefieva O. A., Zvyagin A. A., Kul O. V., Vasiliev A. A. Selective determination of hydrogen in a mixture with methane using a single metal oxide sensor. *International Journal of Hydrogen Energy*. 2024;82: 523–530. https://doi.org/10.1016/j.ijhydene.2024.07.379

* *Translated by author of the article*

Information about the authors

Alexey V. Shaposhnik, Dr. Sci. (Chem.), Professor at the Department of Chemistry, Voronezh State Agrarian University (Voronezh, Russian Federation).

https://orcid.org/0000-0002-1214-2730

a.v.shaposhnik@gmail.com

Olesya A. Arefieva, graduate student at the Department of Chemistry, Voronezh State Agrarian University (Voronezh, Russian Federation).

https://orcid.org/0009-0000-9629-2615

behappy.89@mail.ru

Alexey A. Zviagin, Cand. Sci. (Chem.), Associate Professor at the Department of Chemistry, Voronezh State Agrarian University (Voronezh, Russian Federation).

http://orcid.org/0000-0002-9299-6639

a.a.zviagin@rambler.ru

Nickolay Yu. Brezhnev, Cand. Sci. (Chem.), Senior Lecturer at the Department of Chemistry, Voronezh State Agrarian University (Voronezh, Russian Federation).

https://orcid.org/0000-0002-3287-8614

brezhnevnick@gmail.com

Elena A. Vysotskaya, Dr. Sci. (Biol.), Professor at the Department of Processes and Apparatuses of Processing Industries, Voronezh State Agrarian University (Voronezh, Russian Federation).

https://orcid.org/0009-0005-5992-7139

Murka1979@mail.ru

Alexey A. Vasiliev, Dr. Sci. (Tech.), Head of the Laboratory of Sensor Systems, Dubna State University (Dubna, Moscow region, Russian Federation).

http://orcid.org/0000-0002-7416-1638

A-A-Vasiliev@yandex.ru

Stanislav V. Ryabtsev, Dr. Sci. (Phys.-Math.), Head of the Institute of Physics, Voronezh State University (Voronezh, Russian Federation).

https://orcid.org/0000-0001-7635-8162

ryabtsev@phys.vsu.ru

Sergey Yu. Turishchev, Dr. Sci. (Phys.-Math.), Associate Professor, Head of the General Physics and Physical Materials Science Department, Voronezh State University (Voronezh, Russian Federation).

https://orcid.org/0000-0003-3320-1979

tsu@phys.vsu.ru

Received April 3, 2025; approved after reviewing April 21, 2025; accepted for publication May 15, 2025; published online December 25, 2025

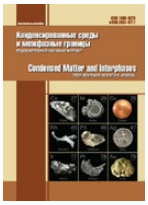

ISSN 1606-867X (Print)
ISSN 2687-0711 (Online)
Condensed Matter and Interphases
Kondensirovannye Sredy i Mezhfaznye Granitsy
https://journals.vsu.ru/kcmf/

Anniversaries

https://doi.org/10.17308/kcmf.2025.27/13343

Congratulations to Professor A. G. Syrkov

V. I. Margolin✉

Saint Petersburg Electrotechnical University «LETI»,
5 lit. F, Professor Popov st., Saint Petersburg 197022, Russian Federation

Abstract

On the eve of the 250th anniversary of the first graduating class of engineers at the St. Petersburg Mining Institute of Empress Catherine II, the 165th anniversary of the birth of academician N. S. Kurnakov and the 120th anniversary of the discovery of Weimarn's law it is important to remember those who continue to preserve the memory of these significant events. Professor A.G. Syrkov, celebrating his seventieth birthday, and his research team have been following their own unique path. By arranging international seminars and symposiums on relevant scientific topic "Nanophysics and Nanomaterials" (N&N), the event planners always dedicate a portion of the presentations to the work of outstanding scientists who stood at the origins of Russian schools in the fields of materials science, nanotechnology and metallurgy.

For citation: Margolin V. I. Congratulations to professor A. G. Syrkov. *Condensed Matter and Interphases*. 2025;27(4): 696–702. https://doi.org/10.17308/kcmf.2025.27/13343

Для цитирования: Марголин В. И. Поздравления профессору А. Г. Сыркову. *Конденсированные среды и межфазные границы*. 2025;27(4): 696–702. https://doi.org/10.17308/kcmf.2025.27/13343

Professor of the St. Petersburg Mining University of Empress Catherine II, Full Member of the Russian Academy of Natural Sciences, organizer and scientific head of the international symposium "Nanophysics and Nanomaterials" Andrey Gordianovich Syrkov will celebrate his 70th birthday at the end of January 2026. We congratulate him on this wonderful milestone anniversary and wish him robust health, new creative projects, well-being, success and good luck in his scientific and educational activities and in his dedicated labors and initiatives!

Born on January 29, 1956 in Leningrad. In 1979, he graduated with honors from the Leningrad Lensovet Institute of Technology (Technical University) and was assigned to the position of assistant at the Solid State Chemistry Department of Leningrad State University named after A.A. Zhdanov. While studying in a correspondence postgraduate program, he prepared and defended his Candidate of Sciences dissertation (PhD thesis) ahead of schedule in 1984 in the specialty «Physical Chemistry». His work focused on surface reactions in the chemical metallization of silica and hydridopolysiloxane. The work was carried out under the supervision of the Rector

✉ Vladimir I. Margolin, e-mail: v.margolin@mail.ru

of Leningrad State University, Corresponding Member of the USSR Academy of Sciences V.B. Aleskovsky – the founder of the world–famous scientific school in the field of nanotechnology by the method of molecular layering and chemical assembly of solids, the author of the "framework" hypothesis and concepts of informational and quantum synthesis of highly organized substances and materials [1,2]. In 1988, A.G. Syrkov became the head of the Faculty of Advanced Training "Scientific Foundations and Methods of solid-state Technology" of Leningrad State University. Since 1989, he has been an associate professor; in 1990, he received the academic title of Associate Professor.

In 1996, he joined Metal Polymer CJSC where he completed the implementation of the results of his doctoral research at the Prometey Central Scientific Research Institute of Structural Materials and the Research Institute of "Energostal". In 1999, he defended his doctoral thesis "Hydride solid-state synthesis of metallic substances and its fundamental patterns" at St. Petersburg State Technological Institute (Technical University) in the specialty "Chemistry and Physics of Surfaces". In this work, Syrkov A.G. formulated a new scientific direction – the influence of the reducing agent on the structure and reactivity of dispersed metallic materials.

From 1996 to 2001, he worked as Deputy Director for Scientific Research at Metal Polymer CJSC and concurrently as Director for Science and Development at Pimtek LLC (St. Petersburg). Here he began to develop formulations of industrial lubricants that have been repeatedly tested on the conveyors of leading brewing companies in Russia. At the same time, he heads the retraining of specialists at St. Petersburg State University Faculty of Advanced Training "Scientific foundations and methods for obtaining modern detergents." In 2001, at the invitation of Professor E.I. Boguslavsky begins teaching at the Department of General and Technical Physics (GTP) of the St. Petersburg State Mining Institute (Technical University). At the department, he continued to research and create new lubricating and corrosion-resistant materials,developing and expanding relevant sections of physics, physical chemistry, as well as metallurgy and materials science [3–5].

Since 2001, A.G. Syrkov has been actively publishing in the scientific journal "Condensed Matter and Interphases" [6–8]; since 2004, also in the scientific-technical and industrial journal "Tsvetnye Metally" [9]. Both journals are included in the list of the Higher Attestation Commission of Russia (HAC) and in the international citation-analytical database Scopus. In 2005, on the initiative of Professor I.. Beloglazov (1950-2011) and the leadership of the «Ore and Metals» Publishing House, he became a member of the editorial board for the special thematic issue «Nanostructured Metals and Materials» published based on the journals "Tsvetnye Metally" and "Non-ferrous Metals" (Moscow) [10, 11]. From 2012 to 2021, he was a member of the editorial board of the scientific journal "Journal of Mining Institute" (a HAC-listed journal and a Q1 journal in Scopus). From 2013 to 2017, he was a member of the editorial board of the scientific journal "Smart Nanocomposites"; since 2018, he is a member of the editorial board of the journal "Smart Nanocomposites Letters" (USA). Syrkov A. G. is a reviewer for articles in the following journals: Journal of Mining Institute; Tsvetnye Metally; Condensed Matter and Interphases; Izvestiya VUZ; Glass Physics and Chemistry; Journal of Surface Investigation: X-Ray, Synchrotron and Neutron Techniques.

In 2003, Syrkov A. G. successfully applied for and moved from the position of associate professor to the position of professor; in 2006, he received the academic title of Professor in the Department of General and Technical Physics (GTP). In 2003, he organized the scientific seminar «Nanophysics and Nanomaterials» and became its scientific director. Since 2013, by order of the Rector of the Mining University (SPMI), the seminar has officially held the status of an international seminar (symposium) [12–14].

The annually held «Nanophysics and Nanomaterials» (N&N) symposium serves not only for the traditional exchange of scientific and technical information, discussions on presentations, but also for the preliminary defense of materials for future Candidate and Doctor of Sciences dissertations. Over the 22 years of the symposium's operation, hundreds of degree candidates from 15 universities in Russia and Belarus, including Moscow State University,

Saint Petersburg State University, Voronezh State University, Belarusian State Technological University; from universities in China, Egypt, Vietnam; and from academic institutes in Russia, Belarus, Azerbaijan (Ioffe Physico-Technical Institute of the Russian Academy of Sciences, Institute of Metallurgy of the Ural Branch of the Russian Academy of Sciences (IMET UrB RAS), Institute of Chemistry of Silicates of the RAS, Institute of High-Molecular Compounds of the RAS, Institute of Geology of the Karelian Research Centre of the RAS (IG KarRC RAS), Joint Institute of Machine Building of the National Academy of Sciences of Belarus, Metal–Polymer Research Institute of National Academy of Sciences of Belarus, etc.) have presented their research results at its plenary sessions, section meetings, and round tables. Among the organizations that have presented their reports at the N&N symposium are also Princeton University, West Virginia University (USA), University of Campinas (Brazil), IMC Montan (UK), and Beneq (Finland).

The most important and distinctive feature of the N&N symposium, conducted under the leadership of A.G. Syrkov, is that a portion of the presentations at the meetings is always dedicated to the memorial dates and great scientists who made decisive contributions to the formation of famous national scientific schools in metallurgy, materials science, nanotechnology, as well as the physics, chemistry, and technology of low-dimensional structures and materials. The reports presented on this topic necessarily analyze not only the biographical data of scientists, but also the connection with modern research, the real directions of the development of the works of these scientists in the 21st century [14–16]. The authorship of the cited works clearly

Professor Syrkov A. G. with his research team, which organizes and conducts the International Symposium “Nanophysics and Nanomaterials» (since 2003)

demonstrates the active participationof students and postgraduates from the Mining University. Leading Professor of the GTP Department A. G. Syrkov gives lectures on physics and nanotechnology to about two hundred students every semester.As a result, these students know who N. S. Kurnakov, P. P. Weimarn, V. B. Aleskovsky, L. A. Sena, I. N. Beloglazov are and what these scientists did for the priority of Russian science. This mission of the N&N symposium and Professor Syrkov's lectures is extremely important today for the patriotic education of the young generation.

In 2008, A. G. Syrkov was elected a Corresponding Member of the Russian Academy of Natural Sciences, and in 2012, a Full Member of the Russian Academy of Natural Sciences in the mining and metallurgy section. Currently, Andrey Gordianovich Syrkov is the Scientific Supervisor for the «Nanotechnology» direction at the Mining University, an expert for UNESCO, the National Research Centre «Kurchatov Institute» (Moscow), and the London-based Institute of Materials, Minerals and Mining (IOM3). In 2024, he became a member of the Materials Science Section of the St. Petersburg Branch of the Russian Academy of Sciences (by invitation of Academician V. Ya. Shevchenko). A. G. Syrkov is a recognized specialist in the physics, chemistry, and technology of metal surfaces [17–19]. He developed the theory and patented methods for the solid-phase hydride synthesis of nanostructured metallic materials and the layering of variously sized quaternary ammonium compound molecules on metals [8, 20, 21]. He has original works in the field of nonlinear properties of surface-modified metals [3, 14, 28]. The developments of Syrkov A. G. and his students have been implemented at ten enterprises in the mineral resource sector of Russia and Belarus with a total annual economic effect exceeding 100 million rubles [3, 5, 14].

In addition to active scientific and organizational work, Syrkov A.G. conducts intensive research together with his postgraduates, students, and faculty members–young Ph.D. (Candidate of Sciences) holders [3, 15, 16] (see team photo). Professor Syrkov A. G. leads the Mining University's world-class research direction «Nanostructured highly hydrophobic metals and solid-state methods for their synthesis» [14, 17, 23]. In recent years, under his leadership, projects No. 5279 and No. 8635 under the thematic plan of fundamental research within state assignments of the Russian Ministry of Science and Higher Education, and contract No. 18017 with GMC Company (Moscow) have been executed; the research team participated in the implementation of several state contracts (2012–2020) and in research under a grant from the Foundation for Assistance to Innovations (contract No. 16679GU/2021) in 2021–2023 [23, 24]. A.G. Syrkov is a co-author of more than 220 scientific works, 8 monographs, 15 textbooks, and 17 inventions. The research team he led won a competition and received two awards from the International Fund "Generation" in the nomination "Best scientific team in the Field of Nanomaterials and Nanotechnology". A. G. Syrkov has supervised 3 Doctors and 15 Candidates of Sciences to successful dissertation defenses, including two international scholars.

His successful supervision of postgraduates in 2021-2024 has been repeatedly acknowledged with letters of appreciation and an award from the leadership of the St. Petersburg Mining University. Students and postgraduates not only at SPMI but also at St. Petersburg State Technological Institute (Technical University) and Saint Petersburg Electrotechnical University "LETI" study from books and textbooks on nanotechnology written by Syrkov. In 2019, "LETI" University purchased an additional print run of Syrkov A. G.'s book [25], dedicated to surface physics and the laws of P. P. Weimarn, from the SPbPU publishing house. Currently, students from 11 groups at "LETI" study from this book, including those specializing in the Department of Microradioelectronics and Radio Equipment Technology. The university leadership of SPMI and the book's author received a formal letter of appreciation from the Vice-Rector of «LETI».

At the International N&N symposium organized by A. G. Syrkov, where he is a co-chairmanof the organizing committee, in addition to presentations by young scientists, many substantial plenary lectures have been delivered by: Professor Y. Nakanishi (Shizuoka University, Japan); I. Kaganovich (Princeton University, USA); M. Brzhezinskaya (Helmholtz Centre,

Germany); Corresponding Member of the NAS of Belarus N. R. Prokopchuk; S. N. Saltykov (NLMK); N. N. Rozhkova (IG KarRC RAS); V. N. Pak; N. M. Barbin (IMET UrB RAS) and others. A special mention deserves the preliminary defense of materials related to a scientific discovery (Diploma No. 509), conducted at N&N by Professor A. S. Mustafayev [17, 23].

The scientific level of presentations at N&N is such that articles and chapters based on their materials are published in publications included in the Scopus database [18, 26, 27], including high-quartile journals [28–30]. These materials align with the global trend of advanced research in nanotechnology, nanoelectronics [31–33], and related fundamental research [34–36]. By dedicating presentations and articles to the anniversaries of N. S. Kurnakov, P. P. Weimarn, V. B. Aleskovsky, K. F. Beloglazov, I. N. Beloglazov [14, 16, 23], the participants of the N&N symposium make an invaluable contribution to preserving the historical memory of the representatives of the best national scientific schools in metallurgy, nanotechnology, and materials science [37]. On the initiative of N&N Organizing Committee members from St. Petersburg State Mining Institute (Technical University), since 2021, a special Professor P. P. Weimarn Prize for outstanding scientists in the field of nanotechnology has been awarded at the symposium's annual meetings. It is worth emphasizing the objectivity of the selection of laureates by the N&N Organizing Committee under the leadership of Syrkov A. G. In the year of awarding the prize, its holders, as a rule, independently received confirmation of their merits from other (scientific or government) structures. For instance, M. M. Sychev in 2022, besides the prize, received the Academician Grebenshchikov Prize from the Presidium of the RAS; N. R. Prokopchuk in 2023 received the Order of Labor Glory from the President of Belarus; N. N. Rozhkova (N&N laureate in 2024) in 2025 received the honorary title "Honored Scientist of the Republic of Karelia".

The achievements of our honoree, Professor Syrkov A. G., in studying the historiography of nanomaterials and proving the priority of Russian science (represented by Professor P. P. Weimarn) in the field of nanotechnology deserve special note. In 2023, the editorial board of the Great Russian Encyclopedia (GRE) approached us and Andrey Gordianovich with a request to write an article about the scientific activities of Professor Petr Weimarn of the Mining Institute (SPMI). We provided so much material that we ended up with 3 articles. One of them, the most detailed on the given topic, was presented personally by A. G. Syrkov [38]. This article was highly appreciated by the Editorial Board of Chemical Sciences of the GRE. Considering the jubilarian's other works in this direction [15, 23, 25] (he has a total of 20 works on P. P. Weimarn), the following can be stated. By the end of 2025, A. G. Syrkov has established himself as a unique specialist, perhaps the only one in the world, with such a profound understanding of the essence of P. P. Weimarn's scientific heritage, including the physicochemical meaning of Weimarn's works and issues of historiography. Syrkov A. G. today appears to be the most knowledgeable regarding the details of Weimarn's activities during his three life stages (in St. Petersburg, Yekaterinburg, and Japan), as well as the connections and continuity with the works of N.S. Kurnakov, I.F. Schroeder, Wolfgang Ostwald (Germany), V. B. Aleskovsky, and other renowned scientists. The high professionalism in the field of physicochemistry of nanomaterial production is reflected by the fact that the honoree, as follows from the above, remains an active scientist in the topic that Weimarn worked on [15]. This favorably distinguishes Syrkov A. G.'s works from those of historiographers, who mainly track the chronology of events in a scientist's life.

In our article on the occasion of Professor Syrkov A. G.'s 60th birthday [19], we wrote about some of the jubilarian's hobbies and his birthday celebration traditions. We would like to confirm that Andrey Gordianovich is still interested in the history of his family together with his brother. The family line is very interesting: ancestors Ivan, Fedor, and Dmitry Syrkov in the 16th century, by the tsar's command or as patrons themselves, built over 20 famous churches in Veliky Novgorod, Tikhvin, and other cities [24]. Syrkov Afanasy Konstantinovich, a shipbuilding scientist and uncle of Syrkov A.G., according to a biographical reference book published for the 300th anniversary of St. Petersburg [39], entered the thousand most popular St.

Petersburg (Leningrad) residents of the 20th century. Syrkov A. K. – commander of the Order of Lenin, laureate of the State Prize in Science and Technology, author of books and textbooks on ship and shipyard construction – always served as an example of dedication for Syrkov A. G. Another example for Andrey Gordianovich is his father, Gordian Konstantinovich, a Naval officer who received 18 state awards (medals and badges) for impeccable service on the ships of the Baltic and Northern Fleets. Syrkov A. G. still, if the weather permits, makes a ski run through Alexandrino Park on his birthday. Due to the lockdown in 2021/22, he sings less than before [24], but does so with pleasure. He relates to this milestone with a degree of irony, likening it to a score of 7:0 in favor of the jubilarian and his family. Since the author of this article is closely approaching the "8:0" mark, he has the right to tell the honoree that the fruitful time for writing books and interesting work is not over yet. We wish Andrey Gordianovich good Health and that his sons bring him even more joy than before!

As the main conclusions of this article, the following can be noted. Professor Syrkov A. G. approaches his milestone anniversary with strong results and achievements in scientific and educational activities. His special contribution to the science of nanotechnology and nanostructured metallic materials is associated with the creation of the theory, development of technology, and implementation of highly hydrophobic, corrosion-resistant dispersed materials with an anti-friction surface effect. His scientific, organizational, social and teaching activities are characterized by the successful training of Candidates and Doctors of Sciences for the mineral resource complex of the Union State, high-level professional proof of the priority of Russian science in nanotechnology, which gives the younger generation the opportunity to better know their "roots" and more effectively develop the work of great predecessor scientists.

The editorial board of the journal "Condensed State and Interphases" joins in congratulating and wishing success in all endeavors our great friend and sincerely respected professor Andrei G. Syrkov

References

1. Aleskovskiy V. B. *Chemistry of supramolecular compounds*.* St. Petersburg: Publishing house of St. Petersburg State University, 1996. 256 p.

2. Aleskovskii V. B. Quantum synthesis. *Russian Journal of Applied Chemistry*. 2007;80(11): 1785–1792. https://doi.org/10.1134/s1070427207110018

3. Syrkov A. G., Fadeev D. V., Taraban V. V, Silivanov M. O. Quantitative estimation of nonlinear effects in dependence of integral index of friction for tribosystem from water-repellent properties of a meta-filler. *Condensed Matter and Interphases*. 2014;16(2): 215–219. (in Russ.). Available at: https://elibrary.ru/item.asp?id=21785803

4. Syrkov A. G., Silivanov M. O., Sychev M. M., Rozhkova N. N. Alteration of the acid-base properties of the oxidized surface of disperse aluminum during the adsorption of ammonium compounds and the antifriction effect. *Glass Physics and Chemistry*. 2018;44(5): 474–479. https://doi.org/10.1134/s1087659618050206

5. Syrkov A. G., Prokopchuk N. R. Dispersed iron obtaining by the method of solid state hydride synthesis and the problem of hydrophobi**c**ity of metal. *CIS Iron and Steel Review*. 2021;21(1): 16–22. https://doi.org/10.17580/cisisr.2021.01.03

6. Syrkov A. G., Makhova L. V., Korsakov V. G. Effect of reducing agent on the state of atoms in the surface layer and chemical stability of the resulting metal. *Condensed Matter and Interphases*. 2001;3(4): 323–326. (in Russ.)

7. Syrkov A. G., Pleskunov I. V., Taraban V. V., Kavun V. S., Kushchenko A. N. Changes in the sorption properties of dispersed copper containing ammonium compounds in the surface layer resulting from interaction with water vapours. *Condensed Matter and Interphases*. 2019;21(1): 146–154. (in Russ.). https://doi.org/10.17308/kcmf.2019.21/725

8. Syrkov A. G., Kabirov V. R., Pomogaibin A. P., Kkhan N. K. Electrophilic-nucleophilic properties as a factor in the formation of antifriction and hydrophobic properties of surface-modified metals with ammonium and organosilicon compounds. *Condensed Matter and Interphases*. 2021;23(2): 282–290. https://doi.org/10.17308/kcmf.2021.23/3478

9. Syrkov A. G. Novel ways and fundamentals of metals nanotechnology*. *Tsvetnye Metally*. 2004;4: 67–71. (in Russ.). Available at: https://elibrary.ru/item.asp?id=19019087

10. Syrkov A. G. Methods of physics and chemistry in obtaining nanostructured metals and in nanotribology*. *Tsvetnye Metally*. 2005;9: 12–18. (in Russ.). Available at: https://www.rudmet.ru/journal/1073/article/17492/

11. Beloglazov I. N., Syrkov A. G. Nano-structured metals and materials: urgency of problems and availability of investigations. *Non-ferrous Metals*. 2006;4: 3–4.

12. Syrkov A. G. All-Russian seminar with international participation "Nanophysics and Nanomaterials". *Condensed Matter and Interphases*. 2014;16(1): 103–110. (in Russ.). Available at: https://www.elibrary.ru/item.asp?edn=schkst

13. Syrkov A. G. International seminar-symposium "Nanophysics and Nanomaterials". *Condensed Matter and Interphases*. 2016:18(1): 159–165. (in Russ.). Available at: https://www.elibrary.ru/item.asp?id=25946639

14. Syrkov A. G., Makhovikov A. B., Tomaev. V. V., Taraban V. V. Priority in the field nanotechnologies of the

Mining University in Saint Petersburg — a modern centre for the development of new nanostructured metallic materials. *Tsvetnye Metally*. 2023:8; 5-13. https://doi.org/10.17580/tsm.2023.08.01

15. Syrkov A. G, Kushchenko A. N., Maslennikov A. A. Professor P. P. Weimarn, founder of the science of nanotechnology: development of works in the field of nanodispersed metals production. *Non-ferrous Metals*. 2024;1: 63–71. https://doi.org/10.17580/nfm.2024.01.10

16. Syrkov A. G., Kushchenko A. N., Yachmenova L. A., Bogopriimtseva M. A. Metallurgists K. F. Beloglazov I. N. Beloglazov and nanotechnologies. *Non-ferrous Metals*. 2025;1: 99–108. https://doi.org/10.17580/nfm.2025.01.13

17. Popova A. N., Klimenkov B. D., Grabovskiy A. Y. Scientific school of plasma nanotechnologies and plasma power engineering in Mining university. *Izvestiya VUZ. Applied Nonlinear Dynamics*. 2021;29(2): 317–336. https://doi.org/10.18500/0869-6632-2021-29-2-317-336

18. Sokhovich E. V., Tomaev V. V., Taraban V. V., Pleskunov I. V. Optimized sol-gel synthesis of WO_3 hydrogel for obtaining electrochromic films. *Non-ferrous Metals*. 2023;8: 39–43. https://doi.org/10.17580/tsm.2023.08.07

19. Margolin V. I., Tomaev V. V. Congratulations to professor A. G. Syrkov. *Condensed Matter and Interphases*. 2016;18(1): 166–168. (in Russ.). Available at: https://www.elibrary.ru/item.asp?id=25946640

20. Syrkov A. G., Kushchenko A. N., Silivanov M. O., Taraban V. V. Nanostructured regulation of the surface properties and hydrophobicity of nickel and iron by solid-state reduction and modifying methods. *Non-ferrous Metals*. 2022;5: 54–59. https://doi.org/10.17580/tsm.2022.05.07

21. Beloglazov I. N., Syrkov A. G. *Chemical and physical principles and methods for producing surface-nanostructured metals**. St. Petersburg: St. Petersburg State University Publ.; 2011. 72 p. (in Russ.)

22. Syrkov A. G. *Nanotechnology and nonlinearity of properties of nanomaterials*. St. Petersburg: Publishing house of the Polytechnic University; 2015. 188 p. (in Russ.)

23. Syrkov A. G., Kushchenko A. N., Silivanov M. O. *Nanotechnology and nanomaterials. The significance and development of the works of Kurnakov and Weimarn**. St. Petersburg: Polytech-Press; 2022. 240 p. (in Russ.)

24. Petrov D. A., Syrkov P. G. *Construction and service of the Syrkovs**. St. Petersburg: Publishing house of the Polytechnic University. 2016. 256 p. (in Russ.)

25 Syrkov A. G. *Elements of surface physics and nanotechnology. Weymarn's doctrine and laws**. St. Petersburg: Publishing house of the Polytechnic University, 2018. 207 p. (in Russ.)

26. *New Materials: Preparation, properties and applications in the aspect of nanotechnology*. New York: Nova Science Publishers, Inc.; 2020. 249 p.

27. *Applied Aspects of Nano-Physics and Nano-Engineering*. New York: Nova Science Publishers, Inc.; 2019. 308 p.

28. Pak V. N., Lapatin N. A., Pronin V. P., Yachmenova L. A. Obtaining and electronic emission of planar structures of metallic copper on a porous ceramic substrate. *Tsvetnye Metally*. 2021;5: 55–58. https://doi.org/10.17580/tsm.2021.05.06

29. Tupik V. A., Margolin V. I., Kostrin D. K., Potapov A. A. Deposition of nanoscale metal films with the help of arc discharge. *Tsvetnye Metally*. 2021;6: 55–59. https://doi.org/10.17580/tsm.2021.06.08

30. Mustafaev A. S., Grabovskiy A. Y., Sukhomlinov V. S., Shtoda D. V. Technology for monitoring the surface emission inhomogeneity in plasma electronics devices. *Journal of Applied Physics*. 2024;20: 1 12. https://doi.org/10.1063/5.0233459

31. Latif W. A., Al-Owaidi M. N. Review article: sol-gel method, "synthesis and applications". *World Journal of Advanced Engineering Technology and Science*. 2023;8(2): 160–166. https://doi.org/10.30574/wjaets.2023.8.2.0071

32. Trandsekaran P., Su C.-H., Liu Y.-H., Lu K.-L. Hydrophobic metal-organic frameworks and derived composites for microelectronic applications. *Chemistry – A European Journal*. 2021;23: 16543–16563. https://doi.org/10.1002/chem.202100241

33. Wei. T., Dang S. X. Direct laser texturing technique for metal surfaces to achieve superhydrophobicity. *Materials Today Physics*. 2022;3: 100651. https://doi.org/10.1016/j.mtphys.2022.100651

34. Cai Y., Michiels R., De Luca F., ... Gerritis N. Improving molecule-metal surface reaction networks using the meta-generalized gradient approximation: CO_2, hydrogenation. *Journal of Physical Chemistry C: Nanomaterial Interfaces*. 2024;128: 8611–8620. https://doi.org/10.1021/acs.jpcc.4c01110

35. Sergeev V. V., Cheremisina O. V., Fedorov A. T., Gorbacheva A. A., Balandinsky D. A. Interaction features of sodium oleate and oxyethylated phosphoric acid esters with the apatite surface. *ACS Omega*. 2022;7(3): 3016–3023. https://doi.org/10.1021/acsomega.1c06047

36. Cheremisina O. V., Gorbacheva A. A., Balandinsky D. A., Luo Yunizhou, Ponomareva M. A. Synergetic effect of a mixture of ethoxyphosphoric esters and sodium oleate in aqueous solutions. *Colloids and Surfaces A: Physicochemical and Engineering Aspects*. 2024;685: 1–10. https://doi.org/10.1016/j.colsurfa.2024.133314

37. Borzenkov V. T., Brichkin V. N. International competence Center for Mining Engineering Education under the auspices of UNESCO, and its mission in education, science and culture. *Gornyi Zhurnal*. 2025;8: 4–13. https://doi.org/10.17580/gzh.2025.08.01

38. Petr P. von Weymarn. *Great Russian Encyclopedia*. (in Russ.). Available at: https://bigenc.ru/c/veimarn-piotr-petrovich-fon-b63837

39. Dotsenko V. D., Mironov V. F. *Famous people of St. Petersburg: Biographical dictionary**. St. Petersburg: D.A.R.K. Publishing House; 2003. 368 p.

** Translated by author of the article*

Information about the author

Vladimir I. Margolin, Dr. Sci. (Engin.), Full Professor, Department of Microradioelectronics and Radio Technology, Saint Petersburg Electrotechnical University LETI (Saint-Petersburg, Russian Federation).

https://orcid.org/0000-0002-6322-0727

v.margolin@mail.ru

Received December 1, 2025; published online December 25, 2025

Translated by Vladimir I. Margolin